University of Southampton

Faculty of Engineering and Physical Sciences

Optoelectronics Research Centre

Novel 2D Transition Metal Dichalcogenide Synthesis Methods for Electronic and Photonic Device Applications

by

Omar Adnan Abbas

ORCID ID 0000-0002-3067-5311

Thesis for the degree of Doctor of Philosophy

March 2020

University of Southampton

Abstract

Faculty of Engineering and Physical Sciences

Optoelectronics Research Centre

Thesis for the degree of Doctor of Philosophy

Novel 2D Transition Metal Dichalcogenide Synthesis Methods for Electronic and Photonic Device Applications

by

Omar Adnan Abbas

Soon after the discovery of graphene, two-dimensional transition metal dichalcogenides (2D-TMDC) started to receive global attention. 2D-TMDC are Van der Waals materials like graphene except that they possess excellent semiconducting properties which makes them potential silicon alternatives for next generation electronics and optoelectronics. Nevertheless, finding a technologically applicable production method for these materials is still a key challenge. Despite there is a plethora of precursors that can be used for 2D-TMDC growth, solution-based single source precursors like ammonium tetrathiotungstate $(NH_4)_2WS_4$ and ammonium tetrathiomolybdate $(NH_4)_2MoS_4$ are very attractive for industrialization due to their facile processing route to produce scalable TMDC films as well as cost-effectiveness. Hence, this method was studied intensively during the last decade for MoS_2 while for WS_2 there was no such progress due to complications of depositing uniform single source precursor films.

Therefore, the main goal of this PhD thesis is to explore novel synthesis methods for 2D-WS_2 and 2D-MoS_2 using solution based single source precursors. Additionally, initial validation of these synthesis methods as potential industrial platforms for 2D electronics and photonics was performed by fabricating prototype devices. Leveraging from well-established solution-based synthesis of large area 2D-MoS_2 films, an Indium-2D-MoS_2 metal-semiconductor-metal photodiode was successfully realised using simple metallisation step. Furthermore, for the first time a large area continuous/uniform fewlayer WS_2 films via thermolysis of $(NH_4)_2WS_4$ films was demonstrated which shows a potential application as field effect transistor device.

Finally, using solution-based single source precursors, a revolutionary direct laser synthesis of 2D-WS_2 and 2D-MoS_2 micro-patterns under ambient conditions has been developed. This method offers versatility, simplicity, patternability and the possibility to create TMDC device arrays, including alloys and heterostructures with minimal lithographic or thermal overheads. The results from this work could be the cornerstone towards laser assisted direct writing technology of 2D-TMDCs for electronics and photonics devices and circuits fabrication.

Table of Contents

Table of Tables

Table of Figures

Table of Figures

Table of Figures

Table of Figures

Declaration of Authorship

I, Omar Adnan Abbas, declare that this thesis entitled *Novel 2D Transition Metal Dichalcogenide Synthesis Methods for Electronic and Photonic Device Applications* and the work presented in it are my own and has been generated by me as the result of my own original research.

I confirm that:

1. This work was done wholly or mainly while in candidature for a research degree at this University;
2. Where any part of this thesis has previously been submitted for a degree or any other qualification at this University or any other institution, this has been clearly stated;
3. Where I have consulted the published work of others, this is always clearly attributed;
4. Where I have quoted from the work of others, the source is always given. With the exception of such quotations, this thesis is entirely my own work;
5. I have acknowledged all main sources of help;
6. Where the thesis is based on work done by myself jointly with others, I have made clear exactly what was done by others and what I have contributed myself;
7. Parts of this work have been published as: See Appendix A: List of publications.

Signature:

Date:

To the memory of my uncle ***Osama Adnan Ahmed*** *and my grandfather* ***Adnan Ahmed Nasir***

*Stand on the edge of your dream and **Fight**.*

Mahmoud Darwish

Acknowledgements

This thesis would never have been written without help, support and contribution of many kind people who stood beside me during my Ph.D. years, to only some of whom it is possible to give particular mention here.

First and foremost, I would like to show my deep gratitude to my supervisors Dr. Pier Sazio and Dr. Sakellaris Mailis for their patience, guidance, support and belief in me. Their insightful advices and endless encouragement in both research and life made me think more positively and look at challenges as opportunities. I also want to show my sincere appreciation to my sponsor, The Higher Committee for Education Development in Iraq (HCED Iraq) for their generous financial support which without it, I have never reached this level. Many thanks to Neil Sessions and Kathleen Leblanc who made dealing with complex tools in the clean room easier for me by their technical training and support. To my friends and colleges Adam Lewis and Jon Gorecki who dedicated hours from their busy schedule to help me with my Ph.D. project. I am also very grateful to Prof. Dan Hewak and his group for sharing with me their facilities, knowledge and lab experience. Special thanks to Ioannis Zeimpekis, Kevin Huang and Nikolaos Aspiotis for fruitful discussions and comments; for providing me with equipment and materials that I need to conduct my experiments; and for helping me to obtain spectroscopic data. To He Wang, Ghada Alzaidy and Andrea Ravagli for helping me.

I want to extend my thanks to my wonderful friends whom I met in Southampton during my Ph.D. journey. To Florian Leroi, Joseph Demir, Livio Pizzi, Maria Papa and Kasia Grabska for giving me international experience and for making this journey more enjoyable and unforgettable. To my Iraqi friends Muhammed Fadhel, Firas ma'an, Omar Mubashar, Zeyad Aaber, Haider Muhi, Ahmed Allami, Ahmed Yashar, Nawfal Firas and Yasir Noori for their hospitality, encouragement, support and helpful conversations. To my friend Dr. Muna Mustafa who motivated me through the whole process starting from getting my scholarship ending by writing my thesis.

Last but not least, I wish to thank my family for their understanding and love. To my brother Zaid for taking all duties during my absence. For my lovely sister Rand for her caring, kindness and silly jokes, also, to her little genies my nephew Ahmed and my niece Sala for the happiness they brought to our family. To my brother in law Furat for looking after them.

Finally, words cannot express my extreme gratefulness and thankfulness to my mother Maha, all what I achieved in my life was actually achieved by her sacrifices. From deep of my heart, thank you and I wish I can make you always proud.

Definitions and Abbreviations

A	Area of the diode
A*	Richardson constant
Ar	Argon
AFM	Atomic force microscopy
APCVD	Atmospheric pressure chemical vapour deposition
C_{ox}	Capacitance of silicon dioxide
CVD	Chemical vapour deposition
CVT	Chemical vapour transport
DFT	Density functional theory
DMF	Dimethylformamide
DMSO	Dimethylsulfoxide
e	Electron charge 1.6×10^{-19} coulombs
EDTA	Ethylenediaminetetraacetic acid
FET	Field Effect Transistor
FWHM	Full Width at Half Maximum
H_2	Dihydrogen
I	Electrical current in ampere (A)
Io	Reverse saturation current of the diode
IR	Infra-red
K	Boltzmann constant 1.38×10^{-23} m^2 kg s^{-2} K^{-1}
LED	Light emitting diode
LN	Lithium Niobate
LVDT	Linear variable differential transformer
MIMIC	Micromolding in capillaries

MoS_2	Molybdenum disulphide
MS_2	Transition metal disulphide (molybdenum and tungsten)
MSM	Metal-Semiconductor-Metal photodiode
MX_2	Transition metal dichalcogenide (chemical formula)
n	Ideality factor of diode
N_2H_4	Hydrazine hydrate
NMP	N-methyl-pyrrolidone
PL	Photoluminescence
PLD	Pulsed laser deposition
PVD	Physical vapour deposition
sccm	Standard cubic centimetres per minute
Si	Silicon
SiO_2	Silicon dioxide
T	Temperature in Kelvin
TED	Thermal evaporation deposition
TFT	Thin film transistor
THAB	Tetraheptylammonium bromide
TMDC	Transition metal dichalcogenide
UV	Ultra-violet
WS_2	Tungsten disulphide
XPS	X-Ray photoelectron spectroscopy
μ_{FET}	Field effect mobility
Φ_{metal}, Φ_{SB}	Work function of the metal and Schottky barrier in (eV)
X	Electron affinity of the semiconductor in (eV)

Chapter 1
Introduction

1.1 Motivation

Since the invention of field effect transistor (FET) in the middle of the last century, the demand to improve the efficiency of these devices and increase their number per chip is an unstoppable trend. This trend is expressed by "Moore's law" which predicts that the number of FET devices per chip is doubled every two years. Nowadays, silicon is the core material in semiconductor technology due to its excellent switching properties, abundance, reliability and affordability for commercial integrated circuits fabrication. However, by the end of last millennium, scientists started raising concerns about silicon miniaturization which might reaches the dimensional limits soon [1].One of the possible solutions for this issue is to find other materials that could go further in downscaling. In 2004, Novoselov et al. demonstrated that single atomic sheet of carbon possesses superior carrier mobility which what was called later graphene [2]. The ultra-thin nature of graphene in addition to excellent electrical, optical and mechanical properties triggered tremendous research efforts around the globe in a hope to fabricate graphene FET devices that can substitute silicon devices in near future. After few years, scientific community realised that graphene cannot be a good successor for conventional FET silicon technology due to zero band gap, i.e. it cannot switch-off efficiently.

Nevertheless, the revolutionary concept of 2D materials that has been established by graphene, brought other layered materials that share similar Van Der Waals structure to researchers' labs to explore their properties when they are thinned down to single layer just as graphene. Among these layered materials, transition metal dichalcogenides (TMDC) which are a family of compounds with over forty members received more attention for their electronic structure and properties [3]. Five members of this family have considerable indirect bandgaps in their bulk form (1 eV to 1.35 eV) which are: transition metal disulphides (MoS_2 and WS_2) [4]; transition metal diselenides ($MoSe_2$ and WSe_2) [4]; while molybdenum telluride ($MoTe_2$) has 1 eV band gap [5], its tungsten counterpart (WTe_2) is semimetal [6]. The presence of the band gap in these materials makes them attractive for electronic and optoelectronic applications.

In 2005, Novoselov investigated the carrier mobility of 2D-MoS_2 using backgated FET which shows n-type behaviour but the results were not as impressive as graphene [7]. Six years later, Radisavljevic et al. successfully fabricated a single-layer MoS_2 transistor with a hafnium oxide as a top-gate dielectric which boosts the mobility and the current on-off ratio of the MoS_2 monolayer FET device to be comparable with silicon counterpart [8]. The improvement in the MoS_2 device performance was attributed to high dielectric constant of hafnium oxide that supress Coulomb scattering, thus the predicted theoretical mobility of MoS_2 was realised [8].

Additionally, two groups published their experimental observations in 2010 about bandgap crossover of MoS_2 from indirect band gap in bulk form with 1.2 eV size to direct bandgap with 1.8 eV in monolayer regime which opens the door to investigate MoS_2 as monolayer light emitter [9], [10]. Later, the other transition metal dichalcogenides (WS_2, $MoSe_2$, WSe_2 and $MoTe_2$) showed similar indirect to direct bandgap transition when thickness is minimized to molecularly thin layer as well as excellent transistor characteristics [6]. To date, MoS_2 is the flagship of semiconductor transition metal dichalcogenides due to natural abundance (see Figure 1-1). MoS_2 was widely studied in the past few decades for catalyst and solid lubricant applications before the 2D materials boom [6]. It is also worth mentioning that MoS_2 was the first material has been exfoliated to single atomic layer before the graphene by 18 years [11]. However, this discovery did not reveal the dramatic changes occurring in electronic structure when the thickness of MoS_2 becomes single molecular sheet.

The low dimensionality, mechanical flexibility, tuneable electronic and optoelectronic properties that 2D-TMDC materials can offer, pave the way towards exploiting them in many applications such as transistors, diodes, photodetectors, sensors. Therefore, the number of publications related to these materials has been increased exponentially within the past few years as Figure 1-1 illustrates.

One of key challenges which these papers tried to address is to find a suitable synthesis method for large scale production that can be adaptable with current semiconductor technology to reach the commercialisation stage. To date, there is two main approaches which are the top-down and bottom-up one. Top-down approaches such as mechanical cleavage and liquid exfoliation basically rely on dimensional reduction of bulk TMDC crystals to few layers and monolayers, resulting in high quality TMDC nanosheets and flakes for prototyping and fundamental research but it seems that this route is not suitable for large scale production. The latter approach (bottom-up) is what the researchers try to develop in order to meet industrial requirements. Many precursors and synthesis routes have been proposed and developed to produce transition metal dichalcogenides ultra-thin films with high quality for semiconductor applications. However, many issues related to production methods are still persist and need to be addressed. The main challenges can be summarize in limited lateral dimensions of the 2D-TMDC films, controllability on number of layers (thickness) and quality (crystallinity and stoichiometry) of these produced films, cost-efficiency, complexity, adaptability with current technology, patternability and flexibility of these films for standard device fabrications.

The work presented in this Ph.D. thesis is mainly focuses on finding simple, cost-effective and patternable synthesis approaches of transition metal disulphides via solution based single source precursors that can be used for electronic and optoelectronic devices applications. The first protocol is for large area ultra-thin films and their potential applications as photodetector and FET for MoS_2 and WS_2 respectively. The second route is by laser-induced localized thermolysis of solution based single source precursors for TMDC microstructures and their applications as FET devices.

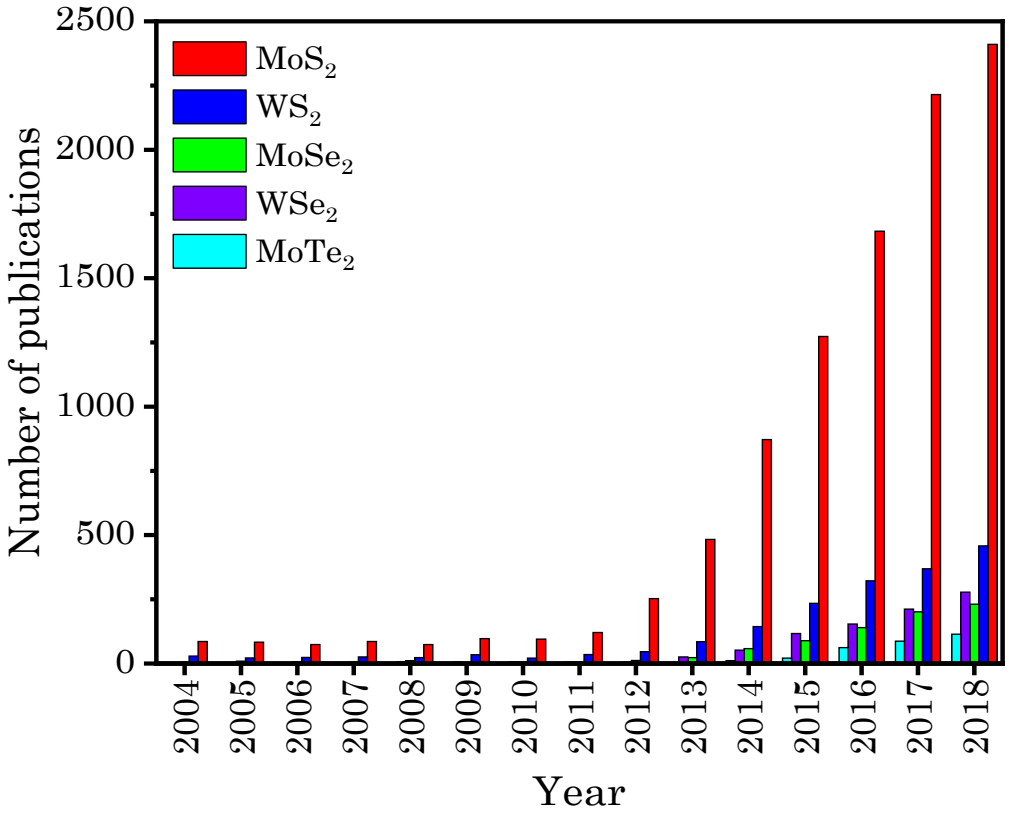

Figure 1-1: Number of publications per year for articles with MoS_2, WS_2, $MoSe_2$, WSe_2 and $MoTe_2$ in their titles.

Note: - the data source is web of science. The search for "MoS_2" included OR operator "molybdenum disulphide" and OR operator "molybdenum disulfide". The search for "WS_2" included OR operator "tungsten disulphide" and OR operator "tungsten disulfide". The search for "$MoSe_2$" included OR operator "molybdenum diselenide". The search for "WSe_2" included OR operator "tungsten diselenide". The search for "$MoTe_2$" included OR operator "molybdenum ditelluride".

1.2 Thesis Layout

Followed by this chapter, Chapter 2 introduces the reader briefly to transition metal disulphides (MS_2) crystal structure and its vibrational modes that can be detected via Raman spectroscopy as well as the phonon vibrations changes when the thickness is reduced up to quantum confinement boundaries. Moreover, electronic band structure is discussed and dramatic transition from indirect to direct bandgap when MS_2 crystals reach the mono and few-layer regime. The two main production methods which are top-down and bottom-up protocols and the literature related to them is reviewed thoroughly. The work on MoS_2 films produced by solution based single source precursor and the devices fabricated by this precursor is surveyed more critically as it is correlated to the experimental work that has been conducted in this Ph.D. project.

Chapter 3 describes the characterisation techniques performed in this work to evaluate thickness, crystallinity and compositions of MoS_2 and WS_2 films and microstructures. It starts with optical microscopy, atomic force microscopy (AFM) and Stylus profilometry to evaluate the thickness of produces films. In addition, Raman spectroscopy is illustrated and its important role to estimate the films thickness and crystallinity which was confirmed by photoluminescence spectroscopy especially in the case of WS_2. X-ray photoelectron spectroscopy (XPS) is an essential characterisation tool to probe the stoichiometry of our produced films and is also described.

Chapter 4 reports the experimental results of large area growth of MoS_2 films via thermal decomposition of solution-based single source precursor and the applications of these films as metal-semiconductor-metal photodiodes. Dark and photocurrent parameters are extracted as well as the proposed photoconduction mechanism is proposed.

Chapter 5 presents our novel approach to utilize solution based single source precursor to create uniform WS_2 few layers films via thermolysis of spin–coated precursors layers. A solvent recipe is suggested to tackle the continuity and uniformity issues of $(NH_4)_2WS_4$ when spun coated to create films. Moreover, a few-layer WS_2 films was used to fabricate FET device from this precursor for the first time.

Chapter 6 demonstrates our novel direct laser writing approach of transition metal disulphides using laser-induced thermolysis of spun-coated solution based single source precursors. The methodology is presented as well as the in-situ Raman/direct laser writing. Moreover, the versatility of our approach by growing MS_2 microstructure on different types of substrates is illustrated. The Stylus profilometry, Raman spectroscopy, PL spectroscopy and XPS spectroscopy assessments for different growth conditions are presented and analysed. Finally, four FET devices are characterized and MoS_2/WS_2 heterostructures that have been created by our method are presented.

Chapter 7 sum up the main findings from the experimental chapters and their contributions. Further suggestions to improve and develop this work in the future is reported as outlook.

Chapter 2
Structure, Properties and Synthesis of MS_2

2.1 Introduction

In this chapter, the fundamental background relevant to two dimensional transition metal disulphide (2D-TMDC) is presented. The structure of MS_2 crystal (where M= Mo Molybdenum, W Tungsten and S= Sulphur) and its analogy to graphene are illustrated. A summary of the structural and electronic properties of MS_2 in a bulk form is stated. Importantly, the dramatic changes that occur on electronic bandgap when thickness decreased from the bulk form to single and few molecular layer thickness are explained. This chapter highlights the significance of 2D-TMDs and give a clear understanding about the promising role of 2D-TMDs in post-silicon electronics and optoelectronics.

Furthermore, most of the novel experimental works that have been achieved in this thesis were mainly focused on exploring new approaches of MS_2 synthesis via single source precursor solutions for semiconductor device fabrication. Thus, this chapter emphasis on the intensive research effort have been directed to produce 2D-TMDs for electronic and optoelectronic applications. A brief review on various synthesis methods of these materials is given which could be classified in two main categories of MS_2 production: Top-Down and Bottom-Up.

The first one utilizes different techniques such as mechanical cleavage, liquid-phase exfoliation and thinning processes of the MS_2 bulk crystals until they reach mono and few molecular layers. The latter one is Bottom-Up approach (also called Vapour Deposition) which normally produces molecularly thin MS_2 films or flakes either via totally physical mechanisms (Physical Vapour Deposition) or via chemical reactions of precursors to prepare MS_2 films (Chemical Vapour Deposition).

However, both routes Physical Vapour Deposition (PVD) and Chemical Vapour Deposition (CVD) are further divided to subcategories. For PVD, there are three physical energy forms where used to transform the bulk MS_2 (powder or target) to thin films which are: heat (Thermal Evaporation Deposition TED), localized heat (Pulsed Laser Deposition PLD) and plasma (MS_2 Sputtering). On the other hand, CVD categorised based on the precursors that used in the initial chemical reactions to synthesize MS_2 which are sulphur with transition metal film, transition metal oxide, transition metal chlorides and thermal decomposition of thiosalts. Thermal decomposition of thiosalts is received more consideration as it is related to the current work of this thesis. Finally, this chapter could be a comprehensive introductory to cope with the recent advances and challenges of 2D-TMDs materials as well as provides the relevant information, concepts and terminology for the next chapters.

2.2 Structure and vibrational modes of MS_2

Similar to graphite, transition metal dichalcogenides family are layered materials, i.e., the atoms are arranged in sheets stacked to each other [12]. Generally, MX_2 is the formula for this family where M (e.g. Mo, W) represents the transition metal atoms sheet sandwiched between two layers of X chalcogenide atoms (e.g. S, Se). Although this family is very diverse (about 40 members), only four compounds (MoS_2, WS_2, $MoSe_2$ and WSe_2) of them received more attention in 2D materials due to their semiconductor properties [13]. However, all work has been conducted in this thesis focuses on disulphides rather than diselenides. The reasons behind this choice are: MS_2 possess excellent electrical and optical properties, with a plethora of precursors to prepare MS_2 with mild growth conditions. Therefore, they are closer for commercialisations in semiconductor industry with respect to their diselenides analogues.

MS_2 lattice structure exhibits a hexagon shape where each layer has broken symmetry because of the M-S bond. These M-S bonds are strong covalent bonds whereas the sulphur layers are bonded to each other by weak Van Der Waals forces which make them easy to split into individual layers. The striking difference in bonds strength is coming from the fact that the transition metal (Mo,W) share the four electrons in the outer shell with the two adjacent sulphur atoms forming S-M-S sheet with thickness about 0.65A^{o} leaving the S-S bonds between sheets to Van Der Waals forces. This structure is extended to all transition metal dichalcogenides family [12]. Due to weak nature of Van Der Waals forces, sulphur atoms can be arranged in different coordination and stacking orders creating different phases of MS_2. These phases are labelled by numbers from 1 to 3 to indicate the required number of MS_2 molecular layer for each individual unit cell, while the letter represents the type of symmetry which is T for tetragonal, H for hexagonal and R for rhombohedral [14].

2H phase is the most common phase with hexagonal symmetry and prismatic sulphur atoms arrangement which repeats itself for every two layers. It exists naturally and it is stable at ambient conditions with semiconductor properties. 3R phase is the second phase with similar sulphur atom arrangements in 2H phase. However, the unit cell repeat itself in each three individual layers, it is also can be found naturally but it is less abundant compared to 2H phase. The latter one is 1T phase, this one has tetragonal symmetry with ant-prismatic sulphur atoms arrangements around the transition metal atom and only one layer is needed for each unit cell. Unlike the two above-mentioned phases, this one is synthetic product that can be obtained through lithium intercalation, also it has a metallic behaviour. 1T phase is metastable phase at ambient condition and can easily converted to 2H [12]–[17]. Figure 2-1 shows the schematic representation of the three different phases with sulphur atoms coordination around the transition metal atom in addition to the number of monolayers that required to create each phase.

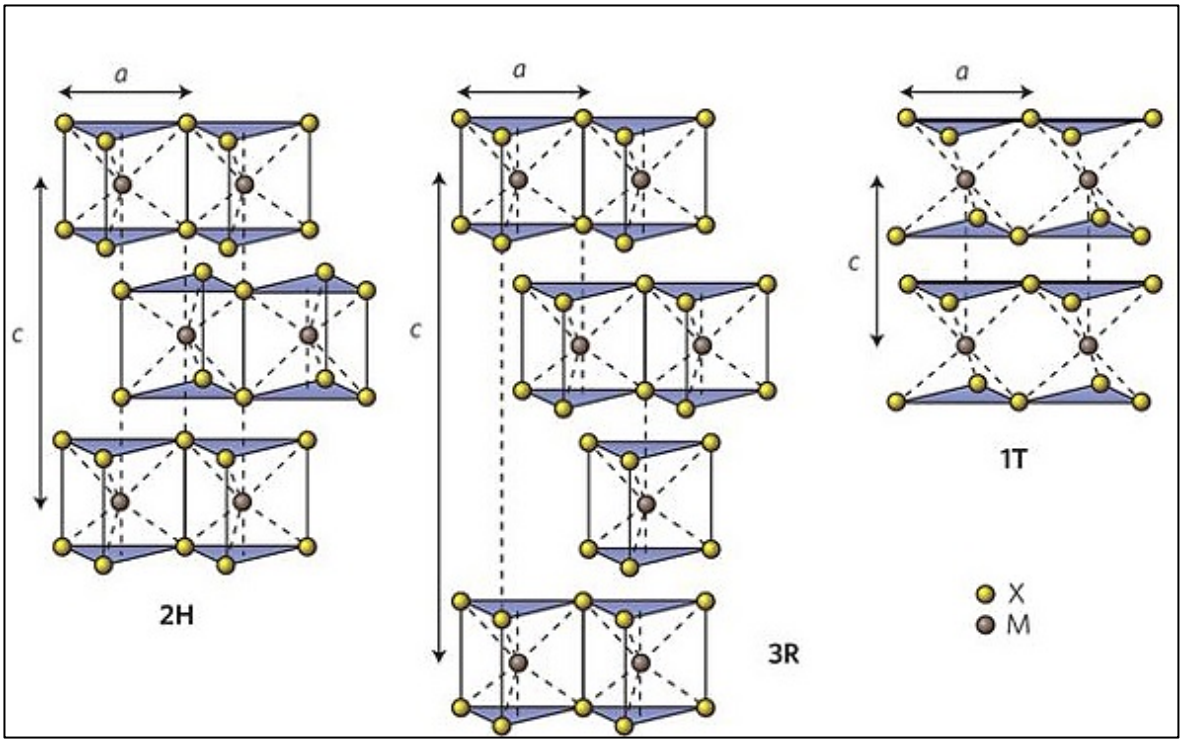

Figure 2-1: Schematic representations for MX_2 2H, 3R and 1T phases where M is the transition metal and X is the dichalcogenides (sulphur) showing the different arrangements for the sulphur atoms and the unit cell length for each phase. This figure is reproduced from ref. [13].

It is worth to mention that due to the strong in-plane covalent bonds between the S-M-S atoms and weak out-of-plane Van Der Waal forces between the S-S layers, TMD possess an excellent mechanical properties comparing with conventional semiconductor materials (such as silicon and germanium) which can be exploited in flexible electronics and optoelectronics [18].

Furthermore, the lattice dynamics of the MS_2 exhibit six vibrational modes which are attributed to the two types of bonds that mentioned earlier, they can be divided into four active first order Raman scattering modes and two active infrared (IR) absorption modes. However, it is not very common to use IR absorption spectroscopy for MS_2 characterisation because of low spatial resolution and cross section depth of this technique. In contrast, Raman spectroscopy has been used intensively in MS_2 characterisation as a non-destructive and powerful tool to estimate the thickness and the quality of MS_2 films, also to have a better understanding about phonon behaviours in the lattice [19], [20].

Among these four modes (E_1g, E^2_2g, E^1_2g and A_1g), only the two latter ones can be studied systematically due two technical issues with probing the two former ones. E^1_2g mode represents the opposite movement of sulphur planes with respect to the transition metal atom plane within each molecular layer. A_1g phonons indicate the perpendicular opposite vibration of the sulphur atoms when the transition atom is in static position in the MS_2 individual monolayer [19], [20]. The next figure (Figure 2-2) depicts the A_1g and E^1_2g vibrational modes and the directions of the atoms movement.

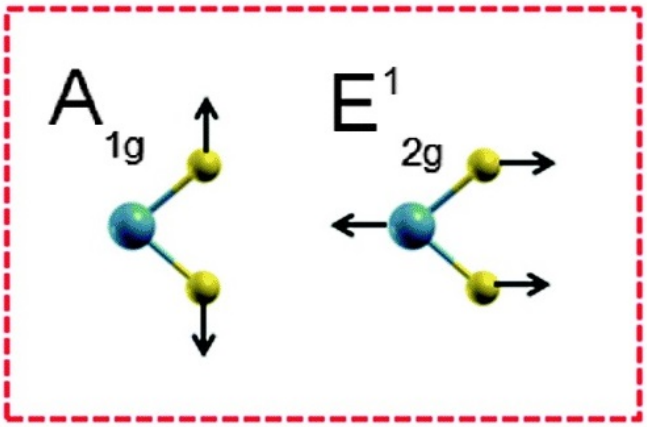

Figure 2-2: Schematic representation of A1g & E_2g phonon modes in MS_2 crystal where the yellow circles represent the sulphur atoms and the green ones represent the transition metal atoms. Arrows shows the direction of the vibrations in each mode. This figure is reproduced with editing from ref. [20].

Certainly, when the number of MS_2 layers are decreased, the Van der Waals forces between the monolayers are repressed causing a drop in restoring forces between layers. Hence, Raman response of A_1g (out-of-plane mode) is affected to be lower value comparing with bulk form (red shift). Conversely, the in-plane mode ($E^1{}_2g$) is suffered from unexpected blue shift when thickness is reduced, due to either the influence of interlayer structural changes induced by stacking or long-range Coulombic interlayer interactions [15], [19], [21], [22]. These opposite shift trends for the both Raman modes have been used as an indicator for the number of layers, where the smaller Raman peak difference shows thinner thickness ranging from bulk through few-layers to single layer for both MoS_2 and WS_2 [15], [19], [20], [22]. However, the Raman peaks difference is more dominant in MoS_2 due to lighter atomic weight of molybdenum comparing with tungsten [20]. Thanks to these findings which highlight Raman spectroscopy as the most useful non-contact characterisation tool used with 2D-TMDC.

Furthermore, when the excitation wavelength of the Raman tool is close to the direct band gap of the TMD, it caused a resonance Raman effect which leads to enhancement of Raman peaks intensity and emerging of two-phonons Raman modes in addition to the first order Raman modes that can be used to study the electronic structure of the MS_2 films [23]. For example, Li et al. shows that when MoS_2 flakes excited with 633 nm visible laser (the direct bandgap for MoS_2 is 1.8 eV), the longitudinal acoustic (second order mode) modes which is originated from the (***M***) point in the Brillouin zone dominates the first order Raman modes $E^1{}_2g$ and A_1g [24]. Similarly, Berkdemir et al. reported a resonant Raman scattering for WS_2 when it excited with 514.5 nm laser wavelength (the direct bandgap for WS_2 is 2 eV). Moreover, it is proved that there is inverse proportional correlation between longitudinal acoustic modes intensity (2LA) and out-of-plane mode (A_1g) intensity as a function of WS_2 thickness which is associated with the Raman peaks difference [25]. The graph below (Figure 2-3) summarize the $E^1{}_2g$ and A_1g peak positions as a function of layer thickness for MoS_2 and WS_2 in addition to position of second order mode for WS_2.

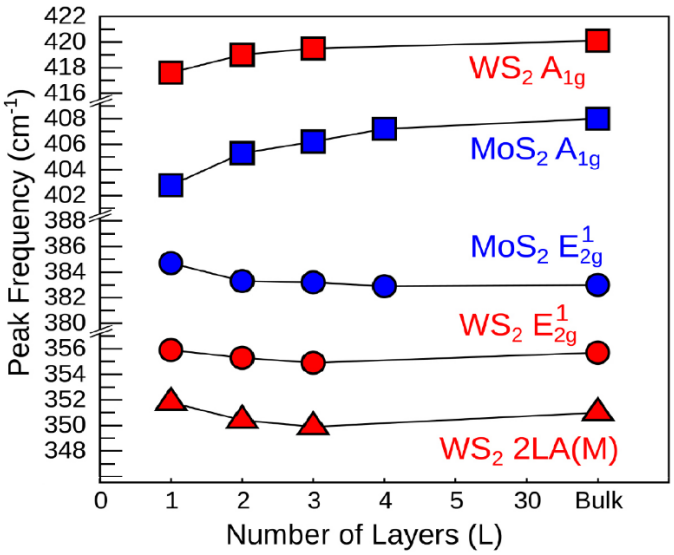

Figure 2-3: A_1g and E^1_2g peak positions for MoS_2 (blue colour) and WS_2 (red colour) with respect number of monolayers. The graph shows increasing in the Raman peaks difference when thickness increased for both materials with higher sensitivity to layer number in MoS_2. 2LA (M) peak position also reported for WS_2. The excitation wavelength is 488 nm for MoS_2 and 532 nm for WS_2. This figure is reproduced with editing from ref. [23].

2.3 Electronic structure of MS_2

In order to employ 2D-MS_2 in future electronic and optoelectronic applications, the electrical and optical properties of these crystals should be evaluated. This need to deeply analyse and understand the electronic band structure of transition metal disulphides in its bulk form and the peculiar changes that occur when the thickness is minimized to a single molecular sheet. Generally, all 2D materials family was born and grown as a result of one concept which is 2D form of layered materials have much more fascinating properties and rich physics with respect to their bulk form.

For example, graphene the first member of this family is one-layer thickness of carbon atoms with honeycomb lattice that has two atomic unit cell which can be exfoliated from the bulk from graphite. This lattice structure enables the energy-momentum diagram to have a linear relationship with both maxima and minima meeting at six corners of the Brillouin zone in the K point (Dirac point) creating gapless semimetal material. The mobility in graphene sheets is the highest ever achieved in any other materials due to massless fermions and the conductivity of this single carbon sheet can exceed 10000 times higher comparing with even very few layers of graphite. This is in addition to many interesting physical phenomena and properties that are beyond the scope of this thesis. However, the main drawback of graphene in semiconductor physics point of view is that graphene has a zero bandgap resulting very low on-off current ratio for FET applications [26]–[28].

Alternatively, bulk transition metal dichalcogenides (MoS_2, WS_2, $MoSe_2$ and WSe_2) share the same lattice structure and mechanical properties with graphite which means that they are easy to exfoliate to individual layers. Furthermore, it has been reported earlier since the 1960s that these materials exhibit semiconductor properties [29] with indirect band gap that range from 1.23, 1.35, 1.09 and 1.2 eV respectively [4]. Hence, they are excellent compensators for graphene as 2D semiconductor.

Theoretical study using density functional theory (DFT) revealed the electronic structure of the bulk, few and monolayer of MS_2. In bulk MS_2, the indirect band gap is created between the minimum of conduction band (CBM) located halfway between **K** point and **Γ** point of Brillouin zone and the maximum of the valance band (VBM) located at the **Γ** point [30]. Calculations estimated the indirect band gap to be 1.2 eV for MoS_2 and 1.3 eV for WS_2 [30]. However, as the number of layers decrease, band gap size is increased until reaching the single layer where CBM and VBM are met exactly at **K** point of Brillouin zone producing direct band gap transition at 1.9 eV for MoS_2 and 2.1 eV for WS_2 monolayers [30]. Apart from direct band gap transition in MS_2 monolayers, reducing the MS_2 layer number to a single layer enhances the Columbic interaction as well as reduce the dielectric constant and screening compared to their bulk counterparts due to the absence of interlayer interactions [31]. As a result, bounded quasiparticles like excitons (neutral bound electron-hole pairs analogous to hydrogen atoms), and trions (bounded two electrons and one hole or vice versa) become more perceptible by photoexcitation processes where excitons, in particular, dominate the optical phenomena in MS_2 monolayer crystal [31]. Therefore, this crossover in band gap type in the MS_2 monolayers, opens the door to explore not only potential 2D electronics and optoelectronics as the MS_2 monolayers are direct 2D semiconductors but also a rich physics behind it can be investigated. Figure 2-4 shows the band gap of MoS_2 and WS_2 in bulk, bilayer and monolayer regimes.

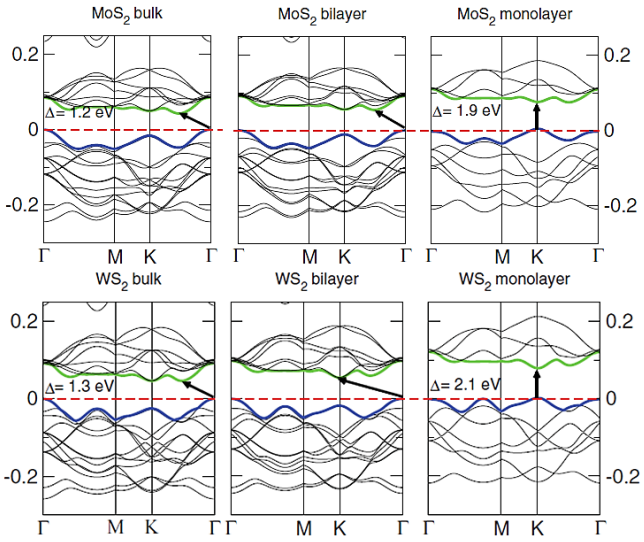

Figure 2-4: Theoretical prediction of indirect bandgap in bulk form and the transition to direct bandgap in monolayer for MoS_2 and WS_2 using DFT calculations. Unlike MoS_2 bilayer, WS_2 bilayer indirect bandgap is initiated from the CBM located in the K point and VBM in the Γ point. This figure is reproduced with editing from ref. [30].

In 2010, Splendiani et al. and Fai Mak et al. confirmed experimentally the emergence of the direct bandgap in MoS_2 monolayer through photoluminescence spectroscopy [9], [10]. Later, strong photoluminescence has been observed in WS_2 molecularly thin flakes compare with few layer and bulk WS_2 with peaks closed to the wavelength that was predicted theoretically announcing 2D WS_2 as a new direct band gap semiconductor [32], [33]. Furthermore, a field effect transistor with MoS_2 monolayer sheet has been fabricated for the first time with halfnium oxide as a dielectric top gate. This device shows high performance with good mobility and high on-off ratio [8]. Similarly, WS_2 monolayers FET exhibit corresponding results [34], [35].

From this section, it could be concluded that the raising of MS_2 as an effective member of the two dimensional family is due to their semiconductor properties which can be modulated readily through controlling the number of layers. These properties are very interesting in next generation electronic and photonic manipulating devices. Moreover, they could be complementary with graphene and other 2D materials to be the LEGO parts to build novel materials with more physics to explore and more potential applications for future.

2.4 Synthesis of MS_2

Since the sophisticated properties of MS_2 monolayers have been revealed, finding a robust growth method is still a considerable challenge to make MS_2 production reach the manufacture stage. Here, a review of the recent advances in synthesising MS_2 ultrathin layers is demonstrated. Basically, there are two essential routes: top-down route and bottom-up one. Generally, the former one produce the highest quality from scientific research point of view as it is monocrystalline. However, the later one is the key factor to provide large scale films that can be applicable in industry. Indeed, the ability of growing MS_2 ultrathin films synthetically with approximate properties that could be close to natural MS_2 or even better is the optimum goal for both academia and industry. The aim from this section is to give a clear understanding about various synthesis approaches of MS_2 and to show the significance of the experimental work that has been implemented in this thesis and how it could be an excellent alternative to the other routes to meet the manufacturing requirements towards realisation of 2D electronics and optoelectronics.

2.4.1 Top-Down Approach

As mentioned earlier, MS_2 layers are bonded to each other by weak Van Der Waals forces and this makes the process of exfoliation to mono and few layers from the bulk form easy to achieve. However, several routes were used to spilt bulk to few and single layers of MS_2 which can be summarised by mechanical cleavage; liquid exfoliation; thinning and/or etching.

2.4.1.1 Mechanical Cleavage

The original method used by Novoselov and his group to exfoliate graphene from graphite [2] is very simple and efficient to get high quality flakes from natural resources for fundamental research studies and prototyping. It is also called Scotch tape or micromechanical cleavage method. In principle, the adhesive tape is pasted to the bulk crystal then it peels off multiple times by folding and unfolding the adhesive type. Thinner flakes with sticky side of the tape is attached and by gentle rubbing to well cleaned SiO_2/Si substrate (normally with 285 nm dioxide thickness to improve the optical contrast between the flake and the substrate) the monolayers could be found on the substrate. Afterward, the substrate with the flakes is washed with isopropanol to remove the residue of the adhesive tape and optical microscopy is used to navigate through the substrate in order to find the monolayer flakes. Figure 2-5 illustrates the procedure of mechanical cleavage of graphene from graphite. MoS_2 and WS_2 single molecular sheets have been obtained by the same method [9], [10], [33], [34]. However, this method has drawbacks like time consuming, very low yield, small lateral flake size and random thickness and position of the output layer which makes it far from using for commercial purposes.

Moreover, it has been observed that mechanical cleavage could be more controllable by using direct in-situ transmission electron microscopy probing technique where a nano-size tungsten tip was used to bend and spilt individually from monolayer up to 23 MoS_2 layers that has been aligned perpendicularly to the tip. Although this nanomechanical cleavage technique is time consuming and need expensive tools to implement, it is very useful to study the mechanical properties such elasticity of MS_2 materials in atomic scale [36].

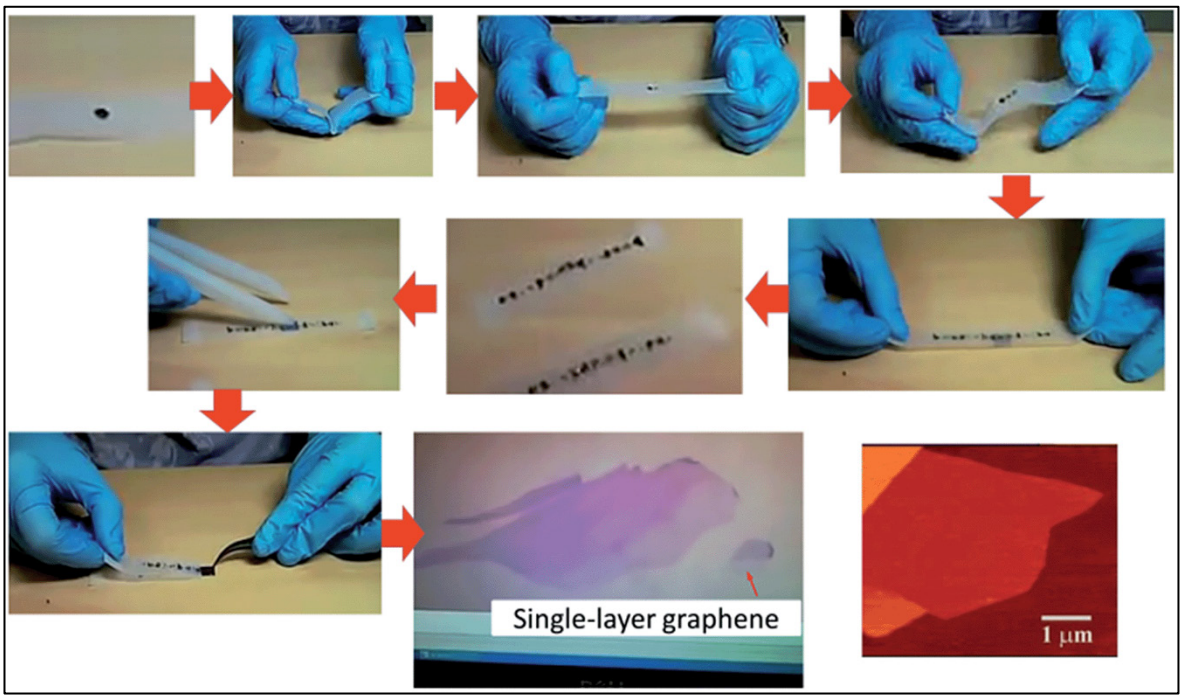

Figure 2-5: Step by step Scotch tape procedure to exfoliate graphene from graphite which is applied for other 2D materials (e.g. MoS_2). This figure is reproduced from ref. [37].

2.4.1.2 Liquid Phase Exfoliation

Generally, this technique is a simple and high yield production method comparing to the previous one. In liquid phase exfoliation, which is also called the dispersion technique, the process could be summarised by dispersing the bulk crystal or the powder of MS_2 in a proper solvent. The solvent has been chosen carefully so its surface tension matches to the weak surface tension of MS_2. By this way, the exfoliation energy is minimized and external source of energy such as ultra-sonic energy or shear stress would be sufficient to permeate within the bulk crystal leading to dispersed nanosheets in the solvent with few and monolayer thickness. Finally, centrifugation is used to selectively filter the size of the sheets (as shown in Figure 2-6) [6].

N-methyl-pyrrolidone (NMP) achieved the highest matching solvent with MS_2 for liquid phase exfoliation [38] when sonication was used for exfoliation. However, unexpectedly significant dispersion results were obtained when mixture of water and ethanol with optimum ratio were applied. Although, the last two solvents are not considerably useful for exfoliating, the resultant mixture of them is very efficient as a result of solubility improvement [39]. It is worth mentioning that composites of TMD and other layered materials could also be produced using this technique [40]. Finally, shear stress has been substituted for the ultra-sonic energy in order to achieve the exfoliation for MS_2 high quality nanosheets by using kitchen blender [41].

From above we can conclude that the liquid phase exfoliation is totally physical exfoliation process that depends on the surface tension between the solvents and MS_2 crystal to disperse and exfoliate it to nanosheets with external source of energy. Generally, liquid phase (dispersion based) exfoliation can produce high quality MS_2 flakes with a mass production rate and low cost although the controllability of the thickness is very low and the electrical device performance is not sufficient for practical applications.

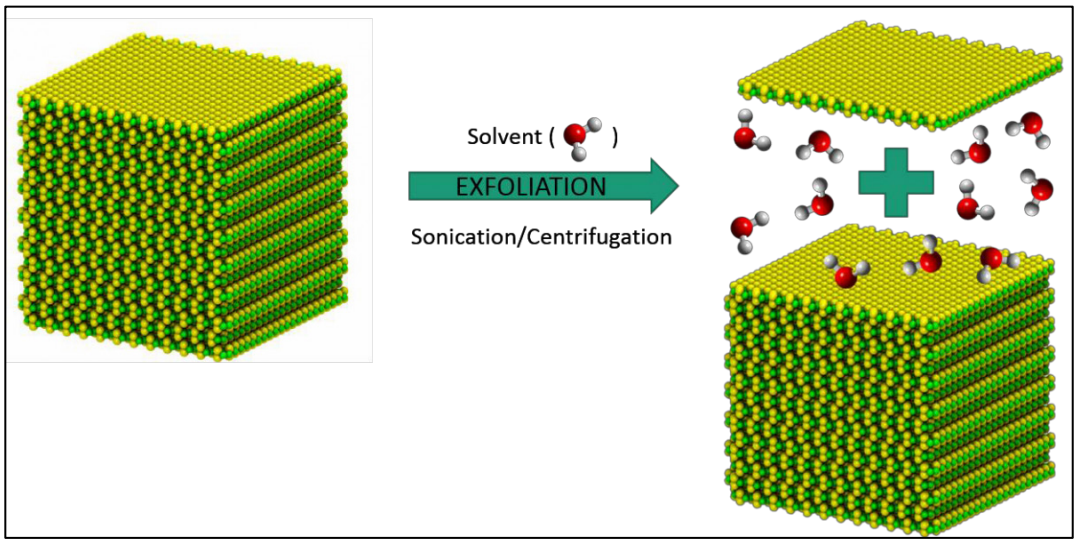

Figure 2-6: Schematic of liquid exfoliation of MoS_2 where the liquid is penetrating through the sheets by sonication and spilt them to individual monolayers that can be filtered by centrifugation. This figure is reproduced from ref. [42].

However, exfoliating the MS_2 crystal chemically by using intercalating agents is another approach that has been studied [6]. It is well known that the chemical reaction between lithium-based liquid compounds and MS_2 crystals leads to intercalate the lithium ions through interlayers of MS_2 (because of its small size) to balance the chemical reaction between lithium based compound and MS_2 crystal, as a result the MS_2 lattice will be expanded which facilitate the exfoliation process. Subsequently, water is added to the mixture to generate hydrogen gas and lithium hydroxide leaving MS_2 nanosheets lithium ion-free. This chemical reaction is violent, with sonication, the process can be accelerated to exfoliate MS_2 to few layer sheets [43], [44]. However, this process is consider as a slow process and the reaction needs days to be totally complete.

To tackle the slow reaction issue, a group modified this technique by designing electrochemical cell where the anode is Li foil and cathode is MoS_2 bulk crystal. During the discharge, lithium ions are penetrated through MoS_2 layers. Afterwards, sonication is applied to accelerate reaction between water and lithium ions in order to produce hydrogen gas that can splits the layers into smaller flakes. Moreover, the battery set up is efficient way to control the thickness of nanosheets by controlling the discharge capacity and voltage of the battery [45]. Importantly, the resultant MS_2 sheets from lithium intercalation method are normally 1T metallic phase and they need an annealing step to recover their semiconductor properties. Although, lithium intercalation is high yield method compare with scotch tape, it is might be not an option for electronics technology due to high impurities and uncontrollable size and thickness and the hazardous reaction due to high flammability of lithium [46].

Very recently, Lin and his group developed a lithium-free electrochemical intercalation method where they substitute lithium by tetraheptylammonium bromide (THAB). The resultant MS_2 nanosheets shows an excellent thickness controllability and high homogenous solution that can be used as MS_2 ink for ink-jet mass production. More importantly, unlike lithium ion, tetraheptylammonium bromide preserve the semiconducting properties of the bulk crystal due to the larger molecular size comparing with lithium ions that still can intercalate between MS_2 layers but with much less electron injections in the MS_2 layers which makes it suitable for high performance electronic applications [47].

2.4.1.3 Thinning and etching

Comparing to TMD family, graphite in general has lower density by multiple times while it has almost the same Van Der Waals forces applied between the layers in TMD. Thus, the interlayer bonding is stronger in graphite which means it needs to higher temperature for sublimation. As a result, thinning of the graphite to graphene by sublimation did not get much attention whereas in TMD case it is much easier to sublimate individual layers due to lower temperature requirement. This fact, leads several groups to study thinning approach more systematically for 2D TMD [6].

Basically, thinning means reducing the thickness of bulk crystal into mono and few layers by removing the topmost layers of the MS_2 bulk crystal. It is totally physical process as it relies on heating of the crystal surface to sublimate the layers uniformly all over the flake of MoS_2 by thermal annealing at low pressure and inert atmosphere or at ambient conditions [48], [49]. Another approach is to preferentially thin the flakes by localized laser energy. However, thermal annealing shows more controllability on number of layers that thinned while the laser thinning is more selective and patternable. It is worth to mention that the effect of the substrate is highly significant in this method as it plays the role of heatsink for the bottom layer which keeps it fairly unaffected by the sublimation of the top layers [6].

Moreover, removing the topmost layers chemically by etching is another alternative that has been reported. Etching could be categorised in two types the first one is dry etching using plasma energy and the latter one is wet etching using liquid etchant agents. In plasma etching, etching species such as argon ions [50] or oxygen [51] with low power and short etching time are used to increase the density of defects between the covalent-bonded atoms in the topmost layer up to the point that the total layer breakdown leaving behind the lower layer without damage. This method has been utilized for MoS_2 rather than WS_2 possibly due to larger lateral size of MoS_2 crystals which provide more possibility to use this technique for patterning the flakes. While wet etching can be used to achieve mono and bilayer using nitric acid where the acid oxidise the edges of the MoS_2 flakes, the etching rate slows down when number of layers decreased and completely stop when reach to mono or bi regime due to the heat sink effect of the substrate [52].

2.4.2 Bottom-Up Approach (Vapour Deposition)

Although Top-Down approach is very beneficial for fundamental studies and can produce fairly good quality transition metal disulphides nanosheets depends on the route that has been used. Unfortunately, most of researches did not manage to develop this approach for large area film production which is an essential step for commercialisation of transition metal disulphides for electronic and optoelectronic applications. As an alternative, vapour deposition technique of transition metal disulphide could be more promising for industrial applications due to large lateral dimensions of MS_2 ultra-thin film that can be prepared by this technique.

Fundamentally, this route divides into two categories: physical vapour deposition (PVD) and chemical vapour deposition (CVD). The former one depends on physical transformation of the MS_2 target or powder to a thin film shape using high energy external source to evaporate the MS_2 powder and deposited on the substrates. The latter one relies on chemical reaction between solid and/or vapour precursors to create the MS_2 films at a required temperature.

2.4.2.1 Physical Vapour Deposition (PVD)

In PVD, the energy that is used to stimulate the deposition could be normally in three different forms; heating, localized heating or bombarding by ions, which can be achieved using thermal evaporation deposition, pulsed laser deposition and sputtering to synthesize MS_2 films.

2.4.2.1.1 Thermal Evaporation Deposition (TED)

In TED, alumina or quartz crucibles are filled with MS_2 powders and mounted inside a quartz tube which is normally positioned at the centre of furnace that goes to high temperature ~ (900 °C-1000 °C). Meanwhile, the substrates (e.g. sapphire, glass, SiO_2/Si) are placed in a distance (tens of centimetres) from the centre of the furnace where the temperature is relatively lower (~650 °C) in the downstream of inert or inert/hydrogen mixture at low pressure. At these conditions, the MS_2 is sublimated from the crucible and carried by the inert gas stream and condense again on the substrates as ultra-thin triangular flakes (as shown in the Figure 2-7). MoS_2 monolayer flakes synthesised by this method was reported [53]–[55] followed by WS_2 nanostructures [56], [57].

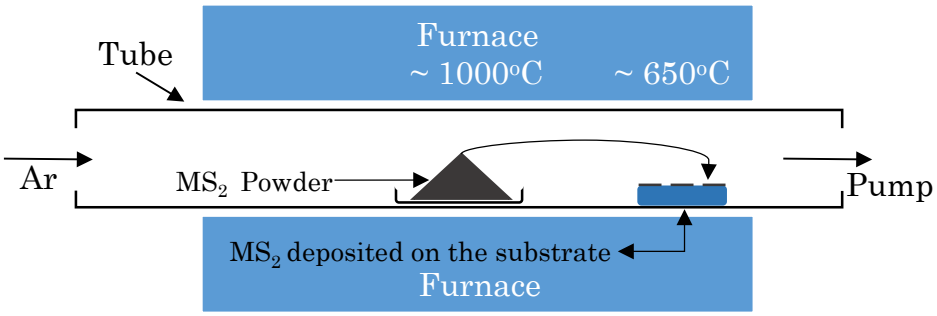

Figure 2-7: Schematic diagram for TED system of MS_2 growth.

For MoS_2, monolayer triangular flakes with 25 µm size has been obtained which demonstrated a valley polarisation at room temperature [53]. Moreover, Gong et al. used the flakes grown by TED method to study Palladium, gold and silver as metal contacts for MoS_2, and found Palladium can form a uniform metal layer over MoS_2 while gold and silver creates a nanoclusters that cause deterioration to the MoS_2 devices [54]. However, they proved that inserting graphene as a conductive buffer layer between the metal and MoS_2 can preserve the electronic properties of metal-semiconductor interface which sheds the light on the importance of using 2D heterostructure to improve 2D semiconductor devices performance[54]. Additionally,

bilayer TED-MoS_2 photodetector has been fabricated by Luo and his group where it indicated a good photosensitivity [55].

However, compared to MoS_2 that is mechanically exfoliated and MoS_2 prepared by CVD, TED-MoS_2 possess a higher density of defects that is attributed to molybdenum atoms replacing one or two sulphur atoms (antisite defects) while in the latter ones, sulphur atom vacancies are the dominant type of defects [58]. Consequently, TED-MoS_2 FET devices performance are severely degraded owing to the type and density of defects with respect to MoS_2 obtained by exfoliation or CVD [58].

Unfortunately, WS_2 has low vapour pressure which leads to complications for transporting it under high temperature and vacuum growth conditions that normally used for TED. Thus, the reports that utilised the pure WS_2 powder are rare and the functionality of the produced flakes as semiconductor devices has not been probed yet [56], [57]. Instead, Modtland et al. suggested a hybrid approach that combine TED and CVD together which is chemical vapour transport (CVT), simply, WS_2 powder is mixed with sodium chloride (NaCl) with a ratio 4:1 to deposit WS_2 triangular flakes on SiO_2/Si substrate with experiment set-up exactly the same used in TED [59]. NaCl was a volatile transport agent which increased the vapour pressure of WS_2 powder by forming tungsten chloride and elemental sulphur at high temperature then transported through the carrier gas to deposit WS_2 monolayer triangles after both products react once again on the substrates which were placed in cooler region of the furnace [59].

Importantly, investigating TED protocol for alloying and heterostructuring of two-dimensional materials is paramount research topic as more favourable properties of these materials could be engineered for electronic and optoelectronic applications. Therefore, TED/CVD method has been employed for creating monolayer $Mo_xW_{1-x}S_2$ alloy where MoS_2 powder and WO_3 powder where placed between two SiO_2/Si substrates then annealed with existence of sulphur in inert gas (Ar) [60]. Furthermore, TED seems a feasible approach to create heterostructure where several groups reported successful growth of MoS_2–$MoSe_2$ and WS_2–WSe_2 lateral heterostructures [61]; WS_2-WSe_2 and WS_2-$MoSe_2$ heterostructures , WS_2-WSe_2-MoS_2 and WS_2-$MoSe_2$-WSe_2 multi-heterostructures and reaching to superlattices (such as WS_2-WSe_2-WS_2-WSe_2-WS_2) [62]; also vertical heterostructure of MoS_2, WS_2 and WSe_2 was grown on CdI_2 nanoplates [63].

2.4.2.1.2 Sputtering of MS_2

Sputtering is a process where MS_2 bulk material bombarding by accelerating particles like positive ions of inert gas (Ar^+ ions) that can ejected MS_2 molecules by momentum transfer due to collision and condensed them again on the substrates that placed in a distance from the target (bulk material) [6]. This process is conducted under vacuum at relatively low temperature where the target normally is connected to high negative voltage source (cathode) while the substrate is grounded, using this circuit connection, enables the ions to attack the target while

the scattered fragments and vapour of MS_2 deposited on the substrate to form a thin film [6]. Ar^+ ions are accelerated either by direct current (DC) or radio frequency (RF), however, direct current (DC) normally is used with metallic targets while radio frequency (RF) is used with insulating targets to prevent building up a net positive charge on the target surface which restrains the deposition [64]. MS_2 are semiconductors which allow them to be deposited by both techniques [6].

However, in order to achieve high deposition rate and avoid high temperature deposition, magnetron sputtering is used with both techniques (DC or RF) [6]. The magnetic field generated by magnetron sputtering could confine and control the charged particles to make the target totally surrounded and covered by the charged particles (positive ions or electrons) which enhance the yield of sputtering [64]. MS_2 targets are commercially available as using sputtering technique for growth of MS_2 thin film is well established and it has been used before for coating MS_2 films for applications like thin film solar cells [6], [65], [66]. Schematic illustration for MS_2 deposition by magnetron sputtering is shown in Figure 2-8:

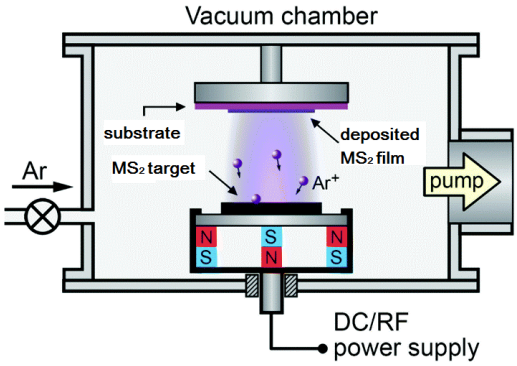

Figure 2-8: Schematic illustration of magnetron sputtering machine for MS_2 films deposition. This figure is reproduced with editing from ref. [6].

However, exploiting sputtering for mono and few-layer MS_2 film deposition was firstly reported by Muratore and his colleagues where they sputtered MoS_2 with varying number of layers (3-6) on SiO_2/Si and pyrolitic graphite substrates at 350°C [67]. The sputtering process was optimised to obtain 4-layer MoS_2 film uniformly deposited over 4cm^2 substrate area but the film suffered from polycrystalline nature with associated with Mo species, which could be reduced when the film thickness increased [67]. Alternatively, Tao et al. sputtered molybdenum metal at very low pressure and high temperature 700 °C while sulphur vapour was introduced simultaneously which leads to monolayer formation of MoS_2 on a sapphire substrate when sputtering power and time were optimised [68]. The FET devices fabricated by this method were p-type with 10^3 on-off ratio and 12.2 cm^2 V^{-1} s^{-1} hole mobility which is comparable with electron mobility of exfoliated MoS_2 (0.1-10) cm^2 V^{-1} s^{-1} [68]. Tao et al. attributed the anomalous p-type behaviour to the sulphur interstitials defects (additional sulphur atoms in the MoS_2 lattice) which acts as p-dopants, these interstitials inserted into the lattice due to high kinetic energy of the MoS_2 formed by sputtering [68]. On other hand, in CVD MoS_2 the main type of defects are the sulphur vacancies in the lattice which acts as n-dopants, thus, the FET fabricated by CVD

MoS_2 normally are n-type even though they are created in sulphur rich environment but the kinetic energy of sulphur atoms is low to form interstitials (p-dopants) [68].

Recently, wafer-scale few-layer and standing layer (vertically aligned) sputtered WS_2 films has been achieved for photodetection applications with broad band spectral response [69], [70]. However, the main issue for growing MS_2 by sputtering technique is the poor crystallinity which has a great impact on the electrical and optical properties of the films. Thus, several groups tried to address this issue by different post-treatment techniques such as electron beam irradiation (EBI) [70], thermal annealing [71] and laser annealing [71]–[74] for both WS_2 [70], [74] and MoS_2 [71]–[74].

2.4.2.1.3 Pulsed Laser Deposition (PLD)

Pulsed laser deposition is one of the physical vapour deposition techniques that has been widely studied for thin film production in the past decades, in particular for oxides thin films [75], [76]. The basic principle of this technique can simply explained as the following: a high power (with energy density ranging from 1 to 5 J/cm^2) pulsed (typically 10-50 ns pulse duration) laser in ultra-violet range is focused to strike a rotating target (bulk material source) under high-vacuum which generates a plasma cloud of the target material due to the high energy. This plasma cloud is subsequently condensed on the pre-heated substrate as a thin-film [75], [76]. Figure 2-9 below depicts the PLD system for MS_2 growth.

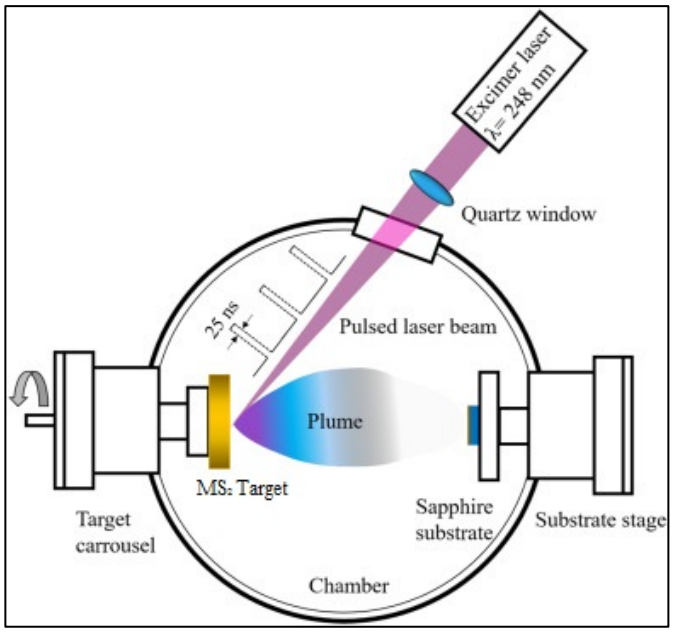

Figure 2-9: Schematic diagram of PLD system for MS_2 film growth. This figure is reproduced with editing from ref. [77].

Several sequential physical phenomena occur during each pulse duration of the laser leading to film deposition which could be explained briefly as below. Firstly, the laser pulses induce the necessary rapid heating to evaporate the target material. As a result, the laser energy absorption is increased by material vapour until it reaches the limit where the plasma is

generated. Simultaneously, the rest of the absorbed laser energy would supply enough energy to heat and accelerate the plasma cloud which contains target particles such as atoms, molecules, ions and electrons that scattered from the target surface. Due to the high density of the target particles which also possessed high kinetic energy, a large number of collisions occurs close to the target surface. Consequently, the area of collisions is perpendicularly expanded with respect to the target surface. Finally, as the whole reaction is under low pressure, a shock wave is created between the accelerated target particles and the inert gas in the container which gradually slow down to be deposited as a thin film on the substrate [75].

For 2D materials grown by PLD, Tiwari has led two groups successfully to prepare MoS_2 films in 2015 followed by WS_2 films in 2018 [77], [78]. Experimental details for both reports are as follows: pulsed KrF excimer laser with 248 nm wavelength and 25 ns pulse duration is used as a source for PLD; sapphire substrates were used to deposit the MS_2 films and both targets were polycrystalline [77], [78]. However, for MoS_2, the substrates were heated up to 700°C at pressure 10^{-6} Torr. While the growth conditions for WS_2 films was 500°C for the substrate temperature and the deposition was conducted in ambient vacuum at a pressure 10^{-5} Torr. For MoS_2, films with modulated layer number ranging from 1-60 molecular layers have been grown over $1cm^2$ substrate whereas with WS_2 the thickness of the deposited film was varied from monolayer up to 25 layer over the same area of the substrate [77], [78]. The MS_2 films with different thicknesses showed excellent colour homogeneity over the whole substrate which was an indication for good thickness uniformity, however, the MS_2 films showed very broad Raman peaks which corresponds to poor polycrystalline films even after post-annealing in WS_2 films at 500°C in Ar environment [77], [78].

In order to improve the growth conditions to produce better MS_2 quality, Loh et al investigated the growth of few-layer (2-5 layers) WS_2 film on silver substrates which form Ag_2S lattice matching phase that can facilitated WS_2 growth [79]. Alternatively, Serna and his group designed a MoS_2 target where sulphur powder was added to the target with a ratio 1:1 for MoS_2 and sulphur [80]. Wafer scale MoS_2 films with 1 to 10 layers thickness could be grown using this method on various types of substrates which also possess relatively low electrical resistivity [80].

Post-annealing effect on optoelectronic properties of multilayer PLD-WS_2 films has been investigated by Wang et al. where they show a clear enhancement in photocurrent, responsivity, detectivity and external quantum efficiency (EQE) with respect to increasing to the annealing temperature [81]. This enhancement in photodetection parameters was attributed to crystallinity improvement via post-annealing [81]. Alternatively, Ho et al studied the effect of the post-sulphurisation of PLD-MoS_2 bilayer FET devices which showed increased on-off ratio of the FET devices due to molybdenum oxide elimination carried out by post-sulphurisation [82].

2.4.2.2 Chemical Vapour Deposition (CVD)

This route is divided to subcategories according to the initial precursors that has been used:-

2.4.2.2.1 Sulphurisation of Transition Metal Thin Films

This route depends on direct chemical reaction between sulphur source and ultra-thin film of transition metal (molybdenum [83]–[92] or tungsten [86], [87], [91], [93], [94]) pre-deposited on the insulating substrates. Pre-deposition of the metallic film could be implemented by e-beam evaporation [83]–[85], [89], [90]; sputtering [86]–[88], [91], [93], [94] or even by sol-gel technique [92]. The insulating substrates used for the deposition are SiO_2/Si [83], [85], [87], [88], [90]–[92], [94]; sapphire [84], [93] and plastic substrate [89]. The growth of MS_2 is normally conducted at low pressure and relatively high temperature (normally between 750-800°C and it can go up to 1100°C) in inert gas environment (nitrogen or argon) to avoid oxidation. The sulphur source is either elemental sulphur vapour ([83], [84], [86]–[88], [91]–[94]) or hydrogen sulphide (H_2S) ([85], [89], [90]). This approach can produce single crystal of MoS_2 and WS_2 [84], [86], [94] or polycrystalline MS_2 films [83], [85], [87]–[93]. Figure 2-10 shows a schematic representation for the CVD system to grow MS_2 by this method.

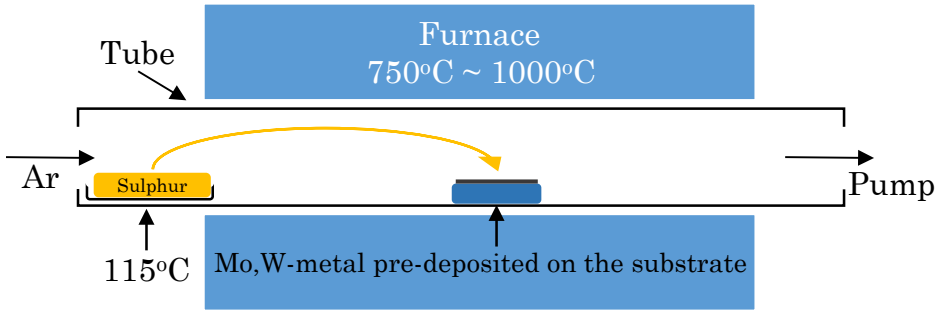

Figure 2-10: Schematic diagram of CVD system to sulphurize pre-deposited Mo, W-metal film.

Zhan et al. was the first group to demonstrate this approach in 2012. Two zone furnace with quartz tube where SiO_2/Si substrates pre-deposited with Mo thin film by e-beam evaporation were located in hot zone and crucible filled with sulphur powder was located on the cold zone. The two zones were heated up to 750°C and 113°C (melting point of sulphur) respectively in nitrogen environment. The results show a p-type polycrystalline MoS_2 mono, bi and tri layers with excellent sheet resistivity in kilo-ohm range but with low mobility between 0.04-0.004 $cm^2/(V.s)$ [83]. However, it is one of the rarest reports that shows p-type behaviour of CVD-MoS_2 with very low on-off ratio possibly due to uncomplete reaction between the deposited metal and sulphur vapour which gives the transistor more metallic characteristics [95].

Generally, reports that used elemental sulphur for sulphurisation process has quite similar growth conditions with Zhan's work. However, the earliest studies focused on MoS_2

synthesis rather than WS_2 using this approach due to lower melting point of molybdenum comparing with tungsten which facilitate the deposition of the initial precursor film [19].

It is worth mentioning that MS_2 layers number and uniformity over the substrate grown by this technique revealed high dependency on deposited transition metal thin film thickness which gives superiority to e-beam evaporation over sputtering deposition technique due to more precision in controlling the film thickness.

Moreover, this approach was developed to improve the crystallinity of MS_2. For example, Laskar et al. used crystalline substrate (sapphire) and increased the growth temperature and succeeded to have single crystal of MoS_2 that has n-type semiconducting behaviour with much higher field effect mobility and on-off ratio comparing to previous study [84]. Similarly, WS_2 was grown on sapphire substrate with similar conditions but with lower annealing temperature resulting polycrystalline films rather than single crystal [93]. These findings highlighted the crucial role of annealing temperature and substrate crystallinity on the quality of the deposited films.

Several groups tried to enhance the sulphurization process which is vital step for the growth of the MoS_2 by switching the sulphur source from the solid elemental form (vapour phase when its heated at low temperature) into gaseous form using hydrogen sulphide (H_2S) (as shown in Figure 2-11) to improve the controllability on number of MoS_2 layers that deposited [85] or to reduce the deposition temperature via plasma-enhanced CVD which enables growth of MoS_2 on plastic substrate leading to more applications in flexible electronics and sensing [89].

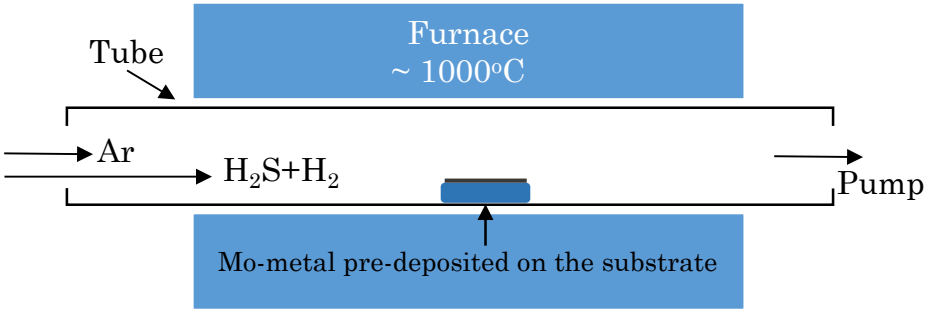

Figure 2-11: Schematic diagram CVD system for MoS_2 growth via of Mo film and H_2S.

Table 2-1 and Table 2-2 summarize the important reports that have been published about growth of MoS_2 and WS_2 films by sulphurisation of molybdenum and tungsten pre-deposited films. The main advantage of this approach is that ultra-thin MS_2 films could be easily produced with large area only limited by substrate lateral dimensions, thanks to pre-deposition step where physical vapour deposition techniques are utilized to coat the whole substrate with the transition metal precursor film.

However, the high melting points of molybdenum (2610 °C) [96] and tungsten (3422 °C) [19] are far beyond the growth temperature (normally 750 °C) of MS_2 which cause some issues associated with MS_2 films when this approach is applied.

These issues could be summarized by low uniformity of MS_2 films due to low thickness controllability of the pre-deposited transition metal films and low electrical performance of the FET devices that fabricated by these films.

Small grain size of MS_2 films (ranging from 5 nm to 30 nm for MoS_2 films [83], [85], [89] and from 50 nm to 200 nm for WS_2 nanometres [86]), high density of grain boundaries and defects formed by uncomplete reaction of transition metal with sulphur [83] are the main causes for degradation in mobility and on-off ratio of the FET devices. Thus, utilizing precursors with lower melting point leads to grow MS_2 films with more preferable electronic and optical properties as these precursors could enhance the uniformity and increase the grain size of MS_2 films.

Table 2-1: Reports of MoS_2 growth via sulphurisation of molybdenum films.

No.	Ref.	Year	Thickness	Deposition Technique	Sulfurization Step	Annealing Temperature	Inert gas	Substrate	Crystallinity/ grain size	Notes/Application
1	[83]	2012	Monolayer & Fewlayer	e-beam evaporation	Sulphur	750 °C	Nitrogen	SiO_2/Si	Polycrystalline 10 to 30 nm	Back-gate FET device, p-type and the mobility is 0.04 $cm^2 V^{-1} s^{-1}$.
2	[84]	2013	Monolayer & Fewlayer	e-beam evaporation	Sulphur	1100 °C	None	Sapphire	monocrystalline	Mobility is 12±2 $cm^2 V^{-1} s^{-1}$.
3	[85]	2014	Bilayer up to 12 layers	e-beam evaporation	H_2S	1000 °C	$H_2S/H_2/Ar$ 1:5:50	SiO_2/Si	Polycrystalline	Top-gate (HfO_2) FET device, n-type and the mobility is 0.12 $cm^2 V^{-1} s^{-1}$ and on-off ratio is 10^5.
4	[86]	2014	Monolayer	sputtering	Sulphur	800 °C	Argon	MgO	Polycrystalline	Top-gate (Al_2O_3) FET device, n-type and the mobility is from 0.005 to 0.01 $cm^2 V^{-1} s^{-1}$.
5	[87]	2014	Monolayer	sputtering	Sulphur	750 °C	Argon	SiO_2/Si	Polycrystalline	Gas sensors.
6	[88]	2014	Trilayer	sputtering	Sulphur	750 °C	Argon	SiO_2/Si	Polycrystalline	Investigating spectroscopic ellipsometry for MoS_2 thickness evaluation.
7	[89]	2015	5-6 layers	e-beam	H_2S	300 °C	Argon	Polyimide	Polycrystalline	Humidity sensor.

Table 2-1: Continued.

No.	Ref.	Year	Thickness	Deposition Technique	Sulfurization Step	Annealing Temperature	Inert gas	Substrate	Crystallinity/ grain size	Notes/Application
8	[90]	2015	Bilayer up to 12 layers	e-beam	H_2S	N/A	$H_2S/H_2/Ar$ 1:5:50	SiO2/Si	Polycrystalline	Studying the changes of MoS_2 work function according to thickness reduction and ambient adsorbents (water and oxygen).
9	[91]	2015	Mono to trilayer	sputtering	Sulphur	750 °C	Argon	Quartz	Polycrystalline	Studying optical nonlinearity of MoS_2
10	[92]	2016	Mono to bilayer	Sol-gel spin-coating	Sulphur	900 °C	H_2/Ar 1:5	SiO_2/Si	Polycrystalline	Back-gate FET device, p-type and the mobility is 9.2 $cm^2 V^{-1} s^{-1}$. All MoS_2 p-n junction diode.

Table 2-2: Reports of WS_2 growth via sulphurisation of tungsten films.

No.	Ref.	Year	Thickness	Deposition Technique	Sulfurization Step	Annealing Temperature	Inert gas	Substrate	Crystallinity/ grain size	Notes/Application
1	[86]	2014	monolayer	sputtering	Sulphur	800 °C	Argon	MgO	Polycrystalline	None
2	[87]	2014	Bulk	sputtering	Sulphur	750 °C	Argon	SiO_2/Si	Polycrystalline	None
3	[91]	2015	mono to trilayer	sputtering	Sulphur	750 °C	Argon	Quartz	Polycrystalline	Studying optical nonlinearity of WS_2
4	[93]	2017	6 layers to bulk	sputtering	Sulphur	750 °C	Argon	Sapphire	Polycrystalline	Studying optical properties of WS_2
5	[94]	2018	Monolayer to bulk	sputtering	Sulphur	800 °C	Argon	SiO_2/Si	Monocrystalline	Investigating the effect of the distance between the tungsten source and the substrate on the thickness and lateral size of WS_2 flakes

2.4.2.2.2 Sulphurisation of Transition metal oxides (MoO_3, WO_3)

Transition metal trioxides have much lower evaporation temperature compared to their metal analogue (MoO_3 between 950 °C to 1050 °C and for WO_3 1200 °C to 1400 °C) [97]. The CVD growth of MS_2 conducts normally between 750 °C to 1000 °C as illustrated in the previous section which is very close to the evaporation temperature of the oxides. This helps to grow MS_2 readily with better crystallinity. This fact, triggered intensive efforts to explore these compounds as solid precursors for MS_2 growth and become the most studied solid precursor for CVD of MS_2.

Generally there are two routes to synthesize MS_2 using the transition metal trioxides, the former one with two-steps where trioxides films are physically deposited by thermal evaporation on the substrate and then sulfurized at inert gas conditions using CVD furnace system at high temperature as shown in Figure 2-12. This route is very similar to what was done with sulphurisation of transition metal films. However, the low evaporation point of transition metal trioxides offers the opportunity to directly react them with sulphur in gaseous state then deposit them on the substrates which is the latter and most studied route using these precursors.

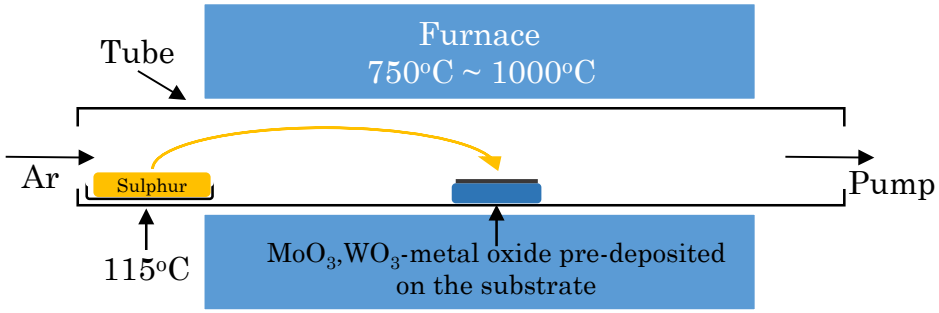

Figure 2-12: Schematic diagram CVD system for MS_2 growth via sulphurisation of pre-deposited metal oxide.

Lin and his co-workers were the first group who demonstrated the former route for MoS_2 where they used sapphire as a substrates and coated it by MoO_3 films (3.6 nm thickness) using thermal evaporation. Firstly, The MoO_3 films were annealed with reduced atmosphere (4Ar: 1H_2) at low pressure at 500 °C for one hour in order to convert MoO_3 to MoO_2 fallowed by second annealing step where the temperature rises up to 1000 °C and sulphur powder boat placed in the upstream of Ar flow at pressure close to atmospheric pressure for 30 min. Similar to sulphurisation of metal films, the deposited MoS_2 thickness shows high dependency on initial trioxide film thickness where the MoS_2 tends to form isolated micro-size islands when the initial trioxide thickness was very low (< 3.6 nm) rather than continuous film. Trilayer MoS_2 polycrystalline continuous films has been achieved by this method. The resultant MoS_2 films has been transferred on SiO_2/Si for FET device fabrications where they show clearly n-type semiconductor behaviour with relatively good on-off ratio 10^5 and 0.8 $cm^2 V^{-1} s^{-1}$ mobility [98].

However, due to reaction of sulphur with the solid form of molybdenum dioxide film, the final MoS_2 has grown as polycrystalline continuous film rather than a single triangular MoS_2

flaks. Additionally, Gutierrez and his group succeeded to grow WS_2 microflakes with triangular shape using the similar methodology where 0.5-2 nm WO_3 thin films are deposited on SiO_2/Si substrates by thermal evaporator then annealed and sulfurized by one step (rather than two steps) using CVD furnace system with flow of Ar at 800 ^oC for 30 min. the flakes were distributed randomly all over the substrates with different orientations and the thickness of the flakes was varied from bilayer in the centre to monolayer at the edges of the flakes which is confirmed by non-uniform photoluminescence intensity distribution over the flakes. However, it was one of the earliest reports that proved experimentally the band gap transition of WS_2 from indirect to direct when thickness minimized to monolayer regime at ambient conditions [99]. Table 2-3 highlights the main reports used sulphurisation of pre-deposited MO_3 films route to grow MS_2 films.

Simultaneously, the second route was started to be explored by two groups to synthesise few and monolayer MS_2. Figure 2-13 depicts the CVD system set up for the MS_2 grown by this approach. The earliest one was conducted by Balendhran and his group where they grow bulk MoS_2 on SiO_2/Si then they exfoliate it to monolayer by mechanical cleavage [100]. However, the output MoS_2 flakes had random shape, size and thickness in addition to the need to extra exfoliation step makes this method limited in terms of functionality.

On another hand, Lee and his group studied this approach more systematically where they placed SiO_2/Si substrates coated by reduced graphene oxide (rGO) facing down a boat containing MoO_3 powder while a boat of sulphur was neighbouring the MoO_3 boat that capped with the target substrate. The CVD furnace system elevated the temperature up to 650 ^oC for 15 min to synthesis the MoS_2 with nitrogen flow at atmospheric pressure. The grown MoS_2 has star shape flakes and sometimes they attach to each other to form a continuous film within millimetre scale where their thickness was between mono to bilayer. The electrical characteristics of these films was measured using backgate FET which shows n-type behaviour with on-of ratio 10^4 and 0.02 $cm^2\ V^{-1}\ s^{-1}$ field effect mobility [101]. Within few months later, Wang et al manged to have FET devices synthesized with the same approach but with superior electrical performance (10^8 on-off ratio and 190 $cm^2\ V^{-1}\ s^{-1}$) using top gate FET configuration and hafnium oxide as a gate dielectric [102].

WS_2 monolayers micro-size flakes has been also produced using direct reaction of vaporized tungsten trioxide and sulphur, where sapphire substrates are placed in the downstream of Ar (or Ar/H_2) flow. Two boats were set in front of the substrates, one contained sulphur was placed in the cold zone (100 ^oC) of the furnace closer to the Ar mainstream and the second one is filled with WO_3 was positioned at the hot zone closer to the substrates region (900 ^oC) of the furnace where they annealed for one hour at low pressure. Ionic-gated FET device was made from these flakes which shows ambipolar behaviour with 100 on-off ratio and mobility 0.46 and 0.28 $cm^2\ V^{-1}\ s^{-1}$ for electrons and holes respectively [103].

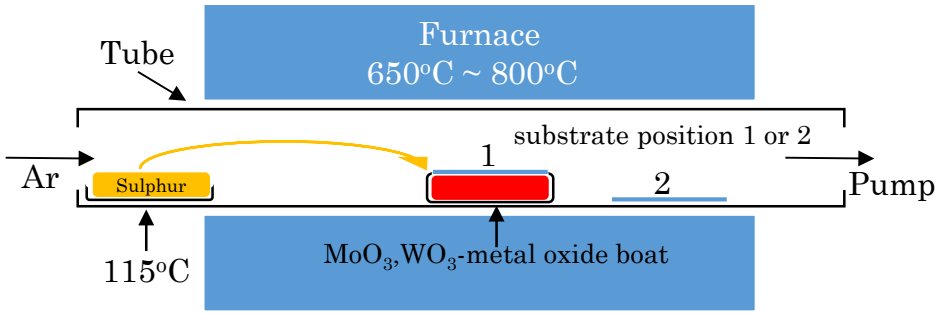

Figure 2-13: Schematic diagram CVD system for MS_2 growth using MO_3 and sulphur powders.

Although the precursors used and the growth conditions are similar, there are two proposed mechanisms for the growth of MS_2. The first one, the transition metal trioxide (MO_3) is reduced to MO_{3-x} or form bulk MS_{2+y} with help of sulphur vapour at high temperature then these species are adsorbed or diffused on the target substrate as a seeds of the flakes and start to form MS_2 crystals as it keep exposing to sulphur at high temperature [101],[104]. The other mechanism, where the MO_3 is directly reacted with sulphur at gaseous state to create MS_2 then deposited and becomes more crystalline on the substrate [103].

The main critical synthesis parameters are annealing temperature and its time duration, substrate type (amorphous or crystalline), precursor amounts and their distance from substrate, gas type and flow. They have a great impact on the crystallinity, thickness, chemical composition, grain boundaries and shape (flakes or continuous film) of final product. Many electronic devices fabricated using this approach show excellent behaviour that could be promising for future semiconductor industry. However, the complexity, reliability and cost-effectiveness of this approach are still an open question. Finally, Table 2-4 and Table 2-5 list the MoS_2 and WS_2 synthesis publications by direct reaction of sulphur with MoO_3 and WO_3 powders respectively.

Table 2-3: MS_2 growth via sulphurisation of transition metal oxide film.

No.	Ref.	Year	Precursor	Deposition	Material	Temperature °C	Substrate	Carrier gas	Thickness	Shape and grain size	Notes
1	[98]	2012	MoO_3	Thermal evaporation	MoS_2	1000	Sapphire	Ar	Trilayer	Polycrystalline Continuous film	Backgate FET device, n-type with 10^5 on-off ratio and 0.8 $cm^2 V^{-1} s^{-1}$ mobility.
2	[105]	2013	MoO_2	CVD	MoS_2	850–950	SiO_2/Si	Ar	monolayer	Rhomboidal microplates ~10 µm	17 Backgate FET devices, n-type with 10^4-10^6 on-off ratio and 0.1-0.7 $cm^2 V^{-1} s^{-1}$ mobility.
3	[106]	2014	MoO_3	Thermal evaporation	MoS_2	800	SiO_2/Si	Ar	monolayer	Triangular ~5 µm	Photodetector max. Responsivity 1.1 mA W^{-1}.
4	[107]	2015	MoO_3	Thermal evaporation	MoS_2	700	SiO_2/Si	nitrogen	monolayer	triangular/spike max flake area 1300 μm^2	Backgate FET device, n-type exceed 10^6 on-off ratio and 8.2-11.4 $cm^2 V^{-1} s^{-1}$ mobility.
5	[108]	2016	MoO_3	e-beam evaporation	MoS_2	500, 750,1000	SiO_2/Si	Ar	2, 4 layers	Polycrystalline Continuous film	Studying the optimum conditions to grow MoS_2 by sulphurisation of Mo-based films.
6	[99]	2012	WO_3	Thermal evaporation	WS_2	800	SiO_2/Si	Ar	monolayer	Triangular (<10 µm)	Investigating photoluminescence in WS_2 flakes.

Table 2-3: Continued.

No.	Ref.	Year	Precursor	Deposition	Material	Temperature °C	Substrate	Carrier gas	Thickness	Shape and grain size	Notes
7	[109]	2013	WO_3	Thermal evaporation	WS_2	750-900	SiO_2/Si	Ar	Mono-few layer	~1 cm^2 continuous film	Investigating optical properties of WS_2 and $W_xMo_yS_2$ alloy.
8	[110]	2015	WO_3	Dip-coating	WS_2	950	Sapphire	Ar	monolayer	Polycrystalline Continuous film	Transfer film shows n-type FET backgate- 0.91 $cm^2 V^{-1} s^{-1}$ and ON/OFF ratio of 10^6. Phototransistor with 18.8 mA W^{-1} responsivity.
9	[111]	2016	WO_3	Sputtering	WS_2	650	SiO_2/Si	Ar	Trilayer	nanocrystalline Continuous film	n-type FET backgate- 17 $cm^2 V^{-1} s^{-1}$ and ON/OFF ratio of 10^4. Photodetector.
10	[112]	2017	WO_3	e-beam evaporation	WS_2	800	SiO_2/Si Sapphire	Ar	monolayer	Polycrystalline Continuous film	Studying the wetting properties of WS_2 thin films.

Table 2-4: MoS_2 growth via direct reaction between sulphur and molybdenum oxide powder.

No.	Ref.	Year	Substrate	Temperature °C	Carrier gas	Thickness	Shape and grain size	notes
1	[100]	2011	Quartz	775-830	Ar	30 nm	Random crystals with few micron size	Mechanical cleavage was used to obtain mono and few layer thickness.
2	[101]	2012	SiO_2/Si	650	nitrogen	Mono-bi layer	~2 mm^2 continuous film	Back-gate FET with n-type behaviour, 10^4 on-off ratio and 0.02 $cm^2\ V^{-1}\ s^{-1}$ mobility.
3	[102]	2012	SiO_2/Si & sapphire	650	Ar	monolayer	~1.5 mm^2 continuous film	Top-gate (HfO_2) FET with n-type behaviour, 10^8 on-off ratio and 190 $cm^2\ V^{-1}\ s^{-1}$ mobility.
4	[113]	2013	Various substrates	650	Ar	monolayer	Centimetres continuous film	Back-gate FET with n-type behaviour, 10^7 n-off ratio and 1.2 $cm^2\ V^{-1}\ s^{-1}$ mobility.
5	[114]	2013	SiO_2/Si	700	nitrogen	monolayer	~1×15 mm continuous film	Back-gate FET with n-type behaviour, 10^5- 10^7 on-off ratio and 1-8 $cm^2\ V^{-1}\ s^{-1}$ mobility.
6	[115]	2013	SiO_2/Si	606	nitrogen	monolayer	Hundreds of microns continuous film	Back-gate FET with n-type behaviour, 0.26 $cm^2\ V^{-1}\ s^{-1}$ mobility.
7	[116]	2013	SiO_2/Si	850	nitrogen	Mono & few layer	1 cm^2 continuous film	Back-gate FET with n-type behaviour, 0.26 $cm^2\ V^{-1}\ s^{-1}$ mobility.

Table 2-4: Continued.

No.	Ref.	Year	Substrate	Temperature °C	Carrier gas	Thickness	Shape and grain size	notes
8	[117]	2013	mica	530	Ar	monolayer	Centimetre-scale film	Investigating the photoluminescence of the monolayer films.
9	[118]	2014	SiO_2/Si	650	Ar	monolayer	Centimetre-scale film	Photodetector with MoS_2/graphene heterostructure. The responsivity 10^7 A/W.
10	[119]	2014	SiO_2/Si	650	Ar	monolayer	Millimetre scale	Studying the effects of promoters on larger area growth of high crystalline films.
11	[120]	2014	Sapphire	650	nitrogen	monolayer	1 cm^2 continuous film	Solar cell with efficiency 5.23 made by heterojunction of MoS_2/Si.
12	[121]	2014	Au foil	530,680	Ar	monolayer	Millimetres scales	MoS_2 monolayer films for hydrogen evolution reaction.
13	[122]	2014	SiO_2/Si	760	Ar	monolayer	2−3 mm width	Studying the changes in the shape of MoS_2 crystal flakes with respect to their distance from the MoO_3 source.
14	[123]	2014	Au foil	530,680	Ar/H_2	monolayer	80 micron edge length of the flake	Investigating the growth parameters in a reduced environment (hydrogen gas flow)

Table 2-4: Continued.

No.	Ref.	Year	Substrate	Temperature °C	Carrier gas	Thickness	Shape and grain size	notes
15	[124]	2015	Au foil	530,680	Ar	monolayer	115 micron edge length of the flake	Investigating the growth parameters with different facets of Au foils.
16	[125]	2015	Sapphire	700	Ar	monolayer	6 mm x 1 cm (continuous film)	Back-gate FET with n-type behaviour, 43 $cm^2 V^{-1} s^{-1}$ mobility.
17	[126]	2015	SiO_2/Si	700	Ar	monolayer	40 micron grain size	Investigating carbon based materials as a reduction agent for MoO_3.
19	[127]	2015	Sapphire	530,850	Ar/O_2	monolayer	350 micron grain size	Back-gate FET with n-type behaviour, $>10^7$ on-off ratio and 90 $cm^2 V^{-1} s^{-1}$ mobility
20	[128]	2015	SiO_2/Si	800	Ar	monolayer	300 micron grain size	Investigating growth parameters and shows a novel transfer method for MoS_2.
21	[129]	2018	Sapphire	650	Ar	monolayer	2 inch wafer	Top-gate (HfO_2) FET with n-type behaviour, 10^7-10^8 on-off ratio and 70 $cm^2 V^{-1} s^{-1}$ mobility.

Table 2-5: WS_2 growth via direct reaction between sulphur and tungsten trioxide powder.

No.	Ref.	Year	Substrate	Temperature °C	Carrier gas	Thickness	Shape and grain size	notes
1	[103]	2013	Sapphire	900	Ar	monolayer	50 micron square	Ionic liquid gate with ambipolar behaviour, 100 on-off ratio and mobility 0.46 and 0.28 $cm^2 V^{-1} s^{-1}$ for electrons and holes.
2	[130]	2013	SiO_2/Si	800	Ar	monolayer	5 microns	Photoluminescence comparative study between monolayer WS_2 and MoS_2.
3	[104]	2013	SiO_2/Si	750	Ar	monolayer	178 micron flake size	Investigating the growth mechanism of WS_2 monolayer.
4	[131]	2014	SiO_2/Si	1070	Ar	monolayer	370 micron flake size	Exploring the effect of sulphur precursor on the growth parameters of WS_2 monolayers.
5	[132]	2015	Au foil	800	Ar	monolayer	400 micron size and Continuous film	Investigating the Au foil as a substrate for ambient pressure chemical vapour deposition. Roll to roll transferring method for WS_2 film to flexible substrates. Back-gate FET with n-type behaviour, 10^6-10^7 on-off ratio and 1~2 $cm^2 V^{-1} s^{-1}$ mobility. Flexible FET with n-type behaviour, 10^5 on-off ratio and 0.99 $cm^2 V^{-1} s^{-1}$ mobility.

Table 2-5: Continued.

No.	Ref.	Year	Substrate	Temperature °C	Carrier gas	Thickness	Shape and grain size	notes
6	[133]	2017	SiO_2/Si	750,800,850,880,900,950	Ar	Mono and few layers	~400 micron flake size	Studying various growth condition of WS_2 monolayer and fewlayers.
7	[134]	2017	Sapphire	920,980	Ar	monolayer	2 inch wafer	Back-gate FET with n-type behaviour, 0.02 $cm^2 V^{-1} s^{-1}$ mobility. Photodetector with 5.5×10^3 on-off ratio and 560 µs rise and decay time. Flexible substrate photodetectors has been fabricated with responsivity of up to 5 mA/W.
8	[135]	2018	Sapphire	1050	Ar	monolayer	405 micron size	Synthesis of WS_2 monolayer by semi-sealed CVD method.
9	[136]	2018	SiO_2/Si	1010	Ar	monolayer	233 micron size	Back-gate FET with n-type behaviour, ~0^7 on-off ratio and 50.5 $cm^2 V^{-1} s^{-1}$ mobility.

2.4.2.2.3 Sulphurisation of transition metal chlorides ($MoCl_5$, WCl_6)

In the past decade, transition metal chlorides ($MoCl_5$, WCl_6) has been utilized for synthesis of MoS_2 and WS_2 nanostructure by reacting with sulphur via atmospheric pressure chemical vapour deposition (APCVD) which makes them good candidates as precursors for synthesis of 2D-MS_2 using CVD processes [137]. Yu et al. were the first group that demonstrated this route with molecularly thin MoS_2 in 2013 where they successfully exploited molybdenum pentachloride ($MoCl_5$) powder as a Mo-based solid precursor then sulfurize it in low pressure argon environment at 850 ^oC to synthesis highly uniform polycrystalline monolayer and few-layer MoS_2 films with centimetre scale size [138]. Their CVD system set up was identical with ones normally used in direct reaction of sulphur and transition metal oxides (MoO_3, WO_3) that previously depicted in Figure 2-13. The only difference is $MoCl_5$ substituted MoO_3. Additionally, different insulating substrates were used to grow MoS_2 films, which were placed in position 2 rather than position 1 (see Figure 2-13). The main advantage of using $MoCl_5$ as precursor compared to transition metal precursors and their oxides precursors is the precise control of the thickness all over the depositing area without coexistence of thicker regions on the film. This is due to self-limiting nature of the chemical reaction between the sulphur and molybdenum pentachloride. However, as the films are polycrystalline in nature, the FET devices fabricated by this method exhibit low mobility between 0.003-0.03 $cm^2\ V^{-1}\ s^{-1}$ [138].

In similar way, WS_2 monolayer triangular flakes were grown on hexagonal boron nitride flake (which serve as a substrate) using sulphurisation of WCl_6 in its solid form which shows high PL yield with extra sharp peak at 2.01 eV with FWHM only 26 meV [139]. The CVD system was similar to what was reported for sulphurization of $MoCl_5$, the only difference is that sulphur boat was placed between WCl_6 boat and the substrate not in the upstream of the inert gas [139]. Alternatively, Thangaraja and his co-workers designed facile experiments in which firstly they drop casted WCl_6 dissolved in ethanol on SiO_2/Si substrate followed by annealing at 750 ^oC in sulphur rich environment where the final WS_2 monolayers flakes had various morphologies like triangular, six pointed star-shaped, butterfly and dendritic shape [140]. It should be mentioned that both synthesis routes for WS_2 were at atmospheric pressure which is relatively more cost effective as there is no need for expensive vacuum systems.

The low evaporation temperature of transition metal chlorides (room-temperature for $MoCl_5$ [141] and 100 ^oC for WCl_6 [142]) permits exploring them as gas phase precursors which they could directly react with a sulphur-based gas phase precursor such as hydrogen sulphide (H_2S) to create MoS_2 and WS_2. Accordingly, Huang and his group synthesised MoS_2 multi-layered films with high uniformity over large area using this approach [141]. $Mo_{26}S_{61}Cl_{13}$ was the final product that deposited on the substrate when $MoCl_5$ and H_2S were directly reacted at room temperature in (APCVD) system then it is totally transformed to polycrystalline MoS_2 film via two-annealing steps where the first one in H_2 flow at 500 °C followed by a second step at 900 °C in H_2S [141].

Meanwhile, another group employed analogous methodology to grow WS_2 where WCl_6 and H_2S were directly reacted in gaseous phase and form WS_2 that deposited on SiO_2/Si substrate at 700 °C with low pressure [142]. The number of deposited WS_2 layers was finely tuned by adjusting the growth time of the reaction where shorter time form thinner layer and vice versa as well as the potential photodetection application for these films has been tested [142]. The modulation of MS_2 films layer number over large area is enhanced remarkably using this technique. The figure below shows the schematic diagram for all gaseous phase growth of MS_2 via reaction of $MoCl_5$ and WCl_6 with H_2S.

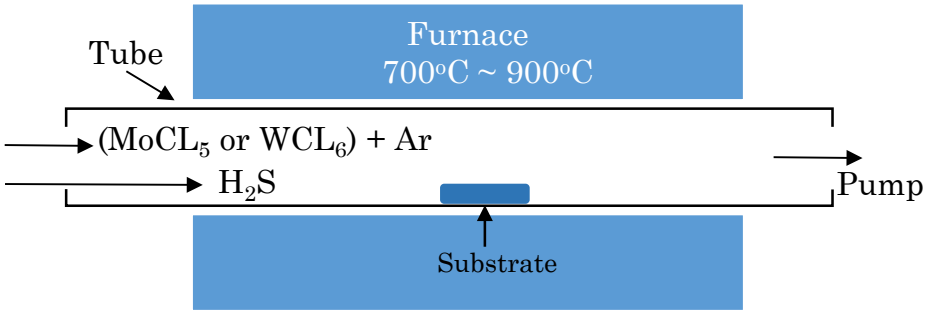

Figure 2-14: Schematic diagram CVD system for MS_2 by reaction of $MoCl_5$ or WCl_6 with H_2S in a gaseous phase.

2.4.2.2.4 Thermolysis of Thiosalts $(NH_4)_2MS_4$

Ammonium tetrathiomolybdate (ATM) $(NH_4)_2MoS_4$ and ammonium tetrathiotungstate (ATT) $(NH_4)_2WS_4$ are chemical compounds that can be exploited as single source precursors for MoS_2 and WS_2 production [6]. Generally, single source precursors are compounds that contain all the necessary reactants to synthesis a product simply by decomposition without additional precursors. In thiosalts case, transition metal and sulphur both exist in the chemical formula and by applying heat they could decompose to MoS_2 and WS_2, however, the total transformation from $(NH_4)_2MS_4$ to MS_2 by thermal decomposition undergoes multiple stages.

In inert gas environment such as argon or nitrogen, $(NH_4)_2MS_4$ thermally decomposes to MS_3 solid product in addition to ammonia (NH_3) and hydrogen sulphide (H_2S) as gaseous phase side products at temperatures between 120°C-280°C. MS_3 is then completely transformed to MS_2 if further annealed at a temperature between 300°C-800°C at the same conditions. However, thermolysis temperature could be reduced significantly when the reaction is conducted under reduced environment (hydrogen gas) where MS_2 can be produced between 290°C-425°C [143]–[145]. Therefore, researchers have been exploring thermal decomposition of thiosalts to grow MoS_2 and WS_2 nanotubes in the beginning of the past decade as a simple, inexpensive and scalable production method [146], [147].

When 2D-TMDC materials became an intriguing research topic, it was the work conducted by Liu and his group that highlight the importance of this route for large scale growth of 2D-MoS_2 films [148]. They dip-coated SiO_2/Si and sapphire substrates in 48 mM solution of

$(NH_4)_2MoS_4$ /dimethylformamide (DMF) and after pre-baking at 120°C, the samples were mounted in CVD system for annealing. The experiment was designed with two-annealing steps where the first step was to anneal the samples in Ar/H_2 gas mixture with low pressure at 500°C to form amorphous MoS_2 films followed by further annealing step to improve the crystallinity of the film at 1000°C in argon with and without sulphurisation treatment. The MoS_2 films were centimetre-scale in size and uniformly trilayer thickness with few bilayer regions. Moreover, the films grown on sapphire showed comparable optical and electrical properties to exfoliated MoS_2 when they annealed in sulphur rich environment with ~10^5 on-off ratio and 6 $cm^2\ V^{-1}\ s^{-1}$ field effect mobility for the FET device with backgate configuration. This study revealed the crucial role of the substrate type (amorphous or crystalline) and sulphurisation step on the structural, optical and electrical properties of the MoS_2 films. The films grown on sapphire with sulphurisation step possessed larger grain size crystals, their Raman and PL (photoluminescence) peaks had stronger intensity and the FETs had better electronic characteristics compared to samples that grown on SiO_2/Si or not sulphurized [148]. Figure 2-15 summarize the essential steps of MoS_2 synthesis via thermolysis of solution-processed ATM salt.

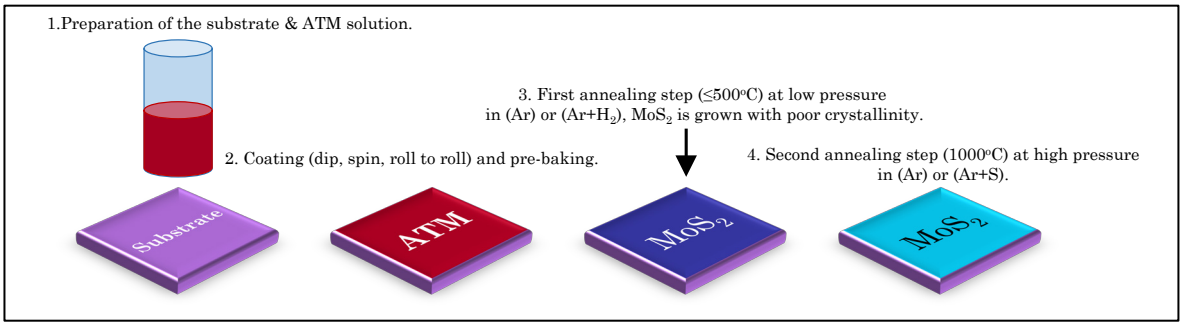

Figure 2-15: Schematic illustration of MoS_2 growth via thermolysis of ATM.

Furthermore, George et al used the same methodology to form bilayer MoS_2 film on SiO_2/Si without extra sulphur [149]. He claimed that $(NH_4)_2MoS_4$ dissolved n-methylpyrollidone (NMP) could be spin coated uniformly onto 2 inch wafer to create continuous layer film that thermally decomposed by two annealing steps (480°C-1000°C respectively) to bilayer MoS_2 film all over the wafer. As-deposited film was used to fabricate backgate FET device which showed ~10^2 on-off ratio and 0.1 $cm^2\ V^{-1}\ s^{-1}$ mobility which was in good agreement with Liu findings for MoS_2 films grown on same substrate type that excluded sulphur treatment [148], [149].

Obviously, synthesis of MoS_2 films by thermolysis requires a solution processing step to coat the samples with continuous and uniform $(NH_4)_2MoS_4$ layer that can be converted to MoS_2 film through annealing. Therefore, a suitable coating technique that can achieve continuity, uniformity, large area coverage, tunability of precursor layer thickness and most importantly compatibility with current semiconductor technology is essential to start producing them for next-generation electronics and optoelectronics. Unfortunately, dip-coating technique that has been proposed by Liu does not meet the previously mentioned standards whereas spin-coating technique seems to be more reliable for this task [148].

However, formulating $(NH_4)_2MoS_4$ solutions for spin-coating using single conventional solvents like DMF, NMP and ethylene glycol normally is insufficient to provide the desirable surface properties for the precursor layer [149]–[151]. This is because either precursor layer is non-uniform and contains high density of surface defects and/or de-wetting areas when a single solvent is used or due to limited ability to tune the concentration of the solution, in particular for low concentrations which eliminates the formation of ultra-thin precursor film [150], [151].

Therefore, searching for an optimum $(NH_4)_2MoS_4$ solution formula that provides wafer-scale coverage of uniform and continuous precursor film via spin coating technique was an intensive area of research during last few years. Three individual groups finally succeeded to achieve this goal by refining three different solution recipe using a mixture of organic solvents and/or binding agents [150], [152], [153].

The first group used a mixture of organic solvents DMF, n-butylamine and 2-aminoethanol to dissolve the Mo-based thiosalt prior to spin-coating on SiO_2/Si substrate which showed excellent uniformity and tunability of the solution-processed precursor. The samples were then annealed via two steps with sulphur (450°C -1000°C) [150]. The thickness of the MoS_2 films were highly dependent on the initial concentration of the precursor solution which can be tuned to form one, three and five stacking layers. The average of mobility was ~0.24 $cm^2 V^{-1} s^{-1}$ and ~10^4 on-off ratio for 100 pentalayer MoS_2 n-type FET devices with top-gate configuration and HfO_2 gate-dielectric [150].

Polymer-assisted solution processing of MoS_2 was an alternative route that Yang and his group proposed. They mixed ATM with linear-polyethylenimine polymer in DMF and 2-aminoethanol solvents with different ATM concentration (from 20 mM up to 300 mM) [152]. Next, the solutions were spin-coated on SiO_2/Si substrate (up to 6-inch wafer size) to form the precursor layer then annealed at 700°C for one hour in (96% Ar/4% H_2) flow without sulphurisation [152]. The minimum MoS_2 films thickness has been achieved using this method was 2 nm which is almost three molecular layers [152]. MoS_2 films with different thickness (2, 6, 9, 18 and 32 nm) were used to fabricate photodetectors which they showed thickness-dependent photocurrent enhancement in multilayer regime (from 2 nm to 9 nm) as the on-off ratio of the current increased from 10^1 to 10^4 before declined to 10^2 when the MoS_2 films become bulk (32 nm thickness). Additionally, the few-layer and bulk MoS_2 films (from 6nm to 32 nm thickness) exhibit a consistent fast photoswitching response with less than 1ms while the trilayer film thickness was much slower, possibly due to the high density of defects [152].

The most recent work to tackle the uniformity issue of ATM film was done by Ionescu and his co-workers where they dissolved a chelating agent (ethylenediaminetetraacetic acid (EDTA)) in Dimethylsulfoxide (DMSO). The solution was used to dissolve ATM to form a homogeneous solution that can create uniform ATM films via spin-coating on wafer-scale [153]. The solution-processed MoS_2 films has been reported with uniformly monolayer thickness on SiO_2/Si wafer

but the electrical performance of double gate FET device with MoS_2 channel indicated that the film has insulating behaviour rather than semiconductor [153].

Moreover, the ATM solution can be used as an ink to pattern samples due to its liquid phase nature, then by thermal annealing, various shapes and morphologies of MoS_2 can be formed. Hung et al. employed micromolding in capillaries (MIMIC) patterning method and ATM solution as an ink to form MoS_2 nanoribbons by thermolysis (non-sulphurized) where 3.9 nm thickness and high aspect ratio (length/width) $\sim 7.4 \times 10^8$ of nanoribbons has been demonstrated on various kinds of substrates [154]. In addition, a MoS_2 nanoribbons back gate FET devices on 300 nm SiO_2/Si substrates were formed with n-type behaviour and mobility ranging from 7.2×10^{-4} to 3.1×10^{-3} $cm^2\ V^{-1}\ s^{-1}$ having been obtained [154].

Between 2016 and 2018, Lim and his groups published two papers, the former one elucidated the possibility of directly growing MoS_2 on plastic substrates while the latter one developed an approach for meter-scale sheets growth of MoS_2 by roll to roll manufacturing process [151], [155]. Both proposed approaches synthesised MoS_2 films by thermal decomposition of ATM without sulphurisation step at relatively low annealing temperature (450°C in H_2/N_2 [151] and 600°C in N_2 [155]) where the resultant films were highly uniform. Ethylene glycol as a single organic solvent was used to prepare three different concentrations of ATM solutions that could be coated uniformly leading to form 3,10 and 28 layer thickness of MoS_2 films in roll to roll process [155]. However, when spin-coating was applied, ethylene glycol was strictly fixed to one concentration and rotational speed to generate uniform and continuous ATM layer that converted later to MoS_2 with five layer thickness [151]. To probe electronic properties, ionic gate thin film transistors were fabricated in both reports, the devices were n-type (with the electron mobility 14 $cm^2\ V^{-1}\ s^{-1}$ for [151] and 0.6 $cm^2\ V^{-1}\ s^{-1}$ for [155]) while the on-off ratios were 500 for [151] and 1000 for [155] respectively. Optoelectronic properties were also investigated by fabricating photodetectors which revealed photocurrent generation under visible light illuminations with sub nano-ampere range for [151] and 1.4 nA for [155]. However, the low photo-generated current and slow photo-response of the photodetectors could be attributed to the low crystallinity of the films due to low annealing temperature.

Xi et al. chose to explore the hydrothermal approach by growing MoS_2 films selectively between and over gold patterns that were pre-deposited as drain-source electrical contacts on 350 nm SiO_2/Si substrates [156]. The ATM was dissolved in deionized water and Hydrazine hydrate (N_2H_4) was added to the solution as a reducing agent. Apart from their function as drain-source contacts for the transistor devices, the gold electrodes played the role of a catalytic activator for the hydrazine hydrate whose inject electrons in ATM to form MoS_2 [156]. The back gate FET devices were n-type with 0.4 $cm^2\ V^{-1}\ s^{-1}$ mobility and 10^6 on-off ratio and the minimum thickness between the contacts for the MoS_2 film was ~12nm [156]. Despite the fact that the substrates were amorphous (SiO_2/Si), the deposition temperature was low (90°C) and there is no extra sulphur added to the reaction which as a consequence resulted poorly crystalline MoS_2 films that can be easily identified by very broad Raman peaks [156].

Nevertheless, the organic-free solution and patterning step minimized carbon contaminations, while using hydrazine hydrate as electron donor to MoS_2 which is also known as excellent chalcogenides solvent, resulted in acceptable semiconducting performance even though the MoS_2 films were almost amorphous [157]. However, the relatively low mobility could be originated from high Schottky barrier between MoS_2 and gold contacts and/or back gate/back contacts configuration [158].

To sum up, growth of two-dimensional molybdenum disulphides by $(NH_4)_2MoS_4$ thermolysis has witnessed rapid developments during the past few years where the dimensionality and functionality of these films has been improved dramatically paving the way towards realisation of 2D electronics and optoelectronics devices. In contrast, to the best of author's knowledge there is comparably little progress in exploiting tungsten-based thiosalt ($(NH_4)_2WS_4$) by thermal decomposition for large-area 2D-WS_2 synthesis. Specifically, for FET's and photodetector applications due to complexities associated with coating continuous and spatially homogenous ATT films that could convert to high quality WS_2 films suitable for device fabrication.

Chapter 3
Characterisation Techniques and Device Applications of MS_2

3.1 Introduction

The main goal of this Ph.D. thesis is to produce MS_2 films and microstructures for electronic and optoelectronic device applications. This inevitably requires using different characterisation tools to assess the quality of these films and microstructures to ensure they can be can be adapted as photodetector and FET semiconductor channels. There are three essential parameters that need to be characterised: thickness, crystallinity and stoichiometry of MS_2. For thickness assessment, optical microscopy, atomic force microscopy (AFM), stylus profilometry, Raman spectroscopy and photoluminescence spectroscopy were used to estimate the thickness of the films and microstructures. Crystallinity was assessed using the FWHM of Raman peaks while X-ray photoemission spectroscopy evaluated the compositions of the films. All these characterisation techniques are briefly described in the first part of this chapter. Additionally, to familiarize the readers with electronic and optoelectronic devices, structure and principle of operations for photodetector and field effect transistor are briefly discussed.

3.2 Characterisation tools

3.2.1 Optical Microscopy

Optical microscopy is a simple characterisation tool which is not restricted by any sample preparation and complicated procedure to be conducted. Several reports showed that optical microscopy can provide non-destructive, rapid and accurate thickness assessments for the 2D-materials flakes [159], [160]. However, choosing proper supporting substrates can facilitate layer number identification of 2D flakes which is found that 90 nm and 285 nm thickness SiO_2/Si is an optimum substrates for optical microscopy [6]. The optical contrast between the flakes and the substrate is the key parameter for layer number identification which can be expressed as Michelson contrast formula [160]:-

$$Contrast = \frac{R_{2D\ material} - R_{dielectric}}{R_{2Dmaterial} + R_{dielectric}} \qquad \text{Equation 3-1}$$

Where $R_{2D\ material}$ and $R_{dielectric}$ are the intensities of reflected light from the surfaces of the 2D flake and from the substrate. When the reflected light intensity from the flake and the substrates are equal, the flakes will be invisible and cannot be detected by optical microscope.

When the reflected light intensity from the flake has lower intensity compared to the substrate reflected light intensity, the visibility of the flake becomes darker than the substrate. This what normally happens with graphene which appears under the microscope darker than the substrate and the optical contrast increased to be darker by increasing the number of layers (see Figure 3-1) [159]. If the reflected light intensity from the flakes is higher than the substrates, the flake will appear lighter than the background [160]. Normally, transition metal dichalcogenides flakes are darker than the substrates when they are in few layer regime (between 1 to 7 layers) and the maximum negative optical contrast can be achieved with three and four layers flakes [159]. However, when thickness of the flakes increased beyond the 7 layers, the flakes becomes brighter (positive optical contrast) than the substrates and the brightness increased by increasing the thickness of the flakes as it can be clearly noticed in Figure 3-2 [159]. It is worth to mention the optical microscope used in this project is Nikon LV100D.

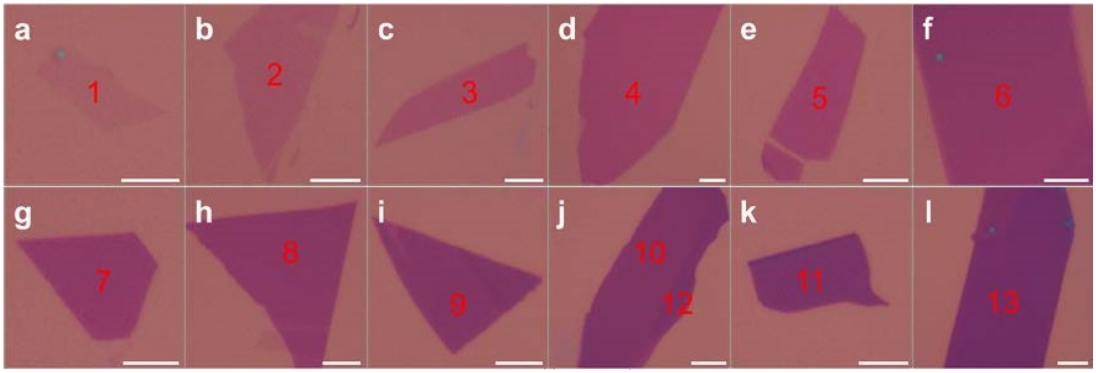

Figure 3-1: (a-I) colour optical microscope images of 2D flakes with different number of graphene layers from 1 to 13 layers on 300 nm SiO_2/Si. The negative optical contrast is increased by increasing number of layers. This figure is reproduced with editing from ref. [159].

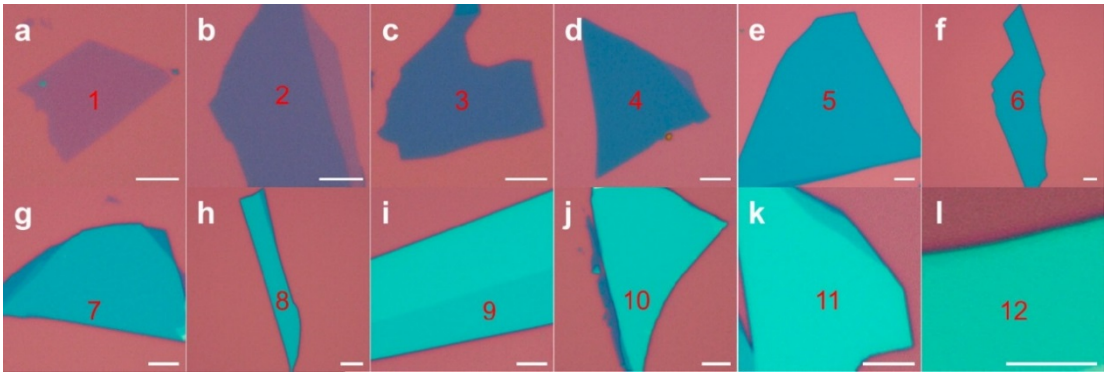

Figure 3-2: (a-I) colour optical microscope images of MoS_2 flakes with different number of layers from 1 to 12 layers on 300 nm SiO_2/Si. Clearly, the negative optical contrast is in the few layer regime from 1 to 7 layers where three (c) and four (d) layers have the maximum negative contrast. From 8 layers (h) to 12 layers the positive optical contrast increased by increasing number of layers. This figure is reproduced with editing from ref. [158].

3.2.2 Stylus profilometry

One of the earliest techniques has been utilized to measure step height, roughness of surface, topologies and morphologies of planer surfaces is stylus profiler [161]. In analogy to the phonograph, the working principle of stylus profiler basically relies on dynamic and direct physical contact between a sharp tip made from hard material such as diamond and the surface of the specimen to study the surface properties [162]. The vertical variations in the surface height are probed by the stylus and converted to analogue electrical signals through linear variable differential transformer (LVDT) followed by analogue to digital conversation via converter to record the height data [161]. This technique can provide precise vertical resolution down to sub-nanometre scale on relatively large lateral dimensions in a short time without the need for sample preparation [162]. Both size and shape of the stylus determine essential parameters such as the lateral resolution and penetration depth. However, there are several drawbacks related to use stylus profilometry to assess surface properties. This includes time consuming 3D mapping, difficulties to visualise small features due to low resolution of the camera equipped with stylus profilers and possibility to damage the surfaces due to excessive force applied to the tip. In this Ph.D. project, KLA Tencor P-16 Stylus Profiler was used to extract the step height of MS_2 microlines at the centre of each line (will be discussed later in section 6.7). To ensure accurate measurements for the thickness of the lines at the centre, the applied force, the sampling rate and scanning speed were reduced to the minimum.

3.2.3 Atomic Force microscopy (AFM)

In the early 1980s, Binnig et al. invented the scanning tunnelling microscope (STM) as an innovative surface metrology technique for atomic scale topography mapping [163]. STM measurements perform by passing tunnelling current from metal tip of the device through electrically conducting or semiconducting sample surface to ensure an electrical circuit with the tip [162]. The operational setup of STM requires an extremely small separation (normally in angstroms) between the tip and the sample surface to let the tunnelling electrons pass from the tip to the sample surface [162]. The height variations of the surface cause dramatic changes in tunnelling current magnitude due to high dependency of tunnelling current on the electrical contacts separation (the metal tip and the surface) [162]. This variations in current magnitude is recorded and then translated to height information of the surface. Although STM is very powerful tool for probe the surfaces properties in atomic scale, its applications are limited only with electrically conductive surfaces.

However, four years later after the invention of STM, Binnig et al. developed atomic force microscope (AFM) which can be used to probe the surface topography of the insulating materials as well as conductive ones [164]. AFM can considered as a hybrid tool that share features with the stylus profiler and STM [164]. Instead of utilizing the tunnel current in STM, AFM employs the interacting forces between the tip and the surface which can be classified in two main

categories [162]. The first one is repulsive forces while the latter is attractive forces, the type of forces that employed also determine the operating mode of the AFM where the contact mode is corresponds to repulsive forces and non-contact mode is assigned to attractive forces [162]. Both forces are originated from several quantum phenomena occurred in atomic scale [165]. The tip of the AFM tip is connected to an elastic cantilever in its free end which acts as force sensor that deflected due to force variations between the tip and the surface [165]. The deflections are caused by either the cantilever bending in contact mode (due to repulsive forces) or from cantilever oscillations in non-contact mode (due to attractive force) which both are detected optically using lasers [162]. Additionally, a third (tapping) mode can be achieved by oscillating the tip in resonance frequency with the cantilever to tapping the sample surface, this mode is very useful to probe soft surfaces and increase the vertical height range detection [162].

Although there is similarities between stylus profiler and AFM in contact mode especially in working principle, the latter one can provide more accurate topographical images due to higher vertical and lateral resolutions which is beneficial for characterising low-dimensional materials [162]. Unlike Stylus profiler, if the surface of the sample can be easily damaged, AFM can provide non-destructive measurements using non-contact mode as well as additional electrical, magnetic information about the surface can be extracted using AFM. The vertical and lateral resolution ranges for stylus profiler, STM tools (including the AFM) and optical profiler can be summarized by Stedman diagram to compare the dimensional limitations of each technique as illustrated in Figure 3-3 [166]. Agilent 5500 scanning probe microscope was used to probe the thickness of WS_2 films in Chapter 5 section 5.5.1.

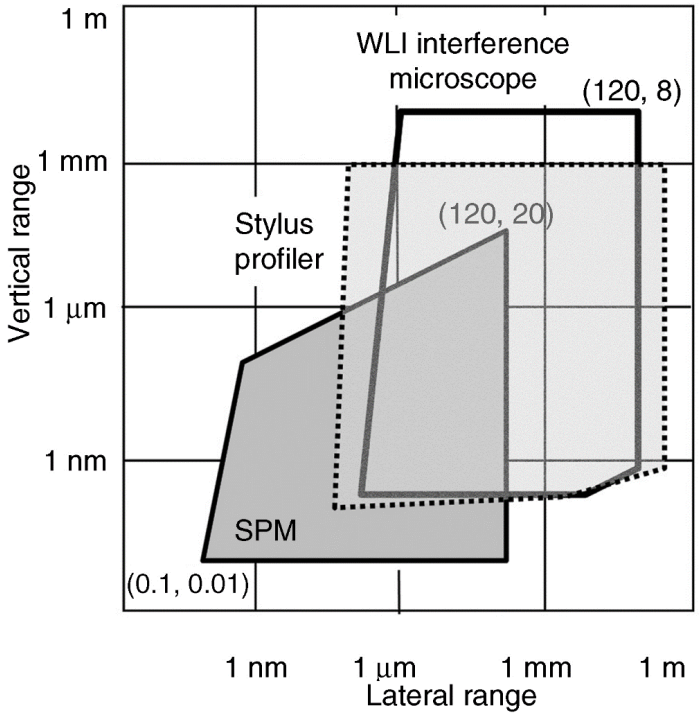

Figure 3-3: Vertical and lateral resolutions (log scale) of various profile measurements tools STM (including AFM), stylus profiler and optical profiler. This figure is reproduced with editing from ref. [162].

3.2.4 Raman spectroscopy

One of clearly observable phenomena of light-matter interaction is scattering. This physical process occurs when the light hits a transparent substance. It leads to the excitation of the electrons of the substance from their ground state to a virtual one due to the absorption of the incident light. Then, photons are re-emitted with exactly the same energy in different directions. This is called Rayleigh scattering and it is defined as an elastic process which means the light pass through the material without any change in its energy. Although Rayleigh scattering is the prominent and the most intense scattering mechanism, it is not the only one.

In the twenties of the last century, C. V. Raman an Indian scientist discovered another type of scattering which known by his name Raman scattering (effect). This kind of scattering is an inelastic process, in other words, the photons are re-emitted with lower or higher energies compared with the absorbed ones. Raman scattering is caused by dropping down the electrons from their virtual states (after incident photons are absorbed) to different vibrational states other than the ground state that they originally excited from. This is due to the changes in vibrational motions of molecules within the lattice, i.e. phonons. If the photons are emitted in lower energies (frequencies) compared to the absorbed ones then it is called Stokes lines while if they are emitted at higher energies then it is called Anti-Stokes. Both of them are normally displaced in the same wavelength interval from Rayleigh scattering lines making them symmetrical shifts. However, the Stokes lines are always stronger in intensity compared to the Anti-Stokes ones due to the difference in the number of excited electrons for both of them which obey to Boltzmann distribution (see Figure 3-4). Therefore, Raman spectroscopy normally utilize the Stokes line rather than Anti-Stokes because of its higher intensity.

Raman spectroscopy and infra-red spectroscopy are both vibrational spectroscopic techniques which makes them closely related to each other. However, there is some essential differences between them. For example, IR spectroscopy works only in IR region while Raman can be performed in IR, visible and near UV as it measures the shift from the main incident wavelength. Also, IR spectroscopy probes the absorption (transmittance) spectra while Raman characterise the scattered one. Most importantly, in order to be vibrational mode active in IR spectroscopy (detectable) it has to alter the dipole moment of the molecule whereas in Raman vibrational mode is active if the net change of polarizability is non-zero [167]–[169]. For linear molecules (centrosymmetric), there is mutual exclusion role between Raman and IR active vibrational mode. In other word, when the mode is Raman active, it will be IR inactive and vice versa which make both Raman and IR spectra are complementary to each other [167], [169]. However, for non-linear molecules, both modes could be active or inactive independent on each other.

Raman spectroscopy is very powerful structural characterisation tool as it is very sensitive to variations for the chemical structure of the material. Typically, Raman peaks frequencies, their shifts, polarisations, widths, intensities can provide important information about the

composition of the material, strain and stress on the material, crystal orientation, crystallinity, thickness of the materials. Additionally, Raman peaks difference is an excellent thickness indicator for 2D-TMDC materials. More details about Raman spectroscopy of MS_2 was discussed early in section 2.2. In this Ph.D. project, Raman spectra have been characterised using Raman spectrometer (Renishaw inVia system) with 633 nm and 532 nm wavelengths. The Raman results in Chapter 4 are obtained using 633 nm excitation wavelength while 532 nm wavelength is used to probe Raman spectra of MS_2 samples in Chapter 5 and Chapter 6 respectively.

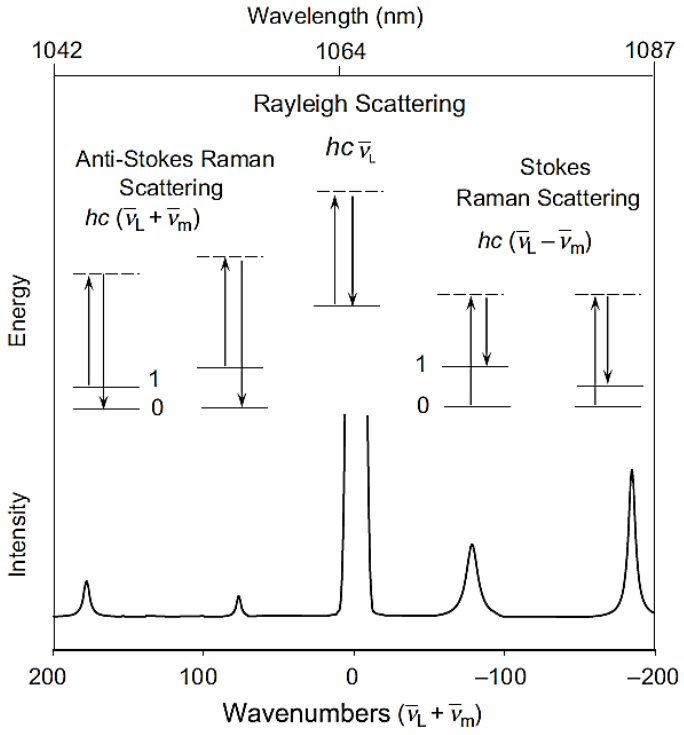

Figure 3-4: Schematic diagram illustrates the Rayleigh, Stokes and Anti-Stokes (Raman) scattering peaks and their energy band transition. The up arrows represent the laser wavelength excitation of electrons to the virtual state while the down arrows represents the relaxation of electrons from the virtual state to the same ground state in Rayleigh, lower vibrational energy level in Stokes lines and higher vibrational energy level in Anti-Stokes peaks. It can be noticed also that both Raman Stokes and Anti-Stokes peaks are much lower in intensity compared to the Rayleigh one. In the meantime, Stokes peaks are stronger compared to Anti-Stokes peaks due to higher number of particles that excited in Stokes peaks as a result of Boltzmann distribution. This figure is reproduced from ref. [167].

3.2.5 Photoluminescence Spectroscopy

Essentially, semiconductor materials are divided in two main categories according to their bandgap structure which are direct and indirect bandgap semiconductors. For direct bandgap semiconductors, the holes in maximum of valence band and the electrons in the minimum of conduction band have the same momentum and only separated by the forbidden energy band (bandgap) in Energy-Momentum diagram. This band structure allows the electrons in the conduction band to recombine with the holes in the valence radiatively as the energy and the momentum in the crystal lattice is already conserved, i.e. photons are released as a consequence of electron-hole pair recombination.

On other hand, for indirect bandgap semiconductors, the top of the valence band and the valley of the conduction band have different momentum values, in other words, they are mismatched. This band structure requires phonon emission or absorption in addition to photon generation from electron-hole pair recombination in order to conserve the energy and momentum in the crystal. Although this indirect optical transition that need electron, photon and phonon might occur, its probability is very low comparing with direct optical transition in direct bandgap semiconductor. As a result, a fast non-radiative decay dominates the transition mechanism in indirect bandgap semiconductor due to its high probability which is the reason behind indirect semiconductors are not commonly used in optoelectronic light emitter devices due to low photons yield.

Basically, one of distinctive features of direct band-gap semiconductors compared to indirect band-gap semiconductor is light generation (luminescence). Photoluminescence spectroscopy utilize electromagnetic radiation with higher energy of the direct bandgap to photoexcite the electrons from the valence band to the conduction band then detect the emitted photons from the crystal. The detected photons can give valuable information about the bandgap size, crystal defects and life time of the carriers (see Figure 3-5).

Generally, transition metal dichalcogenides exhibit layer-dependent bandgap structure as it mentioned earlier in details in section 2.3 where bulk form is indirect bandgap and monolayer regime is direct bandgap with higher energy. Moreover, the bandgap of TMDC is tuneable in the few-layer form where photoluminescence is enhanced until reach its maximum in single layer. Thus, PL spectroscopy is very useful technique not only to study electronic properties of TMD, but also to estimate the thickness of these materials. In this Ph.D. project, Raman spectrometer (Renishaw inVia system) with 532 nm laser excitation wavelength was used to conducted PL spectroscopy for samples in Chapter 5 and Chapter 6. It is worth to mention that this system can be used to study the vibrational and electronic structure concurrently by producing Raman and PL data in the same spectrum.

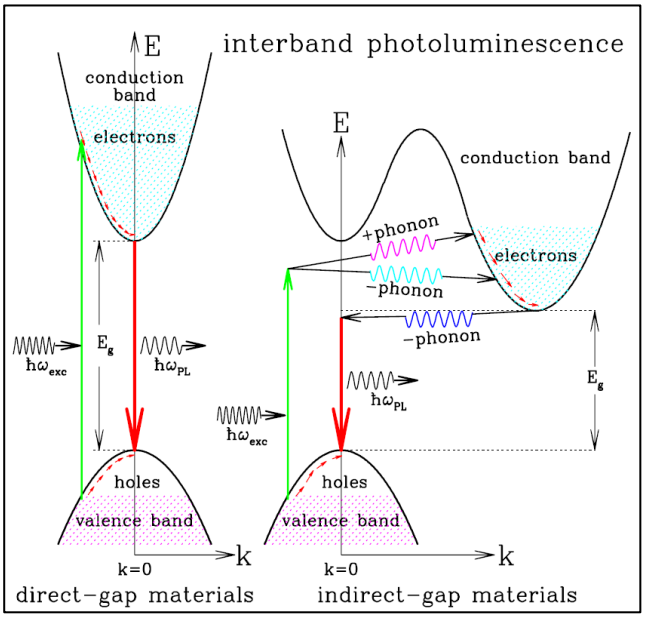

Figure 3-5: Schematic diagram of direct and indirect bandgap semiconductors and their transitions. This figure is reproduced from ref. [170].

3.2.6 X-ray Photoelectron Spectroscopy (XPS)

XPS has been developed as non-destructive spectroscopic characterisation tool to analyse quantitatively the chemical compositions of thin films and materials surfaces normally with few nanometres thickness. When a material surface is bombarded by x-ray beam, electrons are ejected from their shells due to photoelectric effect. The XPS spectrometer measures the kinetic energy and the number of these ejected electrons. Now, as the energy of the x-ray beam is known, the binding energy of these electrons in their atoms and molecules can be determined. The binding energy is equals to the subtraction of the measured kinetic energy after adding an adjustable instrumental correction factor to it (this factor is corresponds to the work function of both the material and the spectrometer) from x-ray beam energy.

Chemical elements are identified using XPS spectroscopy because they possess unique XPS spectral signature (peaks) as a function of binding energy which correspond to the atomic orbitals of these elements. Moreover, the elemental composition the samples can be determined quantitatively through calculating the atomic ratio of elements in the sample [171]. In this Ph.D. project, XPS spectroscopy has been performed using a Thermo fisher scientific Thetaprobe system for samples in Chapter 5 and Chapter 6.

3.3 Semiconductor Device Applications

Although there are various applications where MS_2 can be exploited, the scope of this thesis is mainly focus on electronic and optoelectronic devices which are photodetectors (PD) and thin film transistor (TFT). The next two sections review briefly the principles of operation of these devices.

3.3.1 Photodetectors

Semiconductor photodetectors are sensing devices that normally convert electromagnetic radiation to an electrical signal. Semiconductor photodetectors and light emitting devices such as LEDs and laser diodes, represent the core of current semiconductor optoelectronics technology. Essentially, the current induced by light in photodetectors is generated by two main mechanisms. The first one is called photovoltaic mechanism (mode) while the latter one is the photoconductive mechanism (mode).

To generate photocurrent by photovoltaic mechanism, it is essential to have a built-in electric field (depletion region) without any external field applied (open circuit configuration). When the photons are absorbed near or in the depletion region, the electron-hole pairs are generated and then separated by the built-in electric field where the electrons are collected in the n-type side while the holes are collected in the p-type side. The photogenerated potential difference (the photovoltage) will create current that pass through the external load.

In photoconductive mechanism, the photocurrent is generated when external electric field is applied to the semiconductor while exposing the channel to the light that has energy slightly higher than bandgap energy of the semiconductor. The absorbed photons in channel supply the electrons in the covalent bonds by sufficient energy to be ejected from the valence band and jump to the conduction band leaving holes behind in the valence band. Increasing the intensity of the light means increasing the number of photons that can be absorbed which enhance electron-hole generation mechanism. This leads to increase in photocurrent magnitude. Moreover, increasing the potential barrier (by applying external voltage across the semiconductor channel) suppress the electron-hole recombination mechanism which improves the photocurrent generation, particularly, in p-n and single Schottky barrier photodiode due to broadening of the depletion region (built in electric field). However, this improvement by external electric field for photodiodes is unidirectional and it only works in reverse bias as the forward bias improves the electron-hole recombination. However, for unipolar photoconductor which is normally a single n or p type semiconductor channel with two ohmic metal contacts, the electron-hole separation enhancement due to external electric field is bidirectional. The photodetector device fabricated in this thesis (Chapter 4) is metal-semiconductor-metal Schottky photodiode which utilize photoconduction mechanism.

3.3.1.1 Photodetectors figure of merit:

3.3.1.1.1 Photocurrent:

It is the net current that generated due to the photoexcitation of carriers and it is mathematically represented by [172]–[177]:

$$I_{photo} = I_{illumination} - I_{dark} \qquad \text{Equation 3-2}$$

Where I_{photo} is the photocurrent, $I_{illumination}$ is the current pass through the photodetector when it is illuminated, and I_{dark} is the current pass through device without any exposure to light (dark conditions. Note that the unit is in Ampere (A).

3.3.1.1.2 Responsivity:

Responsivity is the ratio of the output photocurrent (photovoltage) to the effective input power of the incident light [172]–[174], [176]–[180]:

$$R = \frac{I_{photo}}{P_{in}} \qquad \text{Equation 3-3}$$

Where I photo is the photocurrent, P_{in} is the input light power which is the actual light power incident on the device active area, it can be calculated from the equation below [174], [177], [179], [181]:

$$P_{in} = Optical\ power\ denisty\ (Intensity) \times \text{ Effective area of the device} \qquad \text{Equation 3-4}$$

Generally, the responsivity is dependent not only on the input power but also on the incident photon energy (wavelength) as photocarriers need specific energy to overcome the bandgap [176]. Therefore, the responsivity is normally plotted as dependent variable for the wavelength (spectral response) i.e. responsivity vs wavelength [176]. The unit of responsivity is A/W.

3.3.1.1.3 Quantum Efficiency:

Quantum efficiency is the ratio between number of photogenerated carriers per second to the number (incident for external quantum efficiency) or (absorbed for internal quantum efficiency) of photons per second [180], [182]. It is unitless quantity (expressed in % [180]). External quantum efficiency can be expressed as [183], [184]:-

$$EQE = \frac{I_{photo}/q}{P_{in}/h\nu} = R\frac{h\nu}{q} = R\frac{hc}{q\lambda} \qquad \text{Equation 3-5}$$

However, to calculate the internal quantum efficiency IQE, optical losses like reflection and transmission should be taken in account. Therefore, the only the absorbed fraction of light is

considered which represent by Aα was added to the denominator of the above equation to be [185]:-

$$IQE = R\frac{h\nu}{A_\alpha q} \quad \text{Equation 3-6}$$

3.3.1.1.4 Photoconductive gain

It is the number of detected photocarriers by electrodes that is generated by single incident photon [173]. The gain is unitless quantity. The photoconductive gain can be expresses as:

$$G = \frac{\tau_{lifetime}}{\tau_{transit}} = \frac{\tau_{lifetime}\,\mu\,V_{ds}}{L^2} \quad \text{Equation 3-7}$$

Where the $\tau_{lifetime}$ is the lifetime of the photocarriers and $\tau_{transit}$ is the time required for the photocarriers to pass from one electrode to the second one, μ is the mobility of the photocarriers, L is the channel length of the photodetector and V_{ds} is the voltage applied across the channel. Apparently, the gain can be obtained when the photodetector (most likely photoconductors) is illuminated creating electron-hole pairs that have difference in their motilities. Generally, when one of the photocarriers (the minority carriers e.g. holes) are trapped in the channel which makes them have longer lifetime while the second type of the photocarriers (the majority ones e.g. electrons) are free to move (transit) across the channel. This means that single photon can excite multiple electron-hole pairs before they can recombine again due to trapping time of the minority carriers (holes) which make the gain occur. However, there are other processes could enhance the gain other than trapping like avalanche effect and multiple photocarriers generation by high energy photons.

Additionally, the responsivity is improved by improving photoconductive gain according to [184]:

$$R = EQE\frac{q}{h\nu}G \quad \text{Equation 3-8}$$

When the EQE is ignored (considered as 100%) then the gain has the same physical definition of quantum efficiency. However, sometimes the EQE can be defined as absorbance.

However, if trapping time (lifetime) of the minority carriers is longer that is mean the time response of the device will be longer (rise and fall time of the optical detected signal) i.e. the temporal response of the device will be slower. Therefore, there is "gain-bandwidth trade-off" as the bandwidth is strongly inverse proportionally related to the rise time of the detected signal. It is worth to mention that the photoconductor can have higher gain compared with photodiode

3.3.1.1.5 Response (rise/fall time), cut-off frequency and bandwidth:

Response time is the required time for the photodetector to response for the input optical signal, in other word, it measures how fast the device can be switched [186]. It is strongly affected by the traps state (trapping time) and the type of the contact (ohmic or Schottky) in the channel. The most common way to is estimate the response time (rise time) by measuring the time period that the photocurrent increased from 10% to 90% (rise time) and from 90% to 10% for the (fall time). Another approach to determine the response time is by fitting the signal to stretched exponential function.

The response time (rise time) determine the bandwidth of the detector which is the set of the frequencies that the detector operate within. The relation of the response time and the bandwidth can be expressed by [186]:

$$\tau_r = \frac{0.35}{f_{3dB}} \qquad \text{Equation 3-9}$$

Where the τ_r is the response time (rise time) and f_{3dB} is the cut-off frequency (it is so called 3dB bandwidth) which is the frequency that the responsivity of the photodetector falls down to 50% of all its magnitude (-3dB) [186]. As we mentioned that in the previous section that the gain is affected by the lifetime of the photocarriers which as a result affect the response time. Consequently, the responsivity is time dependent (frequency depended) quantity. As it can be seen below:-

$$R(f) = \frac{R_o}{\sqrt{1+(2\pi f\tau)^2}} \qquad \text{Equation 3-10}$$

Where Ro is the responsivity of the photodetector under continuous illumination (DC. COMPONENT). The total bandwidth of the photodetector can be calculated from cut-off frequency (-3 dB bandwidth) using the relationship [186]:-

$$f_{3\,dB} = 0.886\,\Delta f \qquad \text{Equation 3-11}$$

Where the Δf is the full bandwidth of the detector.

3.3.1.1.6 Signal to noise ratio (SNR) and noise equivalent power (NEP):

Signal to noise ratio (SNR) is the ratio of the input signal power to the noise power. It should be more than one in order to the signal be detectable. Moreover, the lower the noise the weaker the optical signal can be detected. Noise equivalent power (NEP) is the minimum optical signal power that make the signal distinguished from the noise (when SNR is equal to unity) in 1 Hz bandwidth. It can be expressed as below [186]:-

$$NEP = \frac{rms\,(i_n)}{R}$$ Equation 3-12

Where rms (i_n) is the mean square of noise current measured for 1 Hz bandwidth. The unit of the noise current is A $Hz^{-1/2}$ and W $Hz^{-1/2}$ for NEP.

3.3.1.1.7 Specific Detectivity

Detectivity is the parameter that quantify the performance of the detector to identify small optical signal, i.e. it is the reciprocal of NEP with W^{-1} as units. However, as the dark current considered as the dominant source of noise in photodetectors which is greatly affected by the area of the active channel, it is more suitable to include the area of the channel in the formula. Therefore, other parameter was wildly used which is specific detectivity and it can be represented by the following formula [186]:

$$D^* = \frac{\sqrt{A\,\Delta f}}{NEP}$$ Equation 3-13

Where A is the area of the channel, Δf is the bandwidth of the detector and NEP is the noise equivalent power. The units of the specific detectivity is cm $Hz^{1/2}$ W^{-1} (jones).

3.3.2 Field effect transistor

Field effect transistor is a three terminal electrical device where the electrical current passing through the semiconductor channel is modulated by applying external electric field. In another word, FET device is able to be totally conductor when it is on-state and be highly resistive to current when it is off-state. Changing between these two states is controlled by the electric field from the gate terminal. The main application of FET is a switch especially in digital electronics but also can be used as a signal amplifier for analogue electronic applications. Nowadays, it is the building block for vast majority of electronic technologies such as computers, mobile phones, screens etc.

There are different configurations of field effect transistors, however as the MS_2 are thin films, thin film transistor (TFT) structure is the most appropriate FET type to utilize these materials as a semiconductor channel. TFT device structure is simply a unipolar semiconductor channel (either n or p-type channel) connected directly to ohmic metal contacts which represent the source and drain while the gate contact is isolated electrically from them by dielectric material. There are four common configurations for TFTs which are: top-gate with bottom-contacts, top-gate with top contacts, bottom-gate with top-contacts and bottom-gate with bottom-contacts (see Figure 3-6). However, in this thesis, top-contacts configuration were used for our backgated devices in sections 5.6 and 6.12 and top-contact with ionic top gated devices in section 6.12.

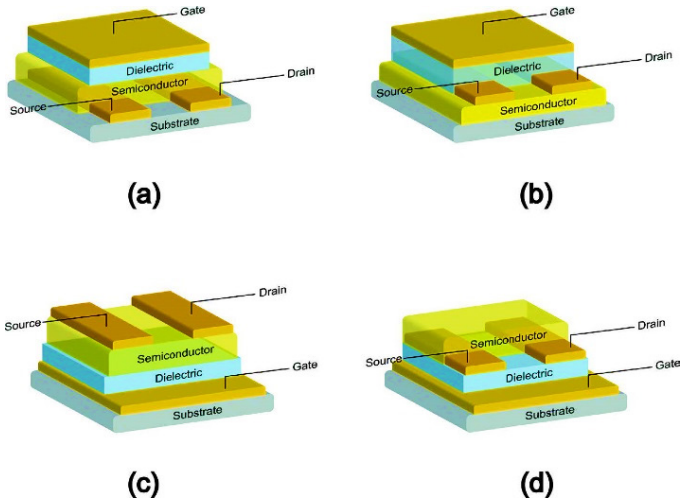

Figure 3-6: Different configurations of TFT devices. (a) top-gate with bottom-contact, (b) top-gate with top contact, (c) bottom-gate with top-contact and (d) bottom-gate with bottom-contact. This figure is reproduced from ref. [187].

3.3.2.1 Figure of merits for FETs:

The main figure of merits for FET devices which need to be characterised are threshold voltage, carrier mobility, on-off ratio, and subthreshold swing.

3.3.2.1.1 Threshold voltage:

V_T is the required gate voltage that turn the FET on, i.e. critical value of the gate voltage where the FET beyond it starts to switch on or off. The most common method to estimate the V_T is by linear extrapolation of the slope in the linear region of Ids-Vg curve for the triode region (linear region of the FET) or $Ids^{0.5}$-Vg for the saturation regime [188], [189].

3.3.2.1.2 On-off ratio:

It is the ratio of the current in on state to the current in the off state. It can be calculated by dividing the maximum current on the minimum current [190]. It is unitless quantity.

3.3.2.1.3 Mobility:

Mobility basically measures how fast the mobile charges can move. The field effect mobility can be extracted from the slope of the linear part of Ids-Vg curve in linear region (linear region of the FET) or Ids0.5-Vg for the saturation regime. Using the formula below [191]:-

$$\mu_{linear} = \frac{L}{w\, C_{ox} V_{ds}} \left(\frac{\partial I_{ds}}{\partial V_g}\right) \textbf{ or } \mu_{Saturation} = \frac{2L}{w\, C_{ox}} \left(\frac{\partial \sqrt{I_{ds}}}{\partial V_g}\right)^2 \quad \text{Equation 3-14}$$

Where L and W are the length and width of the channel, Cox is the capacitance per unit area of the gate dielectric, Vds is the source drain voltage. The unit is $cm^2/V.s$

Chapter 4
Facile Solution-Based Synthesis of MoS_2 Thin Films for Metal-Semiconductor-Metal Photodiode Applications

4.1 Chapter Summary

In early stages of this project, synthesis of MoS_2 thin films via thermolysis of spin coated, single source precursor ammonium tetrathiomolybdate has been demonstrated. The critical parameters to successfully grow uniform MoS_2 thin film has been investigated. Moreover, MSM photodiode has been fabricated via simple metallisation step which shows excellent rectifying and photosensitive behaviour for optoelectronic applications. Raman spectroscopy and spectral response of the device was used to estimate the film thickness and the band gap of the films. The findings stated in this chapter reveal the significance of single source precursor synthesis approach of 2D-molybdenum disulphides semiconductors for optoelectronics applications and open the opportunities to discover the same methodology to grow few-layer WS_2 films for electronic applications which will be discussed in the next chapter.

4.2 Introduction

Light generation and sensing are among most promising applications of 2D materials family [192]. In fact, the discovery of intense photoluminescence from MoS_2 monolayers was the spark for the accelerated pace towards realisation of 2D transition metal disulphides as future materials for electronics, optoelectronics and photonics markets. Although their bulk form were known as a semiconductors since the 1960s, it is the indirect to direct bandgap transition due to quantum confinement to single molecular layer which sheds light on prospective photons-manipulation mechanisms that MS_2 materials could exhibit and how it could be exploited for practical daily life devices.

Photodetectors are well known semiconductor optoelectronics devices which convert light energy to electrical current, and are ubiquitously integrated during the past decades as essential building blocks in imaging, sensing, optical communications and energy harvesting systems. Therefore, it is not surprising that transition metal disulphides have been investigated for this type of applications. Various types of MoS_2 based photodetectors have been fabricated via thermal decompositions of ammonium tetrathiomolybdate like metal-semiconductor-metal (MSM) photodiodes [151], [152], [155], [193], [194]; heterojunction photodiodes [195]–[199] and phototransistors [200]–[202].

Metal-semiconductor-metal (MSM) photodiodes have very fast switching time response comparing to other types of photodetectors making them an excellent option for optical communications [203]. Furthermore, their simple structure facilitate the fabrication process which is compatible with current technology of FET devices fabrications [203]. Metal-semiconductor-metal (MSM) photodiodes basically are two metal electrodes that connected directly on semiconductor slab forming Schottky junctions with end-to-end configuration and an opposite directions. They have rectifying behaviour for the electrical current like any other type of diodes where this behaviour originated from the Schottky barrier between the metal and the semiconductor material. When the active area (semiconductor) is illuminated by light, the carrier concentration is increased due to photoexcitation of the carriers (electrons or holes) and it can be collected by application of electrical field.

In this chapter, the optimum conditions of multi-layered MoS_2 growth via thermolysis approach has been studied and confirmed by Raman spectra. Moreover, MSM diode has been fabricated by very simple metallisation process. The main parameters of the diode such as dark current, ideality factor, rectification ratio and the practical Schottky barrier height has been extracted as well as photodetection parameters such as photocurrent, responsivity. The device shows a broad spectral response from near UV-VIS-near IR, this response has been used to estimate the band gap which is thickness dependent, therefore the ultra-thin nature of the film is confirmed as well.

4.3 Preparation of $(NH_4)_2MoS_4$ solutions and substrates for growth of MoS_2 films

In previous studies, dimethylformamide (DMF) has been used to dissolve $(NH_4)_2MoS_4$, then the solution was spin coated to form MoS_2 precursor layer [149], [204]. However, the solubility and wettability of $(NH_4)_2MoS_4$ solution with (DMF) is not adequate to form that MoS_2 precursor layer uniformly and continuously via spin coating technique over large area. This issue hinders the exploitation of this precursor for practical applications of semiconductors as Yang et el. have proved [150]. Figure 4-1 shows an image of spin-coated $(NH_4)_2MoS_4$ solution with (DMF) over pristine SiO_2/Si substrate, it is clear that clusters were formed rather than a film which severely affect the electrical and optical properties of MoS_2 for device fabrication. In order to tackle this issue, they suggested to add alcohol based-solvents to enhance the solubility of $(NH_4)_2MoS_4$ and oxygen plasma etching to promote the wettability with the substrate [150].

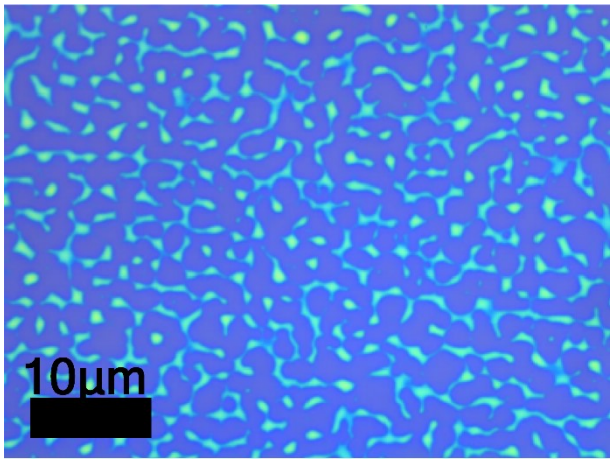

Figure 4-1: Optical microscope image of spin coated 24 mM $(NH_4)_2MoS_4$ solution dissolved in DMF over pristine SiO_2/Si substrate. Reproduced from [150].

The $(NH_4)_2MoS_4$ solution solvents recipe was reformulated to contain (4.5: DMF, 4.5: n-butylamine and 1:2-aminoethanol) in 10 mL volume. Additionally, the SiO_2/Si was etched using oxygen plasma for 10 s with 50 mW power to promote the adhesion of the film with the substrate. The resultant $(NH_4)_2MoS_4$ films were spin coated uniformly over wafer-scale substrates with 2-inches [150]. However, we tested this solvents recipe by dissolving 24 mM $(NH_4)_2MoS_4$ with the same solvents ratio but with lower volume 5 mL then spin coated on different types of substrates like silica, SiO_2/Si, lithium niobate that have been oxygen plasma treated. Unfortunately, the clusters formation issue is still persisted as depicted in Figure 4-2. One explanation for this, is the low viscosity of the whole solvents system, therefore, the solvents ratio has been optimised by increasing 2-aminoethanol ratio and compared to DMF and n-butylamine ratio. The final solvents recipe that has been used to dissolve $(NH_4)_2MoS_4$ is (2: DMF, 2: n-butylamine and 1:2-aminoethanol) in 5 mL total volume. Figure 4-3 shows the excellent uniformity that has been achieved when this solvents recipe was applied.

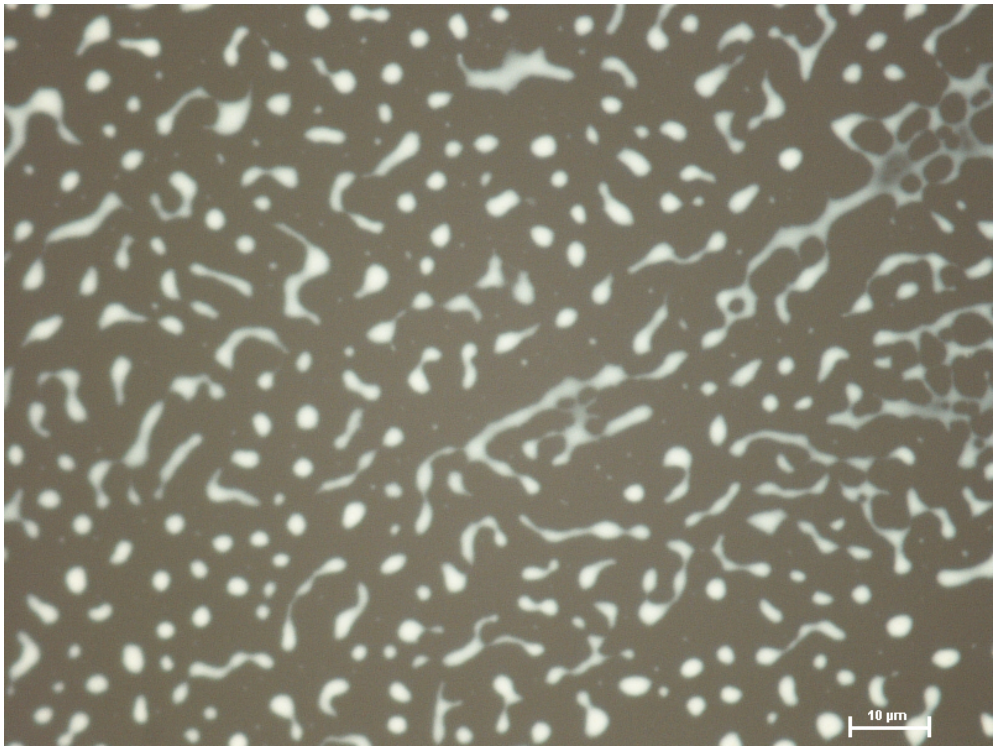

Figure 4-2: Optical microscope image of spin coated (31 mg) 24 mM $(NH_4)_2MoS_4$ solution dissolved in 5 mL solvent mixture with ratio (4.5: DMF, 4.5: n-butylamine and 1:2-aminoethanol) over oxygen plasma treated silica substrate. The substrate was preannealed at 90°C for 5 min to evaporate the solvents.

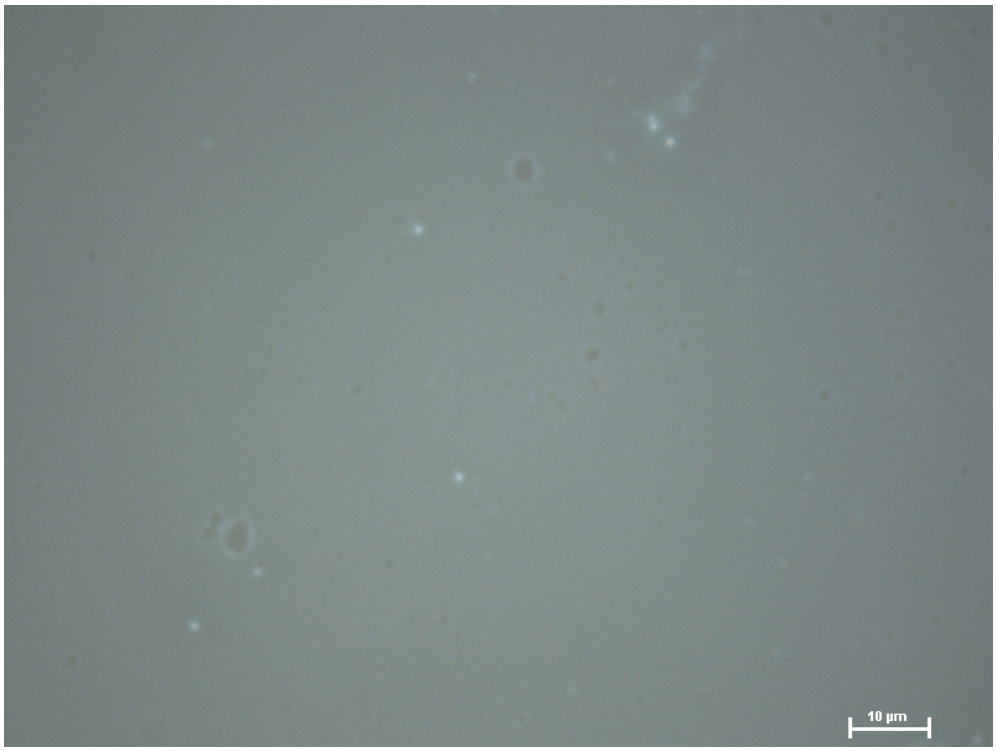

Figure 4-3: Optical microscope image of spin coated (31 mg) 24 mM $(NH_4)_2MoS_4$ solution dissolved in 5 mL solvent mixture with ratio (2: DMF, 2: n-butylamine and 1:2-aminoethanol) over oxygen plasma treated silica substrate. The substrate was pre-annealed at 90°C for 5 min to evaporate the solvents.

Moreover, in order to obtain high wettability of the film with the substrates, several approaches have been applied. Firstly, a standard cleaning process with acetone, isopropanol, ethanol and di-ionized water have been applied but no clear improvement was observed. Similarly, standard substrate cleaning process followed by additional cleaning step using piranha solution did not show any clear changes in wettability although piranha solution is known an agent that improve the hydrophilicity of the substrates. Finally, oxygen plasma etching were used with similar conditions that stated in ref. [150], trivial improvement was noticed. Therefore, we finally increased the power and exposure time to be 1000W for 10 min to improve the wetting of the substrates while the oxygen flow and pressure were remained without any changes (1000 mL/min and 0.1 mbar). The solution after modified recipe for oxygen plasma was adhered on the substrates perfectly as shown in Figure 4-3. However, we anticipate that relatively long time exposure could increase the surface roughness of the substrates.

4.4 Thermal decomposition

As it was mentioned earlier in section 2.4.2.2.4, thermal decomposition of $(NH_4)_2MoS_4$ to synthesize MoS_2 in reducing atmosphere (hydrogen) could be implemented at relatively low temperature and pressure (normally $\leq 500^oC$ and 1 mbar) [148], [150]. Hydrogen plays an important role not only by reducing the required thermal decomposition temperature to deposit MoS_2 but also it helps to eliminate the formation of associated molybdenum oxide that might occur during the annealing process as it was proved earlier [205]. However, the crystallinity is very low at this temperature and it needs to be improved by further annealing at higher temperature (up to 1000^oC) while the pressure could be varied from low (1 mbar) in some reports [150] to medium pressure (666 mbar) in others [148] with or without presence of sulphur. Consequently, many reports designed their annealing process to be in two steps according to these conditions [148]–[151], [153], [155].

In the early stages of this work, several trials have been implemented to obtain MoS_2 films using this two-step annealing approach that was proposed in the literature. Therefore, our thermal annealing conditions for $(NH_4)_2MoS_4$ films were similar to the previous studies. Firstly, $(NH_4)_2MoS_4$ films on SiO_2/Si were placed inside the furnace to be annealed in 100 sccm flow (6% H_2/Ar) at 500^oC (the furnace was pulled towards the samples area when the temperature stabilize at 500^oC) and 1 mbar pressure for 30 min followed by a second annealing step in 100 sccm flow of pure argon at 1000 ^oC for 30 min at low, medium and atmospheric pressure (1500 and 1013 mbar) without sulphurisation.

Although, the amorphous MoS_2 films could be easily obtained after the first annealing step in all the trials, forming high crystalline MoS_2 films after the second annealing step was the main challenge. The high temperature leads to total sublimation of the MoS_2 films while long annealing time (30 min) and low and medium pressure accelerate the sublimation process whilst there was no sulphur source to maintained the stoichiometry of the MoS_2 films.

Thermal decomposition

The evaporation of the MoS_2 films due to high temperature is an issue that has been pointed out earlier by Yang et al. where they suggested that the second annealing step to be at 700°C which is a low temperature enough to eliminate the evaporation of the sulphur in absence of an extra sulphur source [152].

Alternatively, we optimized our second annealing step to preserve the stoichiometry of the MoS_2 films while keeping the temperature at 1000°C to ensure that our films are highly crystalline. SiO_2/Si with 300 nm oxide thickness were cleaved in square shapes with 1.5 cm^2 size and used as substrates then spin coated with $(NH_4)_2MoS_4$ films with two concentrations (24 and 48 mM). The samples were sandwiched to each other in facing-pairs configuration which helps to slow down the evaporation rate of MoS_2 films massively and allows to form the MoS_2 films at 1000°C without any need to external sulphur source. Moreover, the second annealing step has been conducted at atmospheric pressure in order to decelerate the evaporation. Meanwhile, the annealing time was minimized to 15 min then the furnace was pulled away to let the samples cool down rapidly. As the films are thin in nature, there is no need for long annealing time to be highly crystalline. It is also worth to mention that during the ramping of temperature from 500°C to 1000°C, the furnace was pulled away from the samples area until the furnace totally stabilize at 1000 °C. Finally, we succeeded to grow the MoS_2 films at two different precursor concentrations mentioned above at 1000°C without additional sulphurisation. The figure below is a schematic diagram for MoS_2 synthesis via thermolysis of $(NH_4)_2MoS_4$ using two-annealing steps approach.

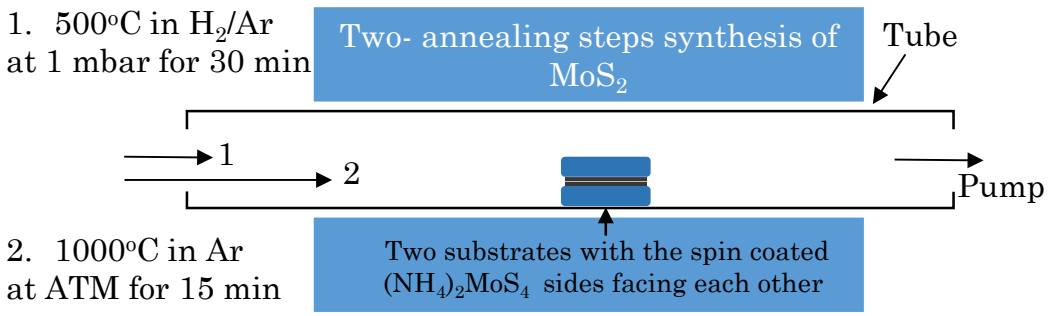

Figure 4-4: Schematic diagram for the CVD furnace system that used to synthesis of MoS_2 via two-step annealing for thermal decomposition of $(NH_4)_2MoS_4$.

4.5 Raman Spectroscopy of MoS_2

In order to confirm the growth of semiconductor MoS_2 films, Raman spectroscopy has been conducted with excitation wavelength 633 nm and 20 mW power using 50X objective. Figure 4-5 illustrates the Raman spectra for MoS_2 films with 24 and 12 mM concentrations respectively. Obviously, the spectra for both concentrations consisted of additional peaks through the whole scanning rage of energies compared to other excitation wavelengths like 325,488 and 532 nm Raman lasers [24]. These peaks becomes prominent because of the resonance of this wavelength (633 nm) with the direct band gap of MoS_2 which enhance the intensity of the second order peaks as mentioned earlier in section 2.2. All peaks were labelled in Figure 4-5 according the literature, reference [24]. Similar to other Raman excitation wavelengths, 633 nm laser use E_2g and A_1g peaks separation technique to identify the number of MoS_2 layers, however, this method can predict up to 4 layers in addition to the bulk form of MoS_2 [24]. Additionally, peaks intensity reduction due to weak coupling and splitting of the convoluted peaks to individual ones could give details about layer number reduction of the films as depicted in Figure 4-5 where the difference in intensity between both concentrations can be realised by silicon peak intensity.

For 12 mM concentration MoS_2 films, the MoS_2 Raman spectra exhibit $E^1{}_2g$ and A_1g peaks at 383.3 and 405.6 cm^{-1} respectively with frequency separation 22.3 cm^{-1}. According the literature this peak positions and the separation are for MoS_2 with 3-4 molecular layers thickness [24]. For the 24 mM concentration MoS_2 films, the E_2g and A_1g peaks are centred at 379.4 and 405.3 cm^{-1} respectively while the frequency difference between the peaks is 25.9 cm^{-1}. This peak difference is similar to what was observed with MoS_2 bulk crystal spectra although a slight red shift is occurred for both peaks positions compared to earlier reported observations possibly due to the strain that grown MoS_2 films suffer compared to the natural flakes [24]. However, for bulk MoS_2, the A_1g intensity dominates the $E^1{}_2g$ peak distinctly as well as the B_1u peak is merged with A_1g to form a shoulder for A_1g peak due to small peaks separation and lower intensity of B_1u [24]. In contrast, in few layer MoS_2 regime (≤4 layers), the $E^1{}_2g$ has similar or slightly overwhelmed A_1g peak intensity and the B_1u peak is split to an individual peak [24]. Although, our MoS_2 with 24 mM concentration shared the same peak difference with bulk MoS_2 natural crystal; the deconvolution using Lorentzian curve fitting for A_1g,B_1u,2LA(M) and A_2u peaks reveals that A_1g peak has lower intensity with respect to $E^1{}_2g$ and B_1u peaks; which is the same trend of few layer MoS_2 regime (≤4 layers).

To sum up, Raman spectroscopy confirms that our 12 mM MoS_2 films are 3-4 layers thickness. Unfortunately, the peak position diagnostic technique to identify the MoS_2 thickness is limited by 4 layers, as a result 24 mM MoS_2 films show bulk form frequency deference between A_1g and $E^1{}_2g$ peaks. However, an estimation based on the analysis of $E^1{}_2g$, A_1g and B_1u peaks intensity and the correlation between them predicts that 24 mM MoS_2 films have multilayer nature rather than bulk. To further support Raman results, photocurrent spectroscopy has been conducted with 24 mM MoS_2 films to estimate the thickness which is discussed in section 4.8.

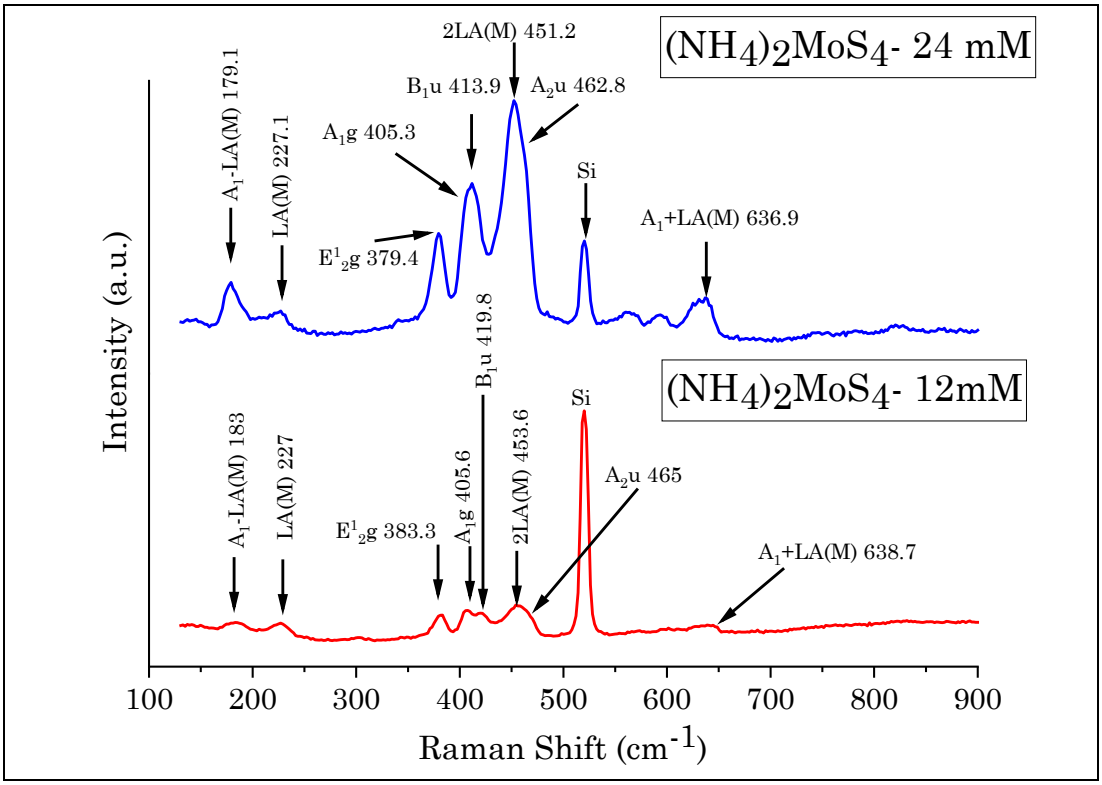

Figure 4-5: Raman spectra of MoS_2 films grown by thermolysis of spin-coated ammonium tetrathiomolybdate with 24 and 12 mM concentrations respectively. The Raman measurement has been performed by Adam H. Lewis.

4.6 Extraction of Dark and photocurrent Parameters of Multi-layered MoS_2 MSM Photodiode

In order to investigate the rectifying and photodetection properties of the solution based synthesized film, a MoS_2 film on SiO_2/Si substrate made by thermal decomposition of spin coated ammonium tetrathiomolybdate with 24 mM concentration has been chosen to be as the semiconductor channel for metal-semiconductor-metal photodiode. The metallisation process was very simple where two Indium metal pieces were cut with approximately 9 mm^2 size and pressed directly on the film which they adhered perfectly as indium is a soft metal, the spacing between the two contacts about 3 mm length and the width of the channel is about 3 mm. The two Indium contacts with the MoS_2 films represent a two terminal photodetector device with metal-semiconductor-metal configuration. Prior the metallisation step, the indium contacts has been etched with 10% hydrochloric acids diluted in di-ionized water to remove the native oxide from the surfaces which might degrade the performance of the contacts.

Indium has a low work function (4.12 eV) [206]–[209] while the electron affinity of multi-layered MoS_2 is about 4 eV [158], [210]–[212]. This means Indium can form a good contacts for MoS_2 with very small Schottky barrier 0.12 eV as the equation below suggests [213]:-

$$\Phi_{SB} = \Phi_{metal} - \chi \qquad \text{Equation 4-1}$$

Where Φ_{SB} is the Schottky barrier and Φ_{metal} is the work function of the metal and χ represents the electron affinity of the semiconductor. However, this Schottky barrier is theoretical one and it could be altered significantly when a real device is fabricated. Figure 4-6 depicts the I-V curve of the photodiode under dark conditions (black line). Clearly the device shows a rectifying diode behaviour when the voltage is swept forwardly from -40V to 40 V (the graph is limited to 30V). This indicates the MoS_2 film synthesized by our method is semiconducting film whereas the Schottky barrier is higher than what was predicted in the equation above as the rectifying behaviour is unidirectional. Moreover, the relatively high working voltages without any breakdown on both directions occurs means that the device could be useful for high power electronics and (optoelectronics). One of the main diode parameters is the rectifying ratio, it could be defined as the ratio of the forward current to the reverse saturation current with the same voltage magnitude in both directions (reverse and forward bias) in dark [214]. The rectifying ratio has been calculated to be 4.09x 10^2 at -40 and 40V for the MoS_2 photodiode. Moreover, the turn on voltage for the diode has been extrapolated from the tangent of the exponential part for the dark current (black line in Figure 4-6) when intersects the x-axis and it is found to be 24V which is quite high turn on voltage due to large active area of the device and relatively small size of contacts.

Generally, the current pass through the Schottky diode (for bulk semiconductors like silicon or gallium arsenide) in both forward and reverse bias can be expressed by thermionic emission mechanism where the carriers (electrons or holes) could overcome the Schottky barrier when they have sufficient thermal energy. This mechanism could be expressed as the model below [215] :-

$$I = I_o[exp\ (eV/KT) - 1] \qquad \text{Equation 4-2}$$

Where I is the current flow through the diode, e is the electron charge 1.6×10^{-19} coulombs, K is Boltzmann constant 1.38×10^{-23} m^2 kg s^{-2} K^{-1}, T is the temperature in Kelvin (298 K for room temperature) and Io is the reverse saturation current which can be expressed as below [215]:-

$$I_o = A\,A^*\,T^2\,exp\ (-e\Phi_{SB}/KT) \qquad \text{Equation 4-3}$$

Where A is the area of the diode in cm^2, A* is Richardson constant for the semiconductor material, T is the temperature in Kelvin, e is the electron charge, K is Boltzmann constant and Φ_{SB} is the Schottky barrier in eV. However, the thermionic emission model is only valid when the reverse saturation current is totally level off in reverse bias (independent of the reverse voltage bias) and the ideality factor (which is a number measures how close the actual device behaves like an ideal diode) is equal to 1 [215], [216].

Extraction of Dark and photocurrent Parameters of Multi-layered MoS2 MSM Photodiode

As shown in Figure 4-7, the reverse saturation current of our device is increased as the reverse bias voltage increased which means that thermionic emission mechanism is not the main mechanism that attributed to the rectifying behaviour of our device. Tunnelling, diffusion or both of these mechanisms were dominating carriers transport in the metal-semiconductor interface [216], [217]. In this case, thermionic-field emission model could be more appropriate to analyse the rectifying behaviour of our device. The equation below describe the thermionic-field emission model [215]:-

$$I = I_o \left\{ exp\,(eV/nKT) - exp\,\left[\left(\frac{1}{n} - 1\right) eV/KT\right]\right\} \quad \text{Equation 4-4}$$

Where all the parameters are mentioned previously while n is the ideality factor. When n is equal to 1, Equation 4-4 is simplified to be Equation 4-2 again. Now, in order to extract the parameters such as the reverse saturation current and the ideality factor, Equation 4-4 could be rearranged to be [218]:-

$$\frac{I\,exp\,(eV/KT)}{exp(eV/KT)-1} = I_o exp(eV/nKT) \quad \text{Equation 4-5}$$

If the natural logarithm is taken for the both sides, Equation 4-5 will be:-

$$\ln\left(\frac{I\,exp\,(eV/KT)}{exp(eV/KT)-1}\right) = \ln I_o + \frac{eV}{nKT} \quad \text{Equation 4-6}$$

Where the left hand side of Equation 4-6 can be plotted as a function of the forward voltage (see Figure 4-8) which I, V, e, K and T are known. To find reverse saturation current Io, the linear extrapolation has been implemented for the actual data from 0 to 1 volt in forward bias which the y-intersect represents ln Io. The reason behind taking small voltage is to avoid the series resistance effect of the diode. The reverse saturation current is 2.363×10^{-10}A.

Moreover, to extract the ideality factor as function of the forward voltage. Equation 4-6 should be derived and rearranged to be [218]:-

$$n(V) = \frac{e}{KT} \frac{dV}{d\ln\left[\frac{I\,exp\,(eV/KT)}{exp\,(eV/KT)-1}\right]} \quad \text{Equation 4-7}$$

The ideality factor as a function of the voltage has been plotted as depicts in Figure 4-9. The ideality factor at 0.25V is 2 which is close to organic and GaAs devices [216]. However, the ideality factor is increased rapidly as the voltage increased due to the effect of the series resistance of the device, large active area as well as the double Schottky contacts configuration [219].

Another important parameter for the diode is the Schottky barrier where it can be calculated from equation 4-3 as the saturation current has been obtained previously. Knowing that the Richardson constant for MoS_2 is 0.70×10^{-6} A cm^{-2} K^{-2} [220], the Schottky barrier for

Indium-MoS_2 interface is 0.38 eV. This value is almost identical with recent value of Indium-MoS_2 Schottky barrier of an FET device at zero gate voltage [221].

To probe the photoresponse of our MSM photodiode, the device has been illuminated by white light source with intensity 1 mW/cm^2 while the source drain voltage has been swept from -40V to 30V. As shown in Figure 4-6, the reverse saturation current under illumination (red line) has been improved dramatically compared to the dark current one which indicates a photocurrent was generated due to the photoconductive nature of the MoS_2 film (blue line). The photocurrent has been calculated and plotted by subtraction of the dark current from the current under illumination ($I_{photocurrent} = I_{under\ illumination} - I_{dark}$) [179], [222]. The contrast ratio is the ratio of the photocurrent to the dark current ($I_{photocurrent} / I_{dark}$) [223], [224] has been calculated to be 96.1 at -40V.

Another important optoelectronic figure of merit is the responsivity which is the ratio of the total photocurrent generated by light to the optical power of this incident light as shown in the equation below [173], [184], [185], [225]:-

$$R = \frac{Photocurrent\ (I_{ph})}{Input\ optical\ Power\ (P_{in})} \qquad \text{Equation 4-8}$$

Where its units in AW^{-1}. The responsivity of our device has been calculated to be 0.022 AW^{-1} at -40V.

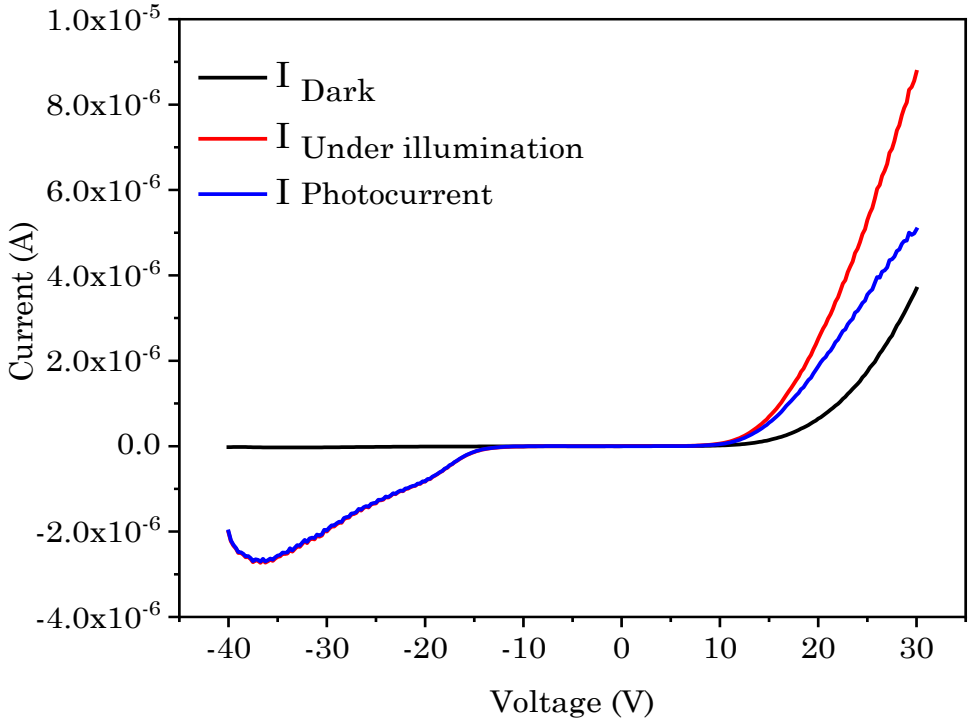

Figure 4-6: Linear graph of I-V characteristics of MoS_2 MSM photodiode where the black line represents the dark current (without illumination), the red line represents the current under white light illumination and the blue line is the photocurrent induced by light.

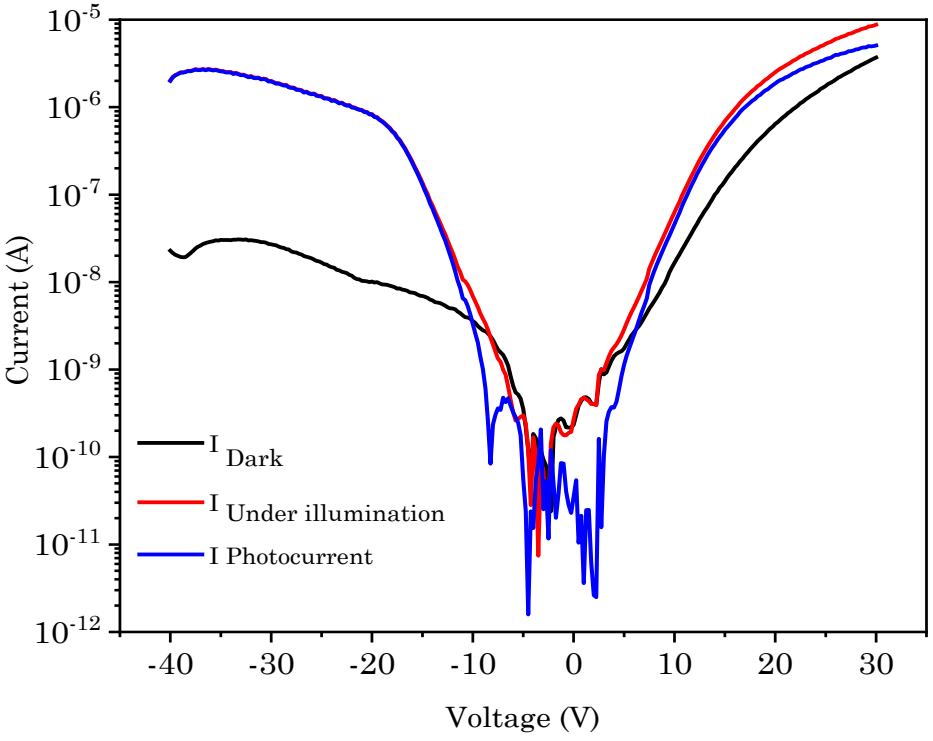

Figure 4-7: Semi-log graph of I-V characteristics of MoS2 MSM photodiode where the black line represents the dark current (without illumination), the red line represents the current under white light illumination and the blue line is the photocurrent induced by light.

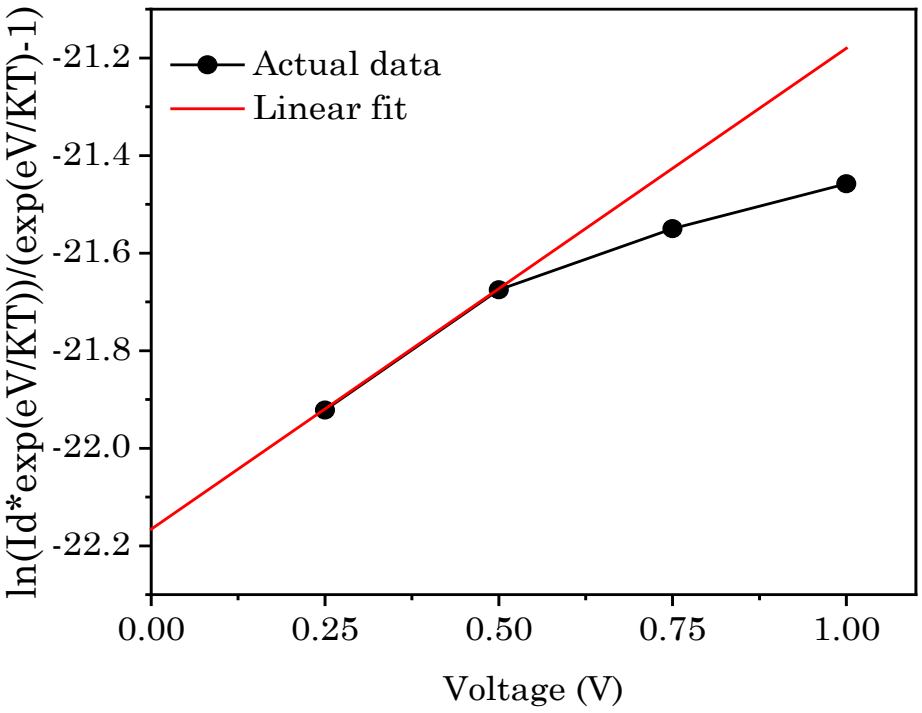

Figure 4-8: ln ((I exp (eV/KT)) / (exp (eV/KT)-1)) as a function of forward voltage. The black dotted line represents the actual data while the red line is the linear fit which its intersection with y-axis represents ln I_o.

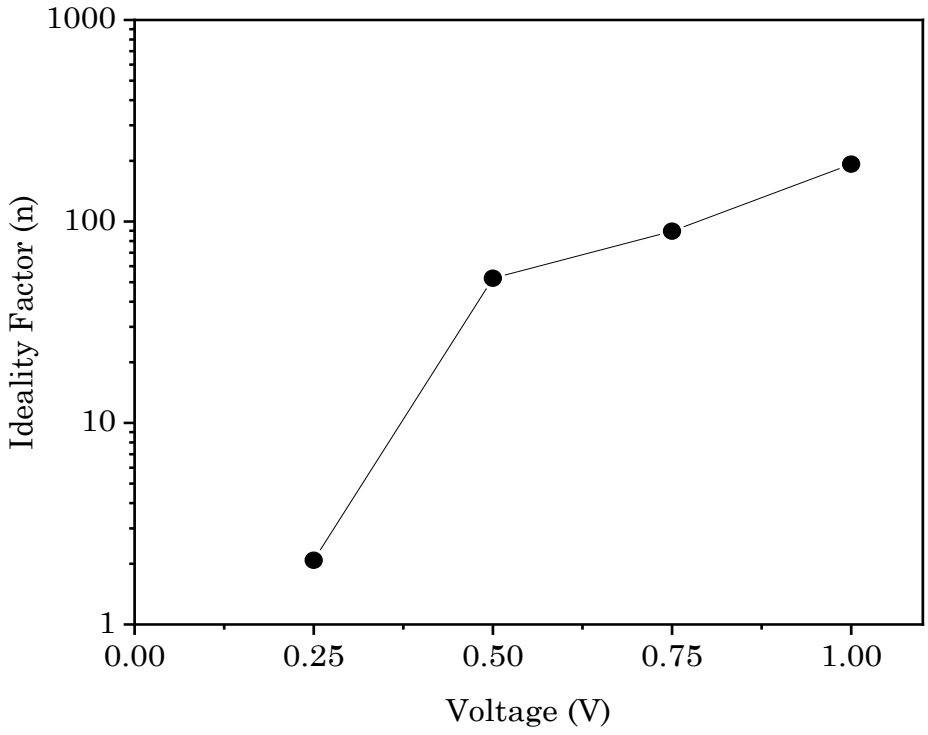

Figure 4-9: semi-log plot of ideality factor as function of the forward voltage. As it is clear the ideality factor was close to 2 only at very small voltage and increased significantly as the voltage increased due to the series resistance of the device.

4.7 Dark and Photocurrent generation mechanism in MSM MoS_2 photodiode.

In previous section, the main rectifying and photodetection parameters were extracted which helps to understand the rise of the dark current and photocurrent in our MSM multi-layered MoS_2 device. However, in order to have clear idea about the mechanism of current generation in dark and under illumination, the energy band diagrams were used to visualize the whole process as shown in Figure 4-10. According to this model, the current generation process is divided to three parts based on biasing regimes: 0 voltage, low voltage and high voltage.

In principle, metal-semiconductor-metal photodiode is two Schottky diodes which are connected back to back via semiconductor channel [203]. When there is no external voltage applied at dark conditions, no current will pass or generated by MoS_2-MSM device in both directions as the net built-it electric field for both Schottky junctions is equal to zero [226]. Under illumination, the light excited (generated) more electrons-hole pairs while the Schottky barriers are still high and there is no biasing voltage to overcome the barrier potentials. Consequently, the majority carriers (electrons) in the conduction band trapped between the two Schottky barriers as they tend to repel from the metal-semiconductor potential barriers due to the built-in electric field [226]–[228]. On contrary, the minority carriers (holes) are attracted to the metal-semiconductor interfaces driven by the same built-in electric fields [226]–[228]. Although, carrier concentration is increased dramatically due to photoexcitation, the net photocurrent at zero voltage is also zero as the carriers are totally trapped between the two electrodes and there is no path to extract them [228]. It is worth to mention photocurrent can be generated when the contacts of photodiode are asymmetrical for example when one contact is Schottky and the second one is ohmic [229] or even the area of the two Schottky contacts are not identical [228]. Under these conditions, The Schottky photodetector could work in photovoltaic regime and photocurrent can flow without the need for external force.

The second state is at low biasing voltage, the Schottky barriers will be modified and there will be some lowering due to external voltage. However, at these voltages the current flow through the two junctions is mainly attributed to the thermionic emission model in both dark and under illumination conditions. Therefore, the electron injection from one Schottky junction can pass smoothly through one junction but it will be repressed by the second junction due to reverse bias condition in the second Schottky junction which increased the height of the barrier. As a result, the output current for both contacts will be limited by the saturation current of this back to back diodes connections which is a voltage and light power independent in this case [230]. In our device the low voltage regime start from -8V to 4V as shown previously in Figure 4-7 where there is no significant difference between the current in dark and under illumination values as well as very low conductivity for both conditions as the main conduction mechanism is attributed to reverse thermionic current.

At high voltages, the tunnelling mechanism start to dominate the current flow rather than the thermionic one and the high external applied voltage remarkably lower the Schottky barriers for both junctions. However, the minority carriers (holes) in the valence band that are trapped in the interface of the metal-semiconductor start to accumulate and crowding in the negative potential junction rather (reverse bias) than positive one (forward bias) which minimize the barrier to be more ohmic-like contact leading to semi linear behaviour in the negative side. At this point, the dark current becomes voltage semi-linear dependent which increase by increasing the reverse bias (see Figure 4-7). When the device becomes under illumination, the majority carriers density increased significantly due to photoexcitation mechanism while the minority carriers (holes) tends to modify the potential barrier to be more ohmic. By the end, the photocurrent will increased more as the device behaves like a photoconductor. However, at high forward bias, the potential lowering is only due to the external voltage while there is no contribution from the minority carriers (holes or traps) to modify the barrier which leads to small Schottky barrier formation in the high forward bias. The current pass through the Schottky junction in high forward bias is exponentially voltage dependent as we can see in Figure 4-6. When the device is illuminated, the electrons injection is improved leads to reducing the turn on voltage and the dynamic resistance of the device as shown in Figure 4-6.

Finally, the three voltage regimes are combined together at dark current, the device shows a behaviour of single Schottky diode with voltage dependent saturation current. Thus, we analyse it as a single device with thermionic-field emission model (see equation 4-4). Under illumination, asymmetrical I-V characteristics is more obvious (see Figure 4-6 and Figure 4-7).

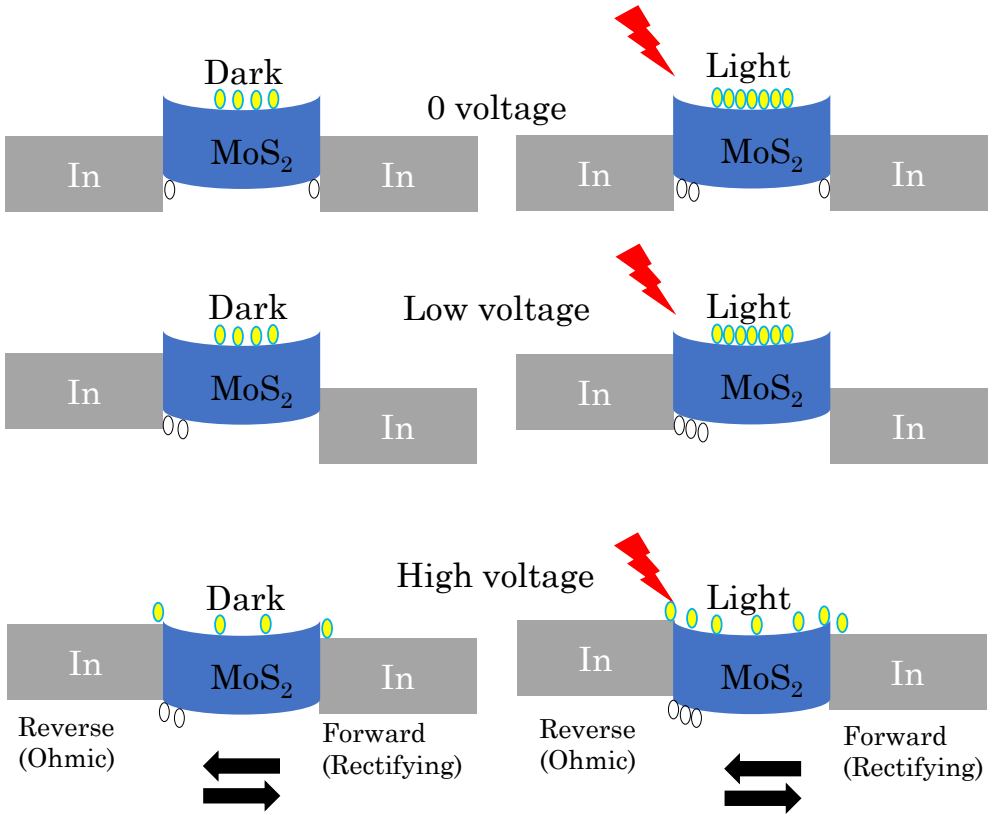

Figure 4-10: Conduction mechanism of MoS_2 MSM photodiode.

4.8 Spectral response of MoS_2 MSM device

Spectral response measurement (photocurrent or responsivity as a function of the wavelength) is a technique used to study the sensitivity of the detector for each specific photon energy (wavelength) to estimate the operational bandwidth of the device. Another advantage of this measurement is the electronic band gap of transition metal dichalcogenides could be estimated using spectral response of the photocurrent [4], [231]. Assuming the optical and electronic band gaps are almost identical in inorganic TMD materials means that the photocurrent is proportional to the absorption coefficient near the absorption edge of the bandgap [4], [231].

Figure 4-11 shows the diagram for the experimental set up of spectral response measurement (photocurrent spectroscopy). Tungsten filament lamp was used as a white light source where the light pass through the collimating lenses to monochromator which manually filtered the required light wavelength. Next, the chopper with audio frequency formed discrete optical signals that were collected and focused on the MSM detector by convex lens. An Operation amplifier circuit (transimpedance amplifier) was connected to amplify the optical signals that detected by the MSM photodetector. The signals from the Op.Amp circuit were measured by Lock-in amplifier and compared to the reference signals from the chopper controller which are both in the same frequency and phase while the oscilloscope is used to monitor the both signals.

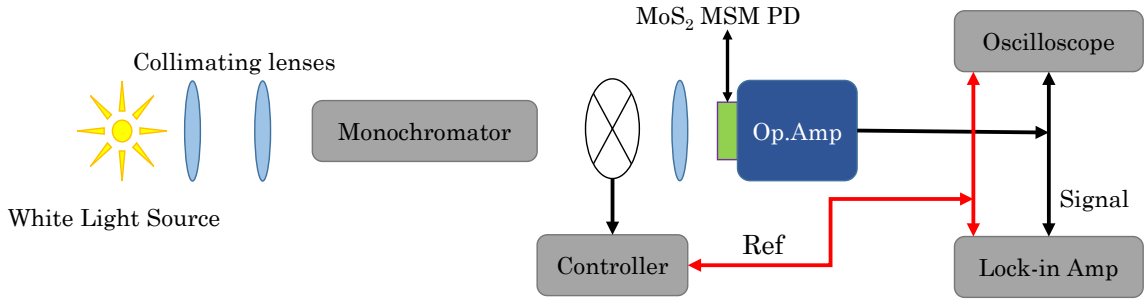

Figure 4-11: Schematic diagram of spectral response measurement experimental set up used for MoS_2 MSM device.

The spectral response was measured from 300 nm to 1200 nm (1 to 4.1 eV) as depicts in Figure 4-12. Generally, the device shows higher responsivity in visible and near infrared region compared to near UV one. There are two noticeable peaks in the spectrum where the current induced by photons is increased rapidly which are at 1.77 eV and 1.98 eV. Although 1.98 eV is unambiguously corresponds to B exciton peak as it was reported earlier, 1.77 eV peak is tends to be red shifted to what was observed with A exciton peak of MoS_2 monolayer indicating that the MoS_2 film is multi-layered [9], [10].

To further confirm the band structure of MoS_2 film, Tauc curve has been plot between the photons energy and $(I_{ph}h\upsilon)^2$ based on the relationship below [231]:-

$$\left(I_{ph}h\upsilon\right)^2 \propto \left(h\upsilon - E_g^{Opt}\right) \qquad \text{Equation 4-9}$$

Where the absorption coefficient is substituted by the photocurrent as they are both have proportional relation [4], [231]. Figure 4-13 represents the relation above, the linear extrapolation of this curve with photon energy axis give the estimated band gap of 1.382 eV. As was mentioned earlier the band gap is thickness dependent in MoS_2. This value of the bandgap is with good agreement for few-layer MoS_2 (between 4-6 layers) [9].

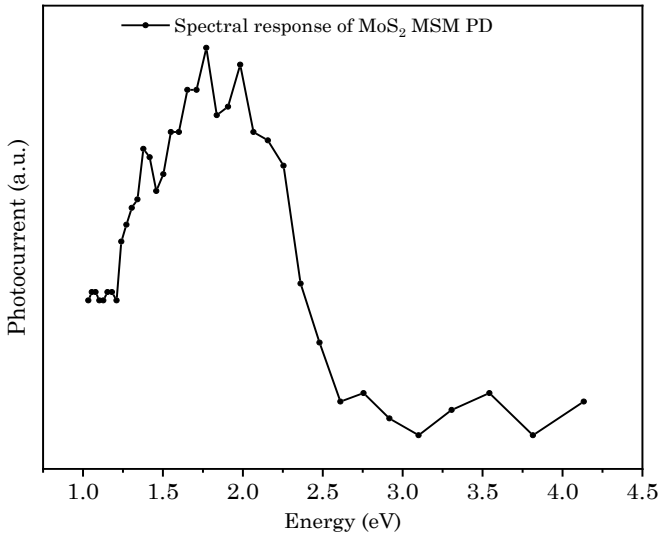

Figure 4-12: Spectral response of MoS_2 MSM photodiode from near IR to near UV spectrum. The spectral response measurement was performed in collaboration with Pier Sazio.

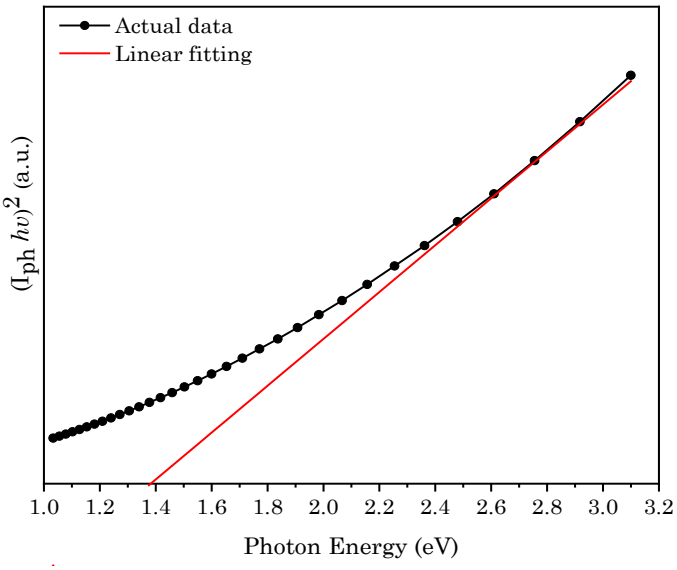

Figure 4-13: Plot of $(Iph h\upsilon)^2$ vs photon energy (eV), the dotted black line represents the actual data while the solid red line is the tangent of the curve where its intersection with photon energy axis is the bandgap of the MoS_2 device.

4.9 Conclusions

To sum up, a facile method to grow few-layer MoS_2 film based on solution-based single source precursor is proposed. Photoelectrical properties of these films are studied by fabrication of metal-semiconductor-metal device using indium metals. These finding indicate that indium can form a metal-semiconductor junction with few-layer MoS_2 that possess relatively low Schottky barrier which enhance optoelectronic performance of the photodiode.

Chapter 5
Solution-Based Synthesis of Few-Layer WS_2 Large Area Continuous Films for Electronic Applications

5.1 Chapter Summary

Unlike MoS_2 ultra-thin films, where solution-based single source precursor synthesis for electronic applications has been widely studied, growing uniform and large area few-layer WS_2 films using this approach has been more challenging. Here, we report a method for growth of few-layer WS_2 that results in continuous and uniform films over centimetre scale. The method is based on the thermolysis of spin coated ammonium tetrathiotungstate ($(NH_4)_2WS_4$) films by two-step high temperature annealing without additional sulphurization. This facile and scalable growth method solves previously encountered film uniformity issues. Atomic force microscopy (AFM) and transmission electron microscopy (TEM) were used to confirm the few-layer nature of WS_2 films. Raman and X-Ray photoelectron spectroscopy (XPS) revealed that the synthesized few-layer WS_2 films are high crystalline and stoichiometric. Finally, WS_2 films as-deposited on SiO_2/Si substrate were used to fabricate a backgated Field Effect Transistor (FET) device for the first time using this precursor to demonstrate the electronic functionality of the material and further validate the method.

5.2 Introduction

2D transition metal dichalcogenides (TMD) have emerged as promising low dimensional semiconductor materials [232] due to their exceptional electrical, optical and mechanical properties [12]. Among the TMD family, MoS_2 has been the first and most investigated member because of its excellent properties such as thickness dependent indirect to direct bandgap transition [9], [10], valley Hall effect [233], high carrier mobility and on-off ratio [8] that makes it suitable for a wide range of electronic applications. A significant number of scientific reports have addressed the synthesis routes of MoS_2. The growth methods reported in the literature include mechanical [8] or liquid exfoliation [38] as well as conventional atomic layer deposition (ALD) [234] and chemical vapour deposition (CVD) [235]. These growth approaches however are still far from being commercially viable due to low yield and/or high costs.

Two significant factors that identify a successful route to commercialization of a material are its compatibility with existing fabrication methods and cost effectiveness. Solution-based synthesis is compatible with existing nanofabrication processes, is scalable at low cost and has already been shown to produce high quality MoS_2 films using a single source precursor such as ammonium tetrathiomolybdate $(NH_4)_2MoS_4$ through thermal decomposition for electronic devices applications [6]. Therefore, several groups have developed approaches for large area solution-based MoS_2 synthesis via two-step thermolysis of $(NH_4)_2MoS_4$ films coated in different ways such as dip, roll to roll and spin coating [148]–[155]. Spin coating of $(NH_4)_2MoS_4$ solution in particular is highly preferable among other coating techniques due to its integration with current semiconductor technology and its ability to control the initial precursor film thickness through spinning speed as well as precursor solution concentration [150], [152]. The main obstacle hindering this coating technique is the low wettability of precursor solutions that utilize common solvents such as dimethylformamide (DMF) and n-methylpyrrolidone (NMP), with commonly used substrates like SiO_2/Si or sapphire. This leads to nonuniform precursor film formation associated with a high density of defects and de-wetted areas after spin coating. To overcome this issue, researchers developed different organic-precursor solution systems for spin coating to enhance the uniformity and controllability of the initial precursor film over large area and eliminate surface defects. These organic-precursor solutions systems are: DMF, n-butylamine and 2-aminoethanol [150]; ethylenediaminetetraacetic acid (EDTA) and dimethylsulfoxide (DMSO) [153]; and linear poly (ethylenimine), DMF and 2-aminoethanol [152].

Similarly, WS_2 is an important TMD material which shows comparable characteristics to MoS_2 but can also offers higher photoluminescence (PL) efficiency, better electrical performance and ambipolar field effect behaviour [33], [35], [236]. Although WS_2 has growth methods similar to MoS_2 such as sulphurization of tungsten metal [86] or tungsten oxides [99], growth of large area and uniform WS_2 ultra-thin films for electronic applications via thermal decomposition of ammonium tetrathiotungstate $(NH_4)_2WS_4$ salt has not been demonstrated successfully. This is

due to the difficulty that is associated with the formation of a thin uniform $(NH_4)_2WS_4$ precursor layer as this salt has poor solubility in most of the common solvents as compared with $(NH_4)_2MoS_4$ [237]. Usage of these solvents in solution-based single source precursor deposition of WS_2 has however been demonstrated for applications that do not require highly continuous WS_2 films, such as surface enhancement Raman scattering (SERS) and creating a carrier injector layer for optoelectronic devices [238], [239]. Another issue in solution-based single source precursor synthesis by thermal decomposition occurs when the second annealing step is relatively high ($\leq 800^{o}C$). In this case, sulphur from $(NH_4)_2MoS_4$ and $(NH_4)_2WS_4$ films evaporates readily and needs to be substituted by adding sulphur in the inert gas flow to preserve the stoichiometry and the quality of the MoS_2 and WS_2 films [148], [150], [238], [239].

Generally, there are three factors that need to be optimized to create a defect-free film from a liquid precursor by spin coating; the wettability of the precursor solution with the substrate, the solubility of precursor in the solvent system and the viscosity of the solution. Wettability can be significantly improved by oxygen plasma treatment of the substrate which promotes the hydrophilicity of the surface [150]. Choosing a solvent capable of achieving high solubility of the precursor helps to eliminate clusters and striation formation due to surface tension. Viscosity can be controlled by the choice of the solvents system and the concentration of the precursor, which affects the coverage of the film over the substrate and the final precursor film thickness [150], [152].

This chapter provide an approach to optimise all three parameters to create uniform large area ultra-thin WS_2 layers via a two-step thermal decomposition of $(NH_4)_2WS_4$ spun-coated precursor solutions. A refined solvent recipe was formulated to improve the wettability and uniformity of the precursor film on the substrate. Additionally, by processing our samples in a "facing pair" manner during the high temperature second annealing step, the composition/stoichiometry of the films was preserved, thus eliminating the need for additional sulphurization. Optical microscopy was used to assess the uniformity and continuity of the precursor films while AFM and TEM evaluated the resulting WS_2 film thickness and morphology. Raman spectroscopy supported the AFM and TEM results to identify the few-layer nature of the films and showed the effect of temperature on the crystallinity of the film. XPS spectroscopy revealed the stoichiometry of WS_2 films when grown on different substrates. Finally, an FET device was fabricated using as-deposited WS_2 film to further elucidate the potential electronic applications of these films.

5.3 Preparation of $(NH_4)_2WS_4$ solutions and the substrates for growth of WS_2 films

Electronic devices such as FETs require continuous and uniform films for the device layer to guarantee high electrical performance. In solution-based synthesis of semiconducting WS_2 films, the main defects are pinholes and de-wetted areas over the substrate that occur in the precursor deposition step. In this work we have tackled these issues by refining the solvents system for the $(NH_4)_2WS_4$.

There are simple solutions for wettability but because $(NH_4)_2WS_4$ is weakly coordinated with most of the solvents [237], the key challenge in making a solution-based uniform ultra-thin WS_2 film is formulating a solution recipe that results in a high solubility of the precursor with the optimum viscosity. Based on this, we chose the most promising solvents reported previously for spin coating, namely (DMF) [204], ethylene glycol [239], (NMP) [149] to investigate which one has the maximum solvation and coverage over the substrate. Preparation of the substrates and precursor solutions for spin coating is described as below :

1.5 x 1.5 cm^2 SiO_2/Si (300 nm SiO_2) and sapphire substrates to assess the optimum spin coating conditions for different solvent solutions. Prior to spin coating, the surface of the substrates was cleaned using acetone, isopropanol and de-ionized water followed by conditioning using oxygen plasma at 0.1 mb pressure (oxygen flow 1000 mL/min) and 1000 W power for 15 min to enhance the wettability. To prepare the solutions, we dissolved 174 mg of $(NH_4)_2WS_4$ in 5 mL of each solvent (DMF, ethylene glycol, NMP) to form 100 mM of precursor solution. After one hour of sonication (at 70^{o}C) the three solutions were spin coated on the substrates at three different speeds (3000, 6000 and 9000 rpm) for 1 min (step 1: ramp 5 sec, dwell time 5 sec, rpm 500; step 2: ramp 5 sec, dwell time 45 sec, rpm 3000, 6000 and 9000). After spinning, the substrates were prebaked at 140oC for 1 min using a hot-plate where the solvents evaporated.

Figure 5-1 (A-C) shows the spin-coated precursor films where $(NH_4)_2WS_4$ is dissolved in DMF, ethylene glycol and NMP solvents respectively (100 mM solution concentration), at 6000 rpm spinning speed. Unfortunately, none of the solvents successfully formed continuous and uniform $(NH_4)_2WS_4$ films. The high concentration and therefore viscosity of the solutions should have facilitated the continuous film formation, opposite to what we observed here. Moreover, the de-wetted regions were significantly enlarged at 9000 rpm which was the peak of the spin coating speed (see Figure 5-2). DMF was promising in terms of forming continuous precursor films with excellent surface coverage at 3000 and 6000 rpm speeds. Unfortunately, we identified high density of clusters that probably consist of insoluble WS_4^{-2} anions. Ethylene glycol based film exhibited lower density of clusters as compared to DMF at 3000 rpm (see Figure 5-2) but had more de-wetted regions, with the wettability deteriorating at moderate and high spin coating speeds, thus preventing the formation of a thin uniform layer. Unlike the previous solvents, NMP showed some more solvation without forming clusters at all spin coating speeds,

indicating a better solvation of $(NH_4)_2WS_4$ by NMP compared to DMF and ethylene glycol solvents. However, the high density of random pinholes assigned to insufficient wetting of the solution with the substrate.

However, it has been reported before that amine-based solvents could be linked with WS_4^{-2} anions via hydrogen bonds leading to form a stable solution [240], [241]. Additionally, it has been shown that n-butylamine and 2-aminoethanol solvents can stabilize the $(NH_4)_2MoS_4$ and bind the solution to create uniform MoS_2 precursor films by spin coating [150]. However, this $(NH_4)_2MoS_4$ solvents recipe contains DMF rather than NMP which leads to non-uniform WS_2 precursor layer formation when it was used for $(NH_4)_2WS_4$ (see Figure 5-3). Based on these facts, we reformulated the recipe of NMP by adding the solvents butylamine and 2-aminoethanol prior to thermal decomposition. The refined recipe for the new solvents system proposed (6 mL total volume) is 3/6 NMP, 2/6 butylamine and 1/6 2-aminoethanol. These solvents were mixed together and dissolved (208, 73, 42 and 21) mg of $(NH_4)_2WS_4$ to create solutions of (100, 35, 20, 10) mM. The solutions were then sonicated for 1 hour at 70°C before being spin coated at 6000 rpm (the same spin-coating recipe was used as before) on the cleaned and oxygen plasma treated substrates (the same oxygen plasma recipe was used as before). Finally, the samples were baked on a hot-plate at 140°C for 1 minute.

Moreover, to ensure good coverage and uniformity of the spin-coated precursor layer, we started with high concentration solution (100 mM), as is evident from Figure 5-1(D) there was a significant improvement of the uniformity without any obvious de-wetted regions over a large area. The few apparent micron-sized defects originated from particles on the substrate. However, further reduction in precursor solution concentration was needed in order to achieve WS_2 films with minimum thickness. Therefore, we used the same solvents recipe with the threshold concentration (35 mM) of $(NH_4)_2WS_4$ that can produce large area and uniform precursor films as shown in Figure 5-1(E-F) respectively. At lower concentrations than this (e.g. 10 or 20 mM), the density of WS_4 anions in the solution were very low leading to formation of isolated micron-sized islands rather than a continuous film (see Figure 5-4).

Preparation of (NH4)2WS4 solutions and the substrates for growth of WS2 films

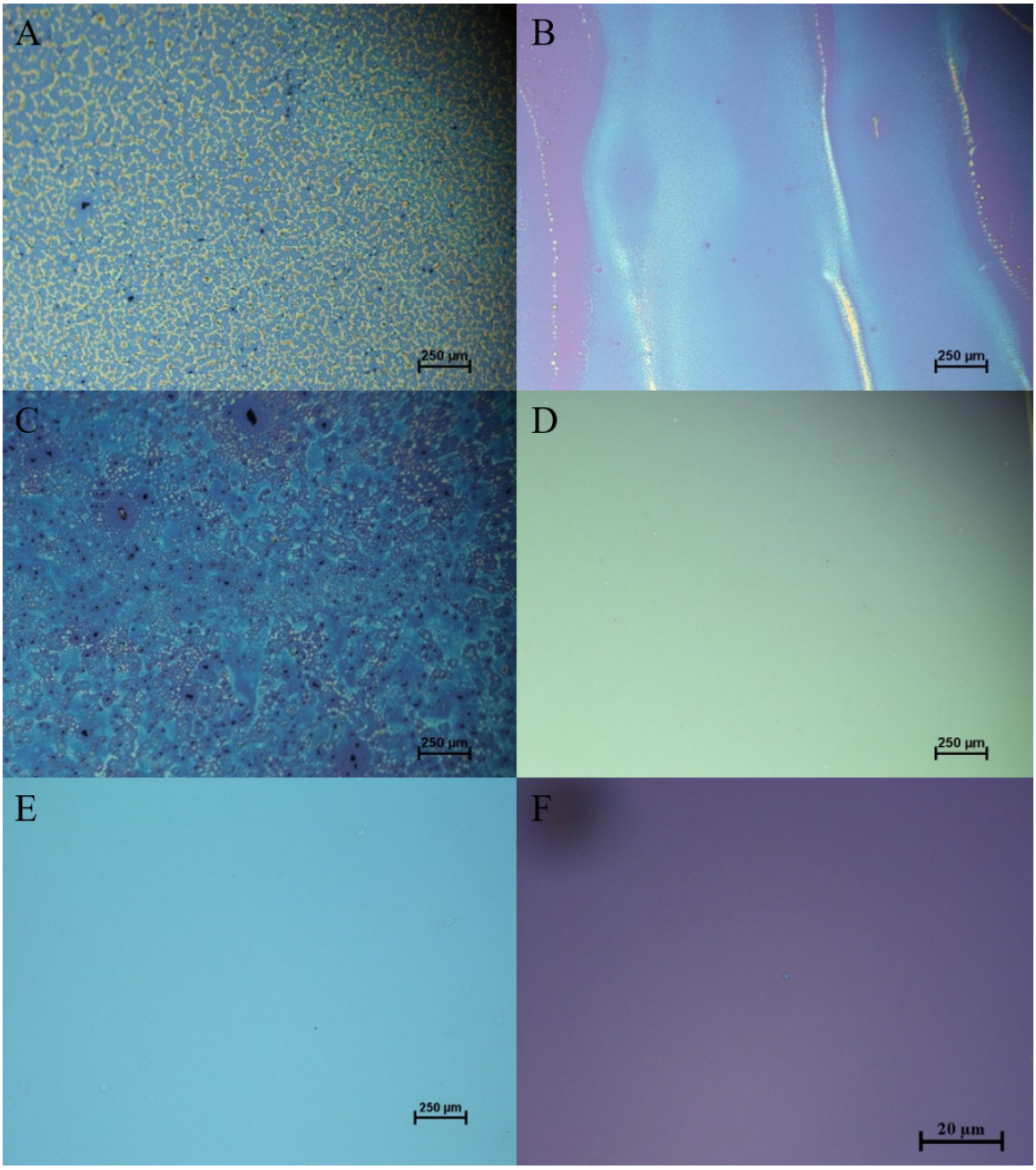

Figure 5-1: Optical microscope images of spin-coated precursor films prepared by dissolving 100 mM of $(NH_4)_2WS_4$ in: (A) dimethylformamide (DMF), (B) ethylene glycol, (C) n-methylpyrrolidone (NMP) and (D) solvent system contains (3 mL NMP/2 mL n-butylamine/1 mL 2-aminoethanol in 6 mL total volume). (E), (F) are optical microscope images of spin-coated precursor films prepared by dissolving 35 mM of $(NH_4)_2WS_4$ in (3 mL NMP/2mL n-butylamine/1mL 2-aminoethanol in 6 mL total volume). All the solutions are spin coated at 6000 rpm for 1 min and prebaked at 140^{o}C for 1 min. Note that (A-E) images were taken using 5X objective while (F) image was taken using 100X objective.

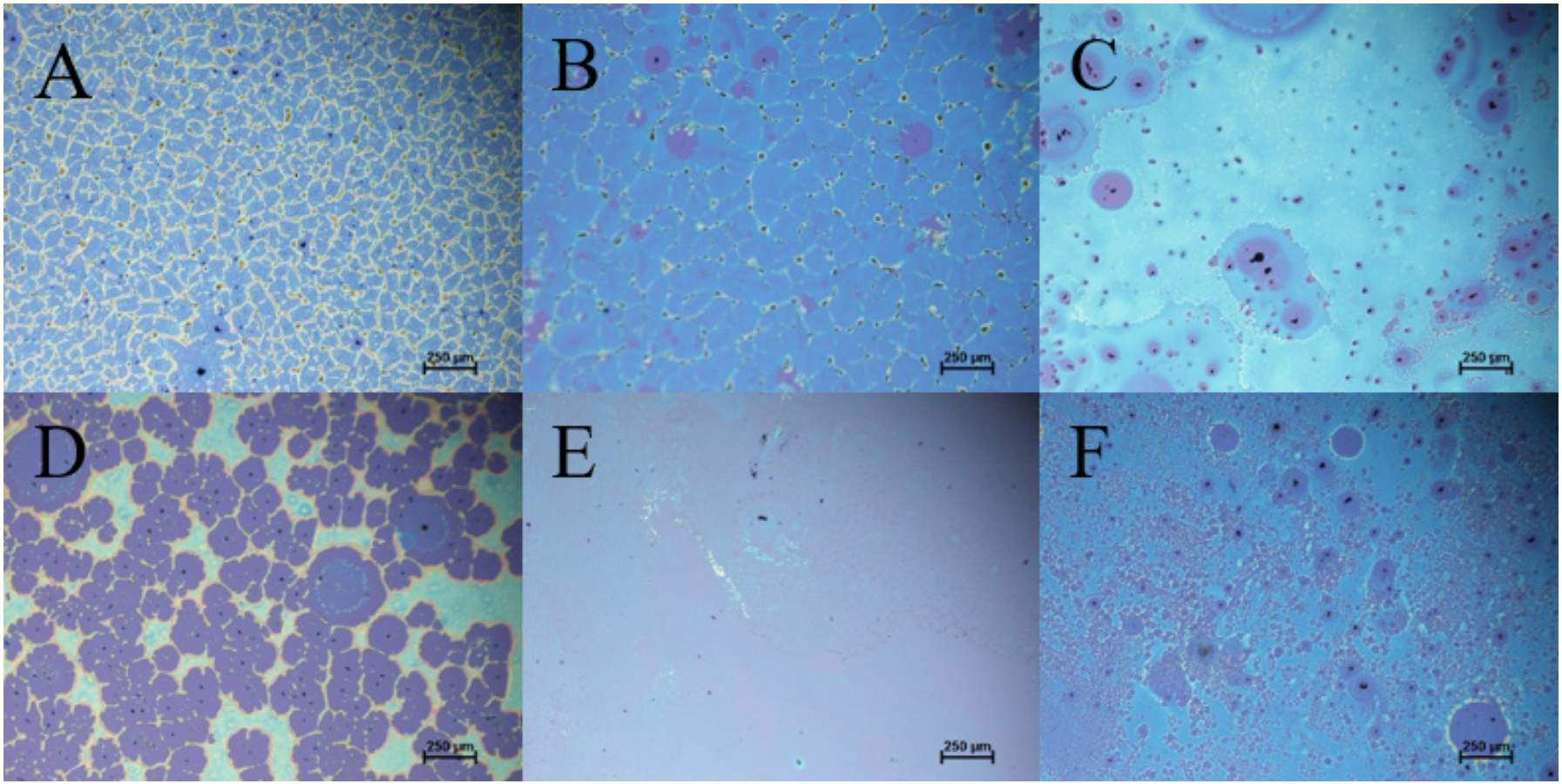

Figure 5-2: Optical microscope images of precursor films prepared by dissolving 100 mM of $(NH_4)_2WS_4$ in: dimethylformamide (DMF) solvent then spun coated at (A) 3000 and (D) 9000 rpm spinning speed respectively; ethylene glycol solvent then spun coated at (B) 3000 and (E) 9000 rpm respectively; n-methylpyrrolidone (NMP) solvent then spun coated at (C) 3000 and (F) 9000 rpm respectively.

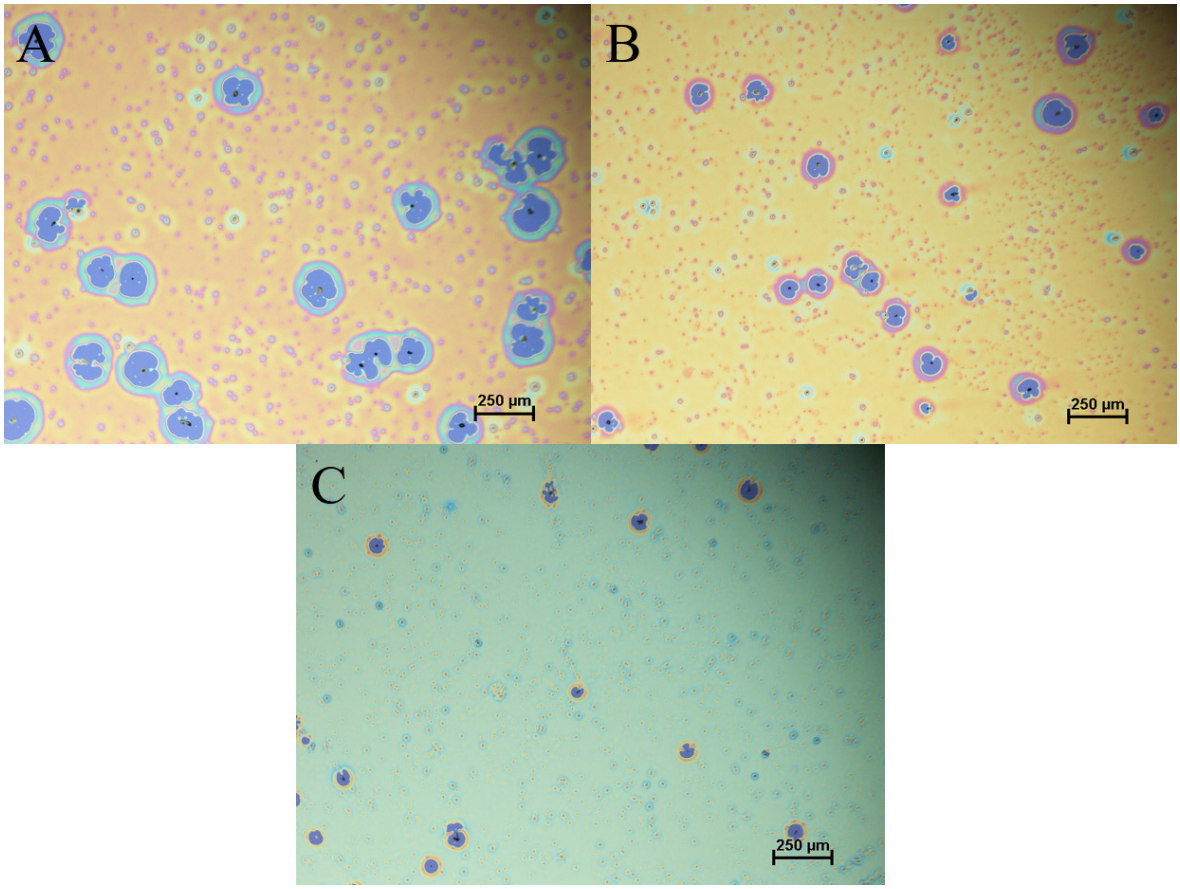

Figure 5-3: Optical microscope images of precursor films prepared by dissolving 100 mM of $(NH_4)_2WS_4$ in 5 mL of (2/5 dimethylformamide (DMF), 2/5 n-butylamine 1/5 2-aminoethanol) then spun coated at: (A) 3000, (B) 6000 and (C) 9000 rpm. This solvent recipe is a modified recipe from ref (150) which can create highly uniform $(NH_4)_2MoS_4$ films by spin-coating that can thermally decompose to produce MoS_2 films. However, when this recipe was applied to create $(NH_4)_2WS_4$ films, large size pinholes (≥50µm) exist in addition to undissolved $(NH_4)_2WS_4$ particles.

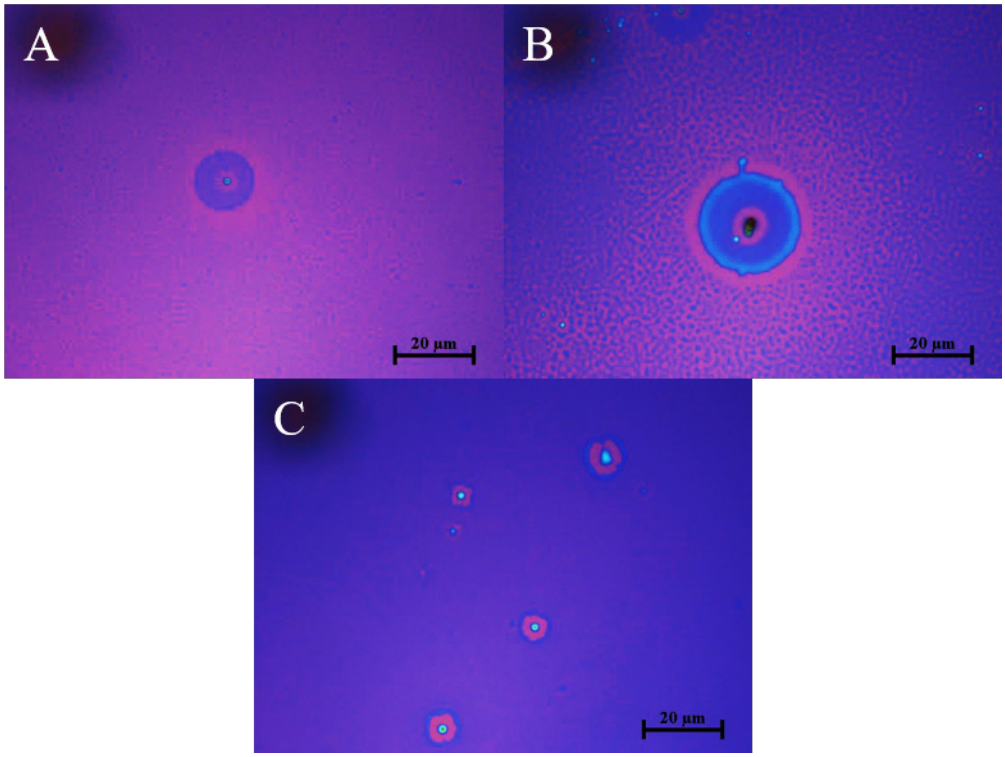

Figure 5-4: Optical microscope images of spin-coated precursor films prepared by dissolving $(NH_4)_2WS_4$ in our solvent recipe which is 6 mL of (3 mL NMP, 2 mL butylamine and 1 mL 2-aminoethanol) using different concentrations (spin coating at 6000 rpm for 1 min). (A) 10 mM concentration: the film is not continuous and contains low density of precursor islands. (B) 20 mM concentration: the film has higher density of precursor islands but still not continuous. (C) 35 mM film is the minimum concentration to create uniform and continuous $(NH_4)_2WS_4$ films. However, few micron-size defects (≤10µm) occurred in this primary sample due to debris or insoluble particles of the precursor which adhered on the surface of the substrates. Almost defect-free precursor films have been obtained (see Figure 5-1(F)) after further optimisation in the sonication process of precursor solution and cleaning procedure of the substrates.

5.4 Thermal decomposition

The final recipe of the proposed precursor solution with 35 mM concentration was used to deposit $(NH_4)_2WS_4$ films on both SiO_2/Si and sapphire substrates with similar results in terms of uniformity. Although $(NH_4)_2WS_4$ thermally decomposes to WS_2 leaving $2NH_3$ and $2H_2S$ as by-products in a reducing atmosphere (with Hydrogen) at 500°C, the crystallinity of the produced film is poor [238]. To improve the crystallinity of the film it is necessary to thermally anneal the samples to high temperature (1000°C). Thus, we designed our growth process with two annealing steps, the first one in reducing atmosphere at 500°C and the second one in inert gas at 1000°C as described in the next page.

The 35 mM concentration samples were used for the thermal decomposition. They were placed in a tube furnace and purged with a 6% H_2 in Ar gas at 8 mb pressure for 5 minutes. The samples were kept in the cold zone and the furnace was programmed to reach 500°C. After 20 minutes of temperature stabilization, the samples were moved in the hot zone of the furnace. After 30 min of annealing at 500°C, the samples were removed from the furnace and were left to cool down naturally while maintaining the flow of gas. To improve the crystallinity of our films we performed a second annealing step at 1000°C. The samples with identical substrates were arranged in film-facing pairs to prevent the reduction of the films (see Figure 4-4). Firstly, the furnace tube was purged with Argon at a pressure of 1 mb for 5 minutes to remove oxygen from the system. The system was then allowed to reach atmospheric pressure under the same 100 sccm Ar flow. After a 40 min temperature ramp, the furnace reached 1000°C to anneal the samples for 15 minutes before removal from the hot zone to let the samples cool down to room temperature under the same gas and pressure conditions. The microscope image below has been taken for the WS2 films after the second annealing step where the optical contrast between the WS2 film and the substrate (SiO_2/Si) is very low due to the few-layer nature of the film.

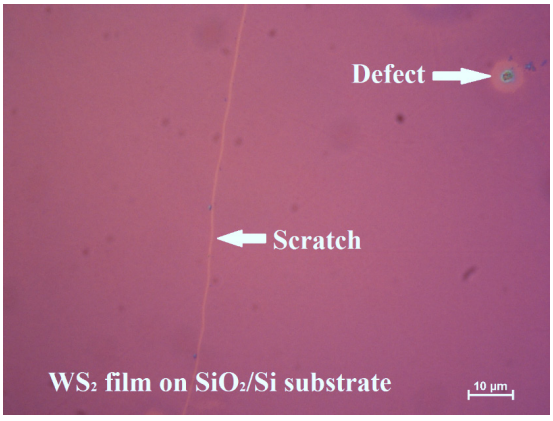

Figure 5-5: Optical microscope image of few-layer WS_2 film grown on SiO_2/Si substrate by two-step thermal decomposition using precursor concentration 35 mM dissolved in our solvent recipe.

5.5 Characterisation

The resultant WS_2 films for both substrates (SiO_2/Si and sapphire) has been assessed using different characterisation tools to evaluate thickness, crystallinity and chemical composition. AFM images were produced using an Agilent 5500 scanning probe microscope. Raman and PL spectroscopy were conducted using Invia Raman Microscope (Renishaw) system with a 532 nm excitation wavelength at 20 mW power and 50X objective. XPS has been performed using a Thermo fisher scientific Thetaprobe system. SEM was performed using a Joel JSM-7500F FEG-SEM. The preparation of TEM lamella was performed by a Zeiss NVision 40 CrossBeam FIB system. TEM was performed in the Loughborough Materials Characterisation Centre using an FEI Tecnai F20. Electrical measurements were performed in air using an Agilent 4155C semiconductor parameter analyser connected to a cascade micropositioning stage.

5.5.1 Atomic Force Microscopy (AFM)

After the second annealing step of WS_2 films grown on SiO_2/Si and sapphire substrates (with 35 mM precursor concentration), the topography and thickness of these samples were assessed by atomic force microscopy (AFM). The average thickness of the films for an area of edges was 6.5 ± 0.68 nm (0.68 nm is the root mean square roughness R_q of the film) for the SiO_2/Si substrate and 6 ± 0.1 nm (0.1 nm is the root mean square roughness R_q of the film) for the sapphire as shown in Figure 5-6. The higher roughness of the film grown on the SiO_2/Si substrate is attributed to the amorphous nature of the substrate and to the increased surface roughness caused by the relatively long time exposed to oxygen plasma. As AFM measurements were taken at the edge of WS_2 films where they are prone to edge effects from the spinning process, therefore, these AFM results represent the maximum thickness of WS_2 films. Additionally, the AFM images confirm the continuity of the WS_2 films with small grains that appear due to the nano-size crystals formed at the WS_2 uniform film.

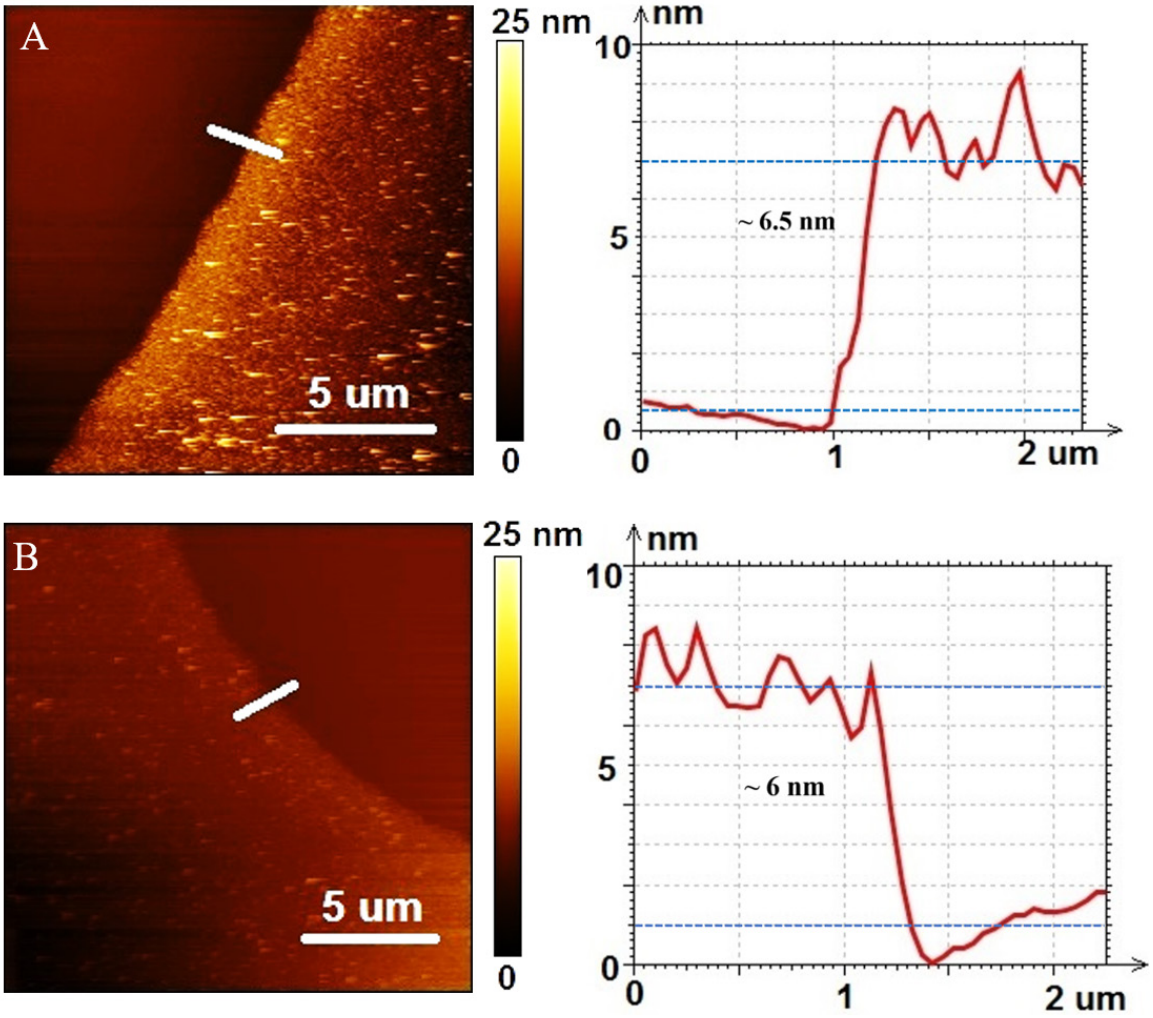

Figure 5-6: Atomic force microscopy (AFM) images of WS_2 films grown on (A) SiO_2/Si (B) sapphire. The AFM measurement has been performed by He Wang.

5.5.2 Transmission Electron Microscopy (TEM)

To evaluate the structure of the WS_2 films at the central area of the samples, TEM was conducted for the film grown on a sapphire substrate. Figure 5-7 shows a TEM image of the WS_2 film demonstrating a highly ordered layered structure. It is apparent from Figure 5-7, the film is uniform and constituted by areas of 2 and 3 layers. The TEM image indicates that the single layer thickness of the WS_2 film is 0.65 nm, in agreement with previously reported WS_2 monolayer thickness [99]. At the bottom right of Figure 5-7 and also in Figure 5-8 arranged columns of atoms are clearly visible.

The TEM lamella was prepared using a Zeiss FIB by Martin Ebert. The thinning process was performed using a gallium ion beam and introduced some damage in some areas. The result of this damage is that the atoms in certain areas were not resolved by the TEM. However, there are a few undamaged areas where the atom columns are clearly discernible (see Figure 5-8).

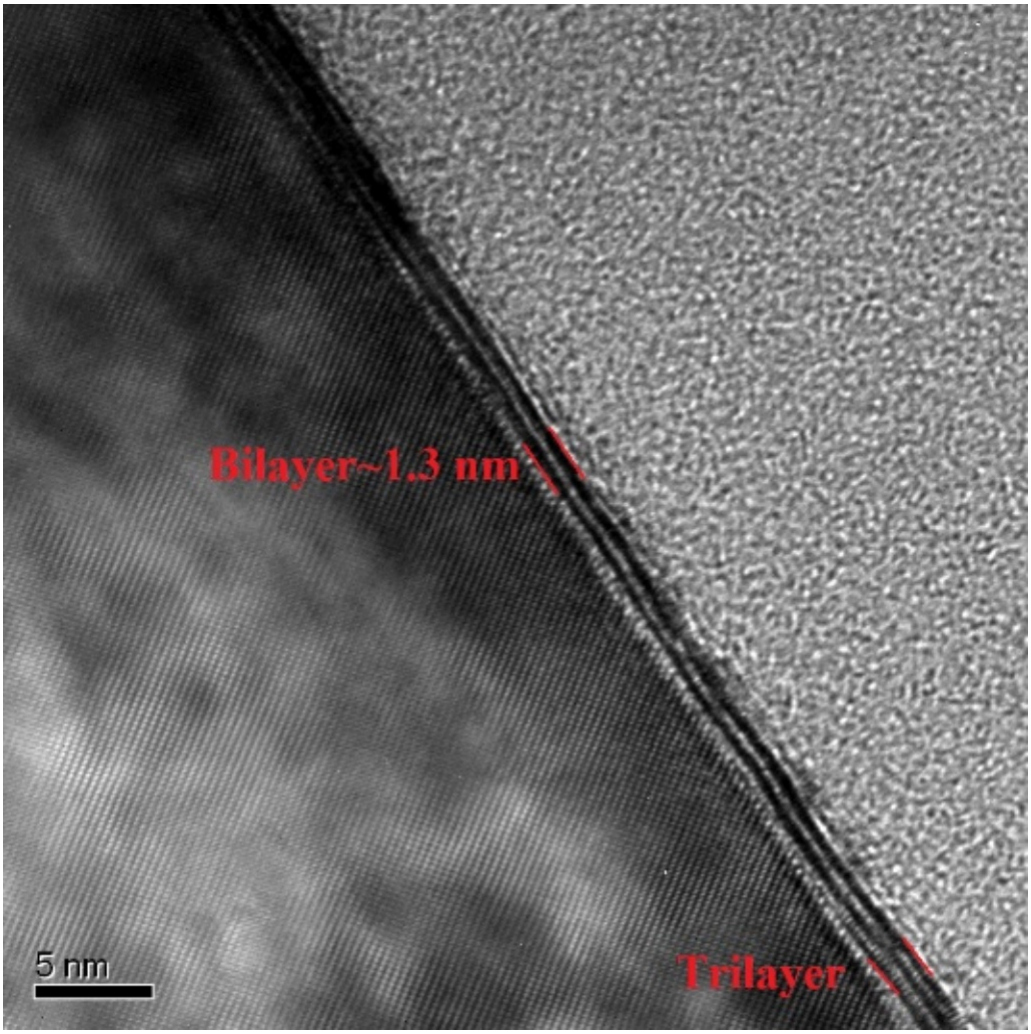

Figure 5-7: TEM image of few-layer WS_2 films grown on sapphire substrate. The crystalline Al_2O_3 atomic lattice is clearly visible on the left hand side of the image. The WS_2 film is viewed at a high angle where bilayer and trilayer regions are also highly visible and are indicated. The bright area on the right hand side is the protective carbon coating. The trilayer region also shows the WS_2 atomic arrangement.

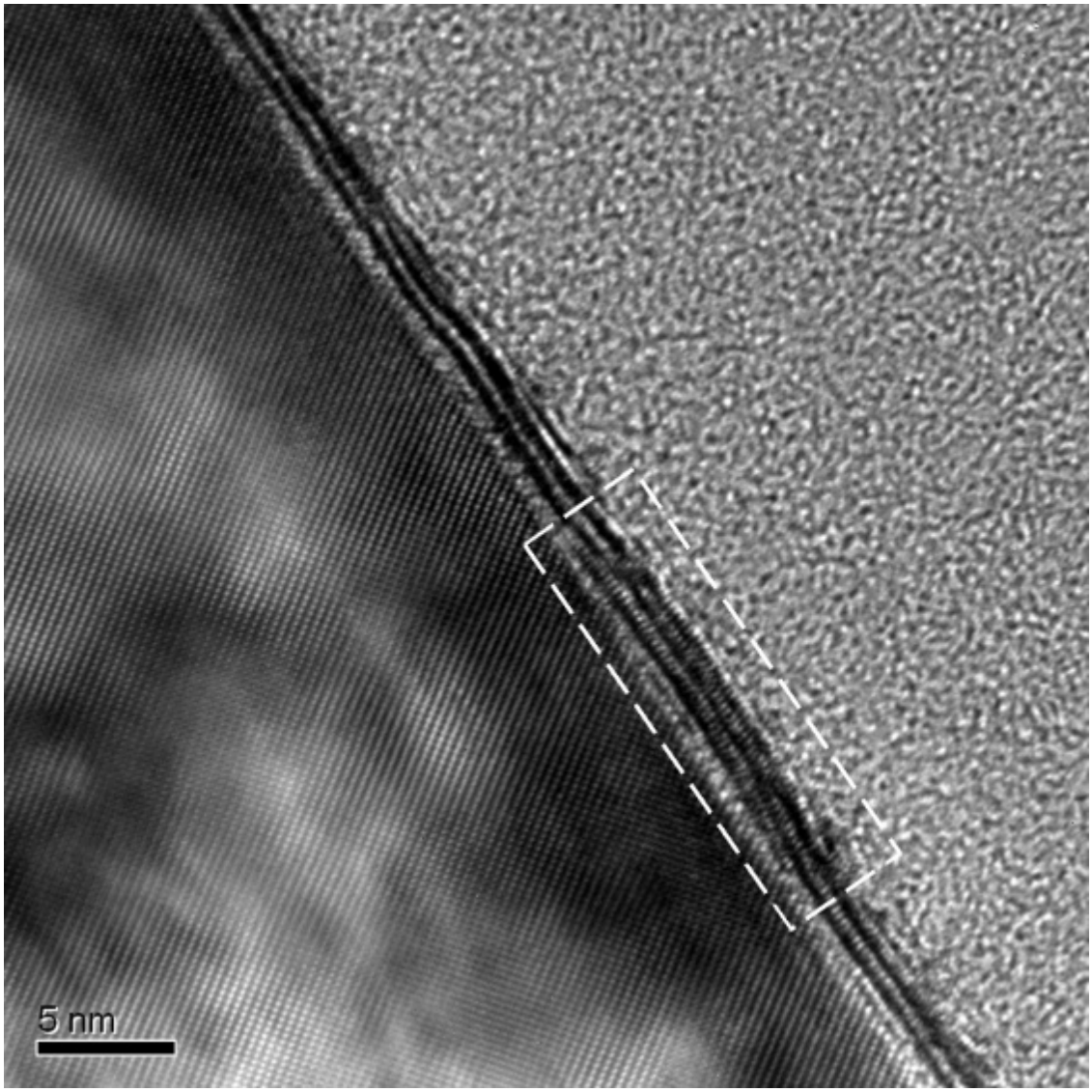

Figure 5-8: TEM image of few-layer WS_2 films grown on sapphire substrate. The crystalline Al_2O_3 atomic lattice is clearly visible on the left-hand side of the image. The WS_2 film is viewed at a high angle where bilayer and trilayer regions are also highly visible. The bright area on the right-hand side is the protective carbon coating. The cross-section of few-layer WS_2 film shows that the atomic columns are clearly visible confirming the crystallinity order of the film as indicated by dotted box.

5.5.3 Raman Spectroscopy

Raman spectroscopy with a 532 nm excitation wavelength was performed to characterize the WS_2 films on both SiO_2/Si and sapphire substrates for each of the two-annealing steps (500°C and 1000°C). The consequence of using a 532 nm pump laser for Raman spectroscopy is an enrichment of the Raman spectra with second order peaks [242]. Multi-peak Lorentzian fitting is applied to deconvolute these peaks which helps to reveal any crystallinity changes between the two-annealing steps and to estimate the thickness of the films. As shown in Figure 5-9 after the 1000°C anneal, the Raman spectra intensity at the centre of the samples were enhanced by X2 for the SiO_2/Si and X4 for the sample grown on sapphire.

Moreover, all peaks become narrower after the second annealing step. The most dramatic change was with the peak labelled LA (M)-TA(M) [243] where its FWHM was reduced from 63.4 cm^{-1} in the first annealing step to 24.4 cm^{-1} in the second annealing step for SiO_2/Si and from 51 cm^{-1} to 28 cm^{-1} for sapphire. Additional peaks that correspond to 2LA (K) mode [244] are also apparent at 385.2 cm^{-1} and 387.7 cm^{-1} for SiO_2/Si and sapphire respectively, which did not exist after the first annealing step. The intensity enhancement in the Raman spectra, the reduction in full width half maximum (FWHM) of all Raman peaks [245], [246] as well as the prominence of additional second order peak (2LA (K)) highlight the significance of the second annealing step at high temperature (1000°C) to promote the crystallinity of the WS_2 films. Furthermore, at 500°C the intensity of the in-plane E^1_{2g} (Γ) dominated the longitudinal 2LA (M) mode whereas at the 1000°C the 2LA (M) peaks increased in intensity which almost overwhelmed the E^1_{2g} (Γ) mode for all substrates. In contrast, the out-of-plane peak A_{1g} (Γ) decreased in intensity at the higher temperature. Consequently, the 2LA (M)/ A_{1g} (Γ) intensity ratio increased dramatically from 0.685 at 500°C to 2.64 at 1000°C for the SiO_2/Si and from 0.285 to 2.26 for the sapphire. Moreover, the Raman peak difference between the in-plane mode E^1_{2g} (Γ) and out-of-plane mode A_{1g} (Γ) at 1000°C is 63.8 cm^{-1} for the SiO_2/Si substrate and 61.2 cm^{-1} for the sapphire substrate. Both the intensity ratio of 2LA (M)/ A_{1g} (Γ) and Raman peaks difference (A_{1g} (Γ)- E^1_{2g} (Γ)) indicate the few-layer nature of the measured WS_2 films on both substrates similar to what has been reported in the literature [25], [93].

Interestingly, after the second annealing step all the peaks from E^1_{2g} (Γ) to 2LA (M)-$2E^2_{2g}$ (M) are shifted to lower wavenumbers compared to their peak positions after the first annealing step at 500°C. The only exception was the longitudinal acoustic mode 2LA (M), which did not shift after the two annealing steps for both substrates. As a result, the separation of the in-plane E^1_{2g} (Γ) and the out-of-plane peak A_{1g} (Γ) Raman peaks after the first annealing step is smaller compared to after the high temperature annealing step (60.8 $cm^{-1}$for SiO_2/Si and 59.9 cm^{-1} for sapphire). This is due to blue shifts that E^1_{2g} (Γ) peaks experience in poor crystalline films as stated previously. However, the intensity ratio of 2LA (M)/ A_{1g} (Γ) peaks is also low (0.685 for the SiO_2/Si and 0.285 for the sapphire) for poor crystalline films. Thus, the layer number estimation of poor crystalline WS_2 films (500°C) using Raman spectra with 532 nm excitation wavelength might be not accurate. The reason behind this is the correlation between Raman peaks difference and the intensity ratio is not valid for poor crystalline WS_2 films (500°C) as opposed to the higher crystalline WS_2 films (1000°C) which show a clear correlation between Raman peak difference and intensity ratio when resonant excitation wavelength is used for Raman spectroscopy [25].

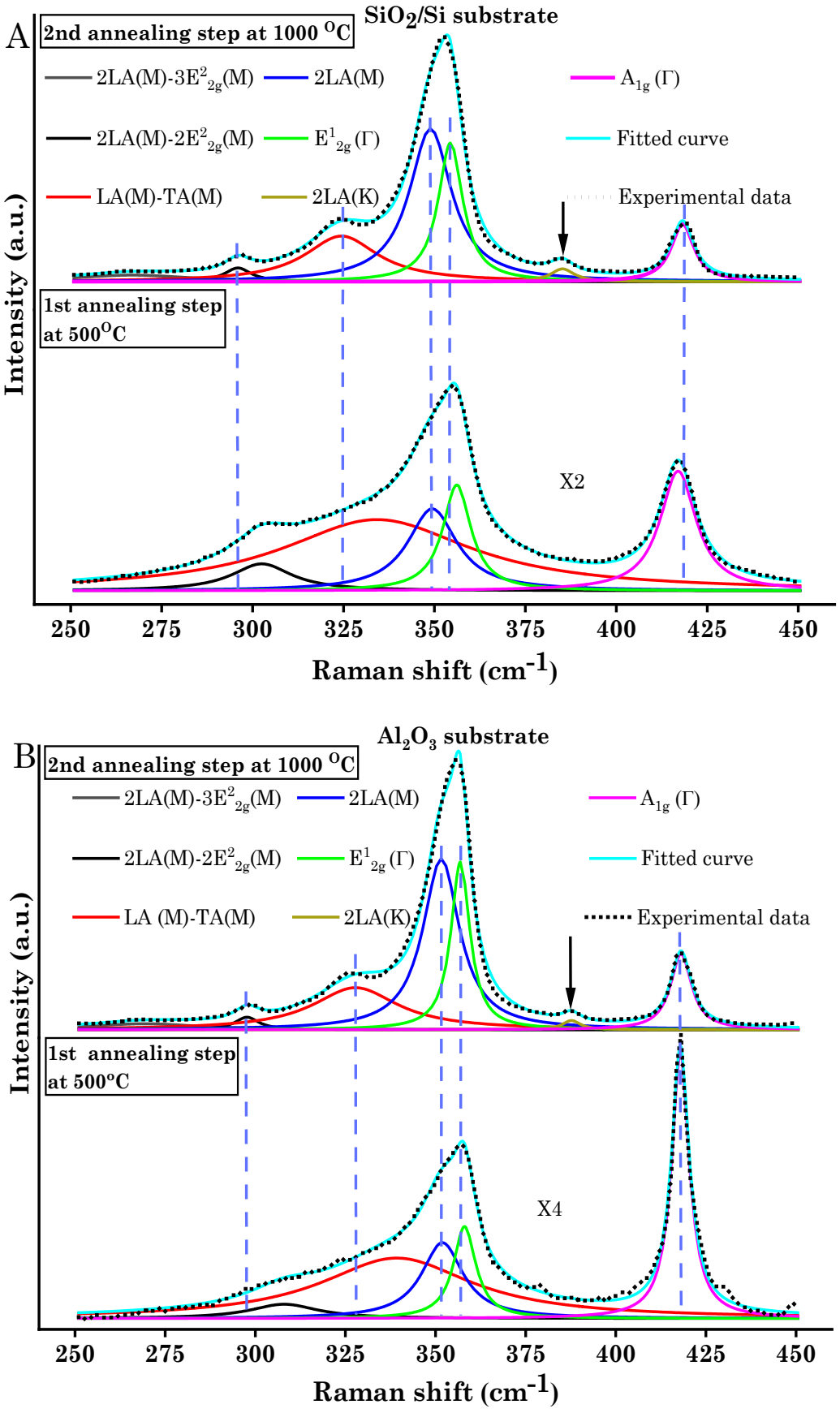

Figure 5-9: Raman spectrum for WS_2 film on (A) SiO_2/Si and (B) Sapphire at the 500°C and 1000°C respectively. The measurement has been performed by Adam H. Lewis.

5.5.4 Photoluminescence Spectroscopy

The PL spectrum of WS_2 films was investigated using the same excitation wavelength, power and objective parameters as the Raman measurements. As shown in Figure 5-10 there is a significant enhancement of the photoluminescence (PL) signal after high temperature annealing for both substrates. The PL intensity enhancement is X4.5 for the SiO_2/Si and X3.5 for the sapphire substrate, this enhancement is attributed to the improvement in film crystallinity. However, the PL peaks intensities are still weak, due to few-layer nature of films. For the SiO_2/Si substrate, the PL peak of WS_2 film is located at 1.984 eV, in agreement with earlier reports for few-layer WS_2 [243], whereas the PL peak position of WS_2 film grown on sapphire substrate is at 2 eV similar to what has been observed before for WS_2 films grown on sapphire [135]. The trivial shift to lower energy in PL peak position of the WS_2 films grown on SiO_2/Si substrate compared to the films grown on sapphire might results from higher strain on the film deposited on SiO_2/Si substrate [244].

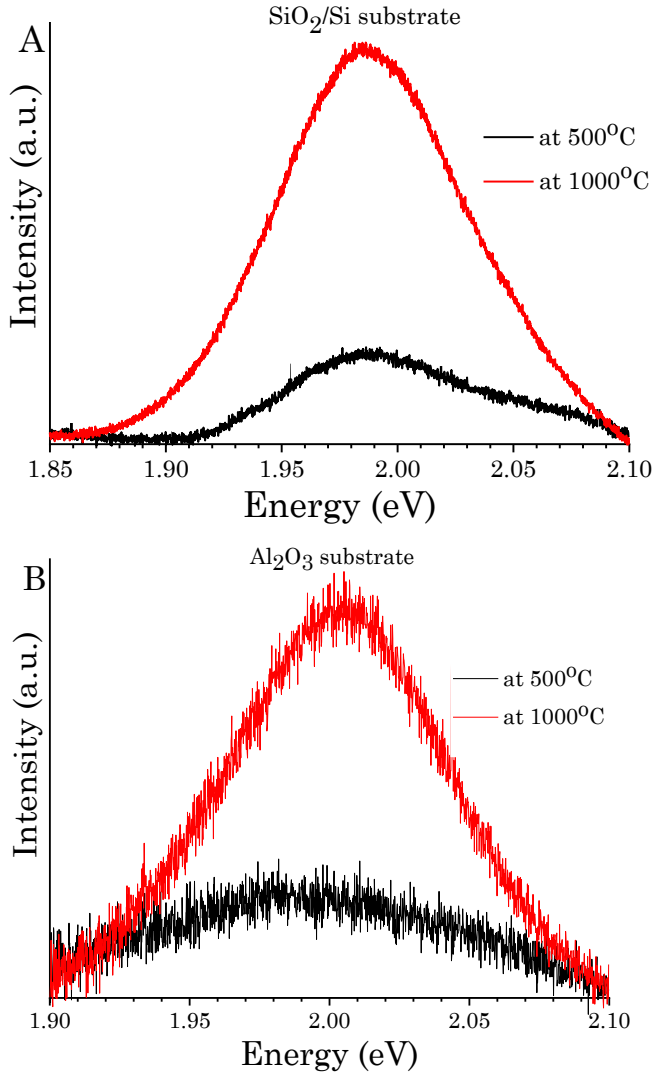

Figure 5-10:PL spectra of WS_2 films on (A) SiO_2/Si and (B) Sapphire at 500°C and 1000°C respectively. The PL measurement has been performed by Adam H. Lewis.

5.5.5 X-Ray Photoelectron Spectroscopy

The composition of the deposited WS_2 films was investigated by high resolution XPS for both substrates where the W and S core levels were studied. The carbon peak in the C1s core level was used as a reference point and was at 284.8 eV for both substrates. The de-convoluted XPS spectra for W and S core levels are shown in Figure 5-11 respectively for both substrates. For the WS_2 film deposited on the SiO_2/Si substrate, two doublets were pronounced in the W core level, the first doublet represents the W^{4+} $f4_{7/2}$ at 33.05 eV and W^{4+} $f4_{5/2}$ at 35.20 eV which is attributed to WS_2 formation, with spin orbit splitting (W^{4+} $f4_{5/2}$-W^{4+} $f4_{7/2}$) of 2.15 eV and an area ratio of W^{4+} $f4_{5/2}$/ W^{4+} $f4_{7/2}$ 0.73. The energy of these peaks corresponds to the 2H phase of WS_2 [247]. The second doublet is located at 36.35 and 38.55 eV respectively and represents the W^{6+} $f4_{7/2}$ and W^{6+} $f4_{5/2}$ peaks that depicts the formation of WO_3 [248]. For sulphur, the S $2p_{3/2}$ and S $2p_{1/2}$ peaks are located at 162.85 and 164.06 eV respectively with spin orbit splitting (S $2p_{1/2}$-S $2p_{3/2}$) 1.21 eV and area ratio S $2p_{1/2}$/ S $2p_{3/2}$ 0.4. This doublet corresponds to S^{2-} sulphur bonded in 2H phase of WS_2 [247]. Fortunately, the absence of S_2^{2-} ligands peaks, which corresponds to the presence of WS_3 and oxidized sulphur species, is a good indicator that the film is stoichiometric for both substrates [248], [249]. The peaks obtained from the WS_2 films on the sapphire are almost identical to films grown on SiO_2/Si. However, there is a shift to lower energies by 0.4 eV for all peaks assigned to WS_2 in both W and S core levels and the oxide content is negligibly increased compared to films grown on SiO_2/Si.

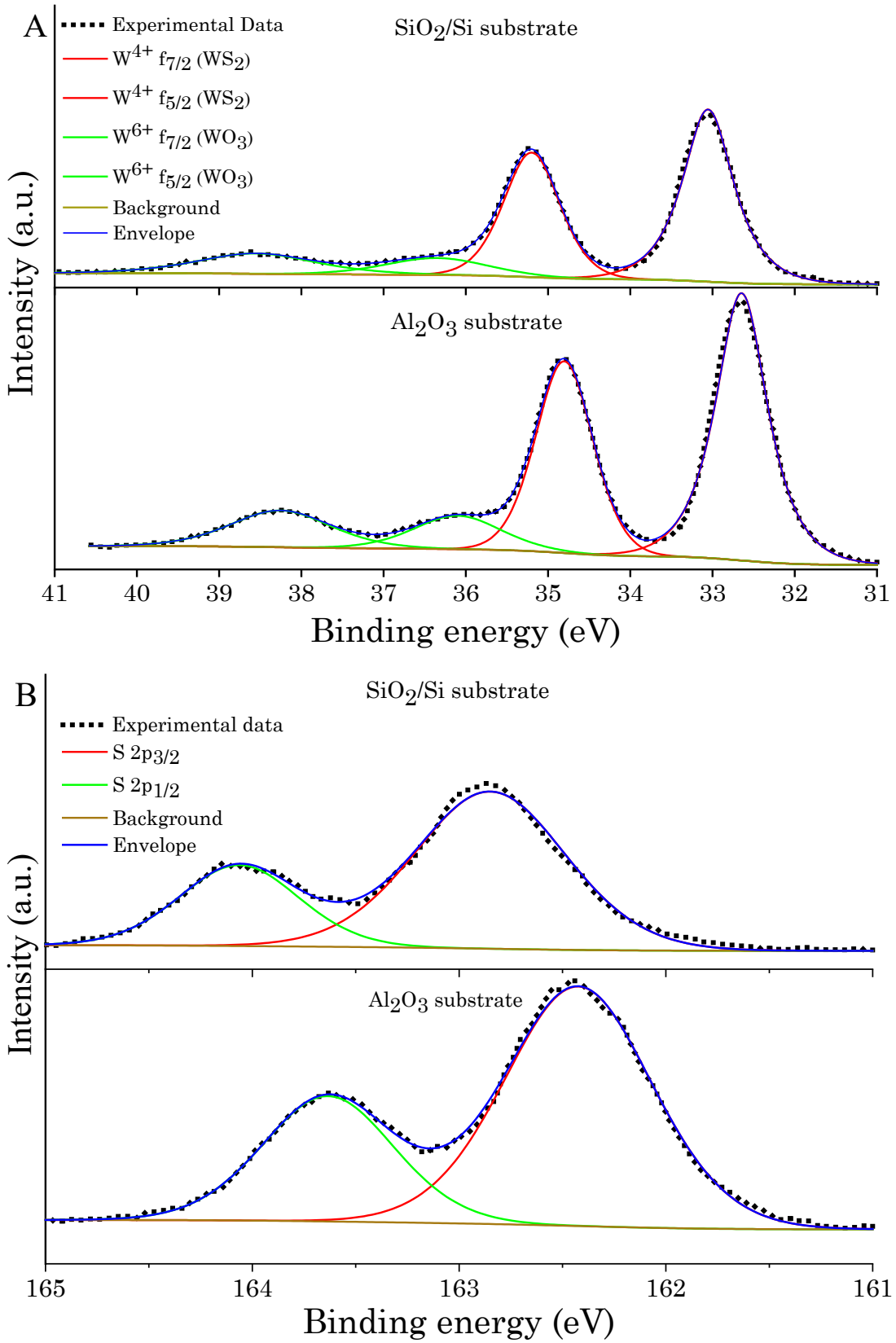

Figure 5-11: XPS spectra of WS_2 films on SiO_2/Si and sapphire substrates (A) W 4f core-level and (B) S 2p core-level spectra. The XPS measurement and the deconvolution of XPS peaks has been performed by Ioannis Zeimpekis.

5.6 FET device fabrication and characterisation

To probe the electronic properties of the WS_2 film, we fabricated a back-gated field effect transistor (FET) using the as-deposited WS_2 films on 300 nm thermally grown SiO_2 on n-type Si substrates (see Figure 5-12 for SEM image of the device). Indium was chosen to make direct contact with WS_2 due to small Schottky barrier which makes it a good choice for ohmic contacts with WS_2 film [221]. The transistor channels were formed by conventional photolithography using S1813 photoresist masking and etched for 2 minutes to remove unwanted WS_2 film regions by Argon ion milling using Oxford Plasma Technology Ionfab 300 plus system. An Argon ion plasma beam was accelerated to 500 V with 100 mA current. The sample placed on a cooled plate (15°C) at an angle of 45° with respect to the beam and rotated at 5 rpm. The samples were then immersed in acetone to remove the photoresist mask and obtain a WS_2 channel of 200 µm width which represents the FET. The length of the channel is 10 µm and was defined by the source and drain electrodes positions as patterned by S1805 photoresist. Indium contacts (10 nm thick) were deposited and capped by 50 nm of Au using an e-beam evaporator followed by lift-off.

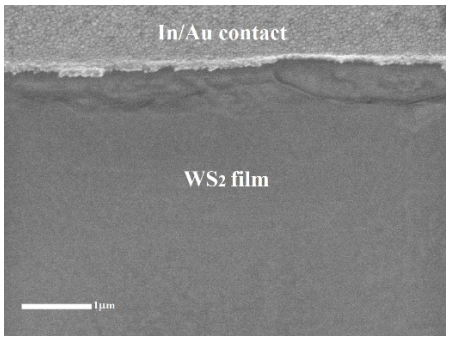

Figure 5-12: An SEM image for a section of few-layer WS_2 FET taken by Ioannis Zeimpekis.

Current voltage measurements were performed in air to evaluate the transfer characteristics of the devices. First, we measured the source-drain current I_{ds} against the voltage between the source and drain V_{ds} for different bottom gate voltages as shown in Figure 5-13 (A), the linearity of this result reveals that the In/Au electrodes make excellent Ohmic contacts with the WS_2 channel. To evaluate the transconductance of the device, the back-gate voltage was swept from -91 V to 100 V in both directions as shown in Figure 5-13 (B). In forward sweep, the device shows n-type behaviour with 6.2×10^{-5} $cm^2/V.s$ field effect mobility, a threshold voltage of -54 V and on/off ratio of 2.5. The field effect mobility was extracted from the slope of the linear part of the transfer curve using the equation [154]:

$$\mu_{FE} = \frac{L}{W\, C_{OX}\, V_{ds}} \frac{\Delta I}{\Delta V_g} \qquad \text{Equation 5-1}$$

Where μ_{FE} is the field effect mobility, L is the channel length (10 µm), W is the channel width (200 µm), C_{ox} is the capacitance of silicon dioxide layer (300 nm) which is (11.5 nF/cm^2), V_{ds} is the source-drain voltage and ($\Delta I/\Delta V_g$) is the transconductance. Interestingly, in backward sweep the FET shows asymmetric ambipolar behaviour with minimum conductivity at 0 V in

the n-type branch. However, the low mobility, on-off ratio and the change of the behaviour (hysteresis) could be partially attributed to adsorbates from ambient and/or dopants that occur during photolithography and lift-off process [110]. The field effect mobility and the on-off ratio of our WS_2 FET devices are comparable with backgated WS_2 FET devices grown by other solution-based approach when they were characterized in air [110]. Additionally, our WS_2 FET devices show comparable performance with MoS_2 FET devices fabricated using identical synthesis processes, where the mobility of MoS_2 devices varied from 10^{-4} to 10^{-2} $cm^2/V.s$ although the back-gate voltage of these devices was swept to much higher voltages [148], [154]. The device field effect characteristics are dictated by the nanocrystalline nature of the film as well as ambient adsorbates. However, as it has been shown with MoS_2 films that are grown in similar ways, we expect a dramatic improvement when the device is optimized and operated in a top-gate configuration with a high-k dielectric such as HfO_2 [150] or ionic liquid gate [151], [155].

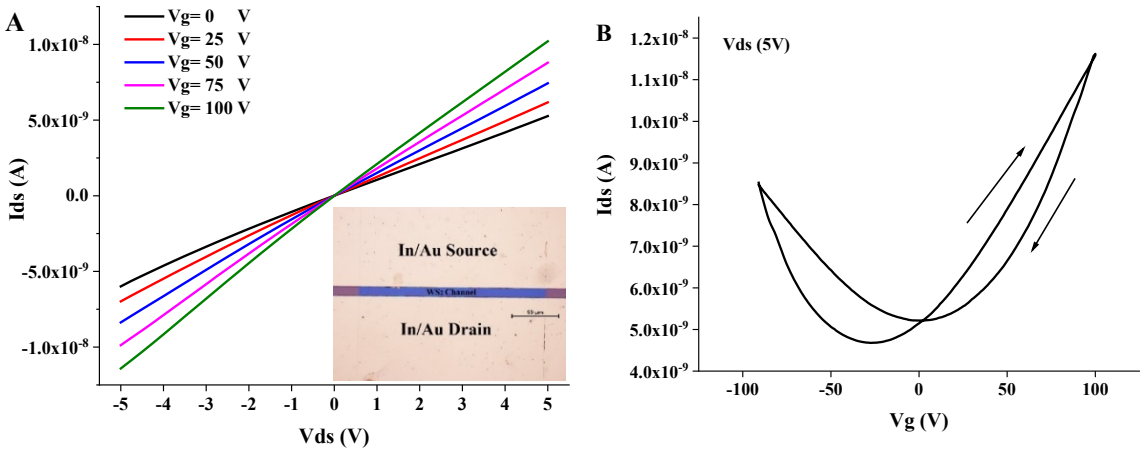

Figure 5-13: Electrical characteristics of back-gated WS_2 FET (A) Ids-Vds (inset: optical microscope image for the actual FET device, the scale is 50 µm.) (B) Forward and backward sweep transfer characteristics.

5.7 Conclusion

In conclusion, we propose a facile and cost-effective growth method that can produce high quality, continuous and ultra-thin WS_2 films for electronic applications. This solution-based method utilizes thermal decomposition of uniform spin coated ammonium tetrathiotungstate films on two different types of substrates with centimetre scale to create thin WS_2 films. The key factor that enables $(NH_4)_2WS_4$ to successfully form a uniform and continuous film is our optimized solvents recipe with volume ratio 3/6 NMP, 2/6 n-butylamine and 1/6 2-aminoethanol that promotes the solubility and wettability of the precursor solution. Different characterization tools were used to confirm the thickness and the quality of the WS_2 films. Finally, we demonstrated for the first time a back-gated FET from an as-deposited WS_2 film grown by our solution based process with an electron mobility reaching $6.2x10^{-5}$ $cm^2/V.s$ which shows comparable performance to MoS_2 devices fabricated by similar synthesis approaches.

Chapter 6
Direct Laser Writing of Two Dimensional Transition Metal Disulphides

6.1 Chapter Summary

Laser technology has been merged with synthesis of two dimensional transition metal dichalcogenides (2D-TMD) films via conventional pulsed laser deposition (PLD) [77]–[80]. Additionally, various post-treatments of 2D-TMD such as thinning [243], [250]–[257], crystallisation [72]–[74], [258], [259], chemical modification (doping) [260]–[268] and patterning [269], [270] have been achieved by lasers since these materials became intriguing. However, to date, 2D-TMD production methods are heavily rely on chemical deposition techniques such as chemical vapour deposition (CVD) [271] and atomic layer deposition (ALD) [272]. These techniques are capital intensive, vacuum-based and require complex lithographic processes for semiconductor device arrays fabrication. Alternatively, some reports suggested localized sulphurization [273], selenization [274] of transition metal oxides utilizing laser power to grow 2D-TMD. Nevertheless, these proposed laser synthesis protocols were suffered from inherent inflexibility as well as they lacked a post-patterning step to remove untreated precursors areas which necessarily precludes them to be developed as facile, fast, low-cost processes. Here we show that spatially selective synthesis of 2D-TMD microstructures can be realised using direct laser writing technique under ambient conditions. Solution-based precursors were spin-coated onto Si/SiO_2 substrates and laser processed under standard room operating conditions result in the formation of 2D MoS_2 and WS_2 microstructures with minimal lithographic or thermal overheads. MoS_2 and WS_2 microstructures were characterised using different spectroscopic tools and their electronic functionally was tested by using them as channels for FET devices. We anticipate that this simple, elegant process can be readily scaled in future via conventional laser printing approaches including raster-scanning or multiple-beam shaping spatial light modulators and digital light engines that potentially enable mass production protocols such as roll-to-roll processing.

6.2 Introduction

Extensive efforts have been dedicated to promote and develop a production method for 2D-TMDC that could be compatible with the current semiconductor technology. Unfortunately, top down synthesis approach like mechanical and liquid exfoliation has several limitations. The former one is extremely low yield while the latter one produces 2D-TMDC sheets with uncontrollable size, thickness and quality [6]. However, a very recent study brought some hope that liquid exfoliation technique could be exploited for device fabrication [47].

On the other hand, in terms of scalability and uniformity of synthesized 2D-TMDC layers, bottom-up approach (e.g. chemical and physical vapour deposition) is more suitable given that the above mentioned challenges still need to be addressed. However, several groups employed thermolysis of solution-based single source precursor particularly for MoS_2 as a simple and cost effective alternative [148]–[153], [155]. This approach shows promising electronic and optoelectronic devices performance in addition to reach roll to roll production stage [148], [152], [155]. Moreover, the solution nature of the precursor offers the opportunity to be prepatterned as wire-like structures prior to the thermal decomposition but with low controllability on thickness and morphology of these wires [154], [275].

Here we show for the first time a new bottom-up approach to grow transition metal disulphides (MoS_2 and WS_2) by laser-induced rapid decomposition of $(NH_4)_2MoS_4$ and $(NH_4)_2WS_4$ films. Surprisingly, we succeeded to grow MoS_2 and WS_2 microstructures directly at ambient conditions without any need for vacuum systems. Moreover, MoS_2 and WS_2 could be simultaneously monitored by Raman spectroscopy directly during formation as our primary results revealed. Thickness, crystallinity, oxide doping of these microstructures can be controlled by precursor concentration, laser power and writing speed.

Unlike other laser post-treatments of TMDC, the untreated areas of the precursors could be removed readily by single developing step leaving behind pristine microstructures. Moreover, transparent substrates can be used, as the formation of the microstructure depends on the absorption of the precursor film to laser wavelength which makes it a reliable method for transparent electronics fabrications.

6.3 Methodology of MS_2 Direct Laser Writing

Our approach for direct laser writing (DLW) of transition metal disulphides is summarised in Figure 6-1. Firstly, the substrates and the precursor solutions {$(NH_4)_2MS_4$ where M is Mo, W} were prepared then followed by spin coating the precursors solutions over targeted substrates. Next, the samples were exposed to visible light (514.5 and 532 nm) by laser irradiation at ambient conditions which triggered localised and rapid decomposition of the precursors to form MS_2 at the exposed areas. At this stage, Raman spectroscopy can be conducted to synthesise and characterise MS_2 simultaneously due to rapid light-matter chemical interaction between the laser and precursor film that induced decomposition of the precursors. Finally, the sample was developed in organic solvent that preferentially remove unexposed area of the film and leaving behind the MS_2 pattern.

Prior to laser writing, it is essential to understand how the precursor's films would interact with the visible green light laser. Therefore, the UV-Visible transmittance spectroscopy has been conducted for ammonium tetrathiomolybdate $(NH_4)_2MoS_4$ with two concentrations (24,48) mM while for ammonium tetrathiotungstate $(NH_4)_2WS_4$ four concentrations (50, 100, 200 and 400) mM films has been tested knowing that silica glass has been used as substrates. However, these concentrations have been chosen carefully where concentrations lower than aforementioned minimum for both precursors will be so transparent as to not absorb the laser energy. On another hand, when the concentrations exceed the aforementioned maximum, the films will be not uniform and the films will start form clusters.

Clearly, for both precursors, optical transmittance is proportionally decreased with respect to elevation of concentrations which indicates higher absorbance with denser precursor films as depicted in Figure 6-2. Moreover, the absorption is increased rapidly in the UV region for all the concentrations of both precursors compared with visible and near IR regions. For ammonium tetrathiomolybdate the transmittance is declined from 91-92 % for wavelengths (514.5-532) nm with 24 mM concentration films to be 83-85 % for the same interval with 48 mM concentration films. Similarly, ammonium tetrathiotungstate transmittance spectrum at 514.5 nm is decreased from 97% at 50 mM to 85% with 400 mM while the 100 and 200 mM have almost identical transmittance (92.5-93%).

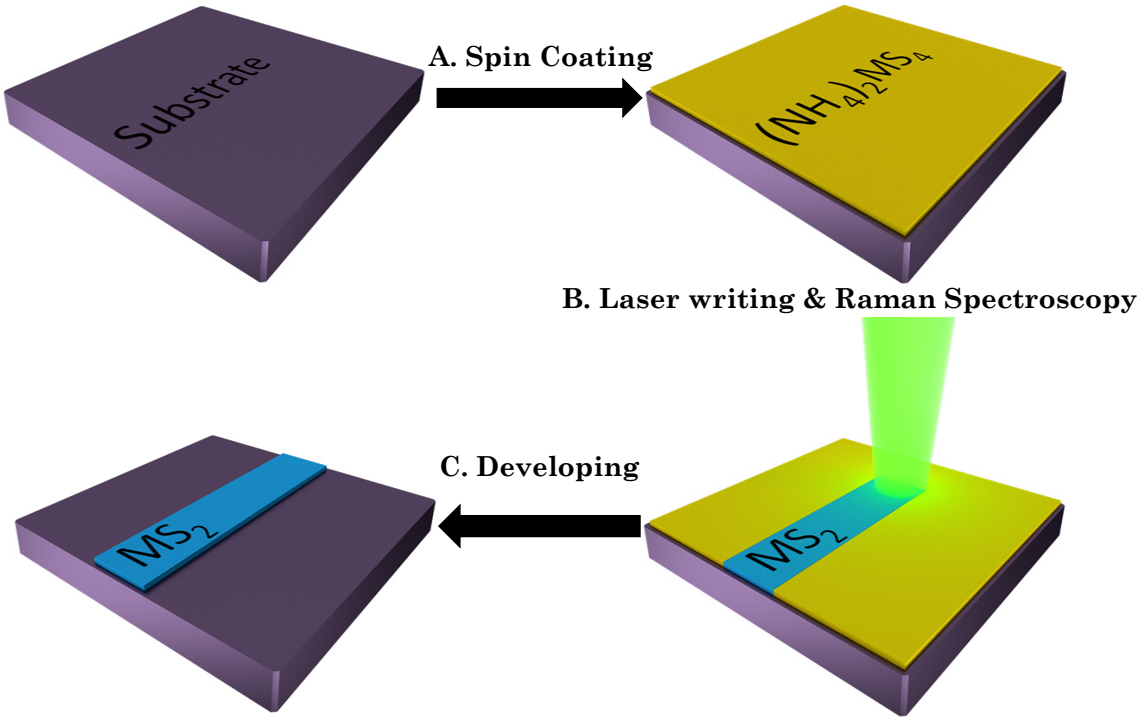

Figure 6-1: Schematic representation of direct laser writing (DLW) of MS_2 where M = Mo, W.

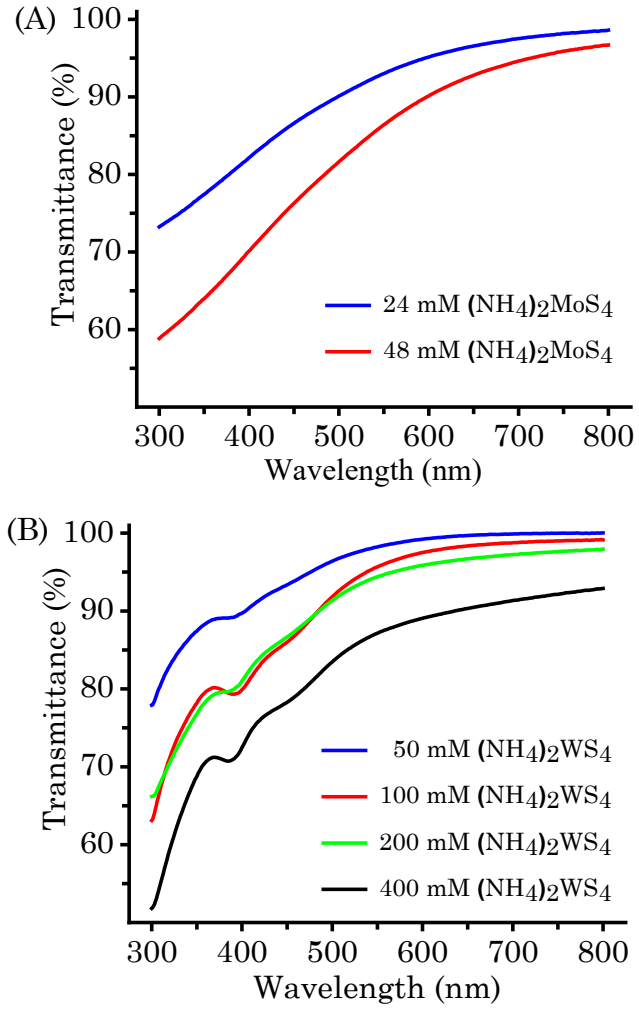

Figure 6-2: UV-VIS spectroscopy of (A) ammonium tetrathiomolybdate with 24 & 48 mM films and (B) ammonium tetrathiotungstate with 50, 100, 200 and 400 mM films.

6.4 In-situ Raman Spectroscopy and Direct Laser Writing of MS_2

It has been proved that *in-situ* Raman spectroscopy could be an excellent monitoring tool to study the dynamics of laser thinning of MoS_2 flakes as well as laser crystallization kinetics for amorphous MoS_2 films deposited by sputtering [73], [255]. In-situ Raman spectroscopy could provide rapid analysis for the layer number and crystallinity of the 2D-TMDS films simultaneously with laser treatment. However, to the author's knowledge there is no reports yet of in-situ Raman with direct laser synthesis which could be a key tool towards quality control of 2D-TMDS films for industrial applications.

To conduct in-situ Raman spectroscopy, two samples with 1.5 cm^2 SiO_2/Si substrates were spun coated by 48 mM concentration of Mo and W precursors respectively. Next, Raman measurements (excitation wavelength 532 nm and 50X objective) have been performed with three different powers 3, 22 and 40 mW using static exposure as shown in Figure 6-3 (A&B). At low power, there are no MoS_2 and WS_2 peaks noticed. Strikingly, at medium power, in plane (378.3cm^{-1}) and out of plane (403.3 cm^{-1}) Raman peaks of MoS_2 are pronounced revealing rapid formation of MoS_2. However, at the same power, there are no WS_2 peaks although both films had the same concentration. At maximum power (40 mW), Raman peaks of MoS_2 (378.6 cm^{-1}, 403.3 cm^{-1}) and WS_2 (351.6 cm^{-1}, 415.6 cm^{-1}) are observed on both Mo and W precursors films. To further confirm MoS_2 and WS_2 rapid laser synthesis by laser energy, a subsequent Photoluminescence spectroscopy has been conducted at the same laser exposed points where Raman spectroscopy has been taken. Unlike MoS_2 case where there is no PL peak in all three powers, WS_2 PL peak at 1.987eV was detected only at the high power indicating a few layer formation of WS_2 [243].

From this simple experiment it can be concluded that laser synthesis of MS_2 by direct laser writing can be combined with Raman spectroscopy, thus providing very useful method for monitoring of the synthesis. Moreover, the optical absorption of the precursor films plays a crucial role to form the 2D-TMD as it can be seen in the medium power where MoS_2 was formed while WS_2 was not due to the lower absorption at this wavelength (see Figure 6-2). Finally, due to lower PL quantum yield of MoS_2 compared to WS_2 [33], [99], [130] , no PL peaks was observed for MoS_2 while WS_2 peaks are clearly noticed at the high power condition.

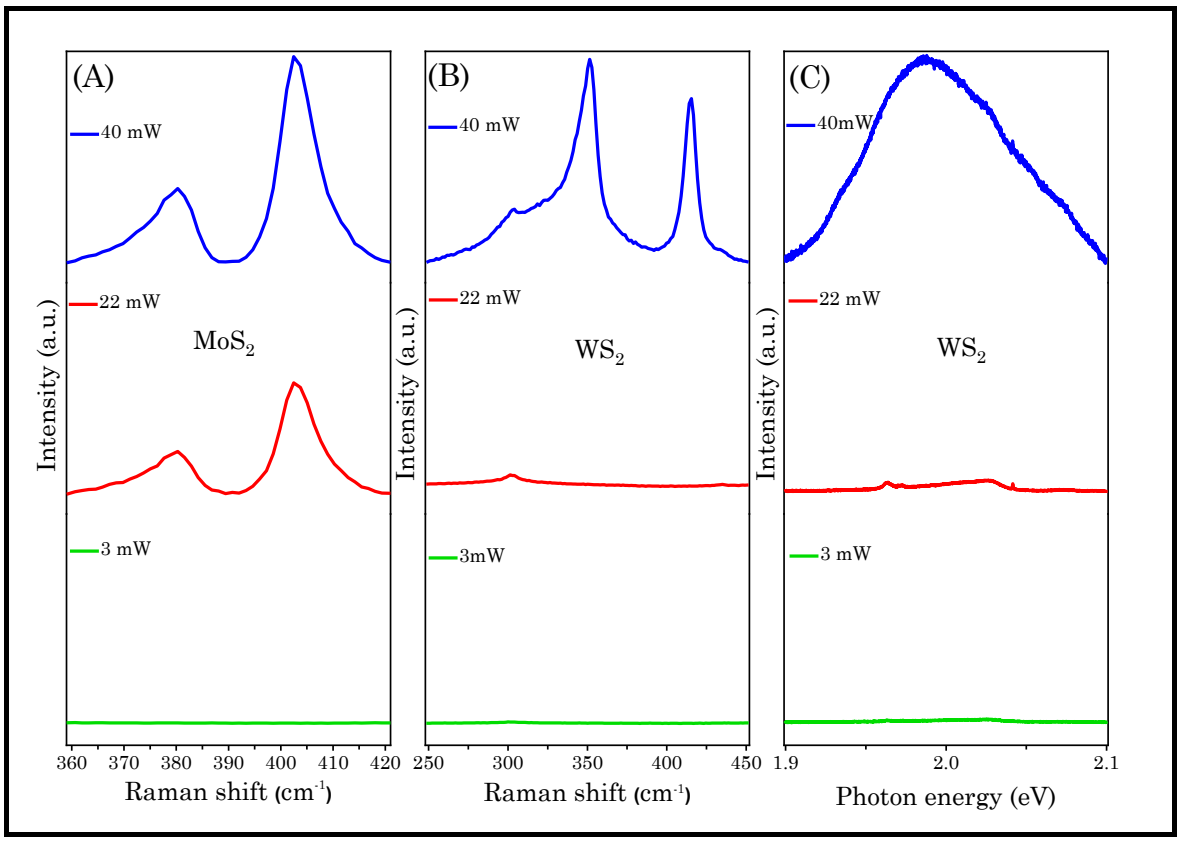

Figure 6-3: In-situ Raman spectroscopy and laser writing of (A) MoS_2 and (B) WS_2 while (C) is PL spectra for WS_2 after laser writing. The Raman measurement has been performed by Adam H. Lewis.

6.5 Microstructures Formation of MS_2 by Direct Laser Writing on Different Types of Substrates

Unfortunately, the parameter space of 532 nm Raman laser system is limited, especially in terms of power where the maximum power is 40 mW. This power is not sufficient to study the effect of laser energy on thickness, crystallinity and oxide doping of the MS_2 films and more powerful and flexible laser writing system is essential to study thoroughly these parameters. Therefore, we switched to CW argon ion laser writing system (514.5) nm with motorizing stage where the laser power is ten times higher than the Raman laser system with two objectives (10, 20 X). Moreover, the motorizing stage can be move in XY directions with controllable speed to tune the exposure time per unit area of the MS_2 films. In term of patterning, this set up offers the opportunity to write different patterns such as dots, lines or continuous films by raster scanning in micrometre scale precision.

However, to investigate the substrate versatility of our approach, various types of substrates have been chosen to grow MS_2 microstructures on them. This versatility demonstrates the potential of our laser writing approach to synthesize MS_2 for wide range of electronic, optoelectronic and photonic applications. These substrates are listed below:-

6.5.1 SiO_2/Si substrate

One of the most common type of substrates used to support 2D materials for characterisation and device fabrication is SiO_2/Si [276]. This can be grown with different oxide thickness which can be identified easily through the colour of the substrates [277]. In this work, we used SiO_2/Si substrates with 285 and 300 nm thicknesses which are normally have blue to violet-blue colour [278]. These oxide thicknesses give optimum optical contrast particularly with MoS_2 films [6], also this relatively high thicknesses are helpful to avoid electrical breakdown of the oxide that readily occur during back-gate FET electrical characterisation. Therefore, we used this substrate to grow continuous films, meanders and microdots of MoS_2 and WS_2. The table below illustrates the conditions to grow MoS_2 films and meanders (individual lines) knowing that the objective lens used in this set up is 10X in both cases.

Table 6-1: Laser writing conditions for 1 mm^2 continues MoS_2 films and meanders. Note: the MoS_2 films were formed by minimising the spacing between the MoS_2 lines to be 2 µm while to grow the individual lines (meanders) the spacing was increased to be 50 µm.

Concentration (mM)	Laser power (mW)	Writing speed (mm/min)	Line spacing (µm)
24	300	50	2
24	300	100	2
48	300	50	2
48	300	100	2
24	300	100	50
24	300	1000	50
24	400	100	50
24	400	1000	50
48	200	100	50
48	300	100	50
48	300	1000	50
48	400	100	50
48	400	1000	50

Figure 6-4 shows 1 mm^2 continuous films of MoS_2 formed by raster laser scanning which deposited on (48, 24) mM concentrations precursors films using 300 mW laser power with 10X while the laser writing speed 50 and 100 mm/min respectively. Moreover, Figure 6-5 shows MoS_2 multiple microlines (meanders) formed by direct laser writing. The laser writing speeds were 100 mm/min for both precursor films (48, 24) mM while the laser powers were 300 and 400 mW respectively (using 10X objective). After laser scanning, there is a clear optical contrast between

the laser treated area and untreated precursor areas. Moreover, when the samples were developed in DMF solvents. The untreated areas were totally dissolved while the MS_2 patterns remained almost unaffected as shown in Figure 6-4 and Figure 6-5 (b, d).

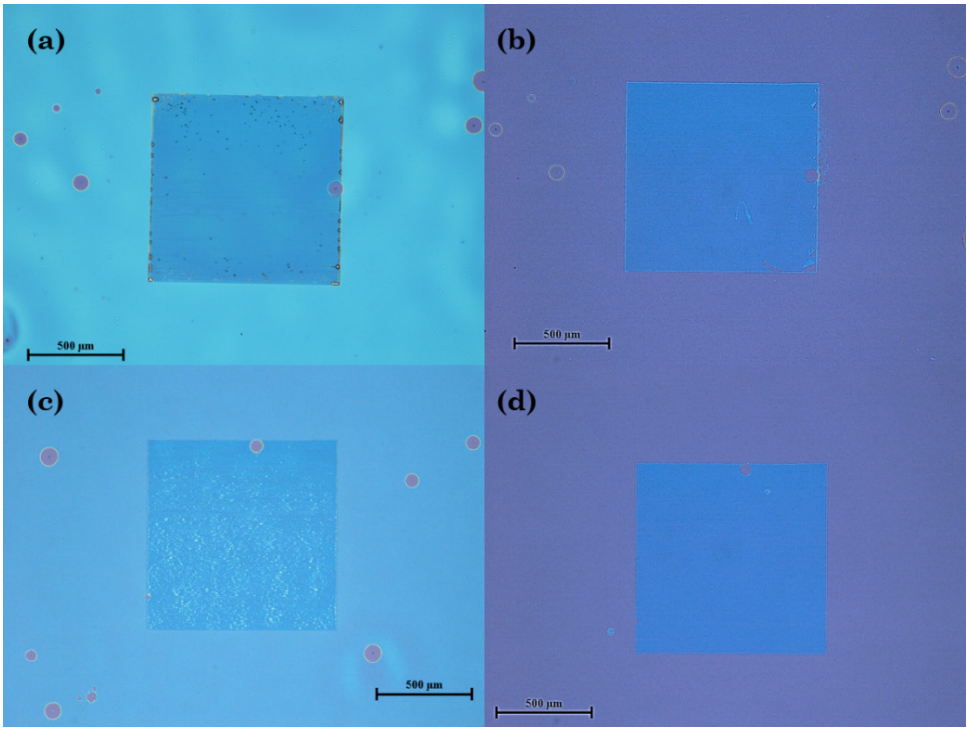

Figure 6-4: MoS_2 films formed by DLW on (a) 48 mM and (c) 24 mM while (b, d) are same samples after removing untreated precursors.

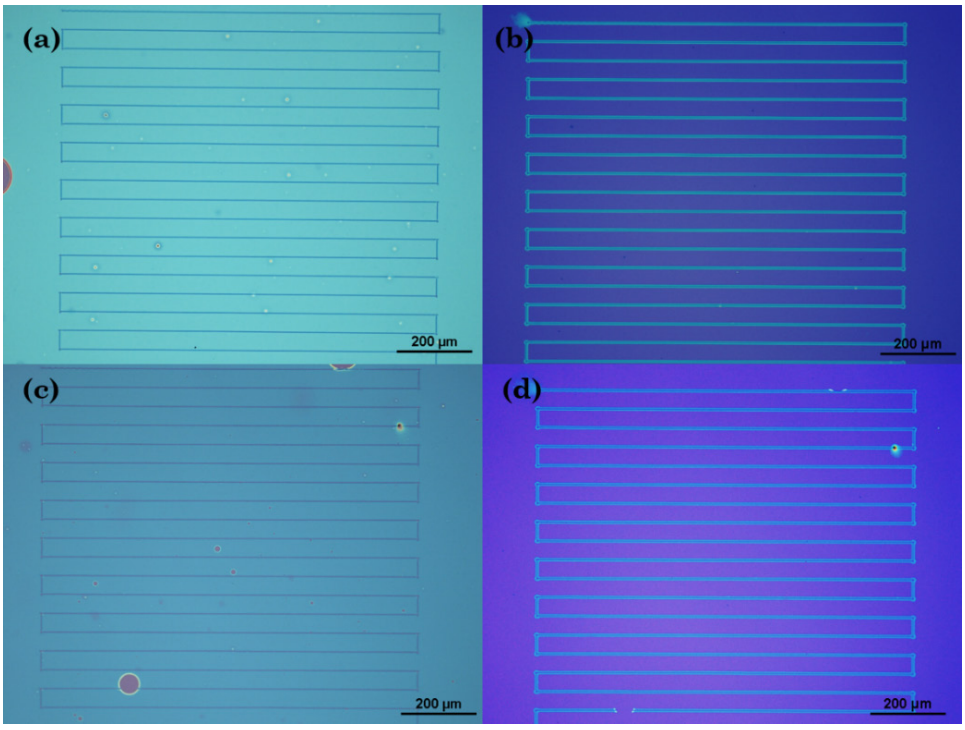

Figure 6-5: MoS_2 meanders formed by DLW on (a) 48 mM and (c) 24 mM precursor films while (b,d) are images for the same samples after removing untreated precursors.

Similarly, WS_2 were grown as films and meanders by direct laser writing as depicted in Figure 6-6. The table below shows different laser writing growth conditions for WS_2. However, some samples with 100 mM concentrations where grown with 250 mW rather than 300 mW due to power instability of the laser but we didn't notice any dramatic changes in the film thickness and crystallinity of the WS_2 structure as the power reduction is not significant.

Table 6-2: Laser writing conditions for 1 mm^2 continues WS2 continues films and meanders, knowing that the objective lens used is 20X.

Concentration (mM)	Laser power (mW)	Writing speed (mm/min)	Line spacing (µm)
50	300	100	2
50	300	100	6
50	300	100	20
100	300	100	2
100	300	100	6
100	300	100	20
200	300	100	2
200	300	100	6
200	300	100	20
400	300	100	2
400	300	100	6
400	300	100	20
100	125	100	2
100	125	100	20
100	150	100	2
100	150	100	20
100	175	100	2
100	175	100	20
100	200	100	2
100	200	100	20
100	225	100	2
100	225	100	20
100	250	100	2
100	250	100	20

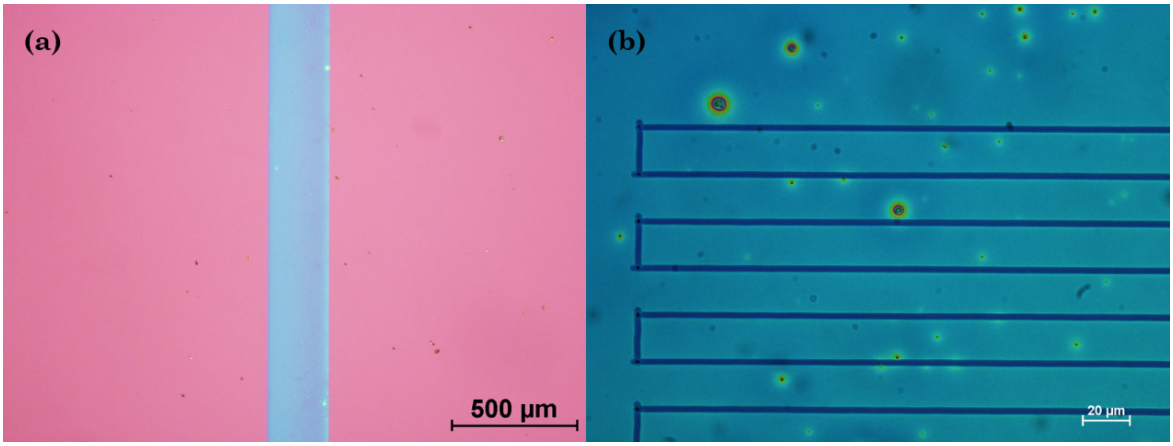

Figure 6-6: (a) WS_2 film with 1 cm length and 200 µm width grown by DLW. (b) is an image of WS_2 microlines. Both the microlines and the film were grown with 250 mW power, 20X objective at 100 mm/min speed on 100 mM $(NH_4)_2WS_4$ precursor film.

Finally, 2 mm^2 WS_2 microdots array has been created by similar direct laser writing set up as depicts in Figure 6-7. A modified optical chopper with two slots and rotating frequency 550 Hz has been used to periodically interrupt the laser writing beam with 250 mW power, 20X objective and 50 mm/min writing speed while the spacing between each individual dotted line is 20 µm. A spin coated $(NH_4)_2WS_4$ with 100 mM concentration film on 285 nm SiO_2/Si were used to grow the WS_2 microdots by direct laser writing. It is noteworthy that Raman spectroscopy has been conducted to confirm the growth of all these MS_2 microstructures as mentioned above.

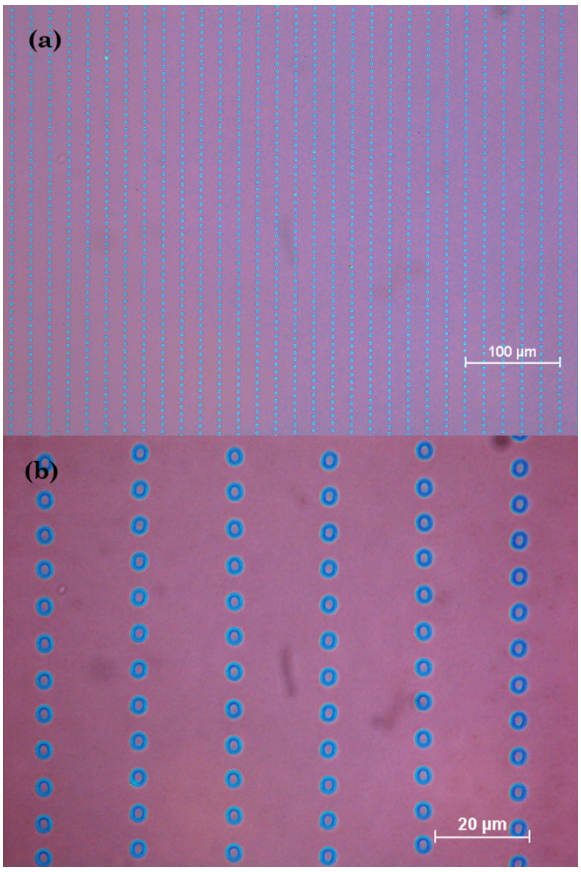

Figure 6-7: WS_2 microdots.

6.5.2 D-shape Fibre and Silica Substrates

Recently, there is increasing demands to functionalise 2D materials in all-optical devices such as optical fibres and optical modulators due to their unique linear and nonlinear properties [192], [279] . For example, D-shape optical fibre with MoS_2 coating has been fabricated as an all-optical modulator device which show excellent nonlinear optical properties and was expected to find it is way for real world applications [280]. However, in this report, the MoS_2 film was made by CVD process and then transferred to the D-shape fibre [280] which is not a reliable method for large scale production.

Instead, we propose direct growth of TMDC on the D-shape fibre by laser writing. The D-shape fibre was immersed in 6 mL of 100 mM of $(NH_4)_2WS_4$ and prebaked at 140°C then the laser system was use to write the WS_2 microline with 250 mW and 100 mm/min speed and 20X objective. After laser writing, the fibre was immersed in NMP solvent to remove the untreated precursor. Figure 6-8 shows the WS_2 line on the D-shape fibre while Figure 6-9 is the Raman spectrum of WS_2 that has been deposited on the fibre. This laser writing technique could be extended for MoS_2 by using $(NH_4)_2MoS_4$ rather than $(NH_4)_2WS_4$.

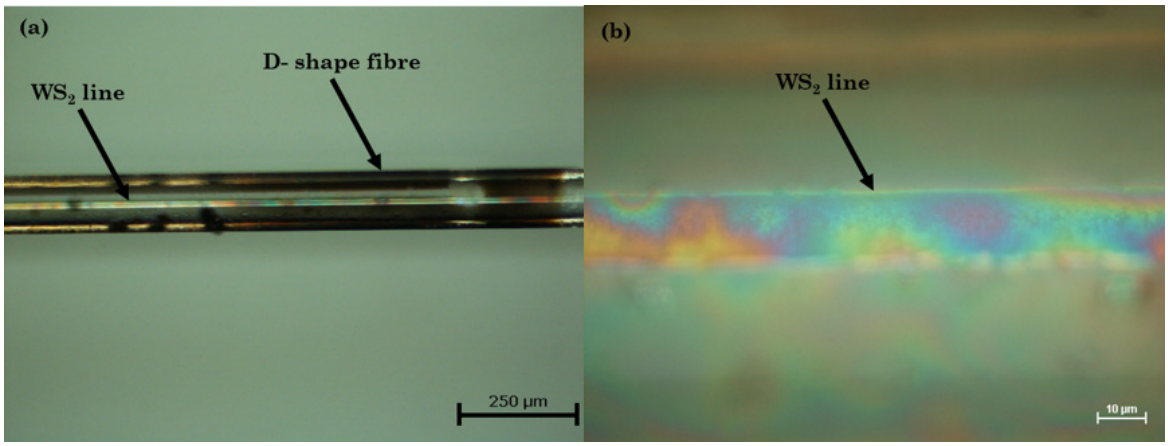

Figure 6-8: WS_2 line on D-shape fibre.

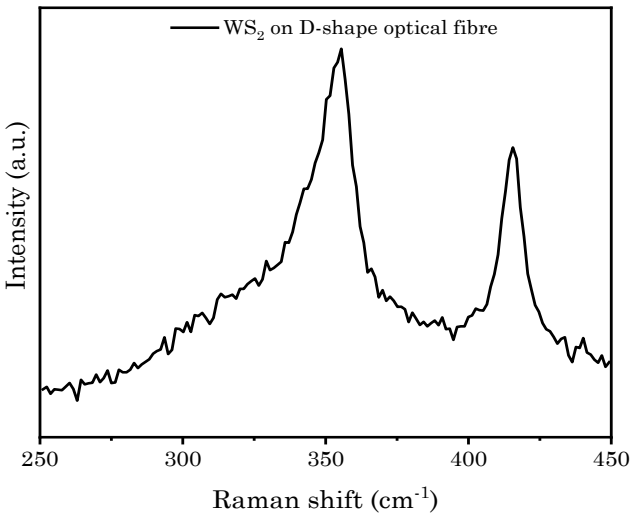

Figure 6-9: Raman spectra of WS_2 line on D-shape optical fibre. The Raman measurement has been performed by Adam H. Lewis.

Furthermore, MoS_2 films and WS_2 meanders were deposited on planar silica substrates at various conditions as summarized in Table 6-3 for MoS_2 films and Table 6-4 for WS_2 meanders. However, these structures were hardly recognized by optical microscopy due to high transparency of these MS_2 structures which made the characterisation step of these structures more complicated. Instead, peripheral edges were used to identify the treated areas after developments as it had higher optical contrasts with transparent silica substrates. Finally, MoS_2 and WS_2 deposition was confirmed by Raman spectra as shown in Figure 6-11.

Table 6-3: MoS_2 films on silica substrates

Concentration (mM)	Laser power (mW)	Writing speed (mm/min)	Line spacing (µm)
48	200	100	2
48	300	100	2

Table 6-4: WS_2 meanders on silica.

Concentration (mM)	Laser power (mW)	Writing speed (mm/min)	Line spacing (µm)
100	125	100	20
100	150	100	20
100	175	100	20
100	200	100	20
100	225	100	20
100	250	100	20

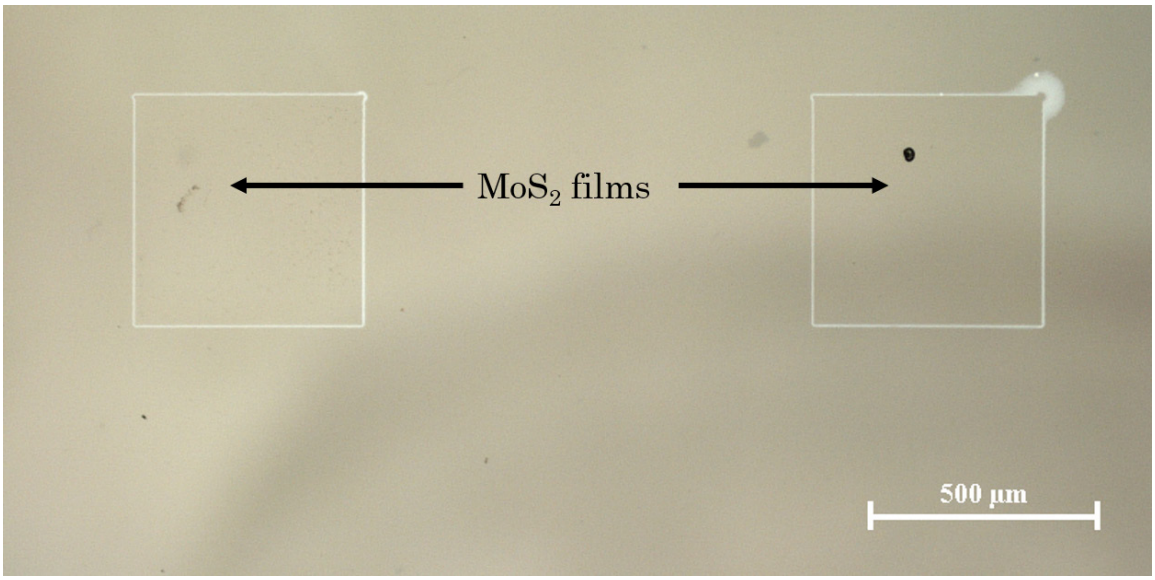

Figure 6-10: MoS_2 film on silica substrate.

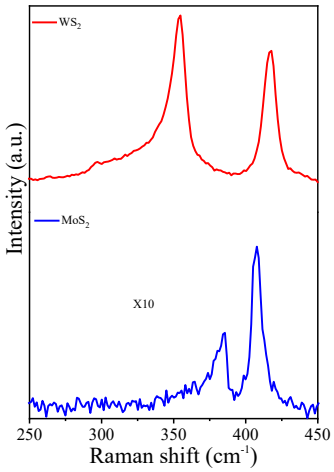

Figure 6-11:Raman peaks of MoS_2 and WS_2 on silica substrate. The Raman measurements have been performed by Adam H. Lewis.

6.5.3 Iron doped Lithium Niobate substrate

Lithium Niobate is one of the most widely functionalized substrates in photonics, electro-optic and piezo-electric devices as this crystal exhibit very broad ranges of properties such as ferroelectricity, piezoelectricity, pyroelectricity, photoelasticity and photorefraction [281]. Therefore, integrating 2D materials with this photonically active substrate can reveal unexplored physics and find novel applications for both 2D materials and lithium niobate. The earliest trial to exploit lithium niobate as substrate for TMD has been conducted by Nguyen et al. [282]. They developed a CVD method to grow MoS_2 monolayers directly on periodically poled lithium niobate where they have demonstrated that MoS_2 monolayer is preferentially deposited on Lithium niobate according the domain direction of the substrate [282]. Moreover, Preciado et al. fabricated a hybrid $MoS_2/LiNbO_3$ acousto-electric device where the acoustics waves generated by the LN substrate manipulated the carrier transport on the MoS_2 film [283].

Here, we propose an alternative protocol to grow MoS_2 microlines directly on the iron doped LN substrate by direct laser writing. DLW technique is more suitable for fabrication of photonic devices such as optical waveguides and modulators where various geometries and configurations can be realised without unnecessary complex lithographic steps. Additionally, this technique is more reliable compared with CVD approach that require a global heating at high temperature which might alters the physical properties of the LN crystal. However, iron doped LN substrate possess a low thermal conductivity and high optical absorption in the visible range, hence, the laser power should be selected carefully to avoid damaging the substrate. We therefore reduced our laser operating power to 100 mW with writing speed 1000 mm/min. The MoS_2 microlines have been grown on 24 mM concentration precursor film. Figure 6-12 illustrates the Raman spectra of MoS_2 on Fe: LN substrate with Raman active peaks at 381.6 and 407.7 cm^{-1} respectively.

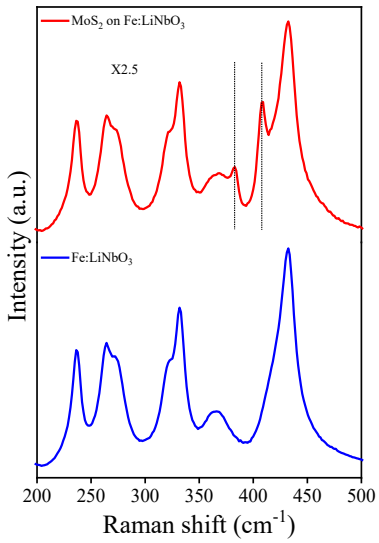

Figure 6-12: Raman peaks of MoS_2 on LN substrate indicated by dash lines. Labels of Raman modes for LN substrate can be found in references [284]–[286]. The Raman measurements have been performed by Adam H. Lewis.

6.6 The Developing Step: Effect of solvents

The developing step via organic solvents is very crucial in this work to create well-defined patterns of MS_2, thus, there is necessity to ensure this step does not modify chemical and physical properties of the MS_2 structure. Therefore, we utilized DMF and NMP solvents to develop the MoS_2 and WS_2 patterns respectively and remove untreated areas of the precursor films. It has been proved that DMF and NMP have high solvation for the $(NH_4)_2MoS_4$ and $(NH_4)_2WS_4$ respectively and because of that they are the initial solvents in the solvents recipe to prepare $(NH_4)_2MoS_4$ and $(NH_4)_2WS_4$ solutions. Additionally, both of them were also reported as solvents to disperse bulk MoS_2 and WS_2 for liquid exfoliation which means fortunately that they do not modify the MS_2 chemically [38].

To further prove that with our developing process, Raman spectra have been taken before and after the developing of MoS_2 pattern in DMF which shows no change in Raman peaks positions or FWHM in the deposited film as shown in Figure 6-13. This is a good indication that our developing step did not affect the quality of the deposited film. However, a trivial decrease in the intensity of the whole spectrum after developing can be easily noticed, that could be attributed to the removal of precursor residues which contains sulphur species that might enhanced the signal intensity of the Raman spectra prior to developing. Similar behaviour was observed when WS_2 pattern is developed by NMP solvent. Nevertheless, excessive developing time (more than 30 sec) of MoS_2 in DMF solvent leads to intercalation of the solvent between the MoS_2 microstructure and the substrate causing partial detachments of the MoS_2 structures due to dispersion by DMF as illustrated in Figure 6-14 [38]. Alternatively, using NMP as developer for MoS_2 and WS_2 is more preferable because no detachments for the patterns have been observed when it was used even with longer developing time.

However, the detachments of MoS_2 flakes and microlines allowed optical microscopy to further identify the few-layer nature of MoS_2 flakes where it is clearly show low optical contrast for single flake of the MoS_2 with the substrate. This optical contrast is increased and the colour is changed to be brighter when the flakes were folded over each other due to increase in the number of the layers (see Figure 6-14).

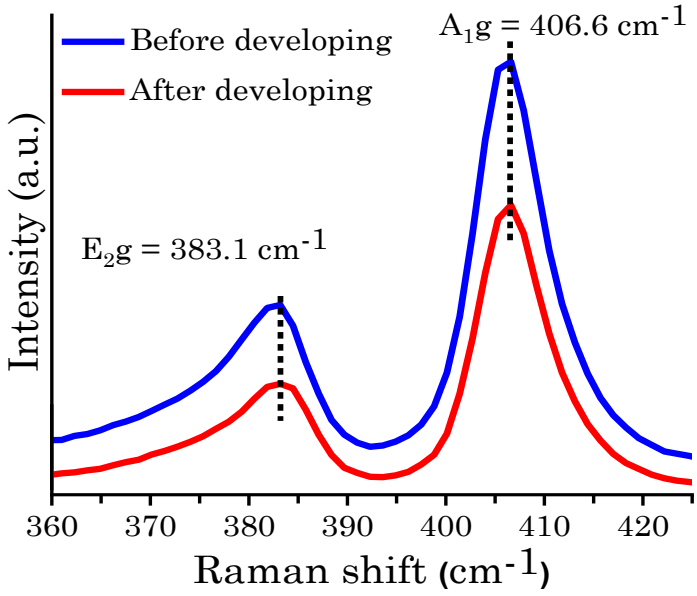

Figure 6-13: Effect of solvent on MoS_2 microlines Raman spectra. The Raman measurements have been performed by Adam H. Lewis.

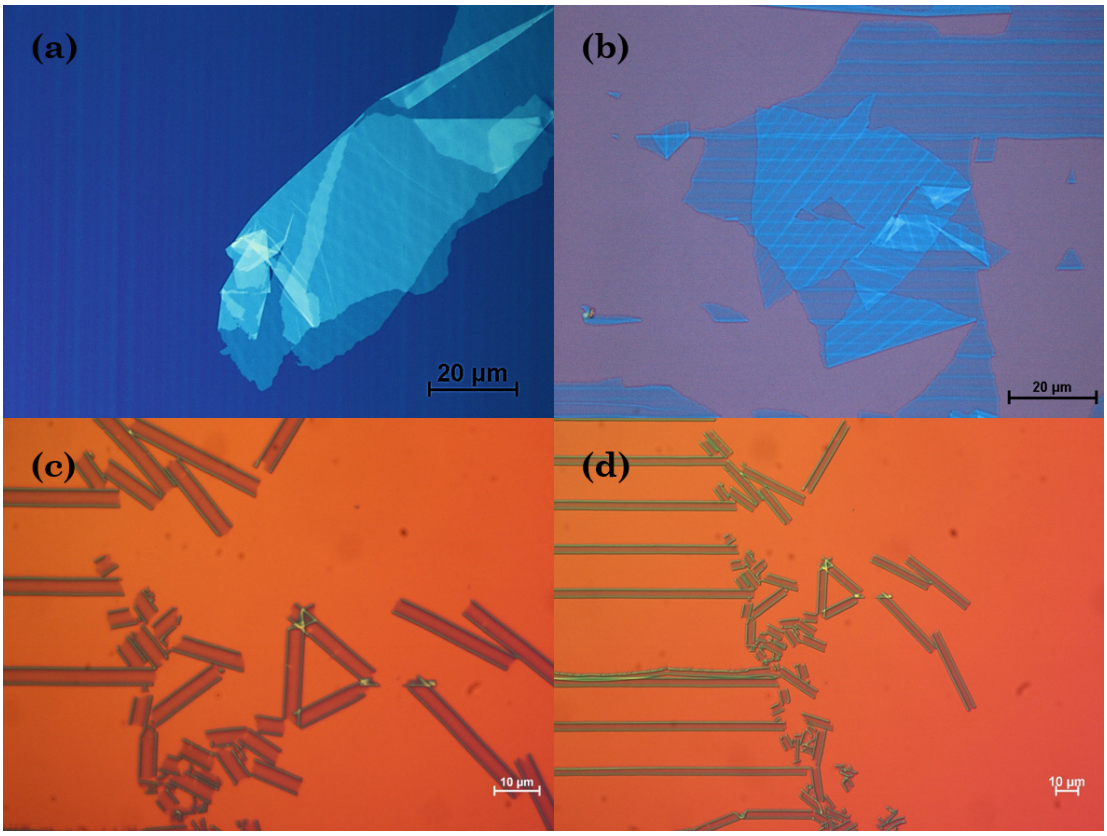

Figure 6-14: Effect of excessive development time in DMF solvent as a developer for MoS_2.

6.7 Stylus Profilometry measurements of MS_2 microlines

To have an estimation about the thickness of the MS_2 microstructure lines induced by laser writing, stylus profilometry has been conducted with different writing conditions for both MoS_2 and WS_2 microlines. Each value in the following bar charts represents the average thickness of four individual lines knowing that the thickness has been recorded at the centre of each line, while the error bars represent the standard deviation from the average thickness for each line.

6.7.1 MoS_2 lines

For MoS_2, two concentrations were used (24, 48) mM to form the precursor films, while two laser power 300 and 400 mW respectively with 10X objective. Another parameter was tested is the writing speed (100, 1000) mm/min. From Figure 6-15 it could be noticed that all lines thicknesses do not exceed 11 nm indicating that all are in multilayer-layer regime. The minimum thickness was bilayer which achieved with 24 mM, 400mW and 100 mm/min conditions. Importantly, the number of MoS_2 layers formed is highly dependent on laser fluence (energy density) rather than the intensity of the laser. This can be noticed clearly where the thickness of the MoS_2 films with slower writing speed is much lower compared with faster writing speed for the same laser intensity. It is worth to mention that MoS_2 microlines can be formed with 48mM precursor film and 200 mW power with 100 mm/min speed with average thickness 8.5±0.5 nm, however, the crystallinity of the MoS_2 produced under this condition is very low.

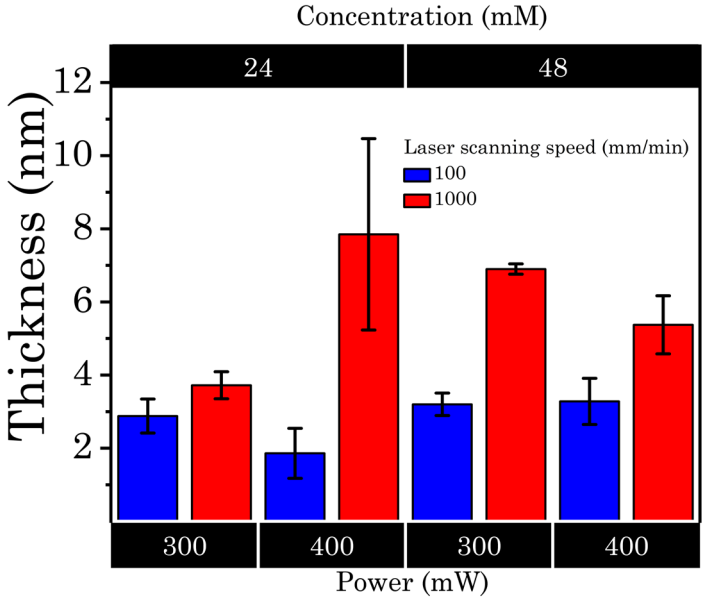

Figure 6-15: Graph represents the average thickness (measured by stylus profilometer) of MoS_2 microlines grown by different laser writing conditions. Error bars represent the standard deviation for four individual microlines. Note: 10x objective was used to focus the laser beam on the precursor film.

6.7.2 WS_2 lines

Similarly, WS_2 microlines have been produced using laser writing, however, the lower absorption of WS_2 precursor film compared with MoS_2 one (see Figure 6-2) necessarily needs higher laser intensity (power density). Therefore, 10X objective was replaced by 20X objective to ensure complete synthesis of WS_2 due to increase in laser intensity. Consequently, the produced WS_2 lines have narrower lateral dimensions (2.5~3.5 µm in width) with respect MoS_2 microlines (which are 4~5 µm in width).

Figure 6-16 depicts a bar chart for microlines produced by four precursor concentrations films with two different writing speed whilst the power was fixed to be 300 mW. Although the laser power ranging from 200-300 mW can form microstructures with almost identical thickness as shown in Figure 6-17 with 100 mM precursor films, 300 mW has been chosen to be fixed with all other precursor concentrations to improve the crystallinity of the WS_2.

Unlike MoS_2 where the writing speed has higher impact on the final thickness with respect to precursor film thickness, Figure 6-16 illustrates that the WS_2 microstructure final thickness is proportional with precursor concentrations while the speed of writing has much less impact of the final thickness. The concentrations from 50 mM and 100 mM readily deposit microlines within few-layer range (from single to five layers). Furthermore, the film with 50mM and 100 mm/min does not show any deposited WS_2 film at the centre of the line when profilometry was conducted possibly because total removal by laser power. Nevertheless, Raman peaks could be detected from the centre of the line which we believe is originated from the WS_2 deposited on the edges of the microlines.

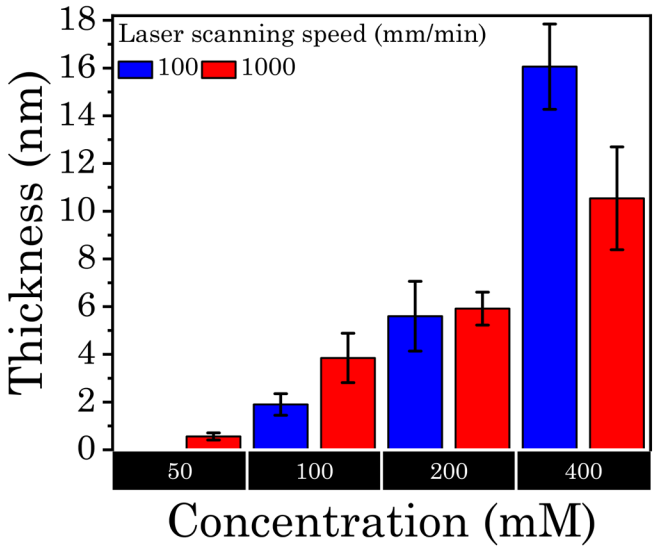

Figure 6-16: Graph represents the average thickness (measured by stylus profilometer) of WS_2 microlines grown by different precursor film concentrations and laser writing speeds. Error bars represent the standard deviation for five individual microlines. Note: the laser power was 300 mW and 20x objective was used to focus the laser beam on the precursor film.

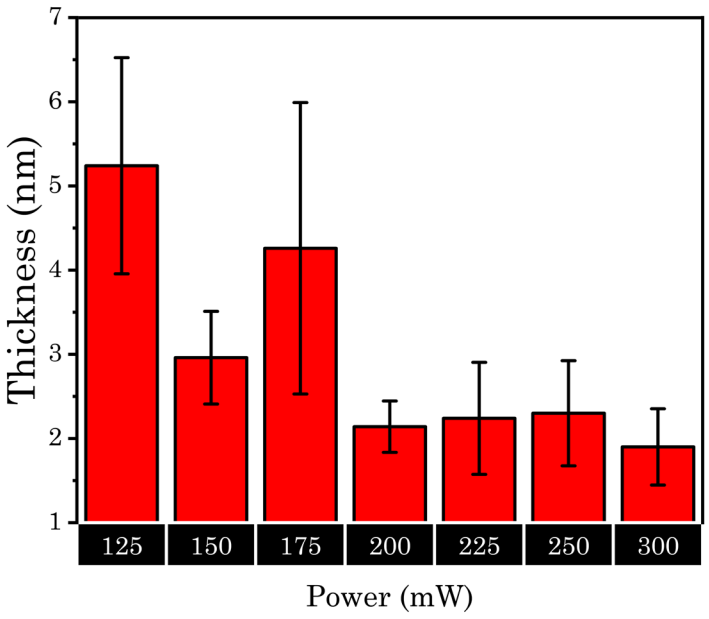

Figure 6-17: Graph represents the average thickness (measured by stylus profilometer) of WS_2 microlines grown by different laser powers on 100 mM concentration precursor films and 100 mm/min writing speed. Error bars represent the standard deviation for five individual microlines. Note: 20X objective was used for laser beam focusing.

6.8 Raman Assessment of MS_2 Microstructure

To probe the crystallinity and oxide content and to further confirm the stylus profilometry analysis of MS_2 microstructures, the same samples have been characterize by Raman system using 532 nm excitation wavelength as below:-

6.8.1 MoS_2

The in-plane (E_2g) Raman mode and out-of-plane (A_1g) Raman mode of MoS_2 for all laser writing conditions are pronounced, indicating complete formation of 2H-MoS_2 microstructure. Strikingly, there is a complete absence of molybdenum trioxide (MoO_3) Raman peaks which are expected to be located at 666 and 820 cm^{-1} respectively [287], [288] as can be noticed in Figure 6-18. This behaviour is similar to what was previously observed with laser thinning of MoS_2 at ambient conditions [250]. Additionally, the intensity of the MoS_2 E_2g and A_1g modes are notably higher for the MoS_2 microstructure with faster writing speed due to larger number of MoS_2 layers. However, the frequency deference between (A_1) and (E_2g) is more reliable technique to estimate the number of MoS_2 layers as it has been proved in the literature where smaller number indicates thinner MoS_2 films [21], [24], [150]. Roughly speaking, the Raman difference is 19 cm^{-1} is for monolayer, 21 cm^{-1} for bilayer, 23 cm^{-1} for trilayer, 24 cm^{-1} for 4 layers and 25 cm^{-1} for five layer to bulk [21], [24], [150]. Figure 6-19 depicts both Raman active modes which indicates a distinguishing reduction in the frequency difference in lower writing speeds because of thinner MoS_2 films formed.

Figure 6-20 shows a summary for Raman peak positions regarding all the growth parameters which clearly show that E_2g is shifted to higher frequencies when the fluence of the laser is higher (lower laser writing speed) while the A_1g is shifted to lower energies. Moreover, the frequency difference indictor has been plotted as shown in Figure 6-21. There is a significant change in frequency difference between the two writing speeds where all the lines at higher speed shows an average difference 25.5 which is for multilayer MoS_2 thickness. Meanwhile, the slower writing speed has a difference ranging from 21.4 cm^{-1} (bilayer MoS_2) to 22.6 cm^{-1} (3 ~4 layers of MoS_2). By comparing Figure 6-15 with Figure 6-21, it could be concluded that the Raman frequency indicator for thickness of MoS_2 confirms stylus profilometry results for MoS_2 microstructures thickness.

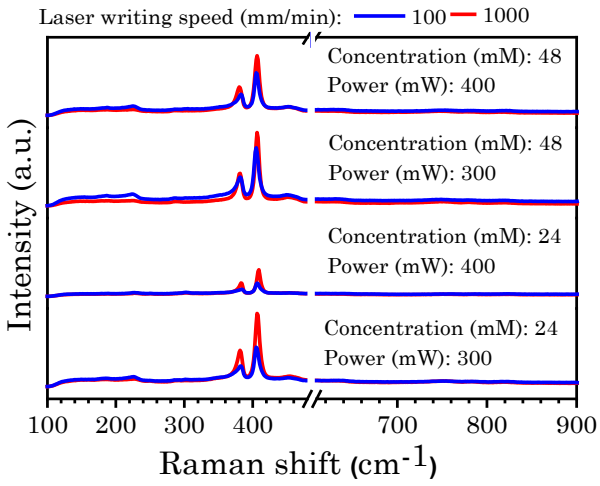

Figure 6-18: Extended Raman spectra of MoS_2 microlines ranging from 100 cm^{-1} to 900 cm^{-1} at different laser writing conditions. No MoO_3 peaks was detected where they normally located at 633 and 820 cm^{-1}. The Raman measurements have been performed by Adam H. Lewis.

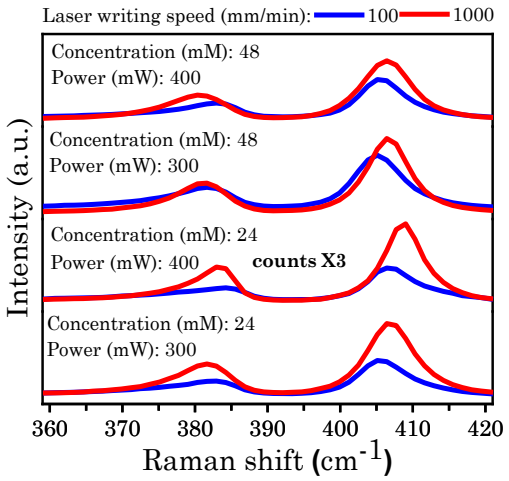

Figure 6-19: The same Raman spectra in Figure 6-18 which highlighting E_2g and A_1g Raman peaks of MoS_2 microlines at different laser writing conditions. The frequency difference between peaks tends to be smaller in lower laser writing speeds.

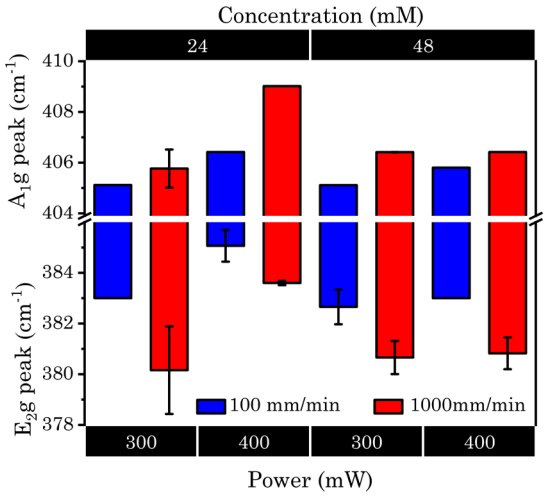

Figure 6-20:Graph represents the average Raman active modes positions (E_2g and A_1g) of MoS_2 microlines as function of different writing conditions. Error bars represents the standard deviation for four individual microlines, note that when the error bars are absent means the four tracks have identical position.

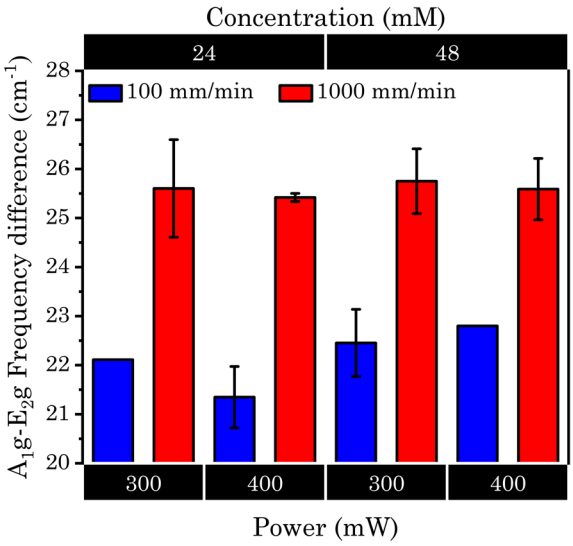

Figure 6-21:Graph represents the average Raman frequency difference of MoS_2 microlines with respect to different writing conditions. Error bars represents the standard deviation for four individual microlines, note that when the error bars are absent means the four tracks have identical difference.

Finally, Lorentzian curve fitting has been performed in order to evaluate the full width half maximum (FWHM) of the MoS_2 Raman active peaks. The FWHM of the peaks can provide valuable information about the crystallinity of the MoS_2 microstructures where narrower width of the peaks represents higher crystallinity of the MoS_2 films [148], [150]. As Figure 6-22 depicts, for all growth conditions, all A_1g peaks are narrower compared to their E_2g counterparts. Moreover, the average FWHM of E_2g peaks at 48 mM films is smaller by at least 1 cm^{-1} with respect to 24 mM films indicating that the 48 mM films can produce MoS_2 with higher crystallinity. This could be attributed to the fact that 48 mM films have higher absorptivity to

the laser wavelength and therefore the temperature profile of the laser is higher enough to improve the crystallinity of the MoS_2 film.

However, there is an anomalous behaviour with 24 mM precursor film that has been deposited with 400 mW laser power with 100 mm/min speed. The average FWHM for both peaks is almost identical and is the smallest compared with other conditions (~6 cm^{-1}) as shown in Figure 6-22. Also, the A_1g peak is shifted to much higher energies compared to all other conditions (409 cm^{-1}) as shown Figure 6-20. It is not fully understood how the growth of MoS_2 at these conditions has this unique feature in terms of crystallinity and A_1g peak shifting, however, styles profilometry revealed that the MoS_2 film at the centre of this microstructure has a pyramid-like profile rather than inverse Gaussian shape which probably increase the strain at the centre of the microstructure leading to narrower width and blue shift for the A_1g peak.

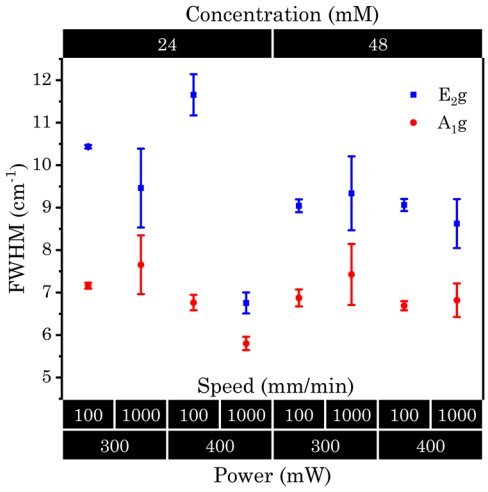

Figure 6-22:The average FWHM of E_2g and A_1g peaks at different laser writing conditions. Error bars represents the standard deviation for four individual microlines, note that when the error bars are absent means the four measurements are identical.

6.8.2 WS_2

Like MoS_2, Raman spectroscopy has been performed to characterise WS_2 microlines at various growth conditions as depicted in Figure 6-23. Similar to what has been observed with MoS_2 lines, the extended Raman spectra did not detect WO_3 Raman active signals that normally found around 710 cm^{-1} and 810 cm^{-1} [289]–[291]. Moreover, the out-of-plane Raman mode A_1g of WS_2 was pronounced for all the growth conditions associated with the convolution peak of in-plane Raman mode E_2g WS_2 and longitudinal acoustic mode 2LA (M). The convolution peak is raised due to resonance of WS_2 direct bandgap with the Raman wavelength (532 nm).

Furthermore, the intensity of the Raman active peaks at lower writing speed is dominating the peaks intensity at higher writing speed for all the precursor concentrations unlike to what has been noticed with MoS_2 structures (see Figure 6-18).

The only exception was at 200 mM precursor films where both writing speeds have Raman peaks that approximately at same height (see Figure 6-24).The prominence of Raman peaks can considered as a sign for quality improvement of WS_2 films. However, to systematically analyse the thickness and the crystallinity of WS_2 microstructure via Raman data, Lorentzian curve fitting has been applied to deconvolute the Raman modes with the same methodology that previously illustrated in section 5.5.2. Figure 6-25 shows an example for deconvolution of the WS_2 first and second order peaks using Lorentzian function which has been applied to all WS_2 Raman data.

It has been reported that if the intensity ratio of 2LA(M) to A_1g is higher than 0.5 then the WS_2 film is in the few-layer regime and it reaches the maximum value at the monolayer to be ≥ 2 [25], [79]. Figure 6-26 shows the average of the intensity ratio for different concentrations of the precursor films and writing speeds. The maximum average value is 1.9 at 50 mM precursor film concentration with 1000 mm/min writing speed, which corresponding to monolayer. By comparing the stylus profilometry chart for WS_2 in Figure 6-16 with intensity Ratio of 2LA (M) and A_1g chart in Figure 6-26, it is readily noticeable that the lower WS_2 thickness at 50 mM concentrations for both speeds and 100 mM films at 100 mm/min speed have the highest intensity ratio and few-layer thicknesses. It is worth to mentioned that the Raman peaks signal that collected for the WS_2 microlines at 50 mM and 100 mm/min shows an average intensity ratio about 1.6 even though we could not measure any film at the centre using profilometry. These peaks are originated from the WS_2 films around the centre which has thickness around mono-to bilayer. However, we did not observe any correlation between energy difference between A_1g and E_2g and the thickness of the films as in the MoS_2 case (see Figure 6-27), possibly due to lower sensitivity of tungsten atoms for vibrational modes changes [20].

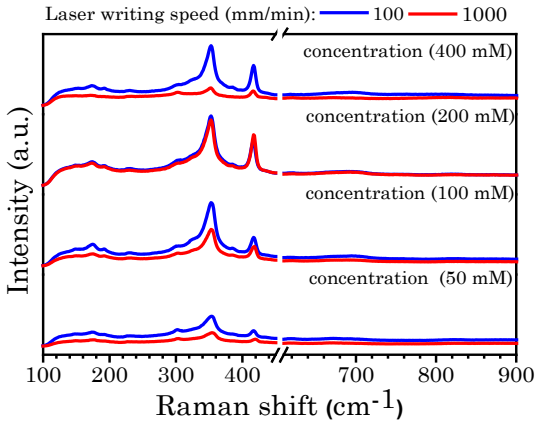

Figure 6-23: Extended Raman spectra of WS_2 microlines ranging from 100 cm-1 to 900 cm-1 at different precursor film concentrations and writing speeds knowing that the power of the laser was fixed to be 300 mW with 20X objective. No WO_3 peaks was detected where they normally located at 710 cm^{-1} and 820 cm^{-1}. The Raman measurements have been performed by Adam H. Lewis.

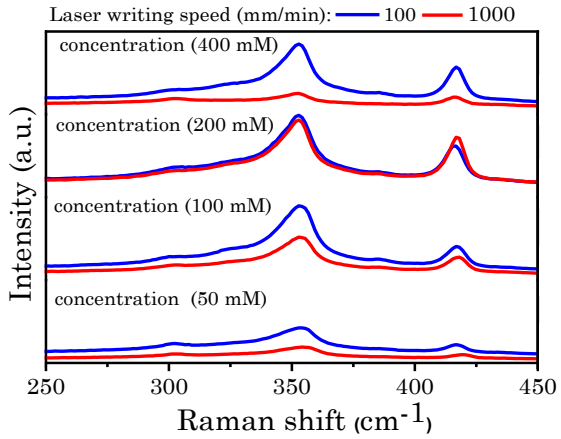

Figure 6-24: The same Raman spectra in Figure 6-23 which highlighting convolution peak of $E_{2}g$ with 2LA (M) and the out-of-plane $A_{1}g$ Raman peaks of WS_2 microlines at different laser writing conditions.

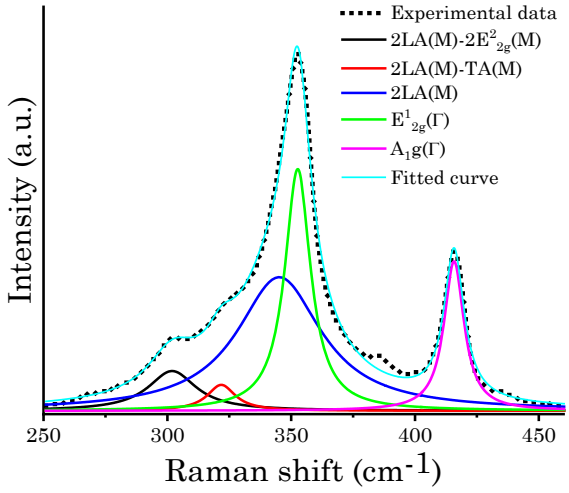

Figure 6-25: Lorentzian curve fitting to deconvolute the WS_2 Raman active peaks.

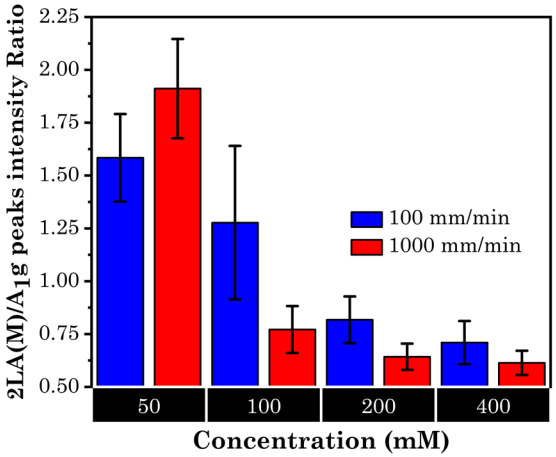

Figure 6-26: The average of Raman peaks intensity ratio of the acoustic mode and the out-of-plane mode for WS_2 microlines. The error bars represent the standard deviation for five individual microlines.

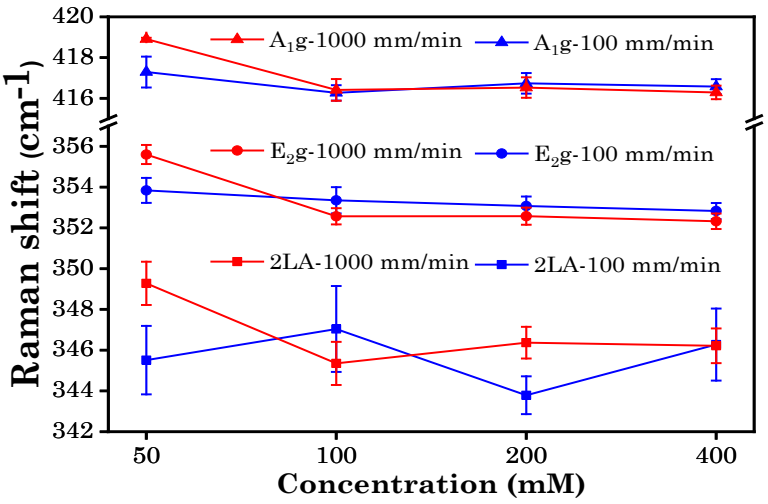

Figure 6-27: The average of 2LA, E_2g and A_1g peak positions as a function of concentration and speed. The error bars represent the standard deviation for five individual microlines.

FWHM of E_2g and A_1g has been analysed to probe the crystallinity changes at different writing conditions as shown in Figure 6-28 and Figure 6-29. There was a clear reduction in FWHM of both peaks as a function of concentration. These findings could be interpreted by higher absorption of laser energy as the precursor film thickness increase where the absorbed laser energy converted to thermal energy which significantly affect the crystallinity of WS_2 films. Comparing the FWHM E_2g and A_1g of WS_2 films grown by pulsed laser deposition (PLD) [81] and laser-thinned CVD-WS_2 [254], our laser written WS_2 lines exhibits lower FWHM for both peaks indicating an improvement in crystallinity when our approach is applied.

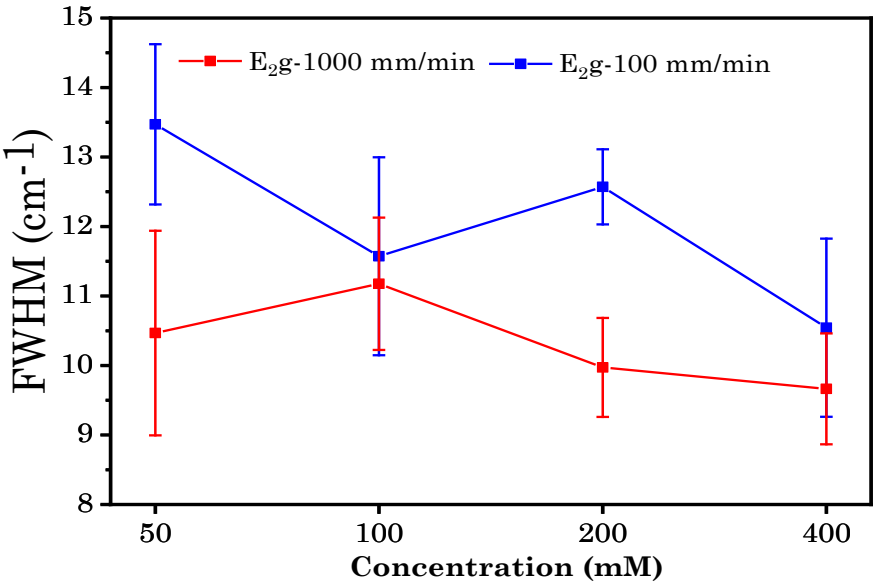

Figure 6-28: The average of FWHM of E_2g peak at different concentrations and writing speed. The error bars represent the standard deviation for five individual microlines.

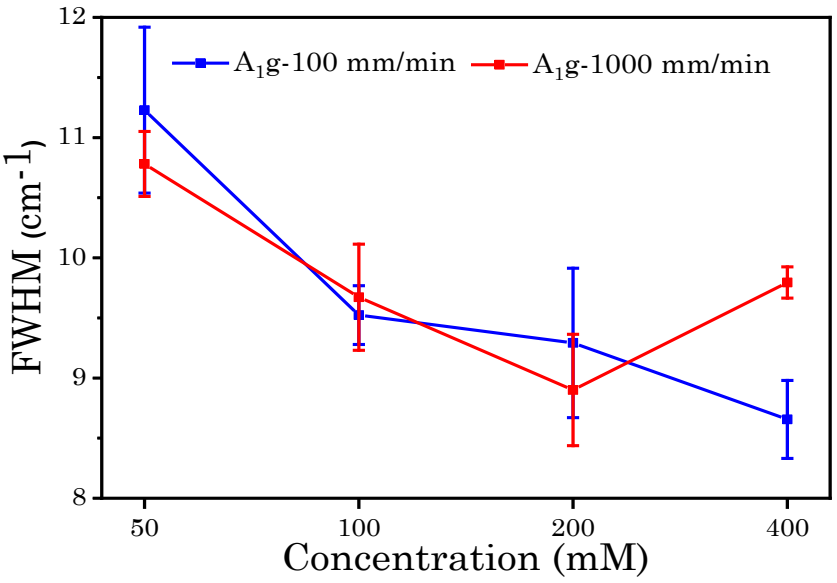

Figure 6-29: The average of FWHM of A_1g peak at different concentrations and writing speed. The error bars represent the standard deviation for five individual microlines.

6.9 Photoluminescence Spectroscopy

MoS_2 and WS_2 bandgaps value and type can be modulated according to molecular layers number [9], [10], [32], [33], Hence, PL spectroscopy could be a powerful characterisation tool to probe the thickness of the laser written microstructure for both materials. Therefore, we used the same Raman laser system with excitation wavelength 532 nm, 22 mW and 50X objective to study the PL for both MoS_2 and WS_2 microstructures. Unfortunately, we did not observe any PL signal with MoS_2 microstructure. However, WS_2 microstructures show a clear PL spectra for all the precursor concentrations with peaks that blue shifted towards 2 eV (the energy of the direct band gap of WS_2 monolayers [109], [292], [293]) when the concentration is reduced. The reason behind the relatively strong PL signals of the WS_2 while there were no detectable PL spectra for MoS_2 is the high quantum yield of WS_2 compared to MoS_2 [33], [130], [293].

At high concentrations 400 and 200 mM, the peak positions for 100 mm/min speed were at 1.984 and 1.987 eV respectively whereas at 1000 mm/min the peaks are shifted to higher energies to be 1.99 and 1.992 eV respectively. Similar PL peak positions has been reported earlier when liquid exfoliated WS_2 flakes were laser etched to few layer thickness [243]. At 100 mM concentration, the trend of the laser writing speed was inversed where the peak at 100 mm/min is located at 2 eV which is assigned to (mono-bilayer) and shifted to lower energy at 1000 mm/min to be at 1.992 eV. Finally, at the lowest concentration 50 mM, the PL peak is located also at 2 eV for 100 mm/min speed while we could not find any peak located at this region at 1000 mm/min. These results highlight the crucial impact of the initial precursor concentrations compared to laser writing speed on the final thickness of WS_2 microstructure formation. Moreover, the PL analysis seems to be in agreement with Raman and profilometry analysis.

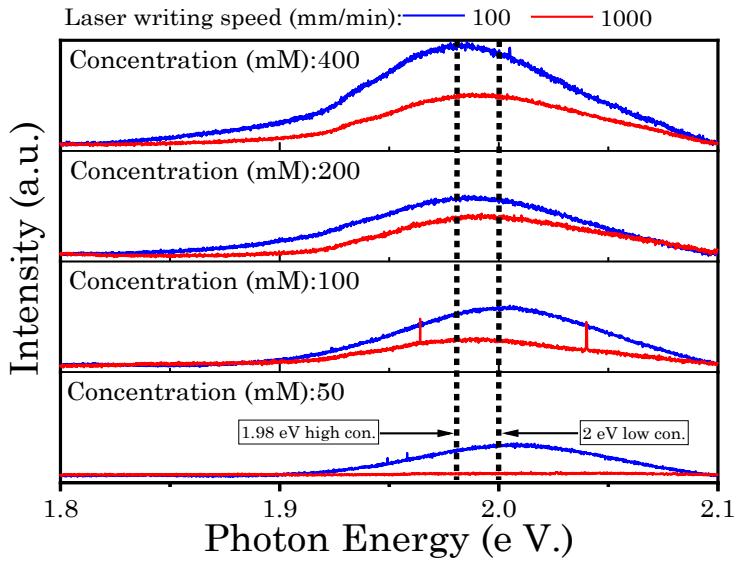

Figure 6-30:WS_2 PL peaks at different laser writing conditions. The PL measurements have been performed by Adam H. Lewis.

6.10 X-Ray Photoelectron Spectroscopy (XPS) of MS_2

6.10.1 The necessity for XPS spectroscopy

The earliest study that has utilized laser energy to thin MoS_2 flakes at ambient conditions confirmed the absence of oxide by the absence of its Raman peaks in the extended Raman spectra of MoS_2 [250]. However, it was reported that atmospheric particles are adsorbed by MoS_2 when the flakes are laser treated under ambient conditions [261]. Most importantly, the density of these adsorbents is increased according to the increasing of the MoS_2 flakes thickness, the laser power and exposure time [261]. However, this study did not reveal the chemical nature of these adsorbents which is a crucial parameter to understand the laser-2D TMDC interaction and chemistry [261]. Therefore, Alrasheed et al. conducted XPS spectroscopy for laser treated MoS_2 flakes and their XPS data analysis demonstrated that MoS_2 flakes tend to be oxidized at high laser power in ambient conditions [265]. Similar observations have been noticed for XPS data of laser-thinned CVD-MoS_2 films [251].

For WS_2, the oxidation of laser thinned liquid exfoliated WS_2 flakes seems to be more obvious where the WO_3 Raman peaks are detectable for thick WS_2 flakes while WS_2 thinner flakes did not show WO_3 raman response indicating lower oxide content [243]. Unfortunately, this study did not conduct XPS spectroscopy to study the effect of the flake thickness on the oxide content for laser post-treated WS_2 flakes. However, the correlation between the degree of oxidation of laser thinned WS_2 flakes and the thickness of these WS_2 flakes [243] is identical to what was previously recorded with laser-induced particles of MoS_2 flakes which were mainly oxide particles [261],[265]. Hence, we could draw a conclusion that the initial thickness of MS_2 flakes plays an important role on the level of oxidation of laser treated MS_2 flakes.

Furthermore, the XPS analysis of laser post-treated CVD-WS_2 films at ambient conditions, particularly the WS_2-CVD, show that the WS_2 contains a significant amount of oxide after laser treatment [253], [263], [264], [273] . The oxide peaks tends to dominate the WS_2 peaks in the XPS spectra even though Raman spectra did not detect /or detect a small oxide signal compared to the WS_2 peaks [253], [263], [264], [273].

Analogously to all previously mentioned papers in this section, our Raman spectra confirmed the formation of MS_2 microstructures and did not detect any oxide peaks for both MoS_2 and WS_2. However, our direct laser writing protocol of MS_2 was performed at ambient conditions which means relying on Raman data only cannot give a complete picture of the MS_2 microstructure stoichiometry and the effects of different growth conditions on it. At this point, XPS spectroscopy becomes an essential characterisation technique to study the composition of these MS_2 microstructures.

Therefore, two specimens of MoS_2 and four specimens of WS_2 with 1 mm^2 size were deposited by raster laser scanning to be used for XPS spectroscopy in order to study the influence of the initial precursor thickness and laser parameters on the stoichiometry of MS_2. The former MoS_2 sample with 24 mM precursor film concentration deposited by 400 mW laser power and 100 mm/min writing speed while the latter sample was 48 mM precursor film with 300 mW laser power and 100 mm/min speed. Moreover, four WS_2 specimens also deposited by raster scanning has been tested with 50, 100, 200 and 400 mM precursor films concentrations with 300 mW power and 100 mm/min speed. Below is the XPS analysis of these data:-

6.10.2 XPS Data of MoS_2 Film Prepared by Laser Raster Scanning

Prior to XPS peaks deconvolution, the carbon peak in the C1s core level which is located at 284.8 eV was used to calibrate the XPS spectra for 24 mM and 48 mM films. For both films, two core levels have been studied, the first one is Mo core level while the latter one is S core level. For Mo core level, both 24 mM and 48 mM films exhibit three doublets and two singlets peaks while for S core level, only one doublet was pronounced as illustrated in Figure 6-31.

In Mo core, the first doublets are labelled as $Mo^{(4+)}3\ d_{5/2}$ and $Mo^{(4+)}3\ d_{3/2}$, this doublet is assigned to MoS_2 and it is located at 228.64 eV and 231.77 eV respectively for 24 mM film while for 48 mM is shifted to higher energies at 229.77 eV and 232.92 eV respectively. Similar trend has been observed in the S core level where the only one doublet labelled as $S^{(2-)}\ P_{3/2}$ and $S^{(2-)}\ P_{1/2}$ that corresponds to MoS_2 is located at 161.38 eV and 162.56 eV respectively for 24 mM film which is shifted to be at 162.49 eV and 163.69 eV respectively for 48 mM film.

This blue shift for both doublets at 48 mM film is attributed to higher temperature profile created by additional laser energy that absorbed due to thicker $(NH_4)_2MoS_4$ film which decompose to more crystalline MoS_2 films compared with 24 mM film where the 48 mM peaks are identical with MoS_2 deposited at 900°C [251]. Moreover, it was reported that MoS_2 XPS

doublets at Mo and S cores levels tends to shift to low frequencies when the temperature for thermal decomposition of $(NH_4)_2MoS_4$ is low which consequently leads to form more amorphous MoS_2 films [294]. This hypothesis is also supported by the analysis of FWHM of Raman peaks of MoS_2 (see Figure 6-22) where the films with higher concentrations have lower FWHM indicating higher crystallinity, i.e., they are annealed at higher temperature. Apparently, both MoS_2 films are substoichiometric as the S/ Mo atomic ratio was revealed to be 1.73 for 24 mM and 1.77 for 48 mM. However, it seems that MoS_2 prepared by thermolysis of $(NH_4)_2MoS_4$ is always sulphur deficient if there is no extra source of sulphur provided where the maximum S/ Mo atomic ratio can be obtained is 1.8 which is comparable to our findings [294].

As it was expected, the XPS spectra readily detected the oxide contents that our films possessed which designated by the second ($Mo^{(6+)}$) and third ($Mo^{(5+)}$) doublets in the Mo core. However, as these oxide species were not detected by Raman spectroscopy, this indicates the oxide species are substitution for sulphur vacancies in the MoS_2 lattice rather than individual oxide layers [72]. The second doublet is labelled as $Mo^{(6+)}3\ d_{5/2}$ and $Mo^{(6+)}3\ d_{3/2}$, this doublet is assigned to MoO_3 formation and it is located at 232 eV and 235 eV respectively for 24 mM film whereas for 48 mM films, the peaks are found at 232.53 eV and 235.88 eV respectively. The last doublet is $Mo^{(5+)}3\ d_{5/2}$ and $Mo^{(5+)}3\ d_{3/2}$ which corresponds to MoS_xO_y formation, the peaks positions for this doublet are 229.44 eV and 232.55 eV respectively for 24 mM film while 230.57 eV and 233.82 eV are the peaks for 48 mM film.

It can be noticed from Figure 6-31 that the intensity of oxide peaks is increased proportionally with respect to the concentration of the precursor films due to higher oxidation level of MoS_2. This behaviour seems to be in analogy to the increase of the oxidation level of laser thinning of thick WS_2 liquid exfoliated flakes compared with thinner WS_2 flakes due to higher temperature profile and slower cooling rate [243]. It is also similar to what was observed with MoS_2 thick flakes where the density of the adsorbents is increased [261],[265]. To analyse this oxide content quantitatively, we calculate the oxide atomic ratio defined as $\{(Mo^{(5+)}+Mo^{(6+)})/(Mo^{(4+)}+Mo^{(5+)}+Mo^{(6+)})\}$ for both films which is 25.7% for 24 mM and 38% for 48 mM film. Fortunately, these oxide content is comparable with what was reported earlier for laser thinning of CVD MoS_2 and even lower for 24 mM film [251].

To sum up, XPS data show that MoS_2 films formed by our direct laser method have a high quality composition and the oxide doping can be controlled via tuning the concentration of the precursor film. Moreover, this method shows superiority in terms of quality of the MoS_2 and the simplicity with respect to other laser treatments of MoS_2 approaches such as laser crystallisation of amorphous sputtered MoS_2 [72], [74] ; laser thinning of CVD MoS_2 [251]. Finally, it is worth mentioning that an oxysulphide singlet with very low intensity is accompanied with $S^{(2-)}$ singlet which both are pronounced at 226.96 eV and 225.81 eV respectively for 24 mM film meanwhile 228.1 eV and 226.93 eV are the peak locations for 48 mM films in Mo core.

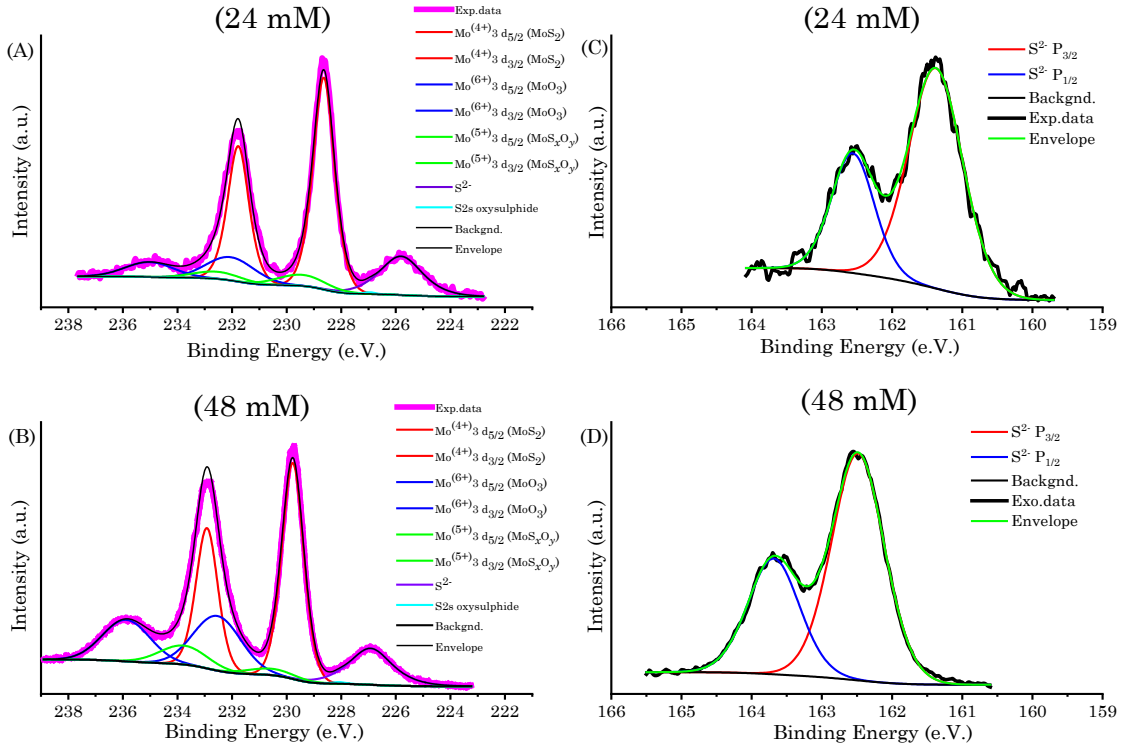

Figure 6-31: XPS spectra for MoS_2 where (A) 24 mM & (B) 48 mM Mo core level while (C) & (D) are S core level for the 24 mM and 48 mM films respectively. The XPS measurements and peaks deconvolution have been performed by Nikolaos Aspiotis.

6.10.3 XPS Data of WS_2 Film Prepared by Laser Raster Scanning

Prior to deconvolution of XPS data for WS_2, the carbon peak C1s at 284.8 eV was used as a reference point to calibrate the XPS spectra. To investigate the composition of WS_2, two core levels were studied the former one is W 4 and the latter one is S core level. For W core level, two doublets are denoted in addition to one singlet for all concentrations, meanwhile one doublet is pronounced in the sulphur core level. Figure 6-32 and Figure 6-33 depict both cores respectively for all the concentrations that has been tested.

The first doublet $W^{(4+)}\,f_{7/2}$ and $W^{(4+)}\,f_{5/2}$ in W core level represents the formation of WS_2, the peaks' positions for this doublet is identical to what was reported previously for WS_2 flakes [295] which are at: 32.25 eV and 34.25 eV for 50 mM film, 32.5 eV and 34.5 eV for 100 mM, 32.23 eV and 34 eV for 200 mM and 32.5 eV and 34.5 eV for 400 mM film. Simultaneously, in S core level, the doublet ($S^{2-}\,P_{3/2}$ and $S^{2-}\,P_{1/2}$) that corresponds to WS_2 is located at: 161.77 eV and 163 eV for 50 mM, 162.16 eV and 163.45 eV for 100 mM, 161.8 eV and 163 eV for 200 mM, and 161.6 eV and 162.8 for 400 mM film. Consequently, the S/W atomic ratio has been calculated to be: 1.84 for 50 mM film, 1.83 for 100 mM film, 2.26 for 200 mM film and finally 1.31 for 400 mM film. Although the stoichiometry for the first two films is slightly sulphur deficient while the third film is over sulphurized, they still in the acceptable composition margin of WS_2. However, we

anticipate that further optimisation for the laser writing conditions, in particular, for the precursor film concentrations could results the desired S/W atomic ratio of 2.

The second doublet $W^{(6+)}\,f_{7/2}$ and $W^{(6+)}\,f_{5/2}$ in W core level corresponds to WO_3 formation, the binding energies for this doublet is identical to what was reported previously for WO_3 [296], [297] which are at: 35.35 eV and 37.46 eV for 50 mM film, 35.8 eV and 37.8 eV for 100 mM film, 35.5 eV and 37.6 eV for 200 mM film, and 35.5 eV and 37.6 eV for 400 mM film. Moreover, the intensity of second doublet peaks in W core level ($W^{(6+)}\,f_{7/2}$ and $W^{(6+)}\,f_{5/2}$) which is assigned to the WO_3 formation, significantly overwhelmed the first doublet of WS_2 indicating that the oxide content is much higher compared to MoS_2 films. However, the oxidisation level is proportional to the precursor film thickness as in the MoS_2 case. Nevertheless, as Raman spectroscopy did not reveal any vibrational modes for the WO_3 (see Figure 6-23) indicating that films formed are oxidised WS_2 rather than two individual layers of WS_2 and WO_3 similar to what was formed in MoS_2 films but with higher level of oxidation for WS_2 films. Compared to the previous reports that conducted XPS analysis for laser treated WS_2, our laser writing of WS_2 microstructures exhibit a comparable amount of oxide [253], [263], [264], [273].

6.11 Discussion of MS_2 characterisation Results

In section 6.7, the analysis of stylus profilometry data highlighted the impact of the initial thickness of the precursor film on the final number of layers of MS_2 microstructure especially with WS_2 case. Additionally, Raman data analysis in section 6.8 confirmed these findings but also proved that the crystallinity of the MS_2 microstructures is improved by increasing the precursor film concentrations which consequently increased the thickness of these microstructures. However, when XPS spectroscopy has been performed and analysed for MS_2 films in section 6.10, the oxidation level of MS_2 is increased as a response to higher precursor concentration films. In other words, using higher concentrations for the precursor films increase the number of MS_2 layers and crystallinity of MS_2 but also increase the oxide content of these films. Therefore, there is a "trade-off" between the smaller number of layers for the MS_2 structure which possess lower crystallinity and oxide content from a side, and thicker MS_2 structures with better crystallinity and higher oxide content. In addition to precursor film thickness, the laser parameters (intensity and speed of writing) have an influence on the final MS_2 thickness and crystallinity but further XPS spectroscopy investigations is needed for these both parameters to understand their effect on the MS_2 composition.

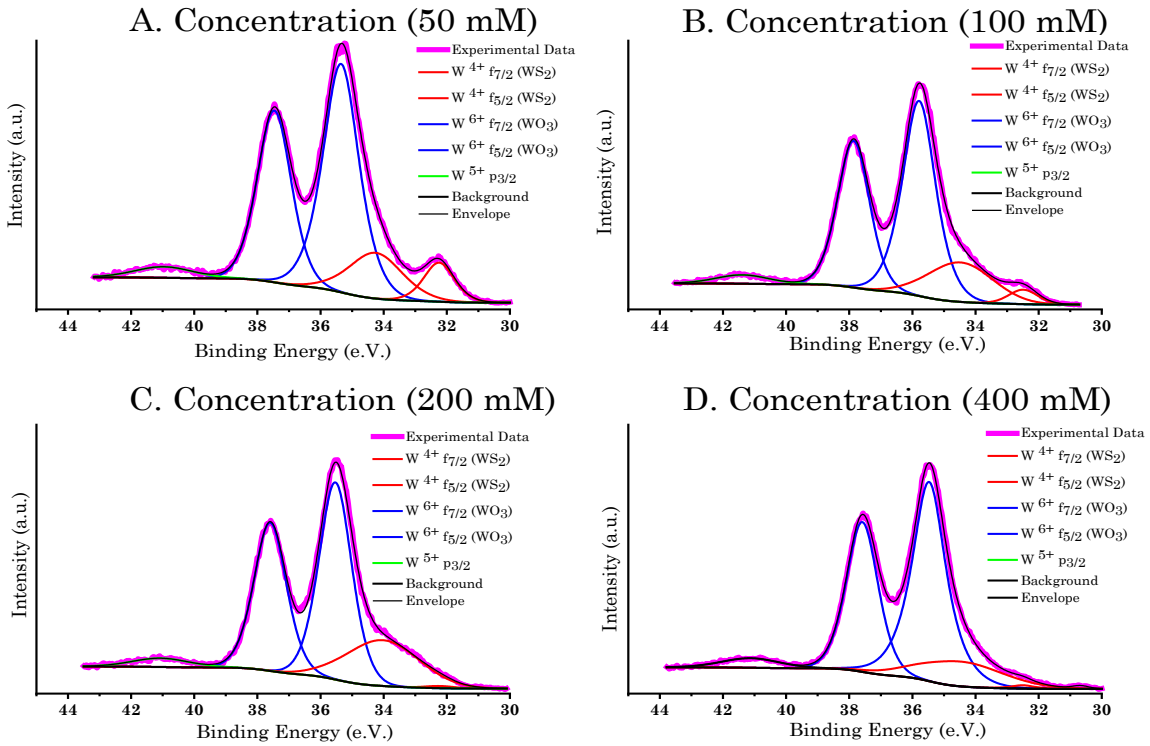

Figure 6-32: W 4 core level for XPS spectra of WS2 for (A) 50 mM, (B) 100 mM, (C) 200 mM and (D) 400 mM.

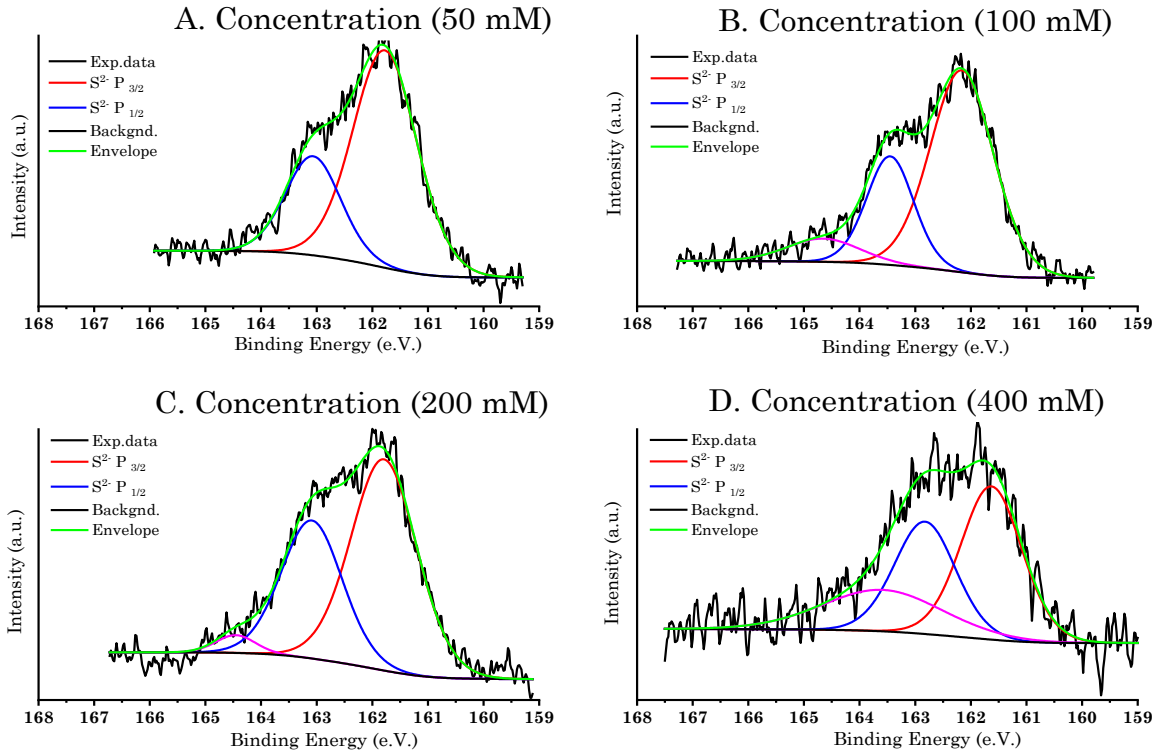

Figure 6-33: S $^{2-}$ core level for XPS spectra of WS2 for (A) 50 mM, (B) 100 mM, (C) 200 mM and (D) 400 mM. The XPS measurements and peaks deconvolution in both figures have been performed by Ioannis Zeimpekis.

6.12 Direct Laser Writing of MS_2 Channels for FET Applications

In order to evaluate the electronic properties of MS_2 deposited by DLW, we fabricated four FET devices with back gate and ionic-gel top gate configurations for both MoS_2 and WS_2 films. The table below illustrates the devices specifications:

Table 6-5: FET devices specifications.

Parameter	MoS_2-Back gate	MoS_2-Ionic gate	WS_2- Back gate	MoS_2-Ionic gate
Concentration (mM)	48	48	100	100
Power (mW)	300	300	250	250
Speed (mm/min)	100	100	100	100
Spacing (µm)	2	2	2	2
Length of channel (µm)	100	10	10	10
Width of channel (µm)	200	250	250	250
In/Au thickness (nm)	10/100	10/50	10/100	10/50

Note that the metal contacts defined the channel length while the channel width was defined by the raster scanning of the laser to form the MS_2. Furthermore, metal contacts were patterned by standard photolithography and deposited by subsequent e-beam evaporation. For photolithography, S1805 were spun coated over the samples for 1 min at 5000 rpm and soft baked for 1 min at 110°C. After UV exposure, the samples were developed in MF-319 developer for 5-6 sec followed by rinsing in de-ionized water. It is worth to mention that S1805 were used to avoid longer developing time in MF-319 which apparently start damaging the MoS_2 films when the developing time exceed 10-20 sec.

Moreover, the ionic-gel gate has been prepared by mixing Lithium perchlorate ($LiClO_4$) and polyethylene oxide (PEO) with mass ratio (1g to 0.12g) and dissolving them in 40 mL of methanol. The solution was heated up at 50°C until it became viscous then drop casted over the FET devices and left for one hour to dry and solidified before the measurements were undertaken. The ionic gel recipe and preparation has been adopted with trivial modifications on the procedure from reference [298].

The output characteristics of back gate MoS_2 and WS_2 FETs are shown in Figure 6-34. Both of the devices reach the minimum output current at zero drain-source voltage regardless of the voltage applied to the gate indicating low leakage gate current. The output characteristics of MoS_2 FET device has a nonlinear Schottky behaviour while the WS_2 device possess an ohmic linear resistance. These behaviours are identical to devices recorded in Chapter 4 and Chapter 5 where MoS_2 films formed Schottky junction with indium while our large area WS_2 FET shows an ohmic behaviour with indium.

Ideally, to have an ohmic contact between the semiconductor channel and the metal contacts, the difference between the work function of the metal contacts and the electron affinity of the semiconductor (Schottky barrier) should be zero or negative value (see Equation 4-1 in page 64). The work function of indium is known to be (4.12 eV) [206]–[209] but the electron affinity for each one of them (MoS_2 and WS_2) has different values in the literature . In some reports, they have equal values (4 eV) for the electron affinity for both MoS_2 [158], [210], [211], [221], [299], [300] and WS_2 [301], [302]. According to this scenario, both of them will form Schottky contacts with the identical small barrier height (0.12 eV) and we should expect a nonlinear S/D current behaviour with same ON-current outputs, which is not the case as we can see in Figure 6-34. Alternatively, previous theoretical predictions have calculated the electron affinity of MoS_2 with a range from 3.75 eV to 4.3 eV while for WS_2 is between 3.5 eV to 4.1 eV and for WSe_2 3.2 eV to 3.7 eV [209], [303]–[308]. In all these reports, the electron affinity of WS_2 and WSe_2 is considerably lower than MoS_2 and therefore should forms higher Schottky barrier that should suppressed significantly the S/D On-current in WS_2 compared with MoS_2 channel. Again, this this not what was observed for our devices (see Figure 6-34).

In contrast, our WS_2 device possess ohmic linear S/D current-voltage relationship with low S/D voltage whereas MoS_2 contact-channel junction is clearly Schottky in nature with much higher working voltage (even though the difference in aspect ratio (L/W) of both channels is considered). Furthermore, our results in Chapter 4 and Chapter 5 support our findings here with the large area MSM MoS_2 device formed back to back Schottky diodes with indium while the WS_2 FET with indium electrodes has a linear output characteristics. Therefore, we speculate a significant lowering in the experimental Schottky barrier height occur when tungsten dichalcogenides (WS_2 and WSe_2) formed a junction with indium metal leading to better ohmic contacts that enhances the electron injection through metal-semiconductor junction. In other word, indium creates contacts with WS2 and WSe_2 with more ohmic linear I-V characteristics and lower resistance compared to MoS_2. In addition to our observation, this hypothesis is supported by the previous studies where the WS_2 films shows lower contact resistance compared to MoS_2 [221]. Moreover, On-current density of WSe_2 backgated FET [309] is superior compared to MoS_2 backgated FET when indium used as contacts for both of them [221]. This contradiction between the expected (theoretical) and experimental indium contacts I-V characteristics with MoS_2 and WS_2 needs to be investigated more thoroughly via TLM Transmission line measurement to have better understanding about indium-MS_2 junction formation.

Moreover, transfer characteristics (S/D current versus gate voltage) for back gated MoS_2 and WS_2 FETs are illustrated in Figure 6-35. Both devices are n-type with linear electron field effect mobility for MoS_2 device is $5.5x10^{-5}$ $cm^2/V.s$ and $1.1x10^{-4}$ $cm^2/V.s$ for WS_2 while the on-off ratio for both devices is ~3 and ~1.2 respectively. These values are comparable with MoS_2 backgated FET devices fabricated using single source precursor (ammonium tetrathiomolybdate) without additional sulphurisation [148], [154]. Additionally, our MoS_2 backgated device has lower threshold voltage to what was previously reported [149].

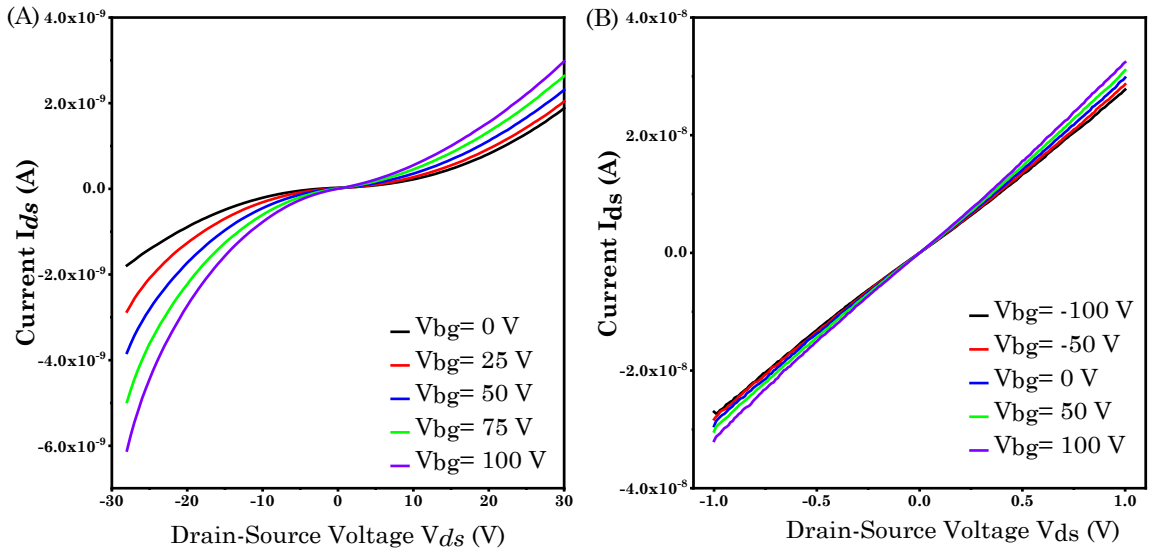

Figure 6-34: Output characteristics of backgated (A) MoS_2 FET and (B) WS_2 FET.

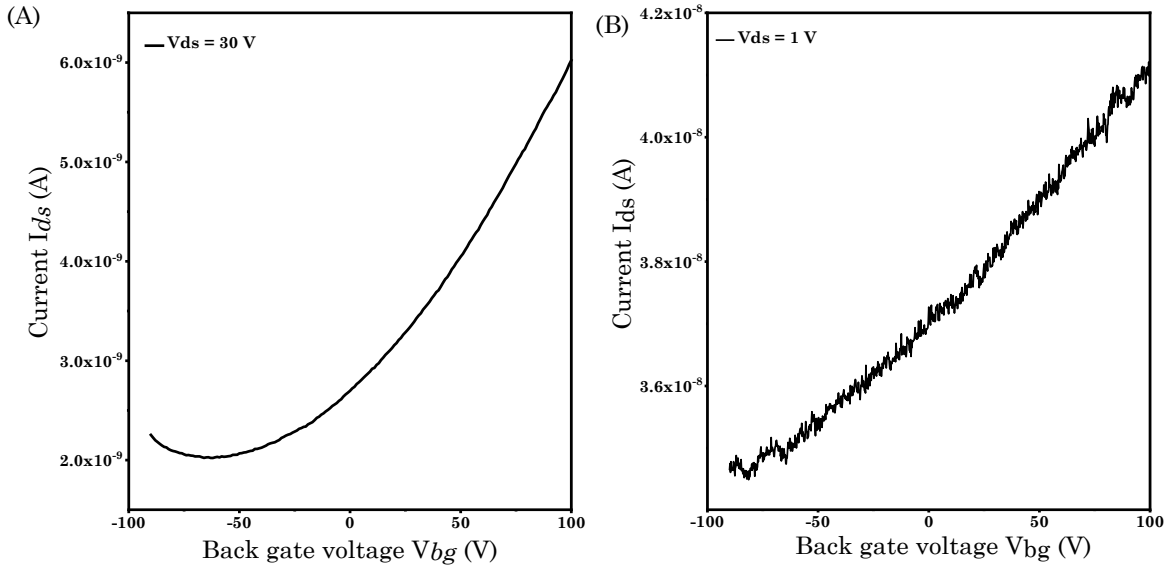

Figure 6-35: Transfer characteristics of backgated (A) MoS_2 FET and (B) WS_2 FET.

Generally, the MoS_2 FET channels fabricated by thermolysis of solution based single source precursor $(NH_4)_2MoS_4$ suffered from low performance and unfortunately our MS_2 FET devices are not an exception [200]. This low performance of our back-gated MS_2 FETs in this chapter and previous chapter (see section 5.6) could be attributed to several factors that severely affect the outputs of these devices which can be summarized as below:-

1. <u>The amorphous nature of the SiO_2/Si substrate:</u>

   Liu et al. have demonstrated that using crystalline substrates such as sapphire rather than SiO_2/Si to grow the MoS_2 improve the mobility of the FET devices by almost two order of magnitude from 10^{-1} $cm^2/V.s$ for SiO_2/Si devices to ~10^1 $cm^2/V.s$ for the sapphire substrates. Thermal stability and higher crystallinity of sapphire rearrange the MoS_2 atoms more uniformly within the crystal lattice and reduce lower oxide content [148].

2. The morphology of the substrate and the film:

Prior the spin-coating of precursor solution, the substrates were treated by oxygen plasma etching for 10-15 min. Although this process is very useful to enhance the wettability of the substrates, it is also has a drawback where the surface roughness of the substrate is increased rapidly [310]. As a result, the scattering of electrons due to surface roughness in the MS_2 FETs will also increase, causing degradation in the mobility of semiconductor channel [213].

3. Organic solvents:

The precursor solutions of $(NH_4)_2MoS_4$ and $(NH_4)_2WS_4$ use organic solvents to create uniform precursor films which means the final MS_2 films are more likely to be contaminated by carbon that passivate the free carriers (electrons) in the semiconductor channel. A simple comparison for field effect mobility and on-off current ratio between MoS_2 FET that fabricated by processing of $(NH_4)_2MoS_4$ aqueous solution [156], [275] and $(NH_4)_2MoS_4$ dissolved in organic solvents [148], [149], [151], [153]–[155] (without additional sulphurization) indicates performance superiority for aqueous based solutions due to lower contamination of carbon.

4. Annealing temperature:

Higher thermal decomposition temperature improves the crystallinity of the MoS_2 film which reduces the resistivity of the film. If the $(NH_4)_2MoS_4$ films are annealed at low temperature, the final MoS_2 films will be amorphous and not reliable for back-gated FET applications [148]. Moreover, Lim et al. enhanced the on-off current ratio by one order of magnitude of their top-ionic gate MoS_2 FET device (synthesized by thermal decomposition of $(NH_4)_2MoS_4$) simply by further annealing at high temperature (from 450°C to 1000°C) [151], [155].

5. Sulphur vacancies and lattice defects:

Our MS_2 films prepared by laser writing of solution based precursor are highly sulphur deficient as there is no additional sulphur source to tailor the vacancies. Consequently, these films become very vulnerable to adsorb a lot of ambient particles such as O_2 and H_2O. These particles will work as p-dopants which recombine with the free electron in the n-type MS_2 films leading to reduce the density of free carriers, the mobility and on-off ratio of the FET devices [311]. It has been reported earlier that the MS_2 FETs exhibit a significant improvement when they work at vacuum rather than ambient conditions [110], [200], [311]. In vacuum, the effect of the adsorbents is eliminated, leaving the electron to move freely in the semiconductor channel when external source drain voltage is applied. Moreover, when these films are grown in sulphur rich environments,

they become more immune to the effect of ambient particles as the density of the sulphur vacancies is significantly reduced.

6. Photolithography:

Using photolithography in MS_2 FET device processing and fabrication necessarily require chemicals like photoresists and developers to create the targeted pattern for devices. However, these chemicals can cause severe damage to the film MS_2, for example, immersing MoS_2 films in MF-319 developer cause uncontrolled partial lift-off which still the chemistry behind this issue is not clear yet [312]. Moreover, photoresists are organic-based materials that readily contaminate the MS_2 films with carbon as well as the photoresists residues might adhere or adsorb to the films after developing [313]. This residues form an insulating layer between the films and the metal contracts interface causing fermi level pining between the MS_2 and the contacts [313]. Therefore, several researches have been conducted to develop photoresist-free patterning step of MS_2 electronic devices [314]–[316].

7. Thickness of the films:

It has been proved that thicker MS_2 films can produce FETs with more efficient electrical performance due to higher carrier concentration and minimizing the impact of dielectric-semiconductor interface issues such as electron scattering and interface charge traps [129], [275].

8. Active area of the device:

Fabricating MS_2 devices with large active area increase the density of grain boundaries due to nanocrystalline nature of solution-based MS_2 films which reduce the efficiency of the devices due to carrier scattering at these boundaries. Fabricating back-gated devices with few micron size improves the mobility of these devices [221].

In order to eliminate some of above mentioned issues, we decided to fabricate FET devices with top-gated configuration using ionic liquid. Ionic liquid can provide much higher capacitance compared with back gate 300nm SiO_2/Si (~1 µF estimated for $LiClO_4$ [317]) dielectric in addition to its role to capsulate the MS_2 films. Significant improvement in on-off current ratio and mobility has been obtained (see Figure 6-36). The mobility of MoS_2 and WS_2 devices has been increased by two order of magnitude compared with backgated devices, however, it is still low for practical application. This low mobility can be attributed to the Schottky barrier and Fermi level pinning due to the existence of photoresist residue. The on-off ratio of WS_2 ionic gated FET device is ~10^4 while for MoS_2 device is >10^2, slightly higher than to what was previously reported for MoS_2 ionic gated FET fabricated with the same precursor [151]. This difference in on-off ratio could be originated from lower off-current of WS_2 can reach possibly due to higher bandgap of WS_2 comparing with MoS_2 [317]. Similar scenario has been noticed before when both materials are grown using the same CVD approach; while MoS_2 shows higher mobility, WS_2 possesses

higher on-off ratio [318]. Another possible explanation to this difference in on-off ratio is the oxide doping type between MoO_3 which is p-type semiconductor [318] while WO_3 has an n-type behaviour [319]. As a result, WO_3 works in favour WS_2 to enhance the on-off ratio whereas MoO_3 species recombine with the free electrons in MoS_2 channel and reducing the on-off ratio.

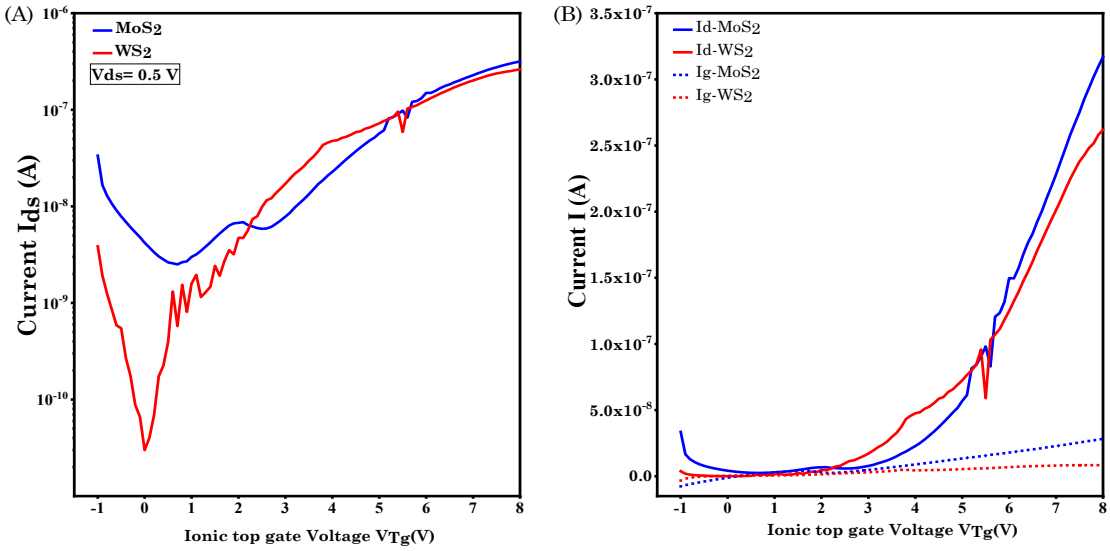

Figure 6-36: Transfer characteristics of MoS_2 and WS_2 top ionic gated FET in (A) log scale (B) linear scale.

Table below summarise the FET parameters extracted from MoS_2 and WS_2 with both back gated and top ionic-gated configuration.

Table 6-6: MS_2 FETs extracted parameters.

Parameter	MoS_2-Back gate	MoS_2-Ionic gate	WS_2- Back gate	MoS_2-Ionic gate
Vth (V)	-50.5	4.45	-	4.33
I(min) nA	2.0225	2.5	34.5	$3x10^{-2}$
I(max) nA	6.0225	317	41.2	261.8
on-off ratio	2.978	127	1.1942	8728
Transconductance (S)	$3.94x10^{-11}$	$8.842x10^{-8}$	$3.4x10^{-11}$	$7.442x10^{-8}$
Capacitance (F/cm-2)	$1.2x10^{-8}$	10^{-6}	$1.2x10^{-8}$	10^{-6}
Mobility ($cm^2/V.S$)	$5.51x10^{-5}$	$7x10^{-3}$	$1.142x10^{-4}$	$6 x10^{-3}$

6.13 MoS_2-WS_2 Heterostructure by Direct Laser Writing

Heterostructuring could be a promising approach to build electronic and optoelectronic circuits that are totally based on 2D materials [320]. So far, chemical and physical vapour depositions (CVD and PVD) are the main routes to synthesize heterostructures of 2D materials. However, solution based single source precursor has not been explored yet to grow vertical 2D heterostructure.

Here, by using laser writing of double layer single source precursor for both MoS_2 and WS_2, we propose a rapid method to create 2D MoS_2-WS_2 vertical heterostructure. This approach can be used to create a large area heterostructure pattern (cross-like) as well as micro-grids with lateral size down to the diffraction limit of the laser spot (see Figure 6-37 and Figure 6-38). Raman spectroscopy confirms the formation of heterostructure in the overlapping area as depicted in Figure 6-37. However, due to higher laser power growth condition of WS_2, it is preferable to start the deposition of WS_2 followed by MoS_2 deposition to avoid destroying the structure underneath by second writing step. The tables below list the growth parameters that have been used to deposit MoS_2-WS_2 large area heterostructure.

Table 6-7: Different growth conditions of MoS_2-WS_2 large area heterostructure (cross-like).

WS_2			**MoS_2**		
Concentration (mM)	Power (mW) With 20X	Speed (mm/min)	Concentration (mM)	Power (mW) With 10X	Speed (mm/min)
100	125	100	48	250	100
100	200	100	48	250	100
100	250	100	48	250	100

Table 6-8: Different growth conditions of MoS_2-WS_2 micro-grid heterostructure.

WS_2			**MoS_2**		
Concentration (mM)	Power (mW) With 20X	Speed (mm/min)	Concentration (mM)	Power (mW) With 10X	Speed (mm/min)
100	200	100	48	250	100
100	250	100	48	250	100

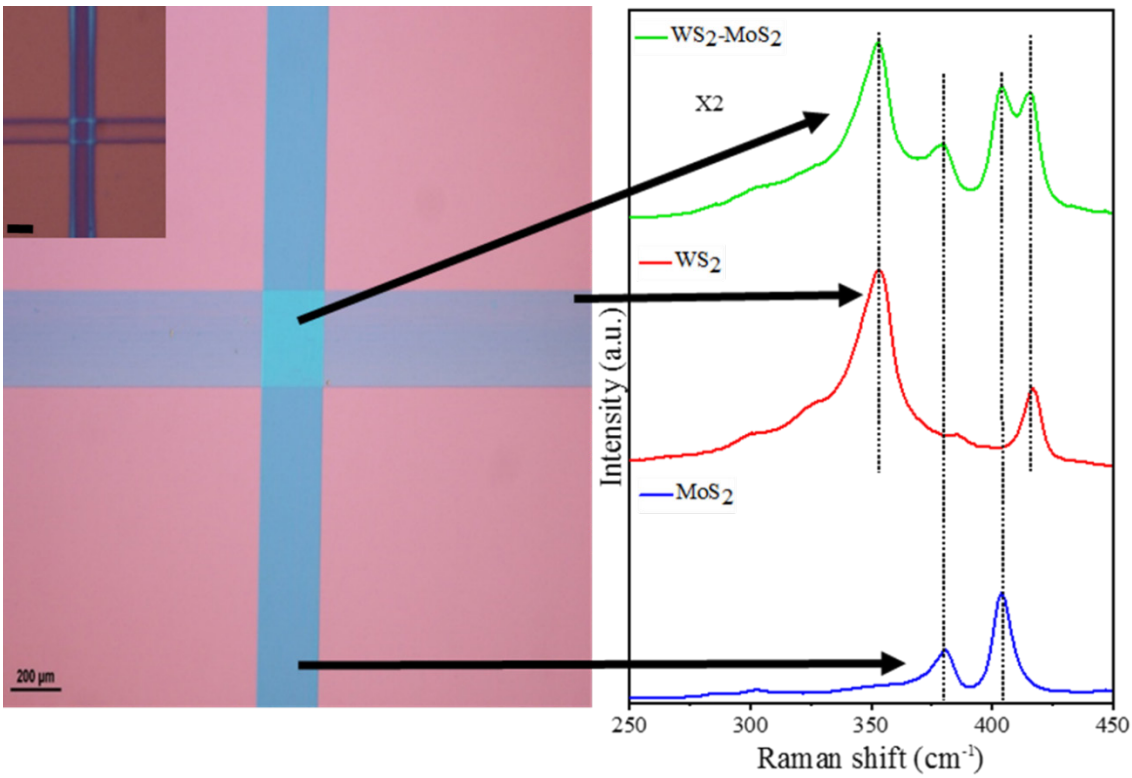

Figure 6-37: Cross-like MoS_2/WS_2 heterostructure with Raman peaks for MoS_2,WS_2 and MoS_2/WS_2 region. The inset is for MoS_2/WS_2 heterostructure with minimum size that the laser diffraction limit permits. The scale bar for the inset is 4 μm. The Raman measurements have been performed by Adam H. Lewis.

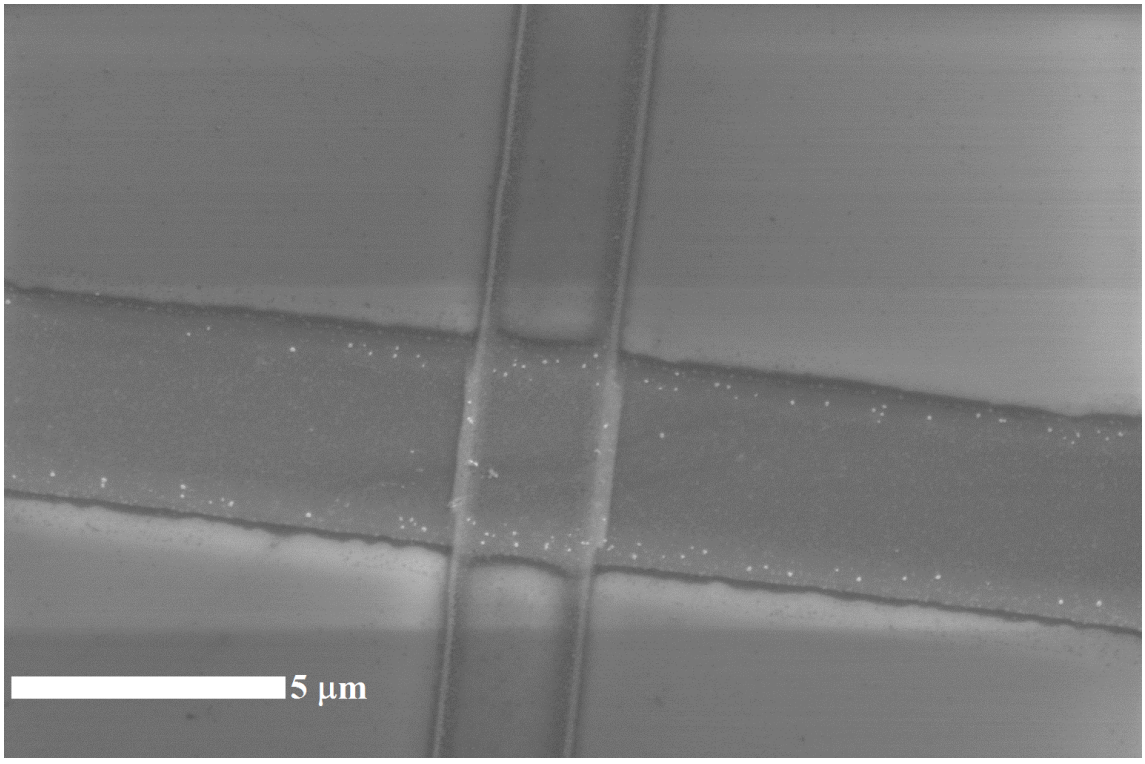

Figure 6-38: Scanning Electron Microscopy (SEM) image of MoS_2/WS_2 heterostructure. The horizontal line is the MoS_2 while the vertical line is the WS_2. The SEM image has been taken by Sakellaris Mailis.

6.14 Conclusion

In summary, we demonstrate a bottom-up, spatially selective laser synthesis approach that utilizing solution-based single source precursors to form 2D transition metal dichalcogenides microstructures and films at ambient conditions. We anticipate that our approach is an excellent candidate to reach manufacturing stage where real time monitoring can be realised readily by in-situ Raman Spectroscopy that is simultaneously performed during laser writing. To explore the versatility of our laser writing approach, MS_2 microstructures have been successfully deposited on different types of substrates. Various spectroscopic techniques revealed that thickness, crystallinity and oxide doping of MS_2 microstructures can be tuned via precursor film thickness and laser writing parameters (power and writing speed). To show the potential electronic applications of MS_2 laser written microstructures, field effect transistors have been fabricated as well as MoS_2/WS_2 heterostructures with dimensions reaching the diffraction limit of the laser. We believe that these findings could be an efficient cost-effective alternative to build 2D materials electronics and optoelectronics commercially and open the door to investigate the possibilities to grown other 2D family members by the same approach.

Chapter 7
Conclusions and Future Outlook

In this final chapter of the thesis, the main findings from previous experimental chapters are concisely stated to summarize the contributions of this Ph.D. project to two-dimensional transition metal dichalcogenides field. Moreover, the future prospects and opportunities emerged from this work which could move the scientific research to industrial stage are stated.

7.1 Thesis Summary

In Chapter 4, a facile route to fabricate metal-semiconductor-metal (MSM) few-layer MoS_2 photodiode was proposed by single deposition-free metallisation step. The MoS_2 films were grown by thermolysis of spin-coated single source precursor uniform films. Although, the initial solvent recipe to prepare uniform precursor layer has been suggested by Yang et al. [150], we optimised the recipe by manipulating the solvents ratio. By doing this, the recipe can be exploited to create uniform $(NH_4)_2MoS_4$ precursor layer on different types of substrates. Moreover, we enhance the wettability of the substrates by increasing the exposure time of oxygen plasma treatment from 10s as Yang et al. reported [150] to 10-15 min to ensure good precursor film coverage on the substrates. Most importantly, we tackled the issue of evaporating the MoS_2 films at the second annealing step by arranging the samples in facing-pair configurations to preserve the stoichiometry of the films. For the MoS_2 photodiode, indium was used for the first time to form the Schottky junction which improves the electron injection through the device due to the small Schottky barrier. The main diode dark parameters were extracted in addition to the photodiode parameters. Finally, we proposed the physical mechanism behind the current flow at both dark and light conditions as well as the few-layer nature of MoS_2 photodiode was revealed by spectral response of the device.

In Chapter 5, based on our knowledge and experience with solution-based synthesis of MoS_2 that have been achieved in Chapter 4, we developed a synthesis approach to grow few layer WS_2 continuous/uniform films over centimetre scales for electronic applications by two annealing-step thermolysis of solution based single source precursor. The crucial challenge was to achieve uniform single source precursor layer for WS_2 due to low coordination of $(NH_4)_2WS_4$ with the common solvents. We proposed a novel solvent recipe to form the precursor layer where a wide range of concentrations can be applied. Various characterisation techniques showed that WS_2 films grown by our approach have high quality. Finally, a backgated FET was fabricated for the first time using this precursor.

In Chapter 6, we extended the opportunities that solution-based single source precursors can provide beyond large area 2D-MS_2 film growth to more reliable approach that can easily be

adopted to build MS_2 electronic devices and circuits. CW laser energy at visible range was applied to selectively decompose solution-based single source precursor films to create MS_2 microstructures followed by single developing step to remove non-exposed areas of the films. The morphological, structural and chemical properties of the MS_2 microstructure can be modulated by the chemistry of the precursors and laser parameters.

To sum up, this Ph.D. thesis has achieved three main goals. First, fabrication 2D-MoS_2 photodiode using simple synthesis and metallisation method is illustrated. Secondly, exploiting ammonium tetrathiotungstate as a cost-efficient solution-based precursor for large area few-layer WS_2 films has been demonstrated for the first time and the electronic functionally of this method is demonstrated. Finally and most importantly, we have developed direct laser writing technique for growth transition metal disulphides that could be the corner stone towards future large-scale production of these materials using various laser printing, writing and lithography techniques such as raster-scanning, multiple-beam shaping spatial light modulators, digital light engines and UV laser photolithography.

7.2 Future work

1. Although synthesis of MS_2 via solution-based single source precursors could be very promising technique for large scale and mass production, several challenges still need to be addressed especially in solvents chemistry, substrates surface activations and device fabrications processes. below is some few suggestions to tackle these issues :-

    - Finding non-organic solvents to prepare the precursor solutions will reduce significantly the films contaminations. Hydrazine seems a very attractive non-organic solvents which could enhance the electrical performance of the MS_2 devices prepared by solution based single source precursors [156].

    - Oxygen plasma treatments was a very powerful process to promote the adhesion between the solution-based single source precursors and the substrates. However, the effect of oxygen plasma treatment on increasing surface roughness could be another reason of low performance of MS_2 devices. Therefore, finding an alternative process that can enhance the wettability without affecting the surface roughness can improve the device performance significantly.

    - Avoiding conventional photo/e-beam lithography as the resists and developers used in these processes alter the properties of MS_2 films and reducing the efficiency of the devices. Instead, finding another resist and developer-free lithographic techniques could be the key to improve the device performance.

2. Synthesis of two dimensional transition metal disulphides (MoS_2 and WS_2) films using ammonium thiometallates {$(NH_4)_2MoS_4$ and $(NH_4)_2WS_4$} as single source precursors has been widely investigated. However, this approach was not explored yet for two dimensional transition metal diselenides ($MoSe_2$ and WSe_2) films although ammonium selenometallates {$(NH_4)_2MoSe_4$ and $(NH_4)_2WSe_4$} have been reported before as single source precursor to grow $MoSe_2$ and WSe_2 nanotubes [321]. One of the challenges to exploit these salts as precursors is that they are not commercially available. Nevertheless, we anticipate if they are prepared in simple and cost effective route they could be good alternative precursors for $MoSe_2$ and WSe_2 films production and laser writing.

3. Metal-Semiconductor-Metal (MSM) photodiodes are very fast switching devices that can be exploited in optical communications. Unfortunately, the temporal response of MoS_2 photodiode has not been investigated in this work. Therefore, we anticipate conducting

future research to study the possibilities for using MSM MoS_2 photodiode for this type of applications.

4. Fabricating WS_2 photodetectors and studying photoelectrical properties of large-area few-layer WS_2 solution based films can be achieved easily.

5. Comparative study of metal-semiconductor junction between indium and few-layer MoS_2 and WS_2 solution based films is essential to understand the Schottky barrier formation and lowering of the barrier in WS_2 films.

6. Choosing laser shorter wavelength (in UV range) for direct writing of MS_2 have the possibility to grow the MS_2 structure using photodecomposition mechanism rather than laser induced-thermal decomposition as well as it can reduce the lateral dimensions of the MS_2 structure to sub-micro scale. This could be the key towards direct laser deposition of MS_2 at very low temperature and reducing the oxide contents. In addition, using pulsed laser to write MS_2 might be an effective way to lower oxide content.

7. Using more controlled conditions to do laser synthesis such as in H_2S or sulphur rich environment could enhance the performance of the devices. Another alternative is to post sulphurize the MS_2 microstructure.

8. Post-annealing of MS_2 microstructures at ambient conditions can grow MO_3 microstructure that can be exploited for electrochromic applications.

9. Extending our laser writing techniques to include transition metal diselenides using ammonium selenometallates {$(NH_4)_2MoSe_4$ and $(NH_4)_2WSe_4$} as solution based precursors will open new opportunities for additional 2D-TMD heterostructures and alloys. These structures can be used to fabricate 2D-TMD functional device arrays.

References

[1] M. Schulz, "The end of the road for silicon?," *Nature*, vol. 399, pp. 729–730, 1999.

[2] K. S. Novoselov *et al.*, "Electric field in atomically thin carbon films," *Science (80-.).*, vol. 306, no. 5696, pp. 666–669, Oct. 2004.

[3] M. Chhowalla, Z. Liu, and H. Zhang, "Two-dimensional transition metal dichalcogenide (TMD) nanosheets," *Chem. Soc. Rev.*, vol. 44, pp. 2584–2586, 2015.

[4] K. K. Kam and B. A. Parkinson, "Detailed photocurrent spectroscopy of the semiconducting group VIB transition metal dichalcogenides," *J. Phys. Chem.*, vol. 86, no. 4, pp. 463–467, 1982.

[5] A. J. Grant, T. M. Griffiths, G. D. Pitt, and A. D. Yoffe, "The electrical properties and the magnitude of the indirect gap in the semiconducting transition metal dichalcogenide layer crystals," *J. Phys. C Solid State Phys.*, vol. 8, no. 1, pp. L17–L23, 1975.

[6] M. Samadi, N. Sarikhani, M. Zirak, H. Zhang, H. L. Zhang, and A. Z. Moshfegh, "Group 6 transition metal dichalcogenide nanomaterials: Synthesis, applications and future perspectives," *Nanoscale Horizons*, vol. 3, no. 2, pp. 90–204, 2018.

[7] K. S. Novoselov *et al.*, "Two-dimensional atomic crystals.," *Proc. Natl. Acad. Sci. U. S. A.*, vol. 102, no. 30, pp. 10451–10453, 2005.

[8] B. Radisavljevic, A. Radenovic, J. Brivio, V. Giacometti, and A. Kis, "Single-layer MoS_2 transistors," *Nat. Nanotechnol.*, vol. 6, no. 3, pp. 147–150, 2011.

[9] K. F. Mak, C. Lee, J. Hone, J. Shan, and T. F. Heinz, "Atomically thin MoS_2: A new direct-gap semiconductor," *Phys. Rev. Lett.*, vol. 105, no. 13, p. 136805, 2010.

[10] A. Splendiani *et al.*, "Emerging photoluminescence in monolayer MoS_2," *Nano Lett.*, vol. 10, no. 4, pp. 1271–1275, Apr. 2010.

[11] P. Joensen, R. F. Frindt, and S. R. Morrison, "Single-layer MoS_2," *Mater. Res. Bull.*, vol. 21, no. 4, pp. 457–461, 1986.

[12] M. Chhowalla, H. S. Shin, G. Eda, L. J. Li, K. P. Loh, and H. Zhang, "The chemistry of two-dimensional layered transition metal dichalcogenide nanosheets," *Nat. Chem.*, vol. 5, no. 4, pp. 263–275, 2013.

[13] Q. H. Wang, K. Kalantar-Zadeh, A. Kis, J. N. Coleman, and M. S. Strano, "Electronics

and optoelectronics of two-dimensional transition metal dichalcogenides," *Nat. Nanotechnol.*, vol. 7, no. 11, pp. 699–712, 2012.

[14] R. J. Toh, Z. Sofer, J. Luxa, D. Sedmidubský, and M. Pumera, "3R phase of MoS_2 and WS_2 outperforms the corresponding 2H phase for hydrogen evolution," *Chem. Commun.*, vol. 53, no. 21, pp. 3054–3057, 2017.

[15] M. Ye, D. Winslow, D. Zhang, R. Pandey, and Y. Yap, "Recent Advancement on the Optical Properties of Two-Dimensional Molybdenum Disulfide (MoS_2) Thin Films," *Photonics*, vol. 2, no. 1, pp. 288–307, 2015.

[16] G.-B. Liu, D. Xiao, Y. Yao, X. Xu, and W. Yao, "Electronic structures and theoretical modelling of two-dimensional group-VIB transition metal dichalcogenides," *Chem. Soc. Rev.*, vol. 44, no. 9, pp. 2643–2663, 2015.

[17] R. Lv *et al.*, "Transition Metal Dichalcogenides and Beyond: Synthesis, Properties, and Applications of Single- and Few-Layer Nanosheets," *Acc. Chem. Res.*, 2014.

[18] L. Gao, "Flexible Device Applications of 2D Semiconductors," *Small*, vol. 13, no. 35, p. 1603994, May 2017.

[19] R. Lv *et al.*, "Two-dimensional transition metal dichalcogenides: Clusters, ribbons, sheets and more," *Nano Today*, vol. 10, no. 5, pp. 559–592, 2015.

[20] H. Zeng and X. Cui, "An optical spectroscopic study on two-dimensional group-VI transition metal dichalcogenides," *Chem. Soc. Rev.*, vol. 44, no. 9, pp. 2629–2642, 2015.

[21] C. Lee, H. Yan, L. E. Brus, T. F. Heinz, J. Hone, and S. Ryu, "Anomalous lattice vibrations of single- and few-layer MoS_2," *ACS Nano*, vol. 4, no. 5, pp. 2695–2700, 2010.

[22] Y. P. Venkata Subbaiah, K. J. Saji, and A. Tiwari, "Atomically Thin MoS_2:A Versatile Nongraphene 2D Material," *Adv. Funct. Mater.*, vol. 26, no. 13, pp. 2046–2069, 2016.

[23] R. Saito, Y. Tatsumi, S. Huang, X. Ling, and M. S. Dresselhaus, "Raman spectroscopy of transition metal dichalcogenides," *J. Phys. Condens. Matter*, vol. 28, no. 35, p. 353002, 2016.

[24] H. Li *et al.*, "From bulk to monolayer MoS_2: Evolution of Raman scattering," *Adv. Funct. Mater.*, vol. 22, no. 7, pp. 1385–1390, 2012.

[25] A. Berkdemir *et al.*, "Identification of individual and few layers of WS_2 using Raman Spectroscopy," *Sci. Rep.*, vol. 3, no. 1, p. 1755, 2013.

[26] F. Bonaccorso, Z. Sun, T. Hasan, and A. C. Ferrari, "Graphene photonics and optoelectronics," *Nat. Photonics*, vol. 4, no. 9, pp. 611–622, 2010.

[27] H. Chang and H. Wu, “Graphene-based nanomaterials: Synthesis, properties, and optical and optoelectronic applications,” *Adv. Funct. Mater.*, vol. 23, no. 16, pp. 1984–1997, 2013.

[28] B. Galindo *et al.*, “Effect of the number of layers of graphene on the electrical properties of TPU polymers,” in *IOP Conference Series: Materials Science and Engineering*, 2014, vol. 64, no. 1, pp. 1–6.

[29] F. Lévy, *Crystallography and Crystal Chemistry of Materials with Layered Structures*, no. 2. 1976.

[30] A. Kuc, N. Zibouche, and T. Heine, “Influence of quantum confinement on the electronic structure of the transition metal sulfide TS_2,” *Phys. Rev. B - Condens. Matter Mater. Phys.*, 2011.

[31] J. Xiao, M. Zhao, Y. Wang, and X. Zhang, “Excitons in atomically thin 2D semiconductors and their applications,” *Nanophotonics*, vol. 6, no. 6. pp. 1309–1328, 2017.

[32] H. Zeng *et al.*, “Optical signature of symmetry variations and spin-valley coupling in atomically thin tungsten dichalcogenides,” *Sci. Rep.*, vol. 3, p. 1608, Apr. 2013.

[33] W. Zhao *et al.*, “Evolution of Electronic Structure in Atomically Thin Sheets of WS_2 and WSe_2,” *ACS Nano*, vol. 7, no. 1, pp. 791–797, 2013.

[34] D. Ovchinnikov, A. Allain, Y. S. Huang, D. Dumcenco, and A. Kis, “Electrical transport properties of single-layer WS_2,” *ACS Nano*, vol. 8, no. 8, pp. 8174–8181, 2014.

[35] W. S. Hwang *et al.*, “Transistors with chemically synthesized layered semiconductor WS_2 exhibiting 10^5 room temperature modulation and ambipolar behavior,” *Appl. Phys. Lett.*, vol. 101, no. 1, p. 013107, 2012.

[36] D. M. Tang *et al.*, “Nanomechanical cleavage of molybdenum disulphide atomic layers,” *Nat. Commun.*, vol. 5, p. 3631, Apr. 2014.

[37] M. Yi and Z. Shen, “A review on mechanical exfoliation for the scalable production of graphene,” *J. Mater. Chem. A*, vol. 3, no. 22, pp. 11700–11715, 2015.

[38] J. N. Coleman *et al.*, “Two-dimensional nanosheets produced by liquid exfoliation of layered materials.,” *Science*, vol. 331, no. 6017, pp. 568–71, Feb. 2011.

[39] K. G. Zhou, N. N. Mao, H. X. Wang, Y. Peng, and H. L. Zhang, “A mixed-solvent strategy for efficient exfoliation of inorganic graphene analogues,” *Angew. Chemie - Int. Ed.*, vol. 50, no. 46, pp. 10839–10842, Sep. 2011.

[40] V. Nicolosi, M. Chhowalla, M. G. Kanatzidis, M. S. Strano, and J. N. Coleman, "Liquid exfoliation of layered materials," *Science*, vol. 340, no. 6139, p. 1226419, 2013.

[41] E. Varrla *et al.*, "Large-Scale Production of Size-Controlled MoS_2 Nanosheets by Shear Exfoliation," *Chem. Mater.*, vol. 27, no. 3, pp. 1129–1139, Feb. 2015.

[42] "Interactions of Nanomaterials with Liquid Media _ DB Group @ MIT ChemE." [Online]. Available: https://dbgroup.mit.edu/nanomaterials-liquid-media.

[43] B. Z. Lin, C. Ding, B. H. Xu, Z. J. Chen, and Y. L. Chen, "Preparation and characterization of polythiophene/molybdenum disulfide intercalation material," *Mater. Res. Bull.*, vol. 44, no. 4, pp. 719–723, 2009.

[44] D. Yang and R. F. Frindt, "Li-INTERCALATION AND EXFOLIATION OF WS_2," *J. Phys. Chem. Solids*, vol. 57, no. 6, pp. 1113–1116, 1996.

[45] Z. Zeng *et al.*, "Single-layer semiconducting nanosheets: High-yield preparation and device fabrication," *Angew. Chemie - Int. Ed.*, vol. 50, no. 47, pp. 11093–11097, Oct. 2011.

[46] A. Gupta, T. Sakthivel, and S. Seal, "Recent development in 2D materials beyond graphene," *Prog. Mater. Sci.*, vol. 73, pp. 44–126, 2015.

[47] Z. Lin *et al.*, "Solution-processable 2D semiconductors for high-performance large-area electronics," *Nature*, vol. 562, no. 7726, pp. 254–258, 2018.

[48] X. Lu, M. I. B. Utama, J. Zhang, Y. Zhao, and Q. Xiong, "Layer-by-layer thinning of MoS_2 by thermal annealing," *Nanoscale*, vol. 5, no. 19, pp. 8904–8908, 2013.

[49] J. Wu *et al.*, "Layer Thinning and Etching of Mechanically Exfoliated MoS2 Nanosheets by Thermal Annealing in Air," *Small*, vol. 9, no. 19, pp. 3314–3319, Aug. 2013.

[50] Y. Liu *et al.*, "Layer-by-layer thinning of MoS_2 by plasma," *ACS Nano*, vol. 7, no. 5, pp. 4202–4209, 2013.

[51] H. Zhu, X. Qin, L. Cheng, A. Azcatl, J. Kim, and R. M. Wallace, "Remote Plasma Oxidation and Atomic Layer Etching of MoS_2," *ACS Appl. Mater. Interfaces*, vol. 8, no. 29, pp. 19119–19126, Jul. 2016.

[52] K. K. Amara, L. Chu, R. Kumar, M. Toh, and G. Eda, "Wet chemical thinning of molybdenum disulfide down to its monolayer," *APL Mater.*, vol. 2, no. 9, p. 92509, Aug. 2014.

[53] S. Wu, C. Huang, G. Aivazian, J. S. Ross, D. H. Cobden, and X. Xu, "Vapor–Solid Growth of High Optical Quality MoS_2 Monolayers with Near-Unity Valley

Polarization," *ACS Nano*, vol. 7, no. 3, pp. 2768–2772, Mar. 2013.

[54] C. Gong *et al.*, "Metal Contacts on Physical Vapor Deposited Monolayer MoS_2," *ACS Nano*, vol. 7, no. 12, pp. 11350–11357, Dec. 2013.

[55] S. Luo *et al.*, "Photoresponse properties of large-area MoS_2 atomic layer synthesized by vapor phase deposition," *J. Appl. Phys.*, vol. 116, no. 16, p. 164304, Oct. 2014.

[56] Y. Fan *et al.*, "Synthesis, characterization and electrostatic properties of WS_2 nanostructures," *AIP Adv.*, vol. 4, no. 5, p. 57105, May 2014.

[57] Y. Fan, J. Li, G. Hao, S. Luo, C. Tang, and J. Zhong, "Synthesis, characterization of WS_2 nanostructures by vapor phase deposition," *J. Appl. Phys.*, vol. 117, no. 6, p. 64302, Feb. 2015.

[58] J. Hong *et al.*, "Exploring atomic defects in molybdenum disulphide monolayers," *Nat. Commun.*, vol. 6, p. 6293, Feb. 2015.

[59] B. J. Modtland, E. Navarro-Moratalla, X. Ji, M. Baldo, and J. Kong, "Monolayer Tungsten Disulfide (WS_2) via Chlorine-Driven Chemical Vapor Transport," *Small*, vol. 13, no. 33, p. 1701232, Sep. 2017.

[60] Z. Lin *et al.*, "Facile synthesis of MoS_2 and $Mo_xW_{1-x}S_2$ triangular monolayers," *APL Mater.*, vol. 2, no. 9, p. 92514, Sep. 2014.

[61] X. Duan *et al.*, "Lateral epitaxial growth of two-dimensional layered semiconductor heterojunctions," *Nat. Nanotechnol.*, vol. 9, p. 1024, Sep. 2014.

[62] Z. Zhang, P. Chen, X. Duan, K. Zang, J. Luo, and X. Duan, "Robust epitaxial growth of two-dimensional heterostructures, multiheterostructures, and superlattices," *Science (80-.).*, vol. 357, no. 6353, pp. 788 LP – 792, Aug. 2017.

[63] R. Ai *et al.*, "Growth of Single-Crystalline Cadmium Iodide Nanoplates, CdI_2/MoS_2 (WS_2, WSe_2) van der Waals Heterostructures, and Patterned Arrays," *ACS Nano*, vol. 11, no. 3, pp. 3413–3419, Mar. 2017.

[64] M. Swain, "Multilayer Film Deposition , Characterization by Reflectometry Techniques and Their Structure Property Correlation," Homi Bhabha National Institute, 2015.

[65] P. J. Kelly and R. D. Arnell, "Magnetron sputtering: a review of recent developments and applications," *Vacuum*, vol. 56, no. 3, pp. 159–172, 2000.

[66] K. Ellmer, "Preparation routes based on magnetron sputtering for tungsten disulfide (WS_2) films for thin-film solar cells," *Phys. Status Solidi Basic Res.*, vol. 245, no. 9, pp. 1745–1760, Sep. 2008.

[67] C. Muratore *et al.*, "Continuous ultra-thin MoS_2 films grown by low-temperature physical vapor deposition," *Appl. Phys. Lett.*, vol. 104, no. 26, p. 261604, Jun. 2014.

[68] J. Tao *et al.*, "Growth of wafer-scale MoS_2 monolayer by magnetron sputtering," *Nanoscale*, vol. 7, no. 6, pp. 2497–2503, 2015.

[69] H.-S. Kim, M. Patel, J. Kim, and M. S. Jeong, "Growth of Wafer-Scale Standing Layers of WS_2 for Self-Biased High-Speed UV–Visible–NIR Optoelectronic Devices," *ACS Appl. Mater. Interfaces*, vol. 10, no. 4, pp. 3964–3974, Jan. 2018.

[70] B. H. Kim, H. H. Gu, and Y. J. Yoon, "Large-area and low-temperature synthesis of few-layered WS_2 films for photodetectors," *2D Mater.*, vol. 5, no. 4, p. 45030, 2018.

[71] W. C. Wong, S. M. Ng, H. F. Wong, W. F. Cheng, C. L. Mak, and C. W. Leung, "Effect of post-annealing on sputtered MoS_2 films," *Solid. State. Electron.*, vol. 138, pp. 62–65, 2017.

[72] B. Sirota, N. Glavin, and A. A. Voevodin, "Room temperature magnetron sputtering and laser annealing of ultrathin MoS_2 for flexible transistors," *Vacuum*, vol. 160, no. August 2018, pp. 133–138, 2019.

[73] R. A. Vilá *et al.*, "In situ crystallization kinetics of two-dimensional MoS_2," *2D Mater.*, vol. 5, no. 1, p. 11009, 2017.

[74] M. E. McConney *et al.*, "Direct synthesis of ultra-thin large area transition metal dichalcogenides and their heterostructures on stretchable polymer surfaces," *J. Mater. Res.*, vol. 31, no. 7, pp. 967–974, 2016.

[75] D. H. Lowndes, D. B. Geohegan, A. A. Puretzky, D. P. Norton, and C. M. Rouleau, "Synthesis of Novel Thin-Film Materials by Pulsed Laser Deposition," *Science (80-.).*, vol. 273, no. 5277, pp. 898 LP – 903, Aug. 1996.

[76] Z. Yang and J. Hao, "Progress in pulsed laser deposited two-dimensional layered materials for device applications," *J. Mater. Chem. C*, vol. 4, no. 38, pp. 8859–8878, 2016.

[77] K. Tian, K. Baskaran, and A. Tiwari, "Growth of two-dimensional WS_2 thin films by pulsed laser deposition technique," *Thin Solid Films*, vol. 668, pp. 69–73, 2018.

[78] G. Siegel, Y. P. Venkata Subbaiah, M. C. Prestgard, and A. Tiwari, "Growth of centimeter-scale atomically thin MoS_2 films by pulsed laser deposition," *APL Mater.*, vol. 3, no. 5, p. 56103, May 2015.

[79] T. A. J. Loh, D. H. C. Chua, and A. T. S. Wee, "One-step Synthesis of Few-layer WS_2 by Pulsed Laser Deposition," *Sci. Rep.*, vol. 5, p. 18116, Dec. 2015.

[80] M. I. Serna *et al.*, "Large-Area Deposition of MoS_2 by Pulsed Laser Deposition with In Situ Thickness Control," *ACS Nano*, vol. 10, no. 6, pp. 6054–6061, Jun. 2016.

[81] H. Wang *et al.*, "Effect of post-annealing on laser-ablation deposited WS_2 thin films," *Vacuum*, vol. 152, pp. 239–242, 2018.

[82] Y. Ho *et al.*, "Post sulfurization effect on the MoS_2 grown by pulsed laser deposition," in *2016 China Semiconductor Technology International Conference (CSTIC)*, 2016, pp. 1–3.

[83] Y. Zhan, Z. Liu, S. Najmaei, P. M. Ajayan, and J. Lou, "Large-area vapor-phase growth and characterization of MoS_2 atomic layers on a SiO_2 substrate," *Small*, vol. 8, no. 7, pp. 966–971, 2012.

[84] M. R. Laskar *et al.*, "Large area single crystal (0001) oriented MoS_2," *Appl. Phys. Lett.*, vol. 102, no. 25, p. 252108, Jun. 2013.

[85] Y. Lee *et al.*, "Synthesis of wafer-scale uniform molybdenum disulfide films with control over the layer number using a gas phase sulfur precursor," *Nanoscale*, vol. 6, no. 5, pp. 2821–2826, 2014.

[86] C. M. Orofeo, S. Suzuki, Y. Sekine, and H. Hibino, "Scalable synthesis of layer-controlled WS_2 and MoS_2 sheets by sulfurization of thin metal films," *Appl. Phys. Lett.*, vol. 105, no. 8, p. 83112, Aug. 2014.

[87] R. Gatensby *et al.*, "Controlled synthesis of transition metal dichalcogenide thin films for electronic applications," *Appl. Surf. Sci.*, vol. 297, pp. 139–146, 2014.

[88] C. Yim *et al.*, "Investigation of the optical properties of MoS_2 thin films using spectroscopic ellipsometry," *Appl. Phys. Lett.*, vol. 104, no. 10, p. 103114, Mar. 2014.

[89] C. Ahn *et al.*, "Low-Temperature Synthesis of Large-Scale Molybdenum Disulfide Thin Films Directly on a Plastic Substrate Using Plasma-Enhanced Chemical Vapor Deposition," *Adv. Mater.*, vol. 27, no. 35, pp. 5223–5229, Aug. 2015.

[90] J. H. Kim, J. Lee, J. H. Kim, C. C. Hwang, C. Lee, and J. Y. Park, "Work function variation of MoS_2 atomic layers grown with chemical vapor deposition: The effects of thickness and the adsorption of water/oxygen molecules," *Appl. Phys. Lett.*, vol. 106, no. 25, p. 251606, Jun. 2015.

[91] S. Zhang *et al.*, "Direct Observation of Degenerate Two-Photon Absorption and Its Saturation in WS_2 and MoS_2 Monolayer and Few-Layer Films," *ACS Nano*, vol. 9, no. 7, pp. 7142–7150, Jul. 2015.

[92] W. Zheng *et al.*, "Patterned Growth of P-Type MoS_2 Atomic Layers Using Sol–Gel as

Precursor," *Adv. Funct. Mater.*, vol. 26, no. 35, pp. 6371–6379, Jul. 2016.

[93] D. H. Li *et al.*, "Dielectric functions and critical points of crystalline WS_2 ultrathin films with tunable thickness," *Phys. Chem. Chem. Phys.*, vol. 19, no. 19, pp. 12022–12031, 2017.

[94] F. Chen, S. Ding, and W. Su, "A feasible approach to fabricate two-dimensional WS_2 flakes: From monolayer to multilayer," *Ceram. Int.*, vol. 44, no. 18, pp. 22108–22112, 2018.

[95] Y. M. Shi, H. N. Li, and L. J. Li, "Recent advances in controlled synthesis of two-dimensional transition metal dichalcogenides via vapour deposition techniques," *Chem. Soc. Rev.*, vol. 44, no. 9, pp. 2744–2756, 2015.

[96] Q. Ji, Y. Zhang, Y. Zhang, and Z. Liu, "Chemical vapour deposition of group-VIB metal dichalcogenide monolayers: engineered substrates from amorphous to single crystalline," *Chem. Soc. Rev.*, vol. 44, no. 9, pp. 2587–2602, 2015.

[97] A. Gavrilyuk, U. Tritthart, and W. Gey, "Photo-stimulated proton-coupled electron transfer in quasi-amorphous WO_3 and MoO_3 thin films," *Philos. Mag.*, 2007.

[98] Y.-C. Lin *et al.*, "Wafer-scale MoS_2 thin layers prepared by MoO_3 sulfurization," *Nanoscale*, vol. 4, no. 20, pp. 6637–6641, 2012.

[99] H. R. Gutiérrez *et al.*, "Extraordinary room-temperature photoluminescence in triangular WS_2 monolayers," *Nano Lett.*, vol. 13, no. 8, pp. 3447–3454, Aug. 2013.

[100] S. Balendhran *et al.*, "Atomically thin layers of MoS_2 via a two step thermal evaporation–exfoliation method," *Nanoscale*, vol. 4, no. 2, pp. 461–466, 2012.

[101] Y. H. Lee *et al.*, "Synthesis of large-area MoS_2 atomic layers with chemical vapor deposition," *Adv. Mater.*, vol. 24, no. 17, pp. 2320–2325, 2012.

[102] H. Wang *et al.*, "Large-scale 2D electronics based on single-layer MoS_2 grown by chemical vapor deposition," in *2012 International Electron Devices Meeting*, 2012, pp. 4.6.1-4.6.4.

[103] Y. Zhang *et al.*, "Controlled growth of high-quality monolayer WS_2 layers on sapphire and imaging its grain boundary," *ACS Nano*, vol. 7, no. 10, pp. 8963–8971, Oct. 2013.

[104] C. Cong *et al.*, "Synthesis and optical properties of large-area single-crystalline 2D semiconductor WS_2 monolayer from chemical vapor deposition," *Adv. Opt. Mater.*, vol. 2, no. 2, pp. 131–136, 2014.

[105] X. Wang, H. Feng, Y. Wu, and L. Jiao, "Controlled Synthesis of Highly Crystalline MoS_2

Flakes by Chemical Vapor Deposition," *J. Am. Chem. Soc.*, vol. 135, no. 14, pp. 5304–5307, Apr. 2013.

[106] N. Perea-López *et al.*, "CVD-grown monolayered MoS_2 as an effective photosensor operating at low-voltage," *2D Mater.*, vol. 1, no. 1, p. 11004, 2014.

[107] G. H. Han *et al.*, "Seeded growth of highly crystalline molybdenum disulphide monolayers at controlled locations," *Nat. Commun.*, vol. 6, p. 6128, Jan. 2015.

[108] S. Vangelista *et al.*, "Towards a uniform and large-scale deposition of MoS_2 nanosheets via sulfurization of ultra-thin Mo-based solid films," *Nanotechnology*, vol. 27, no. 17, p. 10, 2016.

[109] A. L. Elías *et al.*, "Controlled synthesis and transfer of large-area WS_2 sheets: From single layer to few layers," *ACS Nano*, vol. 7, no. 6, pp. 5235–5242, Jun. 2013.

[110] C. Lan, C. Li, Y. Yin, and Y. Liu, "Large-area synthesis of monolayer WS_2 and its ambient-sensitive photo-detecting performance," *Nanoscale*, vol. 7, no. 14, pp. 5974–5980, 2015.

[111] S. Hussain *et al.*, "Layer-modulated, wafer scale and continuous ultra-thin WS2 films grown by RF sputtering: Via post-deposition annealing," *J. Mater. Chem. C*, vol. 4, no. 33, pp. 7846–7852, 2016.

[112] B. K. Choi, I. H. Lee, J. Kim, and Y. J. Chang, "Tunable Wetting Property in Growth Mode-Controlled WS_2 Thin Films," *Nanoscale Res. Lett.*, vol. 12, no. 1, 2017.

[113] Y. H. Lee *et al.*, "Synthesis and transfer of single-layer transition metal disulfides on diverse surfaces," *Nano Lett.*, 2013.

[114] A. M. van der Zande *et al.*, "Grains and grain boundaries in highly crystalline monolayer molybdenum disulphide," *Nat. Mater.*, vol. 12, p. 554, May 2013.

[115] J. Mann *et al.*, "Facile growth of monolayer MoS_2 film areas on SiO_2," *Eur. Phys. J. B*, vol. 86, no. 5, p. 226, 2013.

[116] S. Najmaei *et al.*, "Vapour phase growth and grain boundary structure of molybdenum disulphide atomic layers," *Nat. Mater.*, vol. 12, p. 754, Jun. 2013.

[117] Q. Ji *et al.*, "Epitaxial Monolayer MoS_2 on Mica with Novel Photoluminescence," *Nano Lett.*, vol. 13, no. 8, pp. 3870–3877, Aug. 2013.

[118] W. Zhang *et al.*, "Ultrahigh-gain photodetectors based on atomically thin graphene-MoS_2 heterostructures.," *Sci. Rep.*, vol. 4, p. 3826, Jan. 2014.

[119] X. Ling *et al.*, "Role of the Seeding Promoter in MoS_2 Growth by Chemical Vapor Deposition," *Nano Lett.*, vol. 14, no. 2, pp. 464–472, Feb. 2014.

[120] M.-L. Tsai *et al.*, "Monolayer MoS_2 Heterojunction Solar Cells," *ACS Nano*, vol. 8, no. 8, pp. 8317–8322, Aug. 2014.

[121] J. Shi *et al.*, "Controllable growth and transfer of monolayer MoS_2 on Au foils and its potential application in hydrogen evolution reaction," *ACS Nano*, vol. 8, no. 10, pp. 10196–10204, Oct. 2014.

[122] S. Wang *et al.*, "Shape evolution of monolayer MoS_2 crystals grown by chemical vapor deposition," *Chem. Mater.*, vol. 26, no. 22, pp. 6371–6379, Nov. 2014.

[123] J. Shi *et al.*, "Monolayer MoS_2 growth on au foils and on-site domain boundary imaging," *Adv. Funct. Mater.*, vol. 25, no. 6, pp. 842–849, Feb. 2015.

[124] J. Shi *et al.*, "Substrate facet effect on the growth of monolayer MoS_2 on Au foils," *ACS Nano*, vol. 9, no. 4, pp. 4017–4025, Apr. 2015.

[125] D. Dumcenco *et al.*, "Large-Area Epitaxial Monolayer MoS_2," *ACS Nano*, vol. 9, no. 4, pp. 4611–4620, Apr. 2015.

[126] Y. Shi *et al.*, "MoS_2 Surface Structure Tailoring via Carbonaceous Promoter," *Sci. Rep.*, vol. 5, p. 10378, May 2015.

[127] W. Chen *et al.*, "Oxygen-Assisted Chemical Vapor Deposition Growth of Large Single-Crystal and High-Quality Monolayer MoS_2," *J. Am. Chem. Soc.*, vol. 137, no. 50, pp. 15632–15635, Dec. 2015.

[128] Z. Lin *et al.*, "Controllable Growth of Large-Size Crystalline MoS_2 and Resist-Free Transfer Assisted with a Cu Thin Film," *Sci. Rep.*, vol. 5, p. 18596, Dec. 2015.

[129] H. Xu *et al.*, "High-Performance Wafer-Scale MoS_2 Transistors toward Practical Application," *Small*, vol. 14, no. 48, p. 1803465, Nov. 2018.

[130] N. Peimyoo *et al.*, "Nonblinking, Intense Two-Dimensional Light Emitter: Monolayer WS_2 Triangles," *ACS Nano*, vol. 7, no. 12, pp. 10985–10994, Dec. 2013.

[131] Y. Rong *et al.*, "Controlling sulphur precursor addition for large single crystal domains of WS_2," *Nanoscale*, vol. 6, no. 20, pp. 12096–12103, 2014.

[132] Y. Gao *et al.*, "Large-area synthesis of high-quality and uniform monolayer WS_2 on reusable Au foils," *Nat. Commun.*, vol. 6, p. 8569, Oct. 2015.

[133] P. Liu *et al.*, "Large-Area WS_2 Film with Big Single Domains Grown by Chemical Vapor

Deposition," *Nanoscale Res. Lett.*, vol. 12, pp. 0–9, 2017.

[134] C. Lan *et al.*, "Wafer-scale synthesis of monolayer WS_2 for high-performance flexible photodetectors by enhanced chemical vapor deposition," *Nano Res.*, 2018.

[135] F. Lan *et al.*, "Synthesis of large-scale single-crystalline monolayer WS_2 using a semi-sealed method," *Nanomaterials*, vol. 8, no. 2, p. 100, 2018.

[136] Y. Yue *et al.*, "Two-Dimensional High-Quality Monolayered Triangular WS_2 Flakes for Field-Effect Transistors," *ACS Appl. Mater. Interfaces*, vol. 10, no. 26, pp. 22435–22444, Jul. 2018.

[137] X. L. Li, J. P. Ge, and Y. D. Li, "Atmospheric pressure chemical vapor deposition: An alternative route to large-scale MoS_2 and WS_2 inorganic fullerene-like nanostructures and nanoflowers," *Chem. - A Eur. J.*, vol. 10, no. 23, pp. 6163–6171, Dec. 2004.

[138] Y. Yu, C. Li, Y. Liu, L. Su, Y. Zhang, and L. Cao, "Controlled Scalable Synthesis of Uniform, High-Quality Monolayer and Few-layer MoS_2 Films," *Sci. Rep.*, vol. 3, p. 1866, May 2013.

[139] M. Okada *et al.*, "Direct Chemical Vapor Deposition Growth of WS_2 Atomic Layers on Hexagonal Boron Nitride," *ACS Nano*, vol. 8, no. 8, pp. 8273–8277, Aug. 2014.

[140] A. Thangaraja, S. M. Shinde, G. Kalita, and M. Tanemura, "An effective approach to synthesize monolayer tungsten disulphide crystals using tungsten halide precursor," *Appl. Phys. Lett.*, vol. 108, no. 5, p. 53104, Feb. 2016.

[141] C. C. Huang *et al.*, "Scalable high-mobility MoS_2 thin films fabricated by an atmospheric pressure chemical vapor deposition process at ambient temperature," *Nanoscale*, vol. 6, no. 21, pp. 12792–12797, 2014.

[142] J. Park *et al.*, "Layer-modulated synthesis of uniform tungsten disulfide nanosheet using gas-phase precursors," *Nanoscale*, vol. 7, no. 4, pp. 1308–1313, 2015.

[143] J. L. Brito, M. Ilija, and P. Hernández, "Thermal and reductive decomposition of ammonium thiomolybdates," *Thermochim. Acta*, vol. 256, no. 2, pp. 325–338, 1995.

[144] K. Q. and Y. C. Z. P. F. Xing , L. F. Ma, "THERMAL DECOMPOSITION BEHAVIOR OF AMMONIUM THIO TUNGSTATE in H_2," *Acta Metall. Sin. Lett.*, vol. 12, no. 5, pp. 1171–1174, 1999.

[145] D. Hunyadi, A. L. Vieira Machado Ramos, and I. M. Szilágyi, "Thermal decomposition of ammonium tetrathiotungstate," *J. Therm. Anal. Calorim.*, vol. 120, no. 1, pp. 209–215, 2015.

[146] M. Nath, A. Govindaraj, and C. N. R. Rao, "Simple Synthesis of MoS_2 and WS_2 Nanotubes," *Adv. Mater.*, vol. 13, no. 4, pp. 283–286, Feb. 2001.

[147] J. Chen, S. L. Li, F. Gao, and Z. L. Tao, "Synthesis and Characterization of WS_2 Nanotubes," *Chem. Mater.*, vol. 15, no. 4, pp. 1012–1019, 2003.

[148] K.-K. Liu *et al.*, "Growth of Large-Area and Highly Crystalline MoS_2 Thin Layers on Insulating Substrates," *Nano Lett.*, vol. 12, no. 3, pp. 1538–1544, Mar. 2012.

[149] A. S. George *et al.*, "Wafer Scale Synthesis and High Resolution Structural Characterization of Atomically Thin MoS_2 Layers," *Adv. Funct. Mater.*, vol. 24, no. 47, pp. 7461–7466, 2014.

[150] J. Yang *et al.*, "Wafer-scale synthesis of thickness-controllable MoS_2 films via solution-processing using a dimethylformamide/n-butylamine/2-aminoethanol solvent system," *Nanoscale*, vol. 7, no. 20, pp. 9311–9319, 2015.

[151] Y. R. Lim *et al.*, "Wafer-Scale, Homogeneous MoS_2 Layers on Plastic Substrates for Flexible Visible-Light Photodetectors," *Adv. Mater.*, vol. 28, pp. 5025–5030, 2016.

[152] H. Yang, A. Giri, S. Moon, S. Shin, J. M. Myoung, and U. Jeong, "Highly Scalable Synthesis of MoS_2Thin Films with Precise Thickness Control via Polymer-Assisted Deposition," *Chem. Mater.*, vol. 29, no. 14, pp. 5772–5776, 2017.

[153] R. Ionescu *et al.*, "Chelant Enhanced Solution Processing for Wafer Scale Synthesis of Transition Metal Dichalcogenide Thin Films," *Sci. Rep.*, vol. 7, no. 1, p. 6419, 2017.

[154] Y. H. Hung *et al.*, "Scalable Patterning of MoS_2 Nanoribbons by Micromolding in Capillaries," *ACS Appl. Mater. Interfaces*, vol. 8, no. 32, pp. 20993–21001, 2016.

[155] Y. R. Lim *et al.*, "Roll-to-Roll Production of Layer-Controlled Molybdenum Disulfide: A Platform for 2D Semiconductor-Based Industrial Applications," *Adv. Mater.*, vol. 30, no. 5, p. 1705270, 2018.

[156] Y. Xi *et al.*, "Fabrication of MoS_2 thin film transistors via selective-area solution deposition methods," *J. Mater. Chem. C*, vol. 3, no. 16, pp. 3842–3847, 2015.

[157] D. B. Mitzi, "Solution processing of chalcogenide semiconductors via dimensional reduction," *Adv. Mater.*, vol. 21, no. 31, pp. 3141–3158, 2009.

[158] S. Walia *et al.*, "Characterization of metal contacts for two-dimensional MoS_2 nanoflakes," *Appl. Phys. Lett.*, vol. 103, no. 23, pp. 232105–1, 2013.

[159] H. Li *et al.*, "Rapid and Reliable Thickness Identification of Two-Dimensional Nanosheets Using Optical Microscopy," *ACS Nano*, vol. 7, no. 11, pp. 10344–10353,

Nov. 2013.

[160] I. Jung *et al.*, "Simple Approach for High-Contrast Optical Imaging and Characterization of Graphene-Based Sheets," *Nano Lett.*, vol. 7, no. 12, pp. 3569–3575, Dec. 2007.

[161] M. Conroy and J. Armstrong, "A comparison of surface metrology techniques," *J. Phys. Conf. Ser.*, vol. 13, pp. 458–465, 2005.

[162] J. Schmit, K. Creath, and J. C. Wyant, "Surface Profilers, Multiple Wavelength, and White Light Intereferometry," in *Optical Shop Testing*, Third Edit., D. Malacara, Ed. New York: John Wiley & Sons, Inc, 2007, pp. 667–755.

[163] G. Binnig, H. Rohrer, C. Gerber, and E. Weibel, "Surface Studies by Scanning Tunneling Microscopy," *Phys. Rev. Lett.*, vol. 49, no. 1, pp. 57–61, Jul. 1982.

[164] G. Binnig, C. F. Quate, and C. Gerber, "Atomic Force Microscope," *Phys. Rev. Lett.*, vol. 56, no. 9, pp. 930–933, Mar. 1986.

[165] F. J. Giessibl, "Advances in atomic force microscopy," *Rev. Mod. Phys.*, vol. 75, no. 3, pp. 949–983, Jul. 2003.

[166] M. Stedman, "Basis for comparing the performance of surface-measuring machines," *Precis. Eng.*, vol. 9, no. 3, pp. 149–152, 1987.

[167] P. J. Larkin, "Basic Principles," in *Infrared and Raman Spectroscopy Principles and Spectral Interpretation*, P. J. B. T.-I. and R. S. (Second E. Larkin, Ed. Elsevier, 2011, pp. 7–26.

[168] S. Wartewig, "Basic Principles of Vibrational Spectroscopy," in *IR and Raman spectroscopy: fundamental processing*, 2003, pp. 27–33.

[169] B. Schrader, "General survey of vibrational spectroscopy," in *Infrared and Raman Spectroscopy-Methods and Applications*, 1995, pp. 7–61.

[170] A. Li, "Interaction of Nanoparticles with Radiation," in *Witt, A.N., Clayton, G.C., Draine, B.T. (Eds.), Astrophysics of Dust, vol. 309, ASP Conference Series*, 2004, pp. 417–453.

[171] H. Bluhm, "X-ray photoelectron spectroscopy (XPS) for in situ characterization of thin film growth," in *In Situ Characterization of Thin Film Growth*, G. Koster and G. Rijnders, Eds. Cambridge, U.K.: Woodhead Publishing Series in Electronic and Optical Materials, 2011, pp. 75–98.

[172] J. Wang, J. Han, X. Chen, and X. Wang, "Design strategies for two-dimensional

material photodetectors to enhance device performance," *InfoMat*, 2019.

[173] M. Buscema *et al.*, "Photocurrent generation with two-dimensional van der Waals semiconductors," *Chem. Soc. Rev.*, vol. 44, no. 11, pp. 3691–3718, 2015.

[174] N. M. Abd-Alghafour, N. M. Ahmed, Z. Hassan, and M. Bououdina, "High-performance p–n heterojunction photodetectors based on V_2O_5 nanorods by spray pyrolysis," *Appl. Phys. A Mater. Sci. Process.*, 2016.

[175] F. Wang *et al.*, "2D library beyond graphene and transition metal dichalcogenides: A focus on photodetection," *Chem. Soc. Rev.*, 2018.

[176] K. Thakar and S. Lodha, "Optoelectronic and photonic devices based on transition metal dichalcogenides," *Mater. Res. Express*, vol. 7, no. 1, p. 14002, 2019.

[177] Q. Zhao *et al.*, "The role of traps in the photocurrent generation mechanism in thin InSe photodetectors," *Mater. Horizons*, 2020.

[178] M. Long, P. Wang, H. Fang, and W. Hu, "Progress, Challenges, and Opportunities for 2D Material Based Photodetectors," *Adv. Funct. Mater.*, 2019.

[179] S. R. Tamalampudi *et al.*, "High performance and bendable few-layered InSe photodetectors with broad spectral response," *Nano Lett.*, 2014.

[180] G. Konstantatos and E. H. Sargent, "Nanostructured materials for photon detection," *Nat. Nanotechnol.*, vol. 5, no. 6, pp. 391–400, 2010.

[181] P. Giraud *et al.*, "Field effect transistors and phototransistors based upon p-type solution-processed PbS nanowires," *Nanotechnology*, 2018.

[182] J. Wang, H. Fang, X. Wang, X. Chen, W. Lu, and W. Hu, "Recent Progress on Localized Field Enhanced Two-dimensional Material Photodetectors from Ultraviolet—Visible to Infrared," *Small*. 2017.

[183] N. Li, Z. Lan, L. Cai, and F. Zhu, "Advances in solution-processable near-infrared phototransistors," *Journal of Materials Chemistry C*. 2019.

[184] C. Xie, C. Mak, X. Tao, and F. Yan, "Photodetectors Based on Two-Dimensional Layered Materials Beyond Graphene," *Adv. Funct. Mater.*, vol. 27, no. 19, p. 1603886, May 2017.

[185] N. Huo and G. Konstantatos, "Recent Progress and Future Prospects of 2D-Based Photodetectors," *Adv. Mater.*, vol. 30, no. 51, p. 1801164, Dec. 2018.

[186] J. M. Liu, *Photonic devices*, vol. 9780521551. 2005.

[187] G. R. D. L. João P. Braga, G. G. João P. Braga, Guilherme R. De Lima, and G. G. and L.

F. Santos, “Electrical Characterization of Thin-Film Transistors Based on Solution-Processed Metal Oxides,” in *Design, Simulation and Construction of Field Effect Transistors*, E. by D. Vikraman and H.-S. Kim, Eds. IntechOpen, 2018, pp. 135–155.

[188] A. Ortiz-Conde, F. J. García Sánchez, J. J. Liou, A. Cerdeira, M. Estrada, and Y. Yue, “A review of recent MOSFET threshold voltage extraction methods,” *Microelectron. Reliab.*, vol. 42, no. 4–5, pp. 583–596, 2002.

[189] A. Ortiz-Conde, F. J. García-Sánchez, J. Muci, A. Terán Barrios, J. J. Liou, and C. S. Ho, “Revisiting MOSFET threshold voltage extraction methods,” *Microelectron. Reliab.*, vol. 53, no. 1, pp. 90–104, 2013.

[190] E. Fortunato, P. Barquinha, and R. Martins, “Oxide semiconductor thin-film transistors: A review of recent advances,” *Advanced Materials*, vol. 24, no. 22. pp. 2945–2986, 2012.

[191] H. H. Choi, K. Cho, C. D. Frisbie, H. Sirringhaus, and V. Podzorov, “Critical assessment of charge mobility extraction in FETs,” *Nature Materials*. 2017.

[192] K. F. Mak and J. Shan, “Photonics and optoelectronics of 2D semiconductor transition metal dichalcogenides,” *Nat. Photonics*, vol. 10, no. 4, pp. 216–226, 2016.

[193] D. S. Tsai *et al.*, “Few-layer MoS_2 with high broadband photogain and fast optical switching for use in harsh environments,” *ACS Nano*, vol. 7, no. 5, pp. 3905–3911, 2013.

[194] D. S. Tsai *et al.*, “Trilayered MoS_2 metal -Semiconductor-metal photodetectors: Photogain and radiation resistance,” *IEEE J. Sel. Top. Quantum Electron.*, vol. 20, no. 1, 2014.

[195] Y. Zhang *et al.*, “In Situ Fabrication of Vertical Multilayered MoS_2/Si Homotype Heterojunction for High-Speed Visible-Near-Infrared Photodetectors,” *Small*, vol. 12, no. 8, pp. 1062–1071, 2016.

[196] Z. Lou *et al.*, “High-performance MoS_2/Si heterojunction broadband photodetectors from deep ultraviolet to near infrared,” *Opt. Lett.*, vol. 42, no. 17, pp. 3335–3338, 2017.

[197] P. Xiao *et al.*, “Solution-Processed 3D RGO–MoS_2/Pyramid Si Heterojunction for Ultrahigh Detectivity and Ultra-Broadband Photodetection,” *Adv. Mater.*, vol. 30, no. 31, p. 1801729, Aug. 2018.

[198] R. Zhuo *et al.*, “High-performance self-powered deep ultraviolet photodetector based on MoS_2/GaN p–n heterojunction,” *J. Mater. Chem. C*, vol. 6, no. 2, pp. 299–303, 2018.

[199] C. Jia *et al.*, “A self-powered high-performance photodetector based on a MoS_2/GaAs heterojunction with high polarization sensitivity,” *J. Mater. Chem. C*, 2019.

[200] Y. Lee *et al.*, "Trap-induced photoresponse of solution-synthesized MoS_2," *Nanoscale*, vol. 8, no. 17, pp. 9193–9200, 2016.

[201] J. Yang *et al.*, "MoS_2–InGaZnO Heterojunction Phototransistors with Broad Spectral Responsivity," *ACS Appl. Mater. Interfaces*, vol. 8, no. 13, pp. 8576–8582, Apr. 2016.

[202] X.-M. Zhang, S.-H. Tseng, and M.-Y. Lu, "Large-Area Ultraviolet Photodetectors Based on p-Type Multilayer MoS_2 Enabled by Plasma Doping," *Applied Sciences*, vol. 9, no. 6. 2019.

[203] P. R. Berger, "Metal-semiconductor-metal photodetectors," *Proc. SPIE - Int. Soc. Opt. Eng.*, vol. 4285, no. 2001, pp. 198–207, 2001.

[204] M. Annamalai *et al.*, "Surface energy and wettability of van der Waals structures," *Nanoscale*, vol. 8, no. 10, pp. 5764–5770, 2016.

[205] F. Qi *et al.*, "Effect of hydrogen on the growth of MoS_2 thin layers by thermal decomposition method," *Vacuum*, vol. 119, pp. 204–208, 2015.

[206] H. B. Michaelson, "The work function of the elements and its periodicity," *J. Appl. Phys.*, vol. 48, no. 11, pp. 4729–4733, 1977.

[207] S. Halas and T. Durakiewicz, "Work functions of elements expressed in terms of the Fermi energy and the density of free electrons," *J. Phys. Condens. Matter*, vol. 10, no. 10, pp. 10815–10826, 1998.

[208] T. Drummond, "Work Functions of the transition metals and metal silicides," pp. 1–24, 1999.

[209] F. Wang *et al.*, "Synthesis , properties and applications of 2D non-graphene materials," *Nanotechnology*, vol. 26, no. 29, p. 292001, 2015.

[210] K. Lee, H.-Y. Kim, M. Lotya, J. N. Coleman, G.-T. Kim, and G. S. Duesberg, "Electrical Characteristics of Molybdenum Disulfide Flakes Produced by Liquid Exfoliation," *Adv. Mater.*, vol. 23, no. 36, pp. 4178–4182, Sep. 2011.

[211] S. Das, H. Y. Chen, A. V. Penumatcha, and J. Appenzeller, "High performance multilayer MoS_2 transistors with scandium contacts," *Nano Lett.*, vol. 13, no. 1, pp. 100–105, 2013.

[212] N. Kaushik *et al.*, "Schottky barrier heights for Au and Pd contacts to MoS_2," *Appl. Phys. Lett.*, vol. 105, no. 11, pp. 1–5, 2014.

[213] B. Liu, A. Abbas, and C. Zhou, "Two-Dimensional Semiconductors: From Materials Preparation to Electronic Applications," *Adv. Electron. Mater.*, vol. 3, no. 7, pp. 1–17,

2017.

[214] F. Liu *et al.*, "Van der Waals p–n Junction Based on an Organic–Inorganic Heterostructure," *Adv. Funct. Mater.*, vol. 25, no. 36, pp. 5865–5871, Sep. 2015.

[215] V. L. Rideout, "A review of the theory and technology for ohmic contacts to group III–V compound semiconductors," *Solid. State. Electron.*, vol. 18, no. 6, pp. 541–550, 1975.

[216] P.Stallinga, *Electrical Characterization of Organic Electronic Materials and Devices*. 2009.

[217] B. Roul, M. Kumar, M. K. Rajpalke, T. N. Bhat, and S. B. Krupanidhi, "Binary group III-nitride based heterostructures: band offsets and transport properties," *J. Phys. D. Appl. Phys.*, vol. 48, no. 42, p. 423001, 2015.

[218] S. Averine, Y. C. Chan, and Y. L. Lam, "Evaluation of Schottky contact parameters in metal–semiconductor–metal photodiode structures," *Appl. Phys. Lett.*, vol. 77, no. 2, pp. 274–276, Jun. 2000.

[219] A. J. Chiquito, C. A. Amorim, O. M. Berengue, L. S. Araujo, E. P. Bernardo, and E. R. Leite, "Back-to-back Schottky diodes: the generalization of the diode theory in analysis and extraction of electrical parameters of nanodevices," *J. Phys. Condens. Matter*, vol. 24, no. 22, p. 225303, 2012.

[220] P. Vabbina *et al.*, "Highly Sensitive Wide Bandwidth Photodetector Based on Internal Photoemission in CVD Grown p-Type MoS_2/Graphene Schottky Junction," *ACS Appl. Mater. Interfaces*, vol. 7, no. 28, pp. 15206–15213, Jul. 2015.

[221] Y. Wang *et al.*, "Van der Waals contacts between three-dimensional metals and two-dimensional semiconductors," *Nature*, vol. 568, pp. 70–74, 2019.

[222] L. Jiao *et al.*, "Layer-dependent photoresponse of 2D MoS_2 films prepared by pulsed laser deposition," *J. Mater. Chem. C*, vol. 7, no. 9, pp. 2522–2529, 2019.

[223] G. M. Ali and P. Chakrabarti, "ZnO-based interdigitated MSM and MISIM ultraviolet photodetectors," *J. Phys. D. Appl. Phys.*, vol. 43, no. 41, p. 415103, 2010.

[224] A. Islam, J. Lee, and P. X.-L. Feng, "Atomic Layer GaSe/MoS_2 van der Waals Heterostructure Photodiodes with Low Noise and Large Dynamic Range," *ACS Photonics*, vol. 5, no. 7, pp. 2693–2700, Jul. 2018.

[225] F. Yan, Z. Wei, X. Wei, Q. Lv, W. Zhu, and K. Wang, "Toward High-Performance Photodetectors Based on 2D Materials: Strategy on Methods," *Small Methods*, vol. 2, no. 5, p. 1700349, May 2018.

[226] L. Dong, J. Yu, R. Jia, J. Hu, Y. Zhang, and J. Sun, "Self-powered MSM deep-ultraviolet B-Ga_2O_3 photodetector realized by an asymmetrical pair of Schottky contacts," *Opt. Mater. Express*, vol. 9, no. 3, pp. 1191–1199, 2019.

[227] Z. L. Wang, "Progress in Piezotronics and Piezo-Phototronics," *Adv. Mater.*, vol. 24, no. 34, pp. 4632–4646, Sep. 2012.

[228] H.-Y. Chen *et al.*, "Realization of a self-powered ZnO MSM UV photodetector with high responsivity using an asymmetric pair of Au electrodes," *J. Mater. Chem. C*, vol. 2, no. 45, pp. 9689–9694, 2014.

[229] A. Di Bartolomeo *et al.*, "Hybrid graphene/silicon Schottky photodiode with intrinsic gating effect," *2D Mater.*, vol. 4, no. 2, p. 25075, 2017.

[230] J. Woo and H. Hwang, "Communication—Comprehensive Assessment of a Back-to-Back Schottky Diode with Ultrathin TiO_2 Layer for Cross-Point Selector Applications," *ECS J. Solid State Sci. Technol.*, vol. 5, no. 6, pp. Q188–Q190, Jan. 2016.

[231] J. Quereda, T. S. Ghiasi, F. A. van Zwol, C. H. van der Wal, and B. J. van Wees, "Observation of bright and dark exciton transitions in monolayer $MoSe_2$ by photocurrent spectroscopy," *2D Mater.*, vol. 5, no. 1, p. 15004, 2017.

[232] G. Fiori *et al.*, "Electronics based on two-dimensional materials," *Nat. Nanotechnol.*, vol. 9, no. 10, pp. 768–779, 2014.

[233] K. F. Mak, K. L. McGill, J. Park, and P. L. McEuen, "Valleytronics. The valley Hall effect in MoS_2 transistors.," *Science*, vol. 344, no. 6191, pp. 1489–92, 2014.

[234] L. K. Tan, B. Liu, J. H. Teng, S. Guo, H. Y. Low, and K. P. Loh, "Atomic layer deposition of a MoS_2 film," *Nanoscale*, vol. 6, no. 18, pp. 10584–10588, 2014.

[235] M. Amani *et al.*, "High Luminescence Efficiency in MoS_2 Grown by Chemical Vapor Deposition," *ACS Nano*, vol. 10, no. 7, pp. 6535–6541, 2016.

[236] L. Liu, S. B. Kumar, Y. Ouyang, and J. Guo, "Performance limits of monolayer transition metal dichalcogenide transistors," *IEEE Trans. Electron Devices*, vol. 58, no. 9, pp. 3042–3047, 2011.

[237] K. C. Kwon *et al.*, "Tungsten disulfide thin film/p-type Si heterojunction photocathode for efficient photochemical hydrogen production," *MRS Commun.*, vol. 7, no. 2, pp. 272–279, 2017.

[238] Z. Li *et al.*, "Facile synthesis of large-area and highly crystalline WS_2 film on dielectric surfaces for SERS," *J. Alloys Compd.*, vol. 666, pp. 412–418, May 2016.

[239] K. C. Kwon *et al.*, "Synthesis of atomically thin transition metal disulfides for charge transport layers in optoelectronic devices," *ACS Nano*, vol. 9, no. 4, pp. 4146–4155, 2015.

[240] B. R. Srinivasan, C. Näther, S. N. Dhuri, and W. Bensch, "On the importance of H-bonding interactions in organic ammonium tetrathiotungstates," *Monatshefte fur Chemie*, vol. 137, no. 4, pp. 397–411, 2006.

[241] B. R. Srinivasan, A. R. Naik, C. Näther, and W. Bensch, "Synthesis, spectroscopy and crystal structures of chiral organic ammonium tetrathiometalates showing N-H···S and C-H···S interactions," *Zeitschrift fur Anorg. und Allg. Chemie*, vol. 633, no. 4, pp. 582–588, 2007.

[242] W. Zhao *et al.*, "Lattice dynamics in mono- and few-layer sheets of WS_2 and WSe_2," *Nanoscale*, vol. 5, no. 20, pp. 9677–9683, 2013.

[243] M. A. Bissett, A. G. Hattle, A. J. Marsden, I. A. Kinloch, and R. A. W. Dryfe, "Enhanced Photoluminescence of Solution-Exfoliated Transition Metal Dichalcogenides by Laser Etching," *ACS Omega*, vol. 2, no. 2, pp. 738–745, Feb. 2017.

[244] L. Su, Y. Yu, L. Cao, and Y. Zhang, "Effects of substrate type and material-substrate bonding on high-temperature behavior of monolayer WS_2," *Nano Res.*, vol. 8, no. 8, pp. 2686–2697, 2015.

[245] N. T. McDevitt, J. S. Zabinski, and M. S. Donley, "The use of Raman scattering to study disorder in pulsed laser deposited MoS_2 films," *Thin Solid Films*, vol. 240, no. 1–2, pp. 76–81, 1994.

[246] N. T. McDevitt, J. S. Zabinski, M. S. Donley, and J. E. Bultman, "Disorder-Induced Low-Frequency Raman Band Observed in Deposited MoS_2 Films," *Appl. Spectrosc.*, vol. 48, no. 6, pp. 733–736, 1994.

[247] Y. Sang, Z. Zhao, M. Zhao, P. Hao, Y. Leng, and H. Liu, "From UV to near-infrared, WS_2 nanosheet: A novel photocatalyst for full solar light spectrum photodegradation," *Adv. Mater.*, vol. 27, pp. 363–369, 2015.

[248] S. M. Tan and M. Pumera, "Bottom-up Electrosynthesis of Highly Active Tungsten Sulfide (WS_{3-x}) Films for Hydrogen Evolution," *ACS Appl. Mater. Interfaces*, vol. 8, p. 3948−3957, 2016.

[249] M. M. Alsabban, S. Min, M. N. Hedhili, J. Ming, L.-J. Li, and K.-W. Huang, "Editors' Choice Growth of Layered WS_2 Electrocatalysts for Highly Efficient Hydrogen Production Reaction," *ECS J. Solid State Sci. Technol.*, vol. 5, no. 11, pp. Q3067–Q3071, 2016.

[250] A. Castellanos-Gomez, M. Barkelid, A. M. Goossens, V. E. Calado, H. S. J. Van Der Zant, and G. A. Steele, "Laser-thinning of MoS_2: On demand generation of a single-layer semiconductor," *Nano Lett.*, vol. 12, no. 6, pp. 3187–3192, Jun. 2012.

[251] J. Lu *et al.*, "Improved Photoelectrical Properties of MoS_2 Films after Laser Micromachining," *ACS Nano*, vol. 8, no. 6, pp. 6334–6343, 2014.

[252] L. Hu, X. Shan, Y. Wu, J. Zhao, and X. Lu, "Laser Thinning and Patterning of MoS_2 with Layer-by-Layer Precision," *Sci. Rep.*, vol. 7, no. 1, p. 15538, 2017.

[253] A. Venkatakrishnan *et al.*, "Microsteganography on WS_2 Monolayers Tailored by Direct Laser Painting," *ACS Nano*, vol. 11, no. 1, pp. 713–720, Jan. 2017.

[254] J. Park, M. S. Kim, E. Cha, J. Kim, and W. Choi, "Synthesis of uniform single layer WS_2 for tunable photoluminescence," *Sci. Rep.*, vol. 7, no. 1, p. 16121, 2017.

[255] E. Gu *et al.*, "A real-time Raman spectroscopy study of the dynamics of laser-thinning of MoS_2 flakes to monolayers," *AIP Adv.*, vol. 7, no. 12, p. 125329, 2017.

[256] J. Park *et al.*, "Composition-Tunable Synthesis of Large-Scale $Mo_{1-x}W_xS_2$ Alloys with Enhanced Photoluminescence," *ACS Nano*, vol. 12, no. 6, pp. 6301–6309, Jun. 2018.

[257] L. Gong *et al.*, "Emergence of photoluminescence on bulk MoS_2 by laser thinning and gold particle decoration," *Nano Res.*, vol. 11, no. 9, pp. 4574–4586, 2018.

[258] J. K. Wuenschell and H. Helvajian, "Enhanced laser crystallization of thin film amorphous molybdenum disulfide (MoS_2) by means of pulsed laser ultrasound," *Opt. Express*, vol. 27, no. 4, pp. 5859–5873, 2019.

[259] M. H. Heyne, J.-F. de Marneffe, I. Radu, E. C. Neyts, and S. De Gendt, "Thermal recrystallization of short-range ordered WS_2 films," *J. Vac. Sci. Technol. A*, vol. 36, no. 5, p. 05G501, Jul. 2018.

[260] J. Lu *et al.*, "Atomic Healing of Defects in Transition Metal Dichalcogenides," *Nano Lett.*, vol. 15, no. 5, pp. 3524–3532, May 2015.

[261] B. C. Tran Khac, K. J. Jeon, S. T. Choi, Y. S. Kim, F. W. Delrio, and K. H. Chung, "Laser-Induced Particle Adsorption on Atomically Thin MoS_2," *ACS Appl. Mater. Interfaces*, vol. 8, no. 5, pp. 2974–2984, 2016.

[262] Z. He *et al.*, "Revealing Defect-State Photoluminescence in Monolayer WS_2 by Cryogenic Laser Processing," *ACS Nano*, vol. 10, no. 6, pp. 5847–5855, Jun. 2016.

[263] S. Ma *et al.*, "Enhanced Photocatalytic Activity of WS_2 Film by Laser Drilling to Produce Porous WS_2/WO_3 Heterostructure," *Sci. Rep.*, vol. 7, no. 1, p. 3125, 2017.

[264] P. Atkin *et al.*, "Laser exposure induced alteration of WS_2 monolayers in the presence of ambient moisture," *2D Mater.*, vol. 5, no. 1, p. 15013, 2017.

[265] A. Alrasheed *et al.*, "Surface Properties of Laser-Treated Molybdenum Disulfide Nanosheets for Optoelectronic Applications," *ACS Appl. Mater. Interfaces*, vol. 10, no. 21, pp. 18104–18112, 2018.

[266] T. Afaneh, P. K. Sahoo, I. A. P. Nobrega, Y. Xin, and H. R. Gutiérrez, "Laser-Assisted Chemical Modification of Monolayer Transition Metal Dichalcogenides," *Adv. Funct. Mater.*, vol. 28, no. 37, pp. 1–7, 2018.

[267] G. D. and P. M. D. and M. Drndić, "Laser-induced fabrication of nanoporous monolayer WS_2 membranes," *2D Mater.*, vol. 5, no. 3, p. 35011, 2018.

[268] E. Kim *et al.*, "Site Selective Doping of Ultrathin Metal Dichalcogenides by Laser-Assisted Reaction," *Adv. Mater.*, vol. 28, no. 2, pp. 341–346, Nov. 2015.

[269] S. W. Kim *et al.*, "Patterning of periodic ripples in monolayer MoS_2 by using laser irradiation," *J. Korean Phys. Soc.*, vol. 69, no. 10, pp. 1505–1508, 2016.

[270] R. Rani, Dimple, N. Jena, A. Kundu, A. De Sarkar, and K. S. Hazra, "Controlled formation of nanostructures on MoS_2 layers by focused laser irradiation," *Appl. Phys. Lett.*, vol. 110, no. 8, p. 83101, Feb. 2017.

[271] G.-H. Park, K. Nielsch, and A. Thomas, "2D Transition Metal Dichalcogenide Thin Films Obtained by Chemical Gas Phase Deposition Techniques," *Adv. Mater. Interfaces*, vol. 6, no. 3, p. 1800688, Feb. 2019.

[272] W. Hao, C. Marichy, and C. Journet, "Atomic layer deposition of stable 2D materials," *2D Mater.*, vol. 6, no. 1, p. 12001, 2018.

[273] C. C. Huang *et al.*, "Transfer-Free Growth of Atomically Thin Transition Metal Disulfides Using a Solution Precursor by a Laser Irradiation Process and Their Application in Low-Power Photodetectors," *Nano Lett.*, vol. 16, no. 4, pp. 2463–2470, 2016.

[274] Y. Z. Chen *et al.*, "Ultrafast and low temperature synthesis of highly crystalline and patternable few-layers tungsten diselenide by laser irradiation assisted selenization process," *ACS Nano*, vol. 9, no. 4, pp. 4346–4353, 2015.

[275] S.-K. Lee, J.-B. Lee, J. Singh, K. Rana, and J.-H. Ahn, "Drying-Mediated Self-Assembled Growth of Transition Metal Dichalcogenide Wires and their Heterostructures," *Adv. Mater.*, vol. 27, no. 28, pp. 4142–4149, Jul. 2015.

[276] C. Tan *et al.*, "Recent Advances in Ultrathin Two-Dimensional Nanomaterials," *Chem.*

Rev., vol. 117, no. 9, pp. 6225–6331, May 2017.

[277] J. Henrie, S. Kellis, S. M. Schultz, and A. Hawkins, "Electronic color charts for dielectric films on silicon," *Opt. Express*, vol. 12, no. 7, pp. 1464–1469, 2004.

[278] W. A. Pliskin and E. E. Conrad, "Nondestructive Determination of Thickness and Refractive Index of Transparent Films," *IBM J. Res. Dev.*, vol. 8, no. 1, pp. 43–51, 1964.

[279] Zhipei Sun, "Optical modulators with two-dimensional layered materials," *Nat. Photonics*, vol. 10, pp. 3851–3851, Mar. 2016.

[280] H. Zhang, N. Healy, A. F. J. Runge, C. C. Huang, D. W. Hewak, and A. C. Peacock, "Optical-resonance-enhanced nonlinearities in a MoS_2-coated single-mode fiber," *Opt. Lett.*, vol. 43, no. 13, pp. 3100–3103, 2018.

[281] R. Weis and T. Gaylord, "Lithium Niobate: Summary of Physical Properties and Crystal Structure," *Appl. Phys. A Mater. Sci. Process.*, vol. 37, no. 4, pp. 191–203, 1985.

[282] A. E. Nguyen *et al.*, "Towards Ferroelectric Control of Monolayer MoS_2," *Nano Lett.*, vol. 15, no. 5, p. 3364−3369, 2015.

[283] E. Preciado *et al.*, "Scalable fabrication of a hybrid field-effect and acousto-electric device by direct growth of monolayer $MoS_2/LiNbO_3$," *Nat. Commun.*, vol. 6, pp. 1–8, 2015.

[284] L. Mateos, L. E. Bausá, and M. O. Ramírez, "Micro-spectroscopic characterization of ferroelectric domain structures in Yb^{3+}:$LiNbO_3$ prepared by electron beam writing," *Opt. Mater. Express*, vol. 4, no. 5, pp. 1077–1087, 2014.

[285] G. Stone, B. Knorr, V. Gopalan, and V. Dierolf, "Frequency shift of Raman modes due to an applied electric field and domain inversion in $LiNbO_3$," *Phys. Rev. B*, vol. 84, no. 13, p. 134303, Oct. 2011.

[286] G. F. Nataf, M. Guennou, A. Haußmann, N. Barrett, and J. Kreisel, "Evolution of defect signatures at ferroelectric domain walls in Mg-doped $LiNbO_3$," *Phys. status solidi – Rapid Res. Lett.*, vol. 10, no. 3, pp. 222–226, Mar. 2016.

[287] T. Wang, J. Li, and G. Zhao, "Synthesis of MoS_2 and MoO_3 hierarchical nanostructures using a single-source molecular precursor," *Powder Technol.*, vol. 253, pp. 347–351, 2014.

[288] B. C. Windom, W. G. Sawyer, and D. W. Hahn, "A Raman Spectroscopic Study of MoS_2 and MoO_3: Applications to Tribological Systems," *Tribol. Lett.*, vol. 42, no. 3, pp. 301–310, 2011.

[289] Q. Van Le *et al.*, "$(NH_4)_2WS_4$precursor as a hole-injection layer in organic optoelectronic devices," *Chem. Eng. J.*, vol. 284, pp. 285–293, 2016.

[290] T. Y. Chen, Y. H. Chang, C. L. Hsu, K. H. Wei, C. Y. Chiang, and L. J. Li, "Comparative study on MoS_2 and WS_2 for electrocatalytic water splitting," *Int. J. Hydrogen Energy*, vol. 38, no. 28, pp. 12302–12309, 2013.

[291] A. Hasani *et al.*, "Facile Solution Synthesis of Tungsten Trioxide Doped with Nanocrystalline Molybdenum Trioxide for Electrochromic Devices," *Sci. Rep.*, vol. 7, no. 1, p. 13258, 2017.

[292] Z. Q. Xu *et al.*, "Synthesis and Transfer of Large-Area Monolayer WS_2 Crystals: Moving Toward the Recyclable Use of Sapphire Substrates," *ACS Nano*, vol. 9, no. 6, pp. 6178–6187, 2015.

[293] L. Yuan and L. Huang, "Exciton dynamics and annihilation in WS_2 2D semiconductors," *Nanoscale*, vol. 7, no. 16, pp. 7402–7408, 2015.

[294] L. Sygellou, "An in-situ photoelectron spectroscopy study of the thermal processing of ammonium tetrathiomolybdate, $(NH_4)_2MoS_4$, precursor," *Appl. Surf. Sci.*, vol. 476, pp. 1079–1085, 2019.

[295] D. Voiry *et al.*, "Enhanced catalytic activity in strained chemically exfoliated WS_2 nanosheets for hydrogen evolution," *Nat. Mater.*, vol. 12, no. 9, pp. 850–855, 2013.

[296] Y. Sun *et al.*, "Photoelectrochemical and structural characterization of carbon-doped WO_3 films prepared via spray pyrolysis," *Int. J. Hydrogen Energy*, vol. 34, no. 20, pp. 8476–8484, 2009.

[297] A. Benoit, I. Paramasivam, Y. C. Nah, P. Roy, and P. Schmuki, "Decoration of TiO_2 nanotube layers with WO_3 nanocrystals for high-electrochromic activity," *Electrochem. commun.*, vol. 11, no. 4, pp. 728–732, 2009.

[298] H. Hu *et al.*, "Broadly tunable graphene plasmons using an ion-gel top gate with low control voltage," *Nanoscale*, vol. 7, no. 46, pp. 19493–19500, 2015.

[299] M. Tosun *et al.*, "MoS_2 Heterojunctions by Thickness Modulation," *Sci. Rep.*, vol. 5, no. 1, p. 10990, Jun. 2015.

[300] J. Kang, W. Liu, D. Sarkar, D. Jena, and K. Banerjee, "Computational study of metal contacts to monolayer transition-metal dichalcogenide semiconductors," *Phys. Rev. X*, vol. 4, no. 3, pp. 1–14, 2014.

[301] H. Tan, Y. Fan, Y. Zhou, Q. Chen, W. Xu, and J. H. Warner, "Ultrathin 2D Photodetectors Utilizing Chemical Vapor Deposition Grown WS_2 With Graphene

Electrodes," *ACS Nano*, vol. 10, no. 8, pp. 7866–7873, Aug. 2016.

[302] T. Yamaguchi *et al.*, "Tunneling transport in a few monolayer-thick WS_2/graphene heterojunction," *Appl. Phys. Lett.*, vol. 105, no. 22, p. 223109, Dec. 2014.

[303] J. Kang, S. Tongay, J. Zhou, J. Li, and J. Wu, "Band offsets and heterostructures of two-dimensional semiconductors," *Appl. Phys. Lett.*, vol. 102, no. 1, p. 12111, Jan. 2013.

[304] C. Gong, H. Zhang, W. Wang, L. Colombo, R. M. Wallace, and K. Cho, "Band alignment of two-dimensional transition metal dichalcogenides: Application in tunnel field effect transistors," *Appl. Phys. Lett.*, vol. 103, no. 5, p. 53513, Jul. 2013.

[305] Y. Liang, S. Huang, R. Soklaski, and L. Yang, "Quasiparticle band-edge energy and band offsets of monolayer of molybdenum and tungsten chalcogenides," *Appl. Phys. Lett.*, vol. 103, no. 4, p. 42106, Jul. 2013.

[306] Y. Guo and J. Robertson, "Band engineering in transition metal dichalcogenides: Stacked versus lateral heterostructures," *Appl. Phys. Lett.*, vol. 108, no. 23, p. 233104, Jun. 2016.

[307] C. Zheng *et al.*, "Direct Observation of 2D Electrostatics and Ohmic Contacts in Template-Grown Graphene/WS_2 Heterostructures," *ACS Nano*, vol. 11, no. 3, pp. 2785–2793, Mar. 2017.

[308] D. S. Schulman, A. J. Arnold, and S. Das, "Contact engineering for 2D materials and devices," *Chem. Soc. Rev.*, vol. 47, no. 9, pp. 3037–3058, 2018.

[309] W. Liu, J. Kang, D. Sarkar, Y. Khatami, D. Jena, and K. Banerjee, "Role of metal contacts in designing high-performance monolayer n-type WSe_2 field effect transistors," *Nano Lett.*, vol. 13, no. 5, pp. 1983–1990, 2013.

[310] A. U. Alam, M. M. R. Howlader, and M. J. Deen, "The effects of oxygen plasma and humidity on surface roughness, water contact angle and hardness of silicon, silicon dioxide and glass," *J. Micromechanics Microengineering*, vol. 24, no. 3, p. 35010, 2014.

[311] W. Zhang, J.-K. Huang, C.-H. Chen, Y.-H. Chang, Y.-J. Cheng, and L.-J. Li, "High-Gain Phototransistors Based on a CVD MoS_2 Monolayer," *Adv. Mater.*, vol. 25, no. 25, pp. 3456–3461, 2013.

[312] N. Aspiotis *et al.*, "A lift-off method for wafer scale hetero-structuring of 2D materials," in *EUROMAT 2017: European Congress and Exhibition on Advanced Materials and Processes*, 2017.

[313] P. Bolshakov *et al.*, "Contact Engineering for Dual-Gate MoS_2 Transistors Using O_2 Plasma Exposure," *ACS Appl. Electron. Mater.*, vol. 1, no. 2, pp. 210–219, Feb. 2019.

[314] X. Song *et al.*, "A novel synthesis method for large-area MoS_2 film with improved electrical contact," *2D Mater.*, vol. 4, no. 2, 2017.

[315] Y.-C. Wu *et al.*, "Extrinsic Origin of Persistent Photoconductivity in Monolayer MoS_2 Field Effect Transistors," *Sci. Rep.*, vol. 5, p. 11472, Jun. 2015.

[316] X. Chen, Y. J. Park, T. Das, H. Jang, J.-B. Lee, and J.-H. Ahn, "Lithography-free plasma-induced patterned growth of MoS_2 and its heterojunction with graphene," *Nanoscale*, vol. 8, no. 33, pp. 15181–15188, 2016.

[317] M.-W. Lin *et al.*, "Mobility enhancement and highly efficient gating of monolayer MoS_2 transistors with polymer electrolyte," *J. Phys. D. Appl. Phys.*, vol. 45, no. 34, p. 345102, 2012.

[318] H. Şar, A. Özden, B. Yorulmaz, C. Sevik, N. Kosku Perkgoz, and F. Ay, "A comparative device performance assesment of CVD grown MoS_2 and WS_2 monolayers," *J. Mater. Sci. Mater. Electron.*, vol. 29, no. 10, pp. 8785–8792, 2018.

[319] P. Barquinha *et al.*, "Flexible and Transparent WO_3 Transistor with Electrical and Optical Modulation," *Adv. Electron. Mater.*, vol. 1, no. 5, p. 1500030, May 2015.

[320] A. K. Geim and I. V Grigorieva, "Van der Waals heterostructures," *Nature*, vol. 499, p. 419, Jul. 2013.

[321] M. Nath and C. N. Rao, "$MoSe_2$ and WSe_2 nanotubes and related structures," *Chem. Commun. (Camb).*, no. 21, pp. 2236–2237, 2001.

Appendix A

A.1 Conference Papers

1. **Mailis, Sakellaris**, Abbas, Omar Adnan, Lewis, Adam Henry, Aspiotis, Nikolaos, Huang, Chung-Che, Zeimpekis, Ioannis, Hewak, Daniel and Sazio, Pier-John. ***Direct laser synthesis of two-dimensional transition metal dichalcogenides in ambient conditions.*** The 27th International Conference on Advanced Laser Technologies (ALT'19), Prague, Czech Republic 15-20 Sep 2019. ***(Invited talk)***
2. **Abbas, Omar Adnan**, Lewis, Adam Henry, Aspiotis, Nikolaos, Huang, Chung-Che, Zeimpekis, Ioannis, Hewak, Daniel, Sazio, Pier-John and Mailis, Sakellaris. ***Direct laser synthesis of two-dimensional transition metal dichalcogenides***. Conference on Lasers and Electro-Optics/Europe–European Quantum Electronics Conference, Munich, Germany. 23-27 Jun 2019. ***(Talk)***
3. **Abbas, Omar Adnan**, Wang, He, Lewis, Adam Henry, Sessions, Neil, Aspiotis, Nikolaos, Huang, Chung-Che, Zeimpekis, Ioannis, Hewak, Daniel, Mailis, Sakellaris and Sazio, Pier-John. ***Growth of large-area, uniform, few-layer tungsten disulphide by thermal decomposition of ammonium tetrathiotungstate.*** Conference on Lasers and Electro-Optics/Europe – European Quantum Electronics Conference, Munich, Germany. 23-27 Jun 2019.***(Poster)***

*Conference papers **Not** related to this thesis :-*

4. Aspiotis, Nikolaos, **Abbas, Omar Adnan**, Zeimpekis, Ioannis, Mailis, Sakellaris, Sazio, Pier-John, Huang, Chung-Che and Hewak, Daniel. ***Wafer scale spatially selective transfer of 2D materials and heterostructures***. MRS Fall Meeting 2017, Boston, United States. 26 Nov-01 Dec 2017. ***(Poster)***
5. Aspiotis, Nikolaos, **Abbas, Omar Adnan**, Zeimpekis, Ioannis, Mailis, Sakellaris, Sazio, Pier-John, Huang, Chung-Che and Hewak, Daniel (2017) ***A lift-off method for wafer scale hetero-structuring of 2D materials***. EUROMAT 2017: European Congress and Exhibition on Advanced Materials and Processes, Thessaloniki, Greece. 17 - 22 Sep 2017.***(Talk)***

A.2 Journal papers

1. **Abbas, Omar Adnan**, Zeimpekis, Ioannis, Wang, He, Lewis, Adam Henry, Sessions, Neil, Aspiotis, Nikolaos, Huang, Chung-Che, Hewak, Daniel, Mailis, Sakellaris and Sazio, Pier-John. ***Solution-Based Synthesis of Few-Layer WS_2 Large Area Continuous Films for Electronic Applications***. Scientific Reports, 1696 (1-10), 10, 2020.

   Note :- OAA and IZ contributed equally to this work.

2. **Abbas, Omar Adnan**, Lewis, Adam Henry, Aspiotis, Nikolaos, Huang, Chung-Che, Zeimpekis, Ioannis, Hewak, Daniel, Sazio, Pier-John and Mailis, Sakellaris. ***Laser Printed Two-Dimensional Transition Metal Dichalcogenides***. (In process)

A lift-off method for wafer scale hetero-structuring of 2D materials

N. Aspiotis, O. A. Abbas, I. Zeimpekis, S. Mailis, P. J. Sazio, C. C. Huang and D. W. Hewak

Optoelectronics Research Centre, University of Southampton, SO17 1BJ, UK

The isolation of graphene [1] and closely related materials such as transition metal dichalcogenides [2], has sparked intensive worldwide research efforts towards the large scale deposition of 2D crystals and films [3][4]. So far there has been no clear winner method for the fabrication of wafer scale heterostructures in a low cost and facile manner, which is an imperative step towards the commercialization of 2D integrated circuits. Currently the techniques that have been reported in the literature employ epitaxial growth of single crystal TMDCs and mechanical stacking of CVD grown or exfoliated flakes resulting in 2D flake heterostructures [5][6].

Here we present a large-scale method for fabricating 2D heterostructures based on the common photolithographic patterning technique of lift-off. The procedure consists of the following steps i) the acceptor substrate is patterned using photolithography ii) CVD grown (graphene or MoS_2) film is transferred via a polymer assisted transfer from its original substrate to the acceptor substrate iii) then the polymer is dissolved and finally iv) the 2D material is lifted – off by dissolution of the photoresist layer in suitable solvents. The procedure can be repeated for deposition of additional patterned layer to form heterostructures.

Furthermore, by employing a double layer photoresist method optimized for the 2D materials, where instead of an alkaline developer solvent is used for the development of the pattern, each sequential transfer / patterning step does not interfere with the already transferred layers, and it is the material agnostic nature of this method that makes it suitable for multilayer stacking of patterned films. .

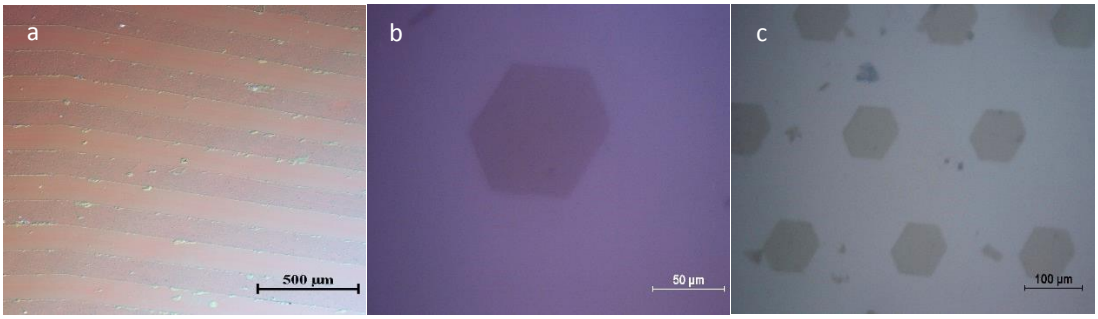

Fig.1. (a) lift-off Graphene (b), Single lift-off MoS_2 hexagon c) MoS_2 hexagonal array

References

[1] K. S. Novoselov,A. K. Geim, S. V. Morozov,D. Jiang,Y. Zhang,S. V. Dubonos, I. V. Grigorieva, A. A. Firsov "Electric Field Effect in Atomically Thin Carbon Films," *Science*, vol. 306, no. 5696, pp. 666–669, 2004.

[2] K. F. Mak, C. Lee, J. Hone, J. Shan, and T. F. Heinz, "Atomically Thin MoS_2 : A New Direct- Gap Semiconductor," *Phys. Rev. Lett.*, vol. 136805, pp. 2–5, 2010.

[3] X. Wang, H. Feng, Y. Wu, and L. Jiao, "Controlled Synthesis of Highly Crystalline MoS_2 Flakes by Chemical Vapor Deposition," *J. Am. Chem. Soc*, vol. 135, no. 14, pp. 5–8, 2013.

[4] C. C. Huang, F. Al-Saab, Y. Wang, J. Y. Ou, J. C. Walker, S. Wang, B. Gholipour, R. E. Simpson, and D. W. Hewak, "Scalable high-mobility MoS_2 thin films fabricated by an atmospheric pressure chemical vapor deposition process at ambient temperature," *Nanoscale*, vol. 6, no. 21, pp. 12792–12797, 2014.

[5] W. S. Mos, Y. Gong, J. Lin, X. Wang, G. Shi, S. Lei, Z. Lin, X. Zou, G. Ye, R. Vajtai, B. I. Yakobson, H. Terrones, M. Terrones, K. Tay, J. Lou, S. T. Pantelides, Z. Liu, W. Zhou, and P. M. Ajayan, "Vertical and in-plane heterostructures from WS_2/MoS_2 monolayers," vol. 13, no. September, p. 8, 2014.

[6] W. J. Yu, Z. Li, H. Zhou, Y. Chen, Y. Wang, Y. Huang, and X. Duan, "Vertically stacked multi-heterostructures of layered materials for logic transistors and complementary inverters.," *Nat. Mater.*, vol. 12, no. 3, pp. 246–52, 2013.

Growth of Large-Area, Uniform, Few-Layer Tungsten Disulphide by Thermal Decomposition of Ammonium Tetrathiotungstate

Omar Adnan Abbas[1], He Wang[2], Adam Henry Lewis[1], Neil Sessions[1], Nikos Aspiotis[1], Chung-Che Huang[1], Ioannis Zeimpekis[1], Dan Hewak[1], Sakellaris Mailis[3] and Pier Sazio[1]

1. Optoelectronics Research Centre, University of Southampton, Southampton, SO17 1BJ, United Kingdom
2. National Centre for Advanced Tribology, University of Southampton, Southampton SO17 1BJ, United Kingdom
3. Skolkovo Institute of Science and Technology Novaya St., 100, Skolkovo 143025, Russian Federation

Two-dimensional transition metal dichalcogenides (2D-TMDCs) such as molybdenum disulphide (2D-MoS_2) and tungsten disulphide (2D-WS_2) are now established as a class of nanomaterials that can be used in numerous applications due to their tuneable physical and chemical properties [1]. However, in terms of electrical characteristics and photoluminescence efficiency, WS_2 typically exhibits superior performance compared with the molybdenum analogue [2,3]. Nevertheless, synthesis of continuous, uniform and thickness controllable 2D-WS_2 films for (opto)electronic device fabrication is more challenging compared with better established 2D-MoS_2 growth protocols. Therefore, the search for alternative precursors and synthesis approaches of 2D-WS_2 that can provide mass production with excellent quality at low cost is highly desirable [1].

Ammonium tetrathiotungstate $(NH_4)_2WS_4$ and ammonium tetrathiomolybdate $(NH_4)_2MoS_4$ have been used as single source precursors for WS_2 and MoS_2 nanotube growth [1]. However, it was mainly the $(NH_4)_2MoS_4$ salt that has been exploited for scalable synthesis of 2D-MoS_2 [1]. The chemistry of $(NH_4)_2MoS_4$ enables the formation of uniform solutions using various solvents that results in regular, continuous films with good controllability of thickness using a variety of substrates and coating techniques [1]. This led to a dramatic extension of 2D-MoS_2 film deposited areas from centimetre scale to wafer scale and very recently with roll-to-roll production [4] combined with excellent optical and electrical characteristics when compared with other precursor systems [1,4]. In contrast, the $(NH_4)_2WS_4$ salt has not yet been explored for scalable growth of 2D-WS_2 films due to the low coordination with many solvents [5] that prevents the creation of uniform/continuous precursor films, which are essential for efficient, large scale semiconductor device fabrication [5].

In this work, we tackle this issue by refining the solvents recipe with n-methylpyrrolidone, n-butylamine and 2-aminoethanol, which significantly improves the continuity, uniformity and thickness controllability for the spin-coated precursor films. This enables the large-area growth of few-layer WS_2 films using thermal decomposition via two-step high temperature annealing without sulphurisation. The few-layer WS_2 films were characterised by optical and atomic force microscopy to confirm the continuity and two-dimensional nature of the deposited WS_2 films. Raman, photoluminescence and x-ray photoelectron spectroscopy indicate growth of highly crystalline films with an optimum composition of WS_2. The electrical response of the WS_2 films grown by this method was investigated by interrogating a back-gate thin film transistor utilising a WS_2 channel as shown in Figure 1.

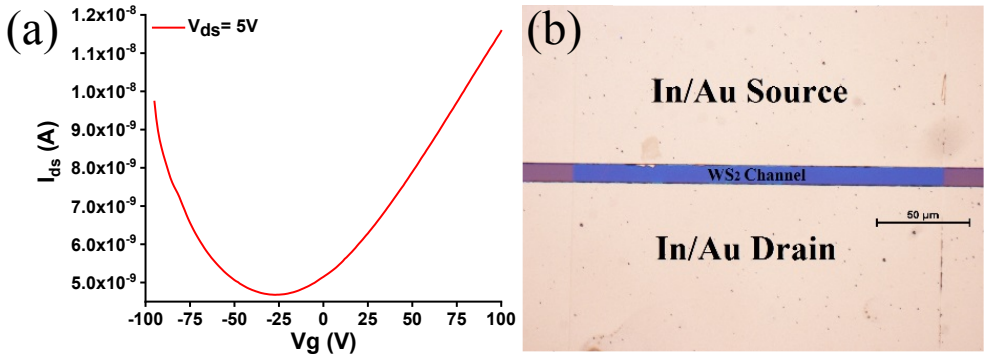

Fig. 1. (a) Transfer characteristics (source-drain current vs gate voltage) of back-gate thin film transistor (TFT) with a WS_2 channel grown by thermal decomposition of $(NH_4)_2WS_4$. (b) Optical microscopy image of the fabricated device.

References

[1] M. Samadi, N. Sarikhani, M. Zirak, H. Zhang, H. L. Zhang, and A. Z. Moshfegh, "Group 6 transition metal dichalcogenides nanomaterials: Synthesis, applications and future perspectives," Nanoscale Horiz. **3**, 90–204 (2018).
[2] L. Liu, S. B. Kumar, Y. Ouyang, and J. Guo, "Performance limits of monolayer transition metal dichalcogenide transistors," IEEE Trans. Electron Devices. **58**, 3042–3047 (2011).
[3] W. Zhao, Z. Ghorannevis, L. Chu, M. Toh, C. Kloc, P. H. Tan and G. Eda, "Evolution of Electronic Structure in Atomically Thin Sheets of WS_2 and WSe_2," ACS Nano. **7**, 791–797 (2013).
[4] Y.R. Lim, J.K. Han, S.K. Kim, Y.B. Lee, Y. Yoon, S.J. Kim, B.K. Min, Y. Kim, C. Jeon, S. Won, J.H. Kim, W. Song, S. Myung, S.S. Lee, K.S. An, and J. Lim, "Roll-to-Roll Production of Layer-Controlled Molybdenum Disulfide: A Platform for 2D Semiconductor-Based Industrial Applications," Adv. Mater. **30**, 1705270 (2018).
[5] K. C. Kwon, S.Choi, K.Hong, D. M. Andoshe, J. M. Suh, C. Kim, K. S. Choi, J. H.Oh, S. Y.Kim, and H. W.Jang, "Tungsten disulfide thin film/p-type Si heterojunction photocathode for efficient photochemical hydrogen production," MRS Commun. **7**, 272–279 (2017).

978-1-7281-0469-0/19/$31.00 ©2019 IEEE

Direct Laser Synthesis of Two-Dimensional Transition Metal Dichalcogenides

Omar Adnan Abbas[1], Adam Henry Lewis[1], Nikos Aspiotis[1], Chung-Che Huang[1], Ioannis Zeimpekis[1], Dan Hewak[1], Pier Sazio[1] and Sakellaris Mailis[2]

1. Optoelectronics Research Centre, University of Southampton, Southampton, SO17 1BJ, United Kingdom
2. Skolkovo Institute of Science and Technology Novaya St., 100, Skolkovo 143025, Russian Federation

The emergence of nanomaterials with their often superior mechanical, electronic and optical properties compared with bulk form demands a robust technology that can synthesize, modify and pattern scalably and cost effectively. This can be fulfilled via laser processing protocols which produce such materials with both high precision and excellent spatial controllability [1]. Direct laser synthesis of nanomaterials such as graphene and nano-structured metal oxides have been explored thoroughly for a wide range of applications [2,3]. However, to date, there are only a few reports associated with the laser processing of two-dimensional transition metal dichalcogenides (2D-TMDCs) [4]. These mainly utilize laser radiation for thinning TMDC films through sublimation down to a single molecular thickness [1]. However, this top-down approach is not practical for large-area and scalable production. In addition, further processing steps such as lithographic patterning are then required for discrete device fabrication.

Here we present a novel method for the local synthesis and patterning of two-dimensional MoS_2 and WS_2 layers. The synthesis of these materials is achieved by spatially selective, visible laser irradiation of suitable precursors coated on the surface of planar substrates under ambient, room temperature conditions. The non-exposed precursor regions are then completely removed in a single step, revealing the synthesised 2D-TMDCs. This method can produce micro-patterned films with lateral dimensions that approach the diffraction limit of the focused laser beam. An example of such laser synthesised MoS_2 tracks can be seen in the optical microscopy image of Figure 1(a) where it clearly shows a well-defined micro-pattern without any precursor residue. Using this method, we have achieved local synthesis of of MoS_2 and WS_2 with thickness down to three molecular layers for MoS_2 and monolayer WS_2 on various glass and crystalline substrates. The quality and thickness of the resulting films can be tuned by modifying the precursor chemistry and laser parameters. Different microprobe and spectroscopic techniques such as optical microscopy, stylus profilometry, Raman spectroscopy, photoluminescence spectroscopy (PL) and X-ray photoelectron spectroscopy (XPS) have been used to assess the quality and thickness of the deposited MoS_2 and WS_2 structures. Finally, we have demonstrated the electronic functionality of our films by fabricating a thin film transistor (TFT). The transfer characteristics (source-drain current vs gate voltage) of such a TFT using a laser-synthesised MoS_2 channel is shown in Figure 1(b).

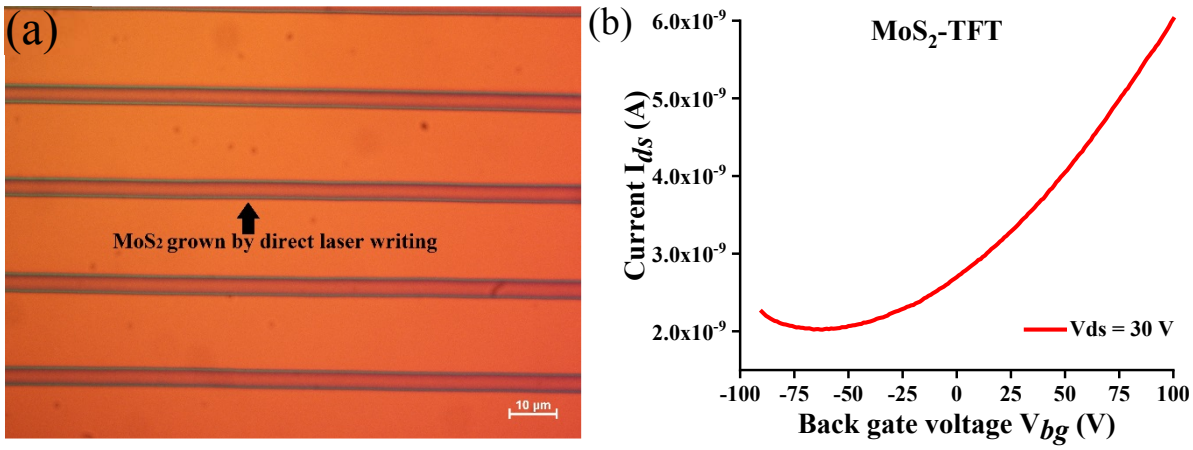

Fig. 1. (a) Optical microscopy image of MoS_2 tracks deposited by direct laser synthesis on SiO_2/Si substrate. (b) transfer characteristics (source-drain current vs gate voltage) of a back-gate thin film transistor (TFT) using a laser synthsised MoS_2 channel.

References

[1] S. Hong, H. Lee, J. Yeo, and S. H. Ko, "Digital selective laser methods for nanomaterials: From synthesis to processing," Nano Today. **11**, 547–564 (2016).
[2] M. F. El-Kady and R. B. Kaner, "Direct Laser Writing of Graphene Electronics," ACS Nano. **8**, 8725–8729 (2014).
[3] H. Palneedi, J. H. Park, D. Maurya, M. Peddigari, G. T. Hwang, V. Annapureddy, J. W. Kim, J. J. Choi, B. D. Hahn, S. Priya, K. J. Lee, and J. Ryu, "Laser Irradiation of Metal Oxide Films and Nanostructures: Applications and Advances," Adv. Mater. **30**, 1705148 (2018).
[4] M. Samadi, N. Sarikhani, M. Zirak, H. Zhang, H. L. Zhang, and A. Z. Moshfegh, "Group 6 transition metal dichalcogenides nanomaterials: Synthesis, applications and future perspectives," Nanoscale Horiz. **3**, 90–204 (2018).

978-1-7281-0469-0/19/$31.00 ©2019 IEEE

LP-I-3

Direct laser synthesis of two-dimensional transition metal dichalcogenides in ambient conditions

S. Mailis[1], O. Abbas[2], A.H. Lewis[2], N. Aspiotis[2], C.C. Huang[2], I. Zeimpekis[2], D. Hewak[2], P. Sazio[2]
[1]Skolkovo Institute of Science and Technology, Photonics and Quantum Materials, Moscow, Russian Federation
[2]University of Southampton, Optoelectronics Research Centre, Southampton, United Kingdom

The emergence of nanomaterials with their often superior mechanical, electronic, magnetic and optical properties compared with bulk, demands a mature and robust technology that can synthesize, modify and pattern both scalably and cost effectively. This can be fulfilled via laser processing protocols which produce such materials with both high precision and excellent spatial controllability [1]. Direct laser synthesis of nanomaterials such as graphene and nano-structured metal oxides have been explored thoroughly for a wide range of applications [2,3]. However, to date, there are only a few reports associated with the laser processing of two-dimensional transition metal dichalcogenides (2D-TMDCs) [4]. These mainly utilize laser radiation for thinning thick TMDC films through sublimation down to a single molecular layer [1]. However, this top-down approach is not practical for large-area and scalable production. In addition, further processing steps such as micro-patterning are then required for discrete device fabrication.

Here we present a novel method for the local synthesis and patterning of MoS_2 and WS_2 2D layers. The synthesis of these materials is achieved by spatially selective, visible laser irradiation of suitable precursors, which are deposited, on the surface of planar substrates under ambient, room temperature conditions. The non-exposed precursor regions are then completely removed in a single step, revealing the synthesised 2D material. This method can produce micro-patterned films with lateral dimensions that can be as narrow as the diffraction limit of the focussed laser beam permits. An example of such laser synthesised MoS_2 tracks can be seen in the optical microscopy image of Figure 1(a). Using this method we have achieved local synthesis of of MoS_2 and WS_2 with thickness down to three layers for MoS_2 and monolayer WS_2 on various glass and crystalline substrates. The quality and thickness of the resulting films can be tuned by modifying the precursor chemistry and laser parameters. Different microprobe and spectroscopic techniques, such as optical microscopy, stylus profilometry, Raman spectroscopy, photoluminescence spectroscopy (PL) and X-ray photoelectron spectroscopy (XPS) have been used to assess the quality and thickness of the deposited MoS_2 and WS_2 structures. Finally, we have demonstrated the electronic functionality of our films by fabricating a thin film transistor (TFT). The transfer characteristics of such a TFT (source-drain current vs gate voltage) using a laser-synthesised MoS_2 channel is shown in Figure 1(b).

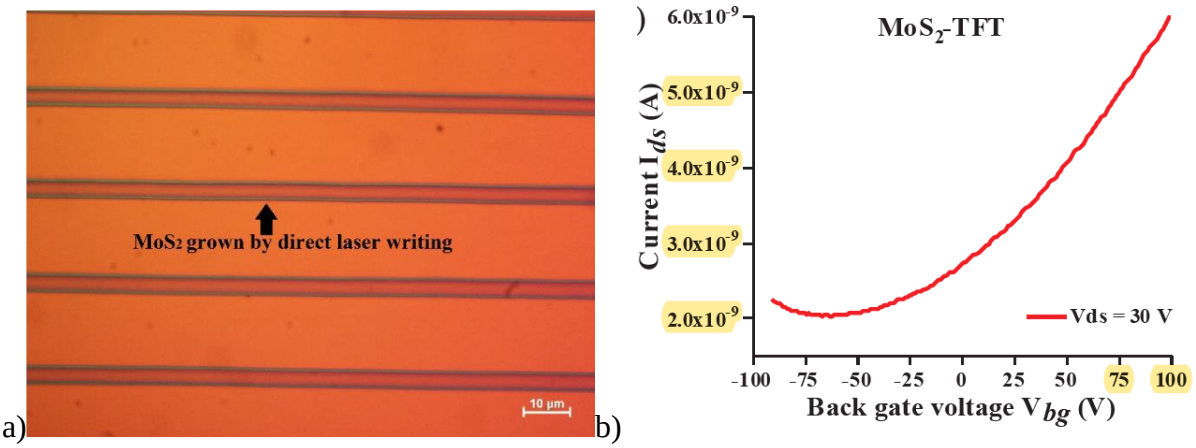

Fig. 1. (a) optical microscopy image of MoS_2 tracks deposited by direct laser synthesis on SiO_2/Si substrte. (b) transfer characteristics (source-drain current vs gate voltage) of a back-gate thin film transistor (TFT) using a laser synthsised MoS_2 channel.

References

[1] S. Hong, H. Lee, J. Yeo, and S. H. Ko, "Digital selective laser methods for nanomaterials: From synthesis to processing," Nano Today. 11, 547–564 (2016).

[2] M. F. El-Kady and R. B. Kaner, "Direct Laser Writing of Graphene Electronics," ACS Nano. 8, 8725–8729 (2014).

[3] H. Palneedi, J. H. Park, D. Maurya, M. Peddigari, G. T. Hwang, V. Annapureddy, J. W. Kim, J. J. Choi, B. D. Hahn, S. Priya, K. J. Lee, and J. Ryu, "Laser Irradiation of Metal Oxide Films and Nanostructures: Applications and Advances," Adv. Mater. 30, 1705148 (2018).

[4] M. Samadi, N. Sarikhani, M. Zirak, H. Zhang, H. L. Zhang, and A. Z. Moshfegh, "Group 6 transition metal dichalcogenides nanomaterials: Synthesis, applications and future perspectives," Nanoscale Horiz. 3, 90–204 (2018).

SCIENTIFIC REPORTS
nature research

OPEN

Solution-Based Synthesis of Few-Layer WS_2 Large Area Continuous Films for Electronic Applications

Omar A. Abbas[1,5], Ioannis Zeimpekis[1,5], He Wang[2], Adam H. Lewis[1], Neil P. Sessions[1], Martin Ebert[3], Nikolaos Aspiotis[1], Chung-Che Huang[1], Daniel Hewak[1], Sakellaris Mailis[1,4] & Pier Sazio[1*]

Unlike MoS_2 ultra-thin films, where solution-based single source precursor synthesis for electronic applications has been widely studied, growing uniform and large area few-layer WS_2 films using this approach has been more challenging. Here, we report a method for growth of few-layer WS_2 that results in continuous and uniform films over centimetre scale. The method is based on the thermolysis of spin coated ammonium tetrathiotungstate ($(NH_4)_2WS_4$) films by two-step high temperature annealing without additional sulphurization. This facile and scalable growth method solves previously encountered film uniformity issues. Atomic force microscopy (AFM) and transmission electron microscopy (TEM) were used to confirm the few-layer nature of WS_2 films. Raman and X-Ray photoelectron spectroscopy (XPS) revealed that the synthesized few-layer WS_2 films are highly crystalline and stoichiometric. Finally, WS_2 films as-deposited on SiO_2/Si substrates were used to fabricate a backgated Field Effect Transistor (FET) device for the first time using this precursor to demonstrate the electronic functionality of the material and further validate the method.

2D transition metal dichalcogenides (TMD) have emerged as promising low dimensional semiconductor materials[1] due to their exceptional electrical, optical and mechanical properties[2]. Among the TMD family, MoS_2 has been the first and most investigated member because of its excellent properties such as thickness dependent indirect to direct bandgap transition[3,4], valley Hall effect[5], high carrier mobility and on-off ratio[6] that makes it suitable for a wide range of electronic applications. A significant number of scientific reports have addressed the synthesis routes of MoS_2. The production methods reported in the literature include mechanical[6] or liquid exfoliation[7] as well as conventional atomic layer deposition (ALD)[8] and chemical vapour deposition (CVD)[9]. These approaches however are still far from being commercially viable due to low yield and/or high costs.

Two significant factors that identify a successful route to commercialization of a material are its compatibility with existing fabrication methods and cost effectiveness. Solution-based synthesis is compatible with existing nanofabrication processes, is scalable at low cost and has already been shown to produce high quality MoS_2 films using a single source precursor such as ammonium tetrathiomolybdate $(NH_4)_2MoS_4$ through thermal decomposition for electronic devices applications[10]. Therefore, several groups have developed approaches for large area solution-based MoS_2 synthesis via two-step thermolysis of $(NH_4)_2MoS_4$ films coated in different ways such as dip, roll to roll and spin coating[11–18]. Spin coating of $(NH_4)_2MoS_4$ solution in particular is highly preferable among other coating techniques due to its integration with current semiconductor technology and its ability to control the initial precursor film thickness through spinning speed as well as precursor solution concentration[13,17]. The main obstacle hindering this coating technique is the low wettability of precursor solutions that utilize common solvents such as dimethylformamide (DMF) and n-methylpyrrolidone (NMP), with commonly used substrates like SiO_2/Si or sapphire. This leads to nonuniform precursor film formation associated with a high density of defects and de-wetted areas after spin coating. To overcome this issue, researchers developed different organic-precursor solution systems for spin coating to enhance the uniformity and controllability of the initial precursor film over large area and eliminate surface defects. These organic-precursor solutions systems are: DMF,

[1]Optoelectronics Research Centre, University of Southampton, Southampton, SO17 1BJ, United Kingdom. [2]National Centre for Advanced Tribology, University of Southampton, Southampton, SO17 1BJ, United Kingdom. [3]School of Electronics and Computer Science, University of Southampton, Southampton, SO17 1BJ, United Kingdom. [4]Present address: Skolkovo Institute of Science and Technology Novaya St., 100, Skolkovo, 143025, Russian Federation. [5]These authors contributed equally: Omar A. Abbas and Ioannis Zeimpekis. *email: pjas@soton.ac.uk

n-butylamine and 2-aminoethanol[13]; ethylenediaminetetraacetic acid (EDTA) and dimethylsulfoxide (DMSO)[16]; and linear poly (ethylenimine), DMF and 2-aminoethanol[17].

Similarly, WS_2 is an important TMD material which shows comparable characteristics to MoS_2 but can also offers higher photoluminescence (PL) efficiency, better electrical performance and ambipolar field effect behaviour[19–21]. Although WS_2 has growth methods similar to MoS_2 such as sulphurization of tungsten metal[22] or tungsten oxides[23], growth of large area and uniform WS_2 ultra-thin films for electronic applications via thermal decomposition of ammonium tetrathiotungstate $(NH_4)_2WS_4$ salt has not been demonstrated successfully. This is due to the difficulty that is associated with the formation of a thin uniform $(NH_4)_2WS_4$ precursor layer as this salt has poor solubility in most of the common solvents as compared with $(NH_4)_2MoS_4$[24]. Usage of these solvents in solution-based single source precursor deposition of WS_2 has however been demonstrated for applications that do not require highly continuous WS_2 films, such as surface enhancement Raman scattering (SERS) and creating a carrier injector layer for optoelectronic devices[25,26]. Another issue in solution-based single source precursor synthesis by thermal decomposition occurs when the second annealing step is relatively high ($\leq$800 °C). In this case, sulphur from $(NH_4)_2MoS_4$ and $(NH_4)_2WS_4$ films evaporates readily and needs to be substituted by adding sulphur in the inert gas flow to preserve the stoichiometry and the quality of the MoS_2 and WS_2 films[11,13,25,26].

Generally, there are three factors that need to be optimized to create a defect-free film from a liquid precursor by spin coating; the wettability of the precursor solution with the substrate, the solubility of precursor in the solvent system and the viscosity of the solution. Wettability can be significantly improved by oxygen plasma treatment of the substrate which promotes the hydrophilicity of the surface[13]. Choosing a solvent capable of achieving high solubility of the precursor helps to eliminate clusters and striation formation due to surface tension. Viscosity can be controlled by the choice of the solvents system and the concentration of the precursor, which affects the coverage of the film over the substrate and the final precursor film thickness[13,17].

We have therefore optimized all three parameters to create uniform large area ultra-thin WS_2 layers via a two-step thermal decomposition of $(NH_4)_2WS_4$ spun-coated precursor solutions. A refined solvent recipe was formulated to improve the wettability and uniformity of the precursor film on the substrate. Additionally, by processing our samples in a "facing pair" manner during the high temperature second annealing step, the composition/stoichiometry of the films was preserved, thus eliminating the need for additional sulphurization. Optical microscopy was used to assess the uniformity and continuity of the precursor films while AFM and TEM evaluated the resulting WS_2 film thickness and morphology. Raman spectroscopy supported the AFM and TEM results to identify the few-layer nature of the films and showed the effect of temperature on the crystallinity of the film. XPS spectroscopy revealed the stoichiometry of WS_2 films when grown on different substrates. Finally, an FET device was fabricated using as-deposited WS_2 film to further elucidate the potential electronic applications of these films.

Results and Discussion

Electronic devices such as FETs require continuous and uniform films for the device layer to guarantee high electrical performance. In solution-based synthesis of semiconducting WS_2 films, the main defects are pinholes and de-wetted areas over the substrate that occur in the precursor deposition step. In this work we have tackled these issues by refining the solvents system for the $(NH_4)_2WS_4$.

There are simple solutions for wettability but because $(NH_4)_2WS_4$ is weakly coordinated with most of the solvents[24], the key challenge in making a solution-based uniform ultra-thin WS_2 film is formulating a solution recipe that results in a high solubility of the precursor with the optimum viscosity. Based on this, we chose the most promising solvents reported previously for spin coating, namely (DMF)[27], ethylene glycol[26], (NMP)[12] to investigate which one has the maximum solvation and coverage over the substrate. Preparation of the substrates and precursor solutions for spin coating is described in Materials and Methods.

Figure 1(A–C), shows the spin-coated precursor films where $(NH_4)_2WS_4$ is dissolved in DMF, ethylene glycol and NMP solvents respectively (100 mM solution concentration), at 6000 rpm spinning speed. Unfortunately, none of the solvents successfully formed continuous and uniform $(NH_4)_2WS_4$ films. The high concentration and therefore viscosity of the solutions should have facilitated the continuous film formation, opposite to what we observed here. Moreover, the de-wetted regions were significantly enlarged at 9000 rpm which was the peak of the spin coating speed (see Fig. S1). DMF was promising in terms of forming continuous precursor films with excellent surface coverage at 3000 and 6000 rpm speeds. Unfortunately, we identified high density of clusters that probably consist of insoluble WS_4^{-2} anions. Ethylene glycol based film exhibited lower density of clusters as compared to DMF at 3000 rpm (see Fig. S1) but had more de-wetted regions, with the wettability deteriorating at moderate and high spin coating speeds, thus preventing the formation of a thin uniform layer. Unlike the previous solvents, NMP showed some more solvation without forming clusters at all spin coating speeds, indicating a better solvation of $(NH_4)_2WS_4$ by NMP compared to DMF and ethylene glycol solvents. However, the high density of random pinholes assigned to insufficient wetting of the solution with the substrate.

It has been reported before that amine-based solvents could be linked with WS_4^{-2} anions via hydrogen bonds leading to form a stable solution[28,29]. Additionally, it has been shown that n-butylamine and 2-aminoethanol solvents can stabilize the $(NH_4)_2MoS_4$ and bind the solution to create uniform MoS_2 precursor films by spin coating[13]. However, this $(NH_4)_2MoS_4$ solvents recipe contains DMF rather than NMP which leads to non-uniform WS_2 precursor layer formation when it was used for $(NH_4)_2WS_4$ (see Fig. S2). Based on these facts, we reformulated the recipe of NMP by adding the solvents butylamine and 2-aminoethanol (see Materials and Methods). Moreover, to ensure good coverage and uniformity of the spin-coated precursor layer, we started with high concentration solution (100 mM), as is evident from Fig. 1(D) there was a significant improvement of the uniformity without any obvious de-wetted regions over a large area. The few apparent micron-sized defects originated from particles on the substrate. However, further reduction in precursor solution concentration was needed in order to achieve WS_2 films with minimum thickness. Therefore, we used the same solvents recipe with the threshold concentration (35 mM) of

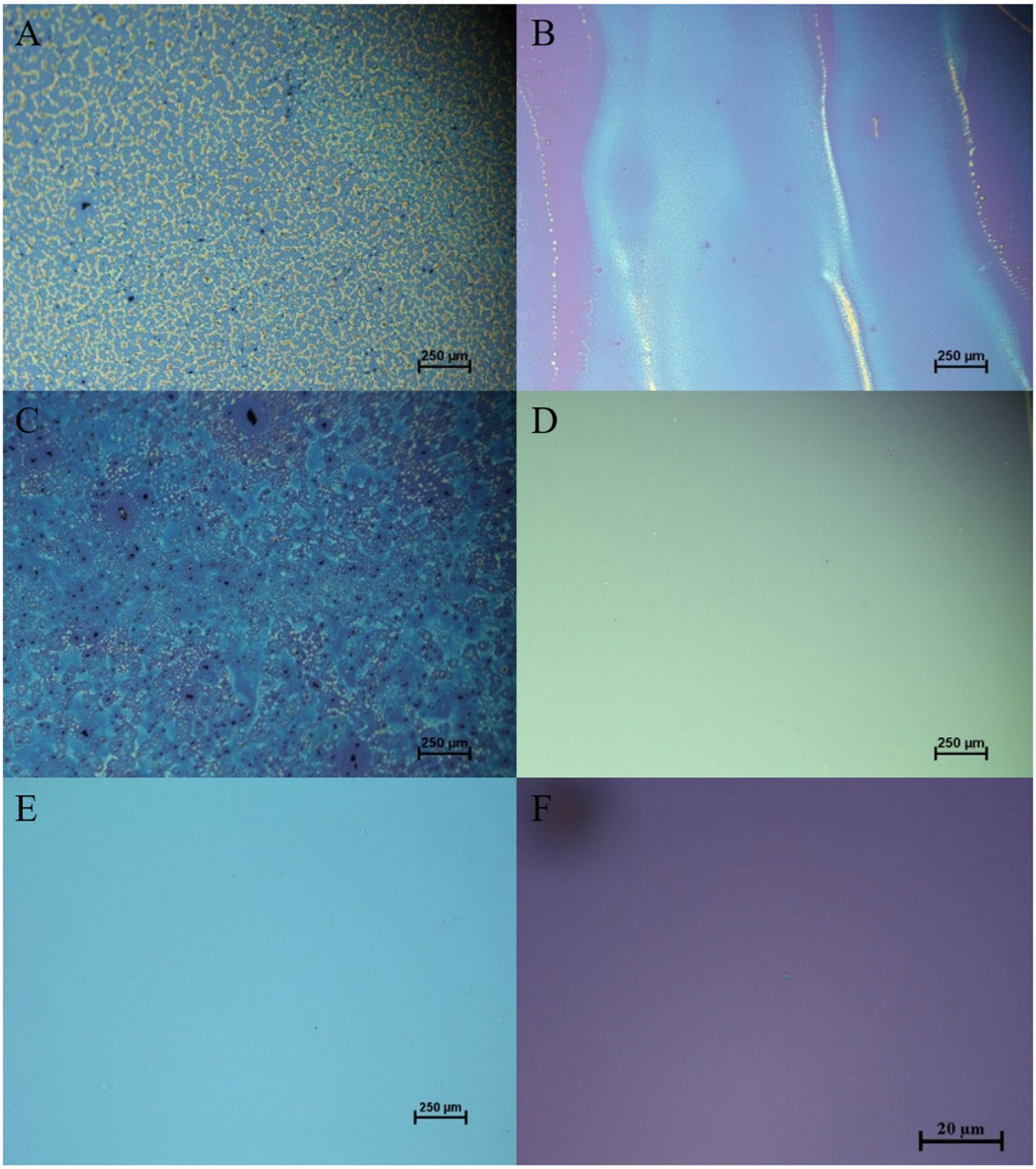

Figure 1. Optical microscope images of spin-coated precursor films prepared by dissolving 100 mM of $(NH_4)_2WS_4$ in: (**A**) dimethylformamide (DMF), (**B**) ethylene glycol, (**C**) n-methylpyrrolidone (NMP) and (**D**) solvent system contains (3 mL NMP/2 mL n-butylamine/1 mL 2-aminoethanol of 6 mL total volume). (**E**,**F**) are optical microscope images of spin-coated precursor films prepared by dissolving 35 mM of $(NH_4)_2WS_4$ in (3 mL NMP/2 mL n-butylamine/1 mL 2-aminoethanol of 6 mL total volume). All the solutions are spin coated at 6000 rpm for 1 min and prebaked at 140 °C for 1 min. Note that (**A–E**) images were taken using 5X objective while (**F**) image was taken using 100X objective.

$(NH_4)_2WS_4$ that can produce large area and uniform precursor films as shown in Fig. 1(E–F) respectively. At lower concentrations than this (e.g. 10 or 20 mM), the density of WS_4 anions in the solution were very low leading to formation of isolated micron-sized islands rather than a continuous film (see Fig. S3).

After the second annealing step of WS_2 films grown on SiO_2/Si and sapphire substrates (with 35 mM precursor concentration), the topography and thickness of these samples were assessed by atomic force microscopy (AFM). The average thickness of the films for an area of edges was 6.5 ± 0.68 nm (0.68 nm is the root mean square roughness R_q of the film) for the SiO_2/Si substrate and 6 ± 0.1 nm (0.1 nm is the root mean square roughness R_q of the film) for the sapphire as shown in Fig. 2. The higher roughness of the film grown on the SiO_2/Si substrate is attributed to the amorphous nature of the substrate and to the increased surface roughness caused by the relatively long time exposed to oxygen plasma. As AFM measurements were taken at the edge of WS_2 films where they are prone to edge effects from the spinning process, therefore, these AFM results represent the maximum thickness of WS_2 films. Additionally, the AFM images confirm the continuity of the WS_2 films with small grains that appear due to the nano-size crystals formed at the WS_2 uniform film.

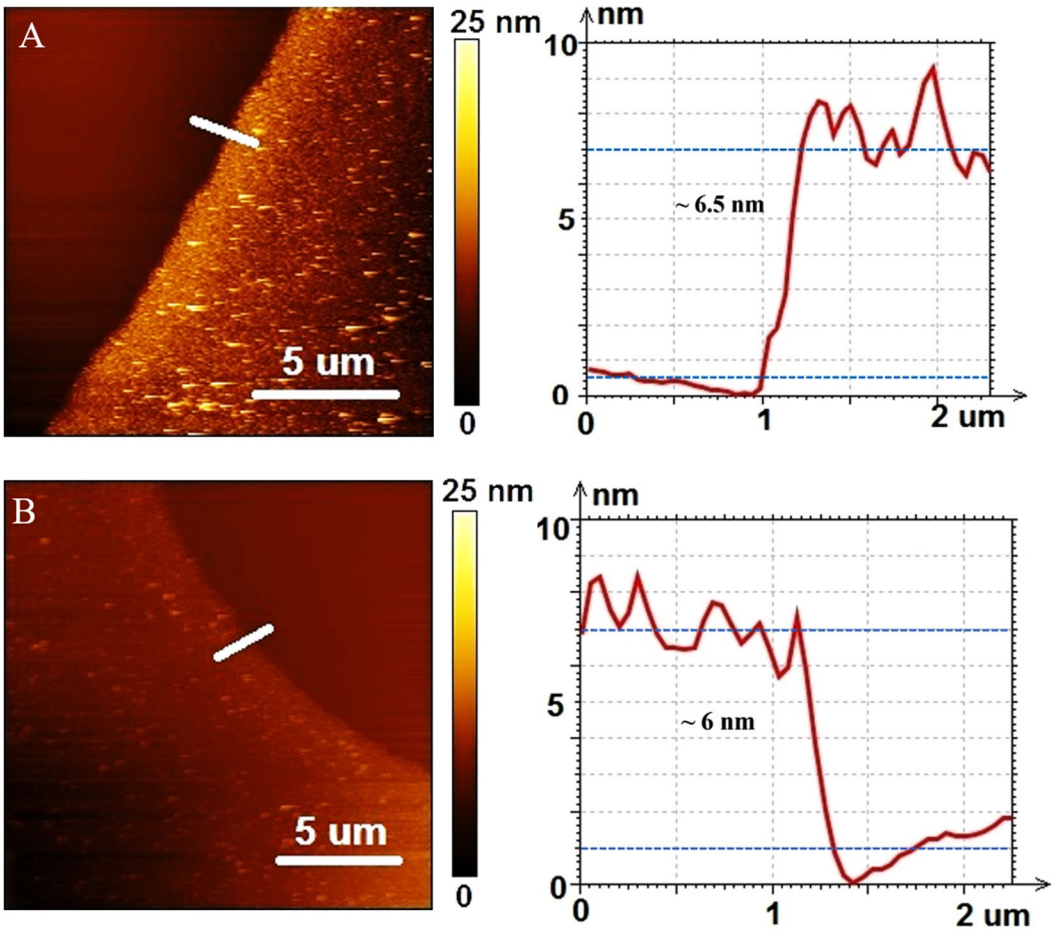

Figure 2. Atomic force microscopy (AFM) images of WS_2 films grown on (**A**) SiO_2/Si (**B**) sapphire.

To evaluate the structure of the WS_2 films at the central area of the samples, TEM was conducted for the film grown on a sapphire substrate. Figure 3 shows a TEM image of the WS_2 film demonstrating a highly ordered layered structure. It is apparent from Fig. 3, the film is uniform and constituted by areas of 2 and 3 layers. The TEM image indicates that the single layer thickness of the WS_2 film is 0.65 nm, in agreement with previously reported WS_2 monolayer thickness[23]. At the bottom right of Fig. 3 and also in Fig. S4 arranged columns of atoms are clearly visible.

Raman spectroscopy with a 532 nm excitation wavelength was performed to characterize the WS_2 films on both SiO_2/Si and sapphire substrates for each of the two-annealing steps (500 °C and 1000 °C). The consequence of using a 532 nm pump laser for Raman spectroscopy is an enrichment of the Raman spectra with second order peaks[30]. Multi-peak Lorentzian fitting is applied to deconvolute these peaks which helps to reveal any crystallinity changes between the two-annealing steps and to estimate the thickness of the films. As shown in Fig. 4 after the 1000 °C anneal, the Raman spectra intensity at the centre of the samples were enhanced by X2 for the SiO_2/Si and X4 for the sample grown on sapphire. Moreover, all peaks become narrower after the second annealing step. The most dramatic change was with the peak labelled LA (M)-TA(M)[31] where its FWHM was reduced from 63.4 cm^{-1} in the first annealing step to 24.4 cm^{-1} in the second annealing step for SiO_2/Si and from 51 cm^{-1} to 28 cm^{-1} for sapphire. Additional peaks that correspond to 2LA (K) mode[32] are also apparent at 385.2 cm^{-1} and 387.7 cm^{-1} for SiO_2/Si and sapphire respectively, which did not exist after the first annealing step. The intensity enhancement in the Raman spectra, the reduction in full width half maximum (FWHM) of all Raman peaks as well as the prominence of additional second order peak (2LA (K)) highlight the significance of the second annealing step at high temperature (1000 °C) to promote the crystallinity of the WS_2 films.

Furthermore, at 500 °C the intensity of the in-plane E^1_{2g} (Γ) dominated the longitudinal 2LA (M) mode whereas at the 1000 °C the 2LA (M) peaks increased in intensity which almost overwhelmed the E^1_{2g} (Γ) mode for all substrates. In contrast, the out-of-plane peak A_{1g} (Γ) decreased in intensity at the higher temperature. Consequently, the 2LA (M)/A_{1g} (Γ) intensity ratio increased dramatically from 0.685 at 500 °C to 2.64 at 1000 °C for the SiO_2/Si and from 0.285 to 2.26 for the sapphire. Moreover, the Raman peak difference between the in-plane mode E^1_{2g} (Γ) and out-of-plane mode A_{1g} (Γ) at 1000 °C is 63.8 cm^{-1} for the SiO_2/Si substrate and 61.2 cm^{-1} for the sapphire substrate. Both the intensity ratio of 2LA (M)/A_{1g} (Γ) and Raman peaks difference (A_{1g} (Γ)- E^1_{2g} (Γ)) indicate the few-layer nature of the measured WS_2 films on both substrates similar to what has been reported in the literature[33,34].

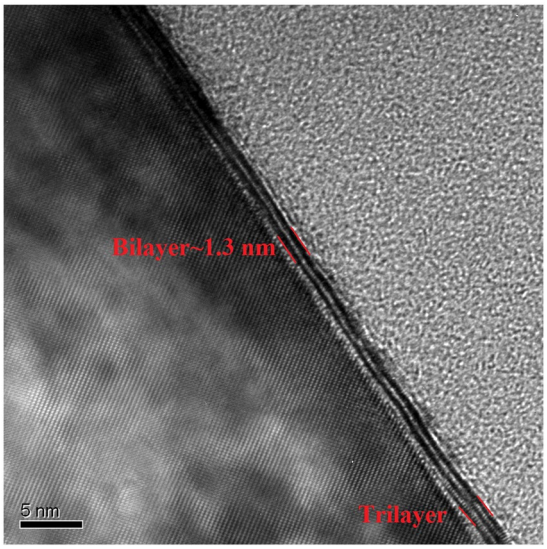

Figure 3. TEM image of few-layer WS_2 films grown on sapphire substrate. The crystalline Al_2O_3 atomic lattice is clearly visible on the left hand side of the image. The WS_2 film is viewed at a high angle where bilayer and trilayer regions are also highly visible and are indicated. The bright area on the right hand side is the protective carbon coating. The trilayer region also shows the WS_2 atomic arrangement.

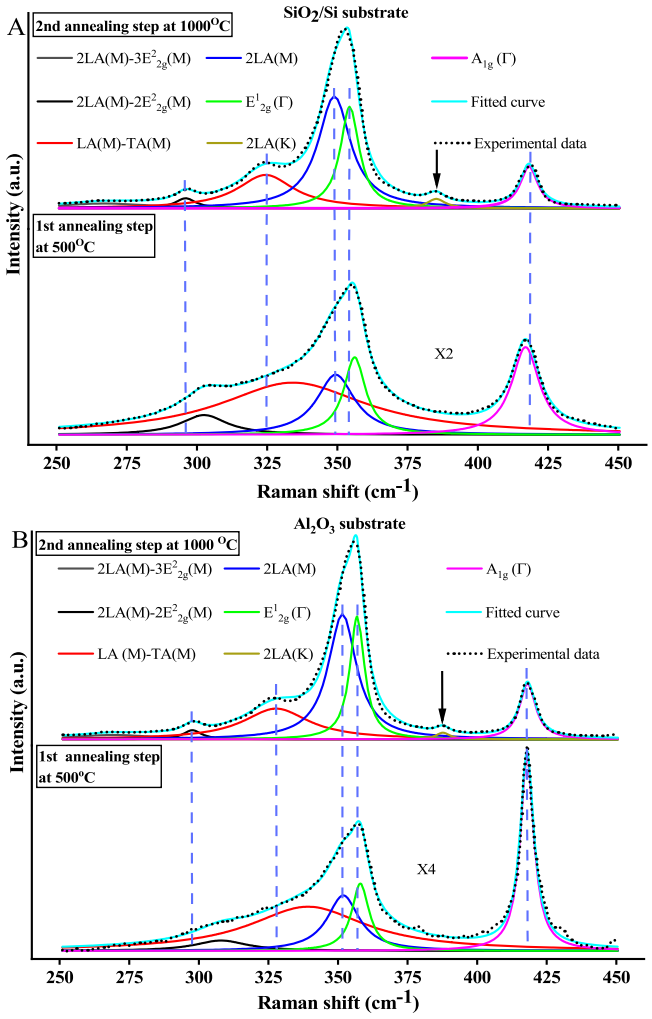

Figure 4. Raman spectra of WS_2 films on (**A**) SiO_2/Si and (**B**) Sapphire at the 500 °C and 1000 °C respectively.

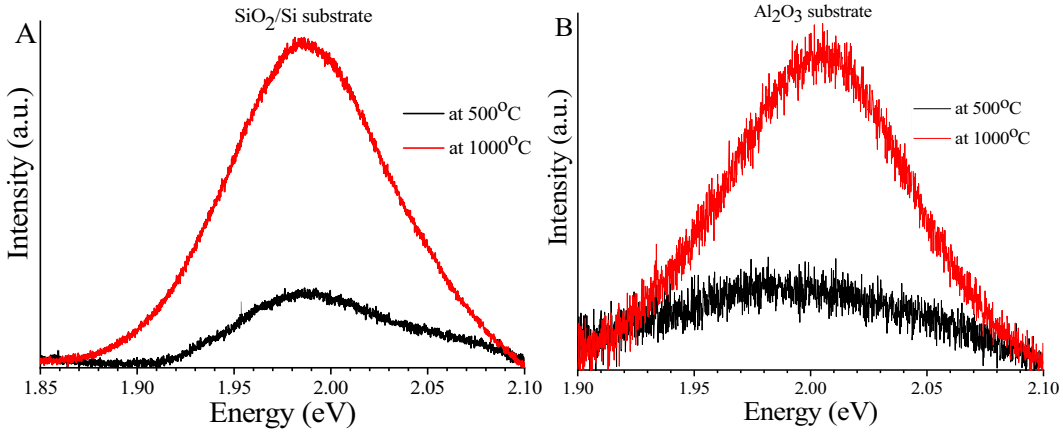

Figure 5. PL spectra of WS_2 films on (**A**) SiO_2/Si and (**B**) Sapphire at 500 °C and 1000 °C respectively.

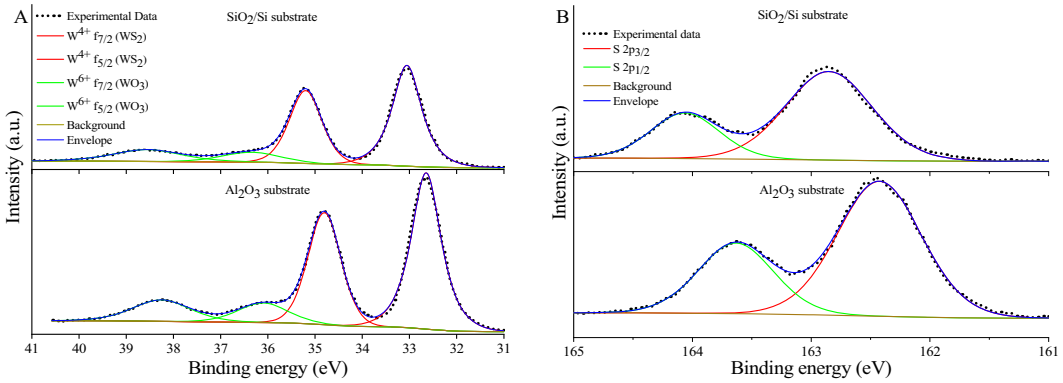

Figure 6. XPS spectra of WS_2 films on SiO_2/Si and sapphire substrates (**A**) W 4 f core-level and (**B**) S 2p core-level spectra.

Interestingly, after the second annealing step all the peaks from E^1_{2g} (Γ) to 2LA (M)-$2E^2_{2g}$ (M) are shifted to lower wavenumbers compared to their peak positions after the first annealing step at 500 °C. The only exception was the longitudinal acoustic mode 2LA (M), which did not shift after the two annealing steps for both substrates. As a result, the separation of the in-plane E^1_{2g} (Γ) and the out-of-plane peak A_{1g} (Γ) Raman peaks after the first annealing step is smaller compared to after the high temperature annealing step (60.8 cm^{-1} for SiO_2/Si and 59.9 cm^{-1} for sapphire). This is due to blue shifts that E^1_{2g} (Γ) peaks experience in poor crystalline films as stated previously. However, the intensity ratio of 2LA (M)/A_{1g} (Γ) peaks is also low (0.685 for the SiO_2/Si and 0.285 for the sapphire) for poor crystalline films. Thus, the layer number estimation of poor crystalline WS_2 films (500 °C) using Raman spectra with 532 nm excitation wavelength might be not accurate. The reason behind this is the correlation between Raman peaks difference and the intensity ratio is not valid for poor crystalline WS_2 films (500 °C) as opposed to the higher crystalline WS_2 films (1000 °C) which show a clear correlation between Raman peak difference and intensity ratio when resonant excitation wavelength is used for Raman spectroscopy[33].

The PL spectrum of WS_2 films was investigated using the same excitation wavelength, power and objective parameters as the Raman measurements. As shown in Fig. 5 there is a significant enhancement of the photoluminescence (PL) signal after high temperature annealing for both substrates. The PL intensity enhancement is X4.5 for the SiO_2/Si and X3.5 for the sapphire substrate and this enhancement is attributed to the improvement in film crystallinity. However, the PL peaks intensities are still weak, due to few-layer nature of films. For the SiO_2/Si substrate, the PL peak of WS_2 film is located at 1.984 eV, in agreement with earlier reports for few-layer WS_2[31], whereas the PL peak position of WS_2 film grown on sapphire substrate is at 2 eV similar to what has been observed before for WS_2 films grown on sapphire[35]. The trivial shift to lower energy in PL peak position of the WS_2 films grown on SiO_2/Si substrate compared to the films grown on sapphire might results from higher strain on the film deposited on SiO_2/Si substrate[32].

The composition of the deposited WS_2 films was investigated by high resolution XPS for both substrates where the W and S core levels were studied. The carbon peak in the C1s core level was used as a reference point and was at 284.8 eV for both substrates. The de-convoluted XPS spectra for W and S core levels are shown in Fig. 6(A,B) respectively for both substrates. For the WS_2 film deposited on the SiO_2/Si substrate, two doublets were pronounced in the W core level, the first doublet represents the W^{4+} $f4_{7/2}$ at 33.05 eV and W^{4+} $f4_{5/2}$ at 35.20 eV which is attributed to WS_2 formation, with spin orbit splitting (W^{4+} $f4_{5/2}$-W^{4+} $f4_{7/2}$) of 2.15 eV and an area ratio of W^{4+}

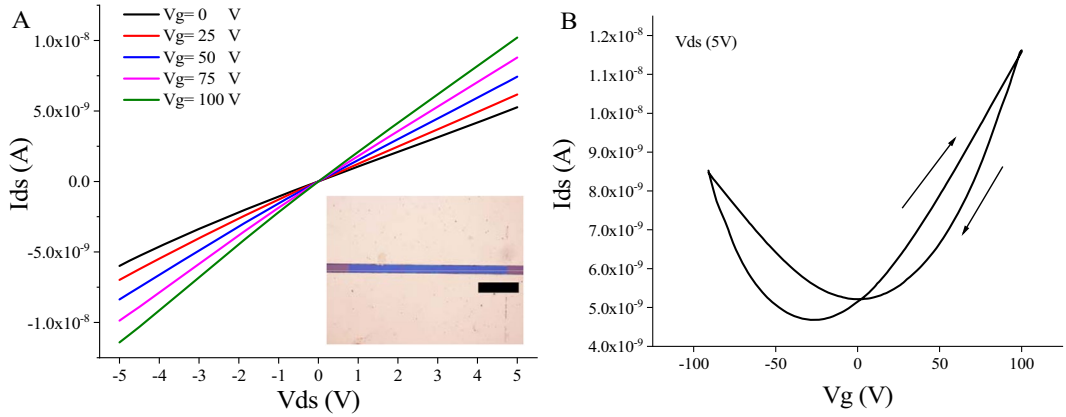

Figure 7. Electrical characteristics of back-gated WS_2 FET (**A**) I_{ds}-V_{ds} (inset: optical microscope image for the actual FET device, the scale is 50 μm). (**B**) Forward and backward sweep transfer characteristics.

$f4_{5/2}/W^{4+}$ $f4_{7/2}$ 0.73. The energy of these peaks corresponds to the 2 H phase of WS_2[36]. The second doublet is located at 36.35 and 38.55 eV respectively and represents the W^{6+} $f4_{7/2}$ and W^{6+} $f4_{5/2}$ peaks that depicts the formation of WO_3[37]. For sulphur, the S $2p_{3/2}$ and S $2p_{1/2}$ peaks are located at 162.85 and 164.06 eV respectively with spin orbit splitting (S $2p_{1/2}$-S $2p_{3/2}$) 1.21 eV and area ratio S $2p_{1/2}$/S $2p_{3/2}$ 0.4. This doublet corresponds to S^{2-} sulphur bonded in 2 H phase of WS_2[36]. Fortunately, the absence of S_2^{2-} ligands peaks, which corresponds to the presence of WS_3 and oxidized sulphur species, is a good indicator that the film is stoichiometric for both substrates[37,38]. The peaks obtained from the WS_2 films on the sapphire are almost identical to films grown on SiO_2/Si. However, there is a shift to lower energies by 0.4 eV for all peaks assigned to WS_2 in both W and S core levels and the oxide content is negligibly increased compared to films grown on SiO_2/Si.

To probe the electronic properties of the WS_2 film, we fabricated a back-gated field effect transistor (FET) using the as-deposited WS_2 films on 300 nm thermally grown SiO_2 on n-type Si substrates (see Fig. S5 for SEM image of the device). Indium was chosen to make direct contact with WS_2 due to small Schottky barrier which makes it a good choice for ohmic contacts with WS_2 film[39]. Current voltage measurements were performed in air to evaluate the transfer characteristics of the devices. First, we measured the source-drain current I_{ds} against the voltage between the source and drain V_{ds} for different bottom gate voltages as shown in Fig. 7(A), the linearity of this result reveals that the In/Au electrodes make excellent Ohmic contacts with the WS_2 channel. To evaluate the transconductance of the device, the back-gate voltage was swept from −91 V to 100 V in both directions as shown in Fig. 7(B). In forward sweep, the device shows n-type behaviour with 6.2×10^{-5} cm^2/V.s field effect mobility, a threshold voltage of −54 V and on/off ratio of 2.5. The field effect mobility was extracted from the slope of the linear part of the transfer curve using the equation:[15]

$$\mu_{FE} = \frac{L}{WC_{OX}V_{ds}} \frac{\Delta I}{\Delta V_g} \quad (1)$$

Where μ_{FE} is the field effect mobility, L is the channel length (10 μm), W is the channel width (200 μm), C_{ox} is the capacitance per unit area of silicon dioxide layer (300 nm) which is (11.5 nF/cm^2), V_{ds} is the source-drain voltage and ($\Delta I/\Delta V_g$) is the transconductance. Interestingly, in backward sweep the FET shows asymmetric ambipolar behaviour with minimum conductivity at 0 V in the n-type branch. However, the low mobility, on-off ratio and the change of the behaviour could be partially attributed to adsorbates from ambient and/or dopants that occur during photolithography and lift-off process. The field effect mobility and the on-off ratio of our WS_2 FET devices are comparable with backgated WS_2 FET devices grown by other solution-based approach when they were characterized in air[40]. Additionally, our WS_2 FET devices show comparable performance with MoS_2 FET devices fabricated using identical synthesis processes, where the mobility of MoS_2 devices varied from 10^{-4} to 10^{-2} cm^2/V.s although the back-gate voltage of these devices was swept to much higher voltages[11,15]. The device field effect characteristics are dictated by the nanocrystalline nature of the film as well as ambient adsorbates. However, as it has been shown with MoS_2 films that are grown in similar ways, we expect a dramatic improvement when the device is optimized and operated in a top-gate configuration with a high-k dielectric such as HfO_2[13] or ionic liquid gate[14,18].

Conclusions

In conclusion, we propose a facile and cost-effective growth method that can produce high quality, continuous and ultra-thin WS_2 films for electronic applications. This solution-based method utilizes thermal decomposition of uniform spin coated ammonium tetrathiotungstate films on two different types of substrates with centimetre scale to create thin WS_2 films. The key factor that enables $(NH_4)_2WS_4$ to successfully form a uniform and continuous film is our optimized solvents recipe with volume ratio 3/6 NMP, 2/6 n-butylamine and 1/6 2-aminoethanol that promotes the solubility and wettability of the precursor solution. Different characterization tools were used to confirm the thickness and the quality of the WS_2 films. Finally, we demonstrated for the first time a back-gated

FET from an as-deposited WS_2 film grown by our solution based process with an electron mobility reaching 6.2×10^{-5} cm^2/V.s which shows comparable performance to MoS_2 devices fabricated by similar synthesis approaches.

Materials and Methods

Preparation of the substrates and $(NH_4)_2WS_4$ solutions for growth of WS_2 films. We used 1.5×1.5 cm^2 SiO_2/Si (300 nm SiO_2) and sapphire substrates to assess the optimum spin coating conditions for different solvent solutions. Prior to spin coating, the surface of the substrates was cleaned using acetone, isopropanol and de-ionized water followed by conditioning using oxygen plasma at 0.1 mb pressure (oxygen flow 1000 mL/min) and 1000 W power for 15 min to enhance the wettability. To prepare the solutions, we dissolved 174 mg of $(NH_4)_2WS_4$ in 5 mL of each solvent (DMF, ethylene glycol, NMP) to form 100 mM of precursor solution. After one hour of sonication (at 70 °C) the three solutions were spin coated on the substrates at three different speeds (3000, 6000 and 9000 rpm) for 1 min (step 1: ramp 5 sec, dwell time 5 sec, rpm 500; step 2: ramp 5 sec, dwell time 45 sec, rpm 3000, 6000 and 9000). After spinning, the substrates were prebaked at 140 °C for 1 min using a hot-plate where the solvents evaporated. Prior to thermal decomposition, the refined recipe for the new solvents system we propose (6 mL total volume) is 3/6 NMP, 2/6 butylamine and 1/6 2-aminoethanol. We mixed these solvents together and dissolved (208, 73, 42 and 21) mg of $(NH_4)_2WS_4$ to create solutions of (100, 35, 20, 10) mM. The solutions were then sonicated for 1 hour at 70 °C before being spin coated at 6000 rpm (the same spin-coating recipe was used as before) on the cleaned and oxygen plasma treated substrates (the same oxygen plasma recipe was used as before). Finally, the samples were baked on a hot-plate at 140 °C for 1 minute.

Thermal decomposition. The 35 mM concentration samples were used for the thermal decomposition. They were placed in a tube furnace and purged with a 6% H_2 in Ar gas at 8 mb pressure for 5 minutes. The samples were kept in the cold zone and the furnace was programmed to reach 500 °C. After 20 minutes of temperature stabilization, the samples were moved in the hot zone of the furnace. After 30 min of annealing at 500 °C, the samples were removed from the furnace and were left to cool down naturally while maintaining the flow of gas. To improve the crystallinity of our films we performed a second annealing step at 1000 °C. The samples with identical substrates were arranged in film-facing pairs to prevent the reduction of the films (see Fig. S6). Firstly, the furnace tube was purged with Argon at a pressure of 1 mb for 5 minutes to remove oxygen from the system. The system was then allowed to reach atmospheric pressure under the same 100 sccm Ar flow. After a 40 min temperature ramp, the furnace reached 1000 °C to anneal the samples for 15 minutes before removal from the hot zone to let the samples cool down to room temperature under the same gas and pressure conditions. See Fig. S7 for optical microscopy image of the final WS_2 film grown on SiO_2/Si.

Device fabrication. The transistor channels were formed by conventional photolithography using S1813 photoresist masking and etched for 2 minutes to remove unwanted WS_2 film regions by Argon ion milling using Oxford Plasma Technology Ionfab 300 plus system. An Argon ion plasma beam was accelerated to 500 V with 100 mA current. The sample placed on a cooled plate (15 °C) at an angle of 45° with respect to the beam and rotated at 5 rpm. The samples were then immersed in acetone to remove the photoresist mask and obtain a WS_2 channel of 200 μm width which represents the FET. The length of the channel is 10 μm and was defined by the source and drain electrodes positions as patterned by S1805 photoresist. Indium contacts (10 nm thick) were deposited and capped by 50 nm of Au using an e-beam evaporator followed by lift-off.

Characterization. AFM images were produced using an Agilent 5500 scanning probe microscope. Raman and PL spectroscopy were conducted using Invia Raman Microscope (Renishaw) system with a 532 nm excitation wavelength at 20 mW power and 50X objective. XPS has been performed using a Thermo fisher scientific Thetaprobe system. SEM was performed using a Joel JSM-7500F FEG-SEM. The preparation of the lamella was performed using a Zeiss NVision 40 CrossBeam FIB system. TEM was performed in the Loughborough Materials Characterisation Centre using an FEI Tecnai F20. Electrical measurements were performed in air using an Agilent 4155C semiconductor parameter analyser connected to a cascade micropositioning stage.

Received: 16 April 2019; Accepted: 14 January 2020;
Published online: 03 February 2020

References

1. Fiori, G. *et al*. Electronics based on two-dimensional materials. *Nat. Nanotechnol.* **9**, 768–779 (2014).
2. Chhowalla, M. *et al*. The chemistry of two-dimensional layered transition metal dichalcogenide nanosheets. *Nat. Chem.* **5**, 263–275 (2013).
3. Mak, K. F., Lee, C., Hone, J., Shan, J. & Heinz, T. F. Atomically thin MoS_2: A new direct-gap semiconductor. *Phys. Rev. Lett.* **105**, 136805 (2010).
4. Splendiani, A. *et al*. Emerging photoluminescence in monolayer MoS_2. *Nano Lett.* **10**, 1271–1275 (2010).
5. Mak, K. F., McGill, K. L., Park, J. & McEuen, P. L. Valleytronics. The valley Hall effect in MoS_2 transistors. *Science* **344**, 1489–92 (2014).
6. Radisavljevic, B., Radenovic, A., Brivio, J., Giacometti, V. & Kis, A. Single-layer MoS_2 transistors. *Nat. Nanotechnol.* **6**, 147–150 (2011).
7. Coleman, J. N. *et al*. Two-dimensional nanosheets produced by liquid exfoliation of layered materials. *Science* **331**, 568–71 (2011).
8. Tan, L. K. *et al*. Atomic layer deposition of a MoS_2 film. *Nanoscale* **6**, 10584–10588 (2014).
9. Amani, M. *et al*. High Luminescence Efficiency in MoS_2 Grown by Chemical Vapor Deposition. *ACS Nano* **10**, 6535–6541 (2016).
10. Samadi, M. *et al*. Group 6 transition metal dichalcogenide nanomaterials: Synthesis, applications and future perspectives. *Nanoscale Horizons* **3**, 90–204 (2018).
11. Liu, K.-K. *et al*. Growth of Large-Area and Highly Crystalline MoS_2 Thin Layers on Insulating Substrates. *Nano Lett.* **12**, 1538–1544 (2012).

12. George, A. S. *et al*. Wafer Scale Synthesis and High Resolution Structural Characterization of Atomically Thin MoS_2 Layers. *Adv. Funct. Mater.* **24**, 7461–7466 (2014).
13. Yang, J. *et al*. Wafer-scale synthesis of thickness-controllable MoS_2 films via solution-processing using a dimethylformamide/n-butylamine/2-aminoethanol solvent system. *Nanoscale* **7**, 9311–9319 (2015).
14. Lim, Y. R. *et al*. Wafer-Scale, Homogeneous MoS_2 Layers on Plastic Substrates for Flexible Visible-Light Photodetectors. *Adv. Mater.* **28**, 5025–5030 (2016).
15. Hung, Y. H. *et al*. Scalable Patterning of MoS_2 Nanoribbons by Micromolding in Capillaries. *ACS Appl. Mater. Interfaces* **8**, 20993–21001 (2016).
16. Ionescu, R. *et al*. Chelant Enhanced Solution Processing for Wafer Scale Synthesis of Transition Metal Dichalcogenide Thin Films. *Sci. Rep.* **7**, 6419 (2017).
17. Yang, H. *et al*. Highly Scalable Synthesis of MoS_2Thin Films with Precise Thickness Control via Polymer-Assisted Deposition. *Chem. Mater.* **29**, 5772–5776 (2017).
18. Lim, Y. R. *et al*. Roll-to-Roll Production of Layer-Controlled Molybdenum Disulfide: A Platform for 2D Semiconductor-Based Industrial Applications. *Adv. Mater.* **30**, 1705270 (2018).
19. Zhao, W. *et al*. Evolution of Electronic Structure in Atomically Thin Sheets of WS_2 and WSe_2. *ACS Nano* **7**, 791–797 (2013).
20. Liu, L., Kumar, S. B., Ouyang, Y. & Guo, J. Performance limits of monolayer transition metal dichalcogenide transistors. *IEEE Trans. Electron Devices* **58**, 3042–3047 (2011).
21. Hwang, W. S. *et al*. Transistors with chemically synthesized layered semiconductor WS_2 exhibiting 10^5 room temperature modulation and ambipolar behavior. *Appl. Phys. Lett.* **101**, 013107 (2012).
22. Orofeo, C. M., Suzuki, S., Sekine, Y. & Hibino, H. Scalable synthesis of layer-controlled WS_2 and MoS_2 sheets by sulfurization of thin metal films. *Appl. Phys. Lett.* **105**, 83112 (2014).
23. Gutiérrez, H. R. *et al*. Extraordinary room-temperature photoluminescence in triangular WS_2 monolayers. *Nano Lett.* **13**, 3447–3454 (2013).
24. Kwon, K. C. *et al*. Tungsten disulfide thin film/p-type Si heterojunction photocathode for efficient photochemical hydrogen production. *MRS Commun.* **7**, 272–279 (2017).
25. Li, Z. *et al*. Facile synthesis of large-area and highly crystalline WS_2 film on dielectric surfaces for SERS. *J. Alloys Compd.* **666**, 412–418 (2016).
26. Kwon, K. C. *et al*. Synthesis of atomically thin transition metal disulfides for charge transport layers in optoelectronic devices. *ACS Nano* **9**, 4146–4155 (2015).
27. Annamalai, M. *et al*. Surface energy and wettability of van der Waals structures. *Nanoscale* **8**, 5764–5770 (2016).
28. Srinivasan, B. R., Näther, C., Dhuri, S. N. & Bensch, W. On the importance of H-bonding interactions in organic ammonium tetrathiotungstates. *Monatshefte fur Chemie* **137**, 397–411 (2006).
29. Srinivasan, B. R., Naik, A. R., Näther, C. & Bensch, W. Synthesis, spectroscopy and crystal structures of chiral organic ammonium tetrathiometalates showing N-H···S and C-H···S interactions. *Zeitschrift fur Anorg. und Allg. Chemie* **633**, 582–588 (2007).
30. Zhao, W. *et al*. Lattice dynamics in mono- and few-layer sheets of WS_2 and WSe_2. *Nanoscale* **5**, 9677–9683 (2013).
31. Bissett, M. A., Hattle, A. G., Marsden, A. J., Kinloch, I. A. & Dryfe, R. A. W. Enhanced Photoluminescence of Solution-Exfoliated Transition Metal Dichalcogenides by Laser Etching. *ACS Omega* **2**, 738–745 (2017).
32. Su, L., Yu, Y., Cao, L. & Zhang, Y. Effects of substrate type and material-substrate bonding on high-temperature behavior of monolayer WS_2. *Nano Res.* **8**, 2686–2697 (2015).
33. Berkdemir, A. *et al*. Identification of individual and few layers of WS_2 using Raman Spectroscopy. *Sci. Rep.* **3**, 1755 (2013).
34. Li, D. H. *et al*. Dielectric functions and critical points of crystalline WS_2 ultrathin films with tunable thickness. *Phys. Chem. Chem. Phys.* **19**, 12022–12031 (2017).
35. Lan, F. *et al*. Synthesis of large-scale single-crystalline monolayer WS_2 using a semi-sealed method. *Nanomaterials* **8**, 100 (2018).
36. Sang, Y. *et al*. From UV to near-infrared, WS_2 nanosheet: A novel photocatalyst for full solar light spectrum photodegradation. *Adv. Mater.* **27**, 363–369 (2015).
37. Tan, S. M. & Pumera, M. Bottom-up Electrosynthesis of Highly Active Tungsten Sulfide (WS_{3-x}) Films for Hydrogen Evolution. *ACS Appl. Mater. Interfaces* **8**, 3948–3957 (2016).
38. Alsabban, M. M. *et al*. Editors' Choice Growth of Layered WS_2 Electrocatalysts for Highly Efficient Hydrogen Production Reaction. *ECS J. Solid State Sci. Technol.* **5**, Q3067–Q3071 (2016).
39. Wang, Y. *et al*. Van der Waals contacts between three-dimensional metals and two-dimensional semiconductors. *Nature* **568**, 70–74 (2019).
40. Lan, C., Li, C., Yin, Y. & Liu, Y. Large-area synthesis of monolayer WS_2 and its ambient-sensitive photo-detecting performance. *Nanoscale* **7**, 5974–5980 (2015).

Acknowledgements

The first author gratefully acknowledge the financial support from The Higher Committee for Education Development in Iraq (HCED Iraq). The authors acknowledge financial support from the UK's Engineering and Physical Sciences Council through National Hub in High Value Photonic Manufacturing (grant EP/N00762X/1).

Author contributions

O.A.A., S.M. and P.S. conceived the idea. O.A.A. and I.Z. composed the manuscript. O.A.A. designed the experiments, synthesised the films, fabricated and characterised the FET device. H.W. performed the AFM and the XPS characterisations under supervision of C.C.H. A.H.L performed the Raman and Photoluminescence spectroscopy. N.P.S helped with fabrication of the device. I.Z. and N.A. analysed the XPS data. I.Z. performed the SEM. M.E. prepared the TEM lamella. The whole work was supervised and managed by D.H., S.M. and P.S.

Competing interests

The authors declare no competing interests.

Additional information

Supplementary information is available for this paper at https://doi.org/10.1038/s41598-020-58694-0.

Correspondence and requests for materials should be addressed to P.S.

Reprints and permissions information is available at www.nature.com/reprints.

Publisher's note Springer Nature remains neutral with regard to jurisdictional claims in published maps and institutional affiliations.

Supplementary Information

Solution-Based Synthesis of Few-Layer WS_2 Large Area Continuous Films for Electronic Applications

Omar A. Abbas[1†], Ioannis Zeimpekis[1†], He Wang[2], Adam H. Lewis[1], Neil P. Sessions[1], Martin Ebert[3], Nikolaos Aspiotis[1], Chung-Che Huang[1], Daniel Hewak[1], Sakellaris Mailis[1,4] & Pier Sazio[1*]

[1]Optoelectronics Research Centre, University of Southampton, Southampton, SO17 1BJ, United Kingdom

[2]National Centre for Advanced Tribology, University of Southampton, Southampton, SO17 1BJ, United Kingdom

[3]School of Electronics and Computer Science, University of Southampton, Southampton, SO17 1BJ, United Kingdom

Present address: [4]Skolkovo Institute of Science and Technology Novaya St., 100, Skolkovo 143025, Russian Federation

[†]These authors contributed equally to this work.

Corresponding Author: Pier Sazio

[*] E-mail: pjas@soton.ac.uk

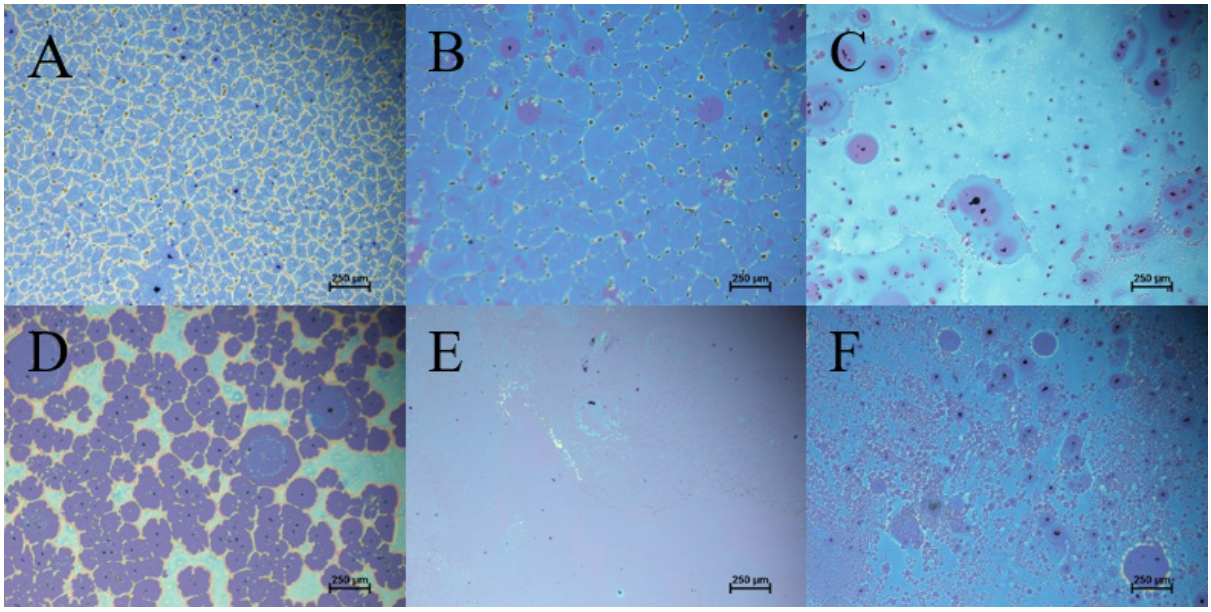

Figure S1. Optical microscope images of precursor films prepared by dissolving 100 mM of $(NH_4)_2WS_4$ in: dimethylformamide (DMF) solvent then spun coated at (A) 3000 and (D) 9000 rpm spinning speed respectively; ethylene glycol solvent then spun coated at (B) 3000 and (E) 9000 rpm respectively; n-methylpyrrolidone (NMP) solvent then spun coated at (C) 3000 and (F) 9000 rpm respectively.

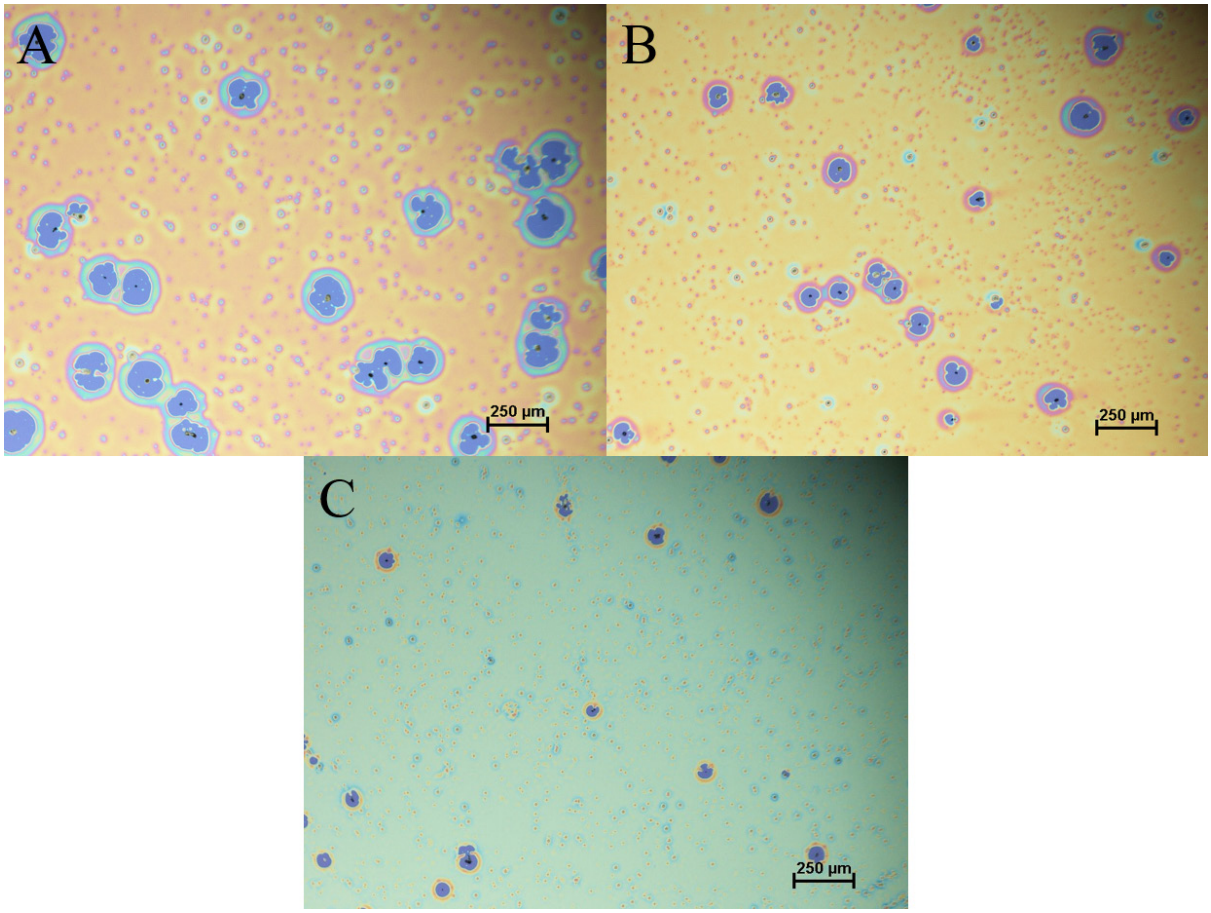

Figure S2. Optical microscope images of precursor films prepared by dissolving 100 mM of $(NH_4)_2WS_4$ in 5 mL of (2/5 dimethylformamide (DMF), 2/5 n-butylamine 1/5 2-aminoethanol) then spun coated at: (A) 3000, (B) 6000 and (C) 9000 rpm. This solvent recipe is a modified recipe from ref (13) which can create highly uniform $(NH_4)_2MoS_4$ films by spin-coating that can thermally decompose to produce MoS_2 films. However, when this recipe was applied to create $(NH_4)_2WS_4$ films, large size pinholes (≥50µm) exist in addition to undissolved $(NH_4)_2WS_4$ particles.

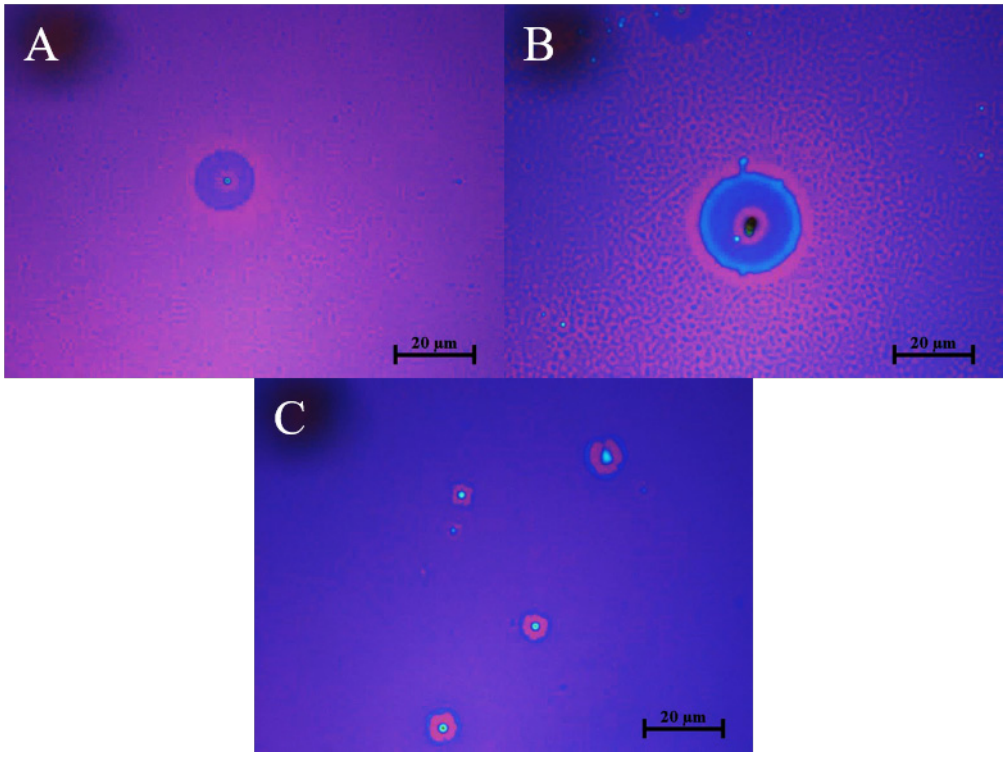

Figure S3. Optical microscope images of spin-coated precursor films prepared by dissolving $(NH_4)_2WS_4$ in our solvent recipe which is 6 mL of (3 mL NMP, 2 mL butylamine and 1 mL 2-aminoethanol) using different concentrations (spin coating at 6000 rpm for 1 min). (A) 10 mM concentration: the film is not continuous and contains low density of precursor islands. (B) 20 mM concentration: the film has higher density of precursor islands but still not continuous. (C) 35 mM film is the minimum concentration to create uniform and continuous $(NH_4)_2WS_4$ films. However, few micron-size defects (≤10µm) occurred in this primary sample due to debris or insoluble particles of the precursor which adhered on the surface of the substrates. Almost defect-free precursor films have been obtained (see Figure 1(F)) after further optimisation in the sonication process of precursor solution and cleaning procedure of the substrates.

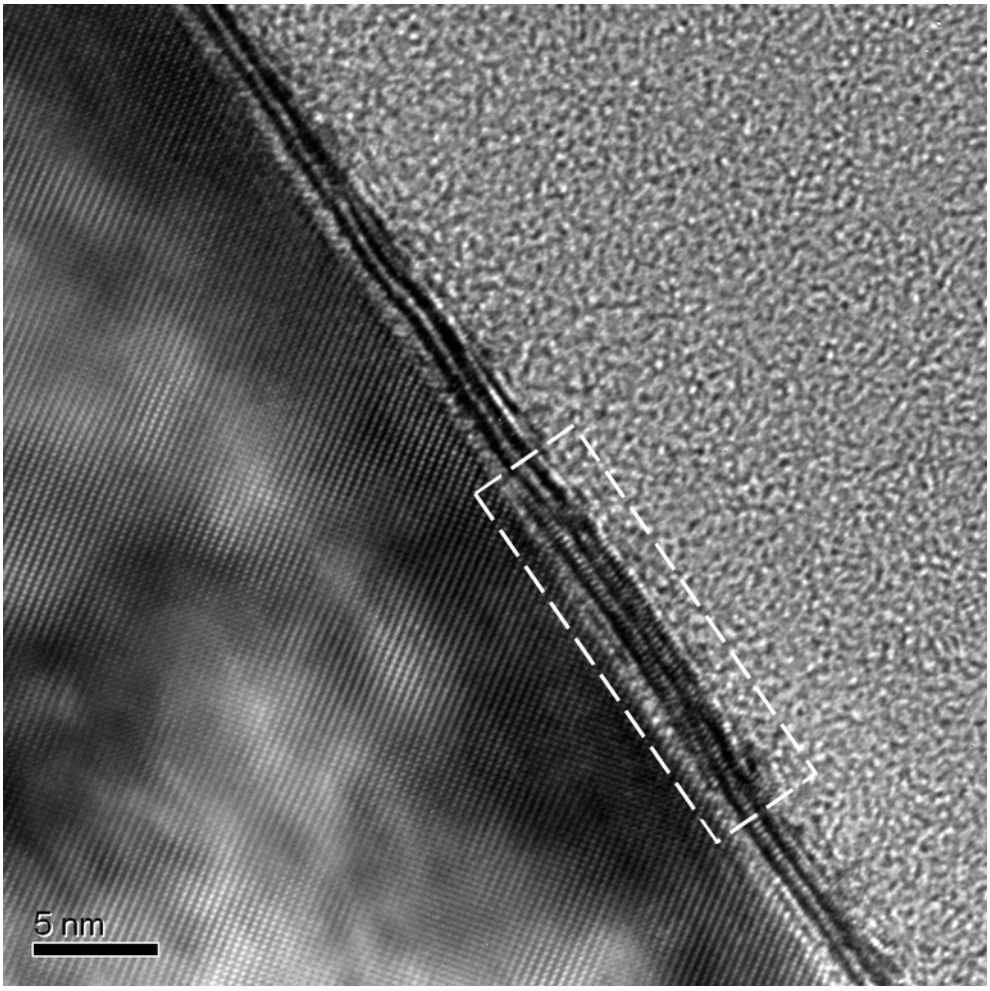

Figure S4. TEM image of few-layer WS_2 films grown on sapphire substrate. The crystalline Al_2O_3 atomic lattice is clearly visible on the left-hand side of the image. The WS_2 film is viewed at a high angle where bilayer and trilayer regions are also highly visible. The bright area on the right-hand side is the protective carbon coating. The cross-section of few-layer WS_2 film shows that the atomic columns are clearly visible confirming the crystallinity order of the film as indicated by dotted box.

It is worth to mention that the TEM lamella was prepared using a Zeiss FIB. The thinning process was performed using a gallium ion beam and introduced some damage in some areas. The result of this damage is that the atoms in certain areas were not resolved by the TEM. However, there are a few undamaged areas where the atom columns are clearly discernible as shown in Fig. S4.

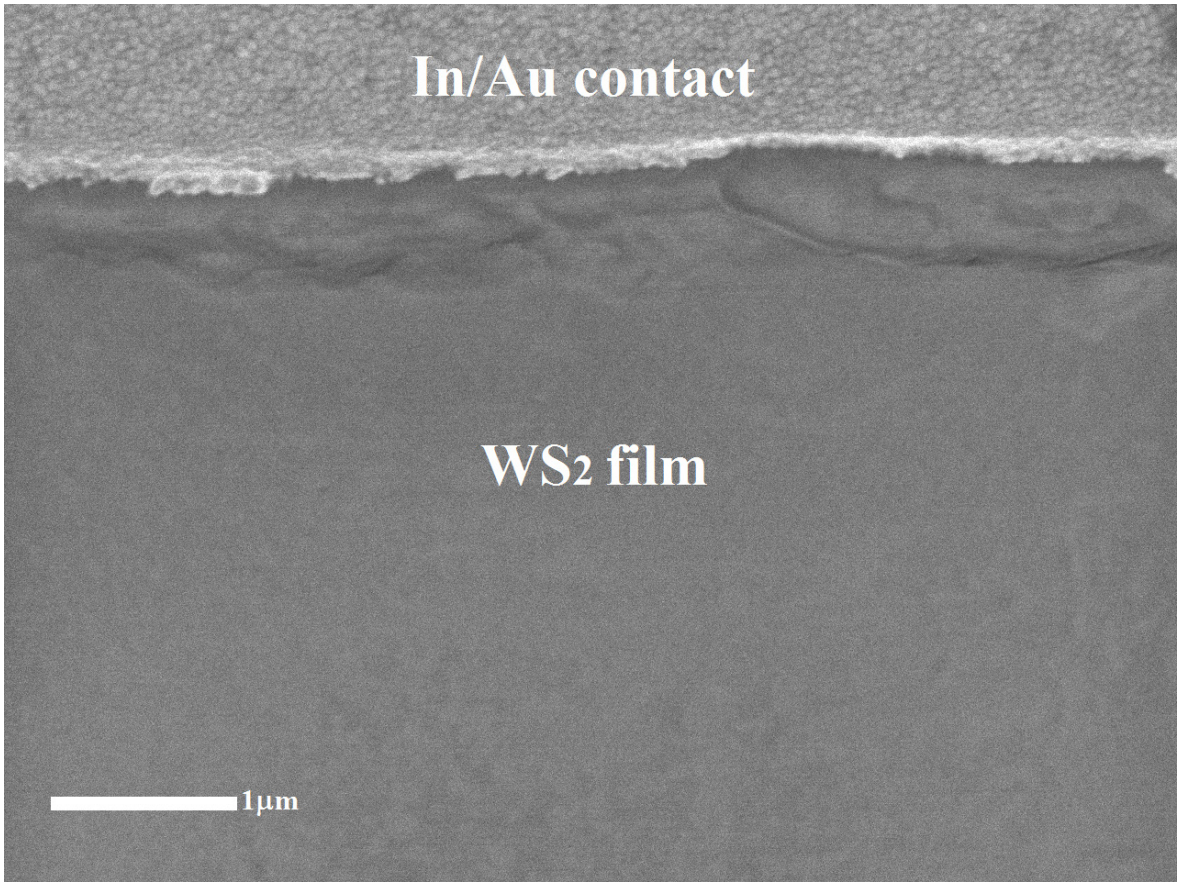

Figure S5. Scanning electron microscopy (SEM) image for a section of few-layer WS_2 FET device which shows the In/Au contact and WS_2 film grown on SiO_2/Si substrate. As can be seen from this SEM image, the WS_2 film is homogenous and featureless due to its high uniformity and is continuous without any discernible defects or pinholes. The darker areas at the interface between the contact and the film and over the film are caused by the residue of the photoresist that occurred due to imperfect lift-off process.

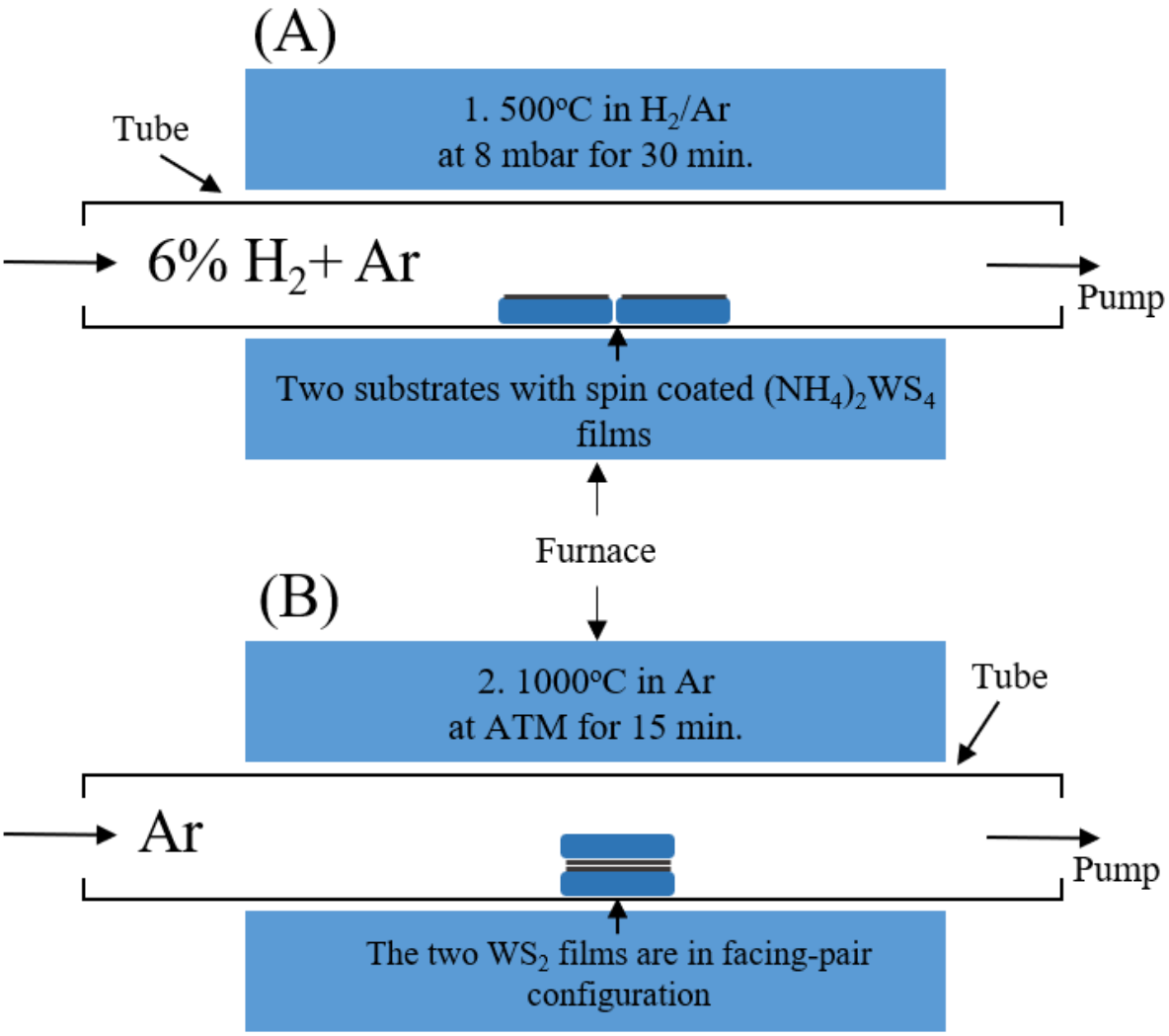

Figure S6. Schematic diagram of WS_2 solution-based synthesis by two annealing steps where (A) is the first annealing step to thermally decompose the spin coated $(NH_4)_2WS_4$ films and (B) is the second annealing step to improve the crystallinity of the WS_2 film.

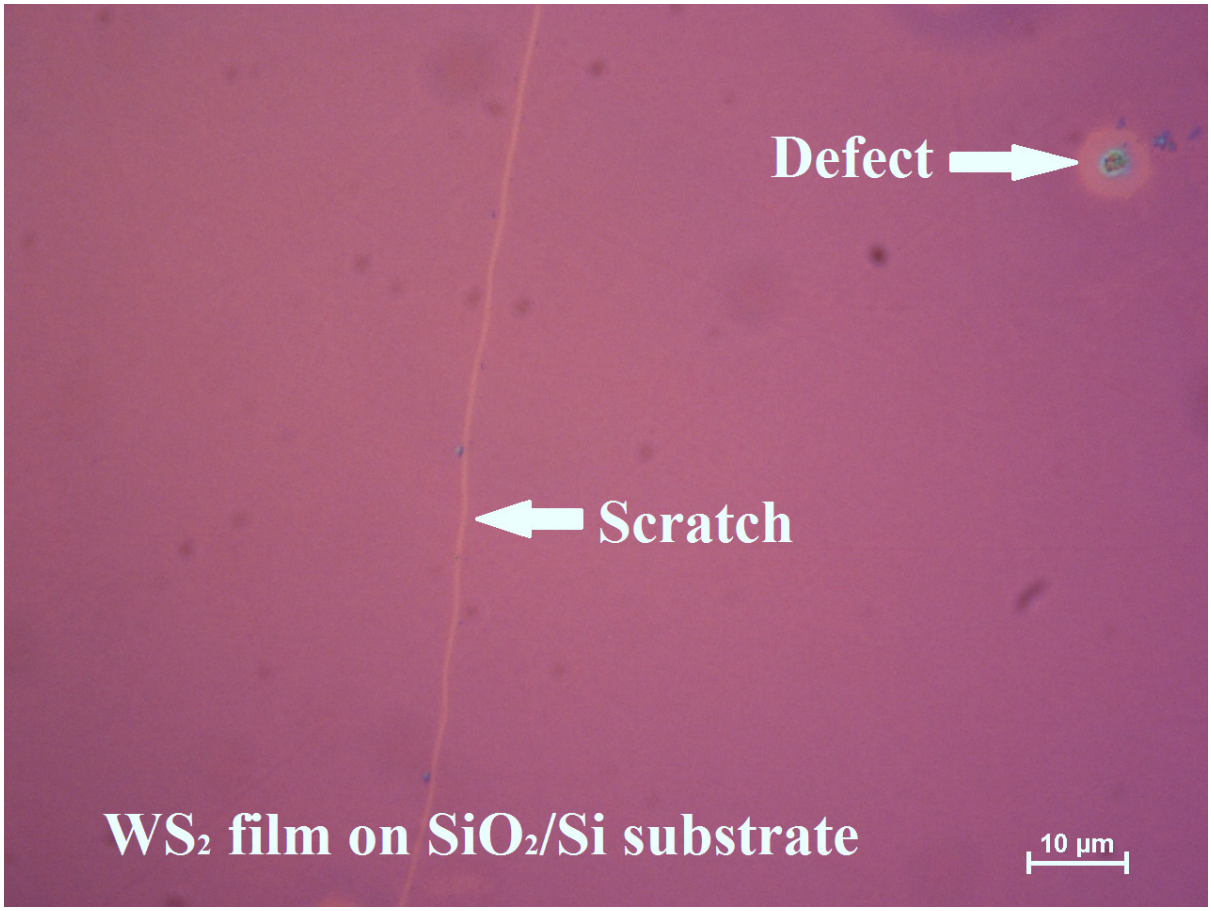

Figure S7. Optical microscope image of few-layer WS_2 film grown on SiO_2/Si substrate by two-step thermal decomposition using precursor concentration 35 mM dissolved in our solvent recipe.